Titre: Title:	High temperature fatigue propagation in astroloy a nickel-base superalloy
Auteur: Author:	Bin Hong
Date:	1989
Type:	Mémoire ou thèse / Dissertation or Thesis
Référence: Citation:	Hong, B. (1989). High temperature fatigue propagation in astroloy a nickel-base superalloy [Mémoire de maîtrise, École Polytechnique de Montréal]. PolyPublie. https://publications.polymtl.ca/56716/

URL de PolyPublie: PolyPublie URL:	https://publications.polymtl.ca/56716/
Directeurs de recherche: Advisors:	J. Ivan Dickson
Programme: Program:	Génie métallurgique

ISBN 0-315-58181-6

Canada

UNIVERSITE DE MONTREAL

HIGH TEMPERATURE FATIGUE PROPAGATION IN ASTROLOY A NICKEL-BASE SUPERALLOY

par

Bin HONG

DEPARTEMENT DE GENIE METALLURGIQUE

ECOLE POLYTECHNIQUE

MEMOIRE PRESENTE EN VUE DE L'OBTENTION

DU GRADE DE MAITRE ES SCIENCES APPLIQUEES (M.Sc.A.)

AVRIL 1989

UNIVERSITÉ DE MONTRÉAL

ÉCOLE POLYTECHNIQUE

Ce mémoire intitulé:

HIGH TEMPERATURE FATIGUE PROPAGATION

IN ASTROLOY

A NICKEL-BASE SUPERALLOY

présenté par: Bin Hong

en vue de l'obtention du grade de maîtrise ès sciences appliquées (M.Sc.A.) a été dûment accepté par le jury d'examen constitué de:

M. Jean-Paul Baïlon, D.Sc.A., président

M. Willian Wallace, D.Sc.

M. J. Ivan Dickson, Ph.D.

SOMMAIRE

Nous avons effectué une étude du comportement de propagation des fissures de fatigue à haute température (650°C) dans un superalliage à base de nickel (Astroloy). L'influence du temps de maintien lors de chaque cycle et du rapport de cyclage mineur (minor cycle load range ratio) sur le comportement de propagation a été également étudiée.

La technique de la chute de potentiel électrique (dc-PD) a été adaptée, étalonnée et mise au point avec succès aux températures jusqu'à 650°C afin de mesurer la longueur des fissures sur les éprouvettes de section carrée présentant une fissure à un coin. La loi de Paris et l'équation de Weibull sous forme log-log ont été utilisées pour analyser les résultats de propagation en fatigue.

Pour une même valeur de ΔK, la fracture d'intensité de contrainte cyclique, la vitesse de propagation était plus élevée à 650°C qu'à la température ambiante surtout pour les valeurs basses et intermédiaires de ΔK. La propagation plus rapide à 650°C devait être reliée à des effets de fluage et de fissuration qui sont fonction du temps, puisque les fissures secondaires et celles présentant un aspect intergranulaire étaient plus nombreuses à 650°C qu'à la température ambiante. Les effets qui dépendent du temps diminuent avec augmentation de la vitesse de propagation (da/dN), ce qui est en accord avec

l'occurrence de moins d'oxidation et de moins de fissuration intergranulaire pour les grandes vitesses de propagation. À ΔK élevé, seulement un léger émoussement des fonds de fissure a été observé cependant, nous avons noté une quantité remarquable de déviations de fissure sur les surfaces de rupture. Ce résultat suggère que les effets d'environnement et de déviation de fissure jouent un rôle plus important que ceux de fluage pour les essais à hautes températures. En général, les résultats indiquent que la fissuration accélérée observée à 650°C était principalement associée à l'occurrence d'une fissuration assistée par l'environnement.

Une augmentation des temps de maintien de qui est passé de 0 sec. à 10 sec. à K_{max} pendant l'essai à 650°C, a augmenté la vitesse de propagation en fatigue dans Astroloy. Une augmentation supplémentaire du temps de maintien jusqu'à 100 sec. n'a produit aucune augmentation supplémentaire significative de la vitesse de propagation. Les observations fractographiques montraient que le temps de maintien de 100 sec. a produit des déviations de la fissure plus prononcées sur les surfaces de rupture, ce qui pouvaient diminuer ΔK_{eff} et compenser pour l'augmentation supplémentaire de la vitesse de fissuration causée par l'influence de l'environnement et du fluage.

L'influence de cyclage mineur sur la vitesse de propagation en fatigue a été observée pendant un essai avec un rapport de 0,1 entre les cycles mineurs et majeurs et pour $\Delta K_{majeur} > 35$ MPa$\sqrt{m}$. Cette influence dépend du rapport de cyclage mineur et majeur, de la fréquence de cyclage mineur, de la forme et de la longueur de fissure, et des effets

cycliques qui pourraient influencer la rupture du film d'oxide au fond de la fissure. Le facteur dominant fut la gamme d'intensité de contrainte pour les cycles mineurs, ΔK_{mineur} puisque les blocs de stries sont apparus clairement à $\Delta K_{mineur} > 3,9$ MPa$\sqrt{m}$.

Deux stries prononcées correspondantes à une région de déviation de la fissure furent présentes au début de chaque bloc et suivies par une région plate constituée de stris fines. Les détails fractographiques montraient que la déviation de la fissure s'est produite après la montée de la charge lors d'un cyclage majeur, et qu'une partie de la propagation pendant les cycles mmineurs suivait généralement le plan de propagation dévié par le cyclage précédent. Les observations suggéraient également que la fissure se soit réinitiée sur un plan à peu près parallèle au plan avant déviation et que des effets de l'interaction entre les cyclages mineurs et majeurs se soient produits.

La microstructure du matériau utilisé dans cette recherche se constitue de grains de grande taille autour desquels se trouvent des grains fins. La fissuration dans les régions des gros grains était transgranulaire. Un mélange de fissuration intergranulaire et transgranulaire a été observé dans les régions des petits grains. Nous n'avons trouvé aucune indication d'une dégradation microstructurale produite lors des essais de fatigue à 650°C pour ce matériau.

ABSTRACT

This research work has investigated the effects of temperature on the fatigue crack propagation behaviour of Astroloy, a nickel-base superalloy. The influence of hold time and minor cycle load range ratio on the high temperature (650°C) crack propagation behaviour was also studied.

An electrical dc-PD technique was successfully adapted, calibrated and implemented at temperatures to 650°C on corner cracked specimens for crack length measurement. The Paris relationship and the Weibull equation in log-log form were used to curve fit the da/dN-ΔK crack propagation data obtained.

The fatigue crack propagation rates increased with increasing temperature especially at low and intermediate ΔK values. These temperature sensitive properties should be related to time-dependent environmental and creep effects, since more intergranular and secondary cracking were observed at 650°C than at room temperature. These time-dependent effects decreased with increasing da/dN values, which is consistent with the lower amounts of fracture surface oxidation and intergranular cracking observed on the fracture surface at high da/dN values. At high ΔK, only a slight amount of crack blunting but significant crack deviations were observed on the fracture surface, which suggests that the environmental and crack deviation effects played a more important role than the creep effects for the high temperature tests. In general, the results suggested that the

accelerated cracking at 650°C was mainly the result of environmentally assisted cracking.

Increasing the hold time at K_{max} during the test at 650°C from 0 to 10 seconds, increased the fatigue crack propagation rate in Astroloy. A further increase of hold time to 100 seconds did not significantly increase the fatigue crack propagation rate further. The fractographic observations indicated that increasing the hold time to 100 seconds results in more pronounced crack deviations on the fracture surface, which can decrease ΔK_{eff} and compensate for the increased time available for the time-dependent contribution to the cracking.

A minor cycle influence on fatigue crack propagation was observed for a 0.1 minor cycle load range ratio test for $\Delta K_{major} >$ 35MPa$\sqrt{m}$. This influence depends on the R-ratio of the minor and major cycle, on the minor cycle frequency, on the shape and length of the crack, and on any cyclic effects which influence the fracture of oxide film at the crack tip. The dominant factor was the minor cycle range of stress intensity, ΔK_{minor}, since blocks or striations clearly appeared for $\Delta K_{minor} > 3.9$ MPa$\sqrt{m}$. Two pronounced striations corresponding to a region of crack deviation were present at the start of each block and followed by a flatter region of fine striations. The fractographic details indicated that the crack deviation occurred after the load increasing portion of the major cycle and that the minor cycle propagation initially followed the deviated crack. These observations also suggested that the crack then reinitiated on a plane close to the

initial fracture plane and that there were interaction effects between the minor and major cycles.

The test material has a necklace microstructure, with the cracking mode in the regions of larger grains being transgranular. A mixture of intergranular and transgranular cracking was found in the regions of small grains. No significant microstructural degradation was found during the fatigue tests at 650°C for this material.

ACKNOWLEDGEMENTS

The mechanical testing portion of this research project was performed at the Structures and Materials Laboratory of the National Aeronautical Establishment, National Research Council of Canada. I wish to thank Dr. W. Wallace for the possibility of using the equipment at this laboratory.

I am specially indebted to my thesis advisor Professor J.I. Dickson for his patience, continuous encouragement and interest in this work. He is a person whom I am thankful for introducing me to this interesting and challenging subject and encouraging me to explore individually and gain experience on a broad scale. Without his guidance, portions of this thesis could not have been accomplished. I also express sincere appreciation to my adviser at the Structures and Materials Laboratory Mr. M.D. Raizenne for his considerable and continuous help with all aspects of the mechanical testing carried out. Thanks for his guidance, encouragement and patience throughout this investigation.

I wish to express my thanks to Dr. W. Wallace, the Head of the Structures and Materials Laboratory, Dr. J.-P. Immarigeon, the Head of the Materials Section, Dr. A.K. Koul, Dr. N. Marchand, Mr. P. Adams, Mr. P. Au, Mr. S.M.R. Pishva and Ms. Li Shiqiong, for helpful discussions.

I wish to thank the technical staff of the Structures and Materials Laboratory for their kind help and technical assistance. In particular, the following people took extra time on my behalf to assist

me in the work performed. These are, Mr. T. Benak, Mr. J. Heath, Mr. R. Gould, Mr. R. Brackett, Mr. P. Blouin, Mr. M. Edkins, Mr. A. Luteyn, Mr. J. Leblanc, Mr. T. Terada, Mr. R. Dainty, Mr. D. Chow, Mr. D. Morphy and Ms. S. Taylor. I would also like to thank Mr. A. Riel, Ms. A. McMackin and Ms. C. Labelle of the Département de Génie Métallurgique. Much appreciation to Mrs. Helen Cuccaro and the typing pool staff at NRC for preparing the manuscript.

A final note of thanks to my parents for their encouragement, understanding and prayers.

TABLE OF CONTENTS

LIST OF TABLES

LIST OF FIGURES

INTRODUCTION

Low Cycle Fatigue (LCF) crack propagation behaviour which replaces creep and stress rupture becomes the dominate failure critical design parameter with the higher requirement of performance in gas turbine discs. A great change in design has occurred such that in the 1960's less than one percent of all rotating components were life limited by LCF where at present LCF has become life limiting for 75 percent of engine disc designs[1].

For ensuring a safe component operating life, the conservative statistical approach, i.e. "safe life" approach, has been to use a lower bound on the mean LCF life that is defined as the number of cycles at which 1 of every 1000 components will develop a crack of 1/32 inch (0.8 mm) in surface length during its design life time[2]. "Safe life" philosophy assumes that components entering service are free from any major and untoward defects, with no inspection required during their design life. This concept, shown schematically in Figure 1[3], also means that 999 out of 1000 disks are prematurely retired from service with many lifetimes of usable service remaining.

In order to continue using these components, a new life management philosophy is now being introduced called "Retirement-for-Cause" (RFC). Figure 2[4] shows the basic RFC concept. For a given component, the number of cycles, N_c, required to propagate a crack from an initial detectable size A_o to critical size A_c can be calculated and verified. An inspection interval is then established at some fraction of N_c designated N_I. It can be seen that over this interval of time,

N_I, no component containing a crack equal to or smaller than A_o could fail catastrophically by reaching A_c.

An advanced design concept for newer components called "damage tolerance" was introduced in the 1970's[1,2], which is an alternative to the "safe life" philosophy currently used in the lifing of critical components in engines. It overcomes two limitations associated with the "safe life" approach[5], these being an inefficient use of available component life and inability to take account of the possible presence of rogue defects which could initiate rapid crack growth and disc failure. These are some basic requirements which should be met before the damage tolerance lifing approach can be successfully implemented[2]:

1. the operational load history of disks should be well known;
2. material crack growth data and fracture behaviour should be available under actual operating conditions;
3. non-destructive inspection (NDI) or other techniques should be available for a sensitive and reliable detection of very small cracks.

Figure 3[2] shows schematically the damage tolerance lifing approach.

High temperature low cycle fatigue (HTLCF) behaviour in service conditions is a key to the implementation of the damage tolerance approach for engine disks. At high temperature, the fracture mechanisms of LCF are more complex, since the fracture may have a time-dependent (creep) component, the fatigue degradation and oxidation is significant, and the crack propagation rate increases with temperature in most applications.

In order to predict the LCF crack propagation rate accurately during laboratory testing, it is necessary to use a realistic loading spectra which is a true representation of the loading condition which the component will experience. In studying the results of these tests which include the effect of overloading and underloading one can determine how a disk material will react when variable amplitude loads are applied to it.

Astroloy alloy is one of the first high strength nickel-base superalloys developed for engine discs and produced by powder metallurgy (P/M) and hot isostatic pressing (HIP) providing good creep and LCF properties. The objective of the present work is to assess the crack propagation life of Astroloy disk material, this property being most important to the damage tolerance design approach.

The goals of this research programme are as follows:

(1) To determine the crack propagation behaviour of Astroloy at room and high temperature.

(2) To analyze the effect of hold time at high temperature on crack propagation rates in Astroloy.

(3) To obtain the high temperature crack propagation data under different minor cycle load range ratios and to estimate their effects on fatigue crack propagation in Astroloy.

(4) To observe the fatigue fracture mode of Astroloy at room and high temperatures, at different hold times and at different minor cycle load range ratios. To find the relationships between the FCP behaviour and the fractographic observations.

(5) To discuss the effect of microstructure variation on crack propagation behaviour through the microstructure characterization of Astroloy.

CHAPTER 1: THE PROCESS METALLURGY AND PHYSICAL METALLURGY OF ASTROLOY

A major objective in gas turbine engineering is the design and manufacture of discs that are both safe and reliable in service. The operating stresses in disks due to centrifugal loads at the rim are greater than 480 MPa, while the operating temperatures on the outer rim are generally no greater than 760°C[6]. Therefore, in the design of aircraft turbine disks the following criteria have to be fulfilled[7] for a material to be used:

(1) The dimensional growth should not exceed a critical value during operation to avoid problems during reassembling after overhaul. Therefore, materials with adequate strength and creep properties must be chosen.

(2) The disk should tolerate an overspeed without rupturing. The burst properties of a disk without significant flaws are determined by the tangential stress and the ultimate tensile strength of the material. If cracks or other comparable flaws are present, the resistance of the disk against unstable fracture is determined by the crack geometry; the stresses perpendicular to the crack and the fracture toughness of the material.

(3) The disk has to tolerate a sufficiently high number of load changes corresponding to a range of 1,000 ∿ 100,000 ground-air-ground cycles. Low cycle fatigue (LCF) is usually considered to be the life-determining factor for such work conditions of disks.

There are a number of superalloys which can fulfill more or less the preceding requirements and were or are being used as turbine disk alloys. They provide the needed high strength at turbine-disk operating temperatures. The capability of those alloys can be compared on the basis of their 100-hour rupture stress at 650°C: Incoloy alloy 901 (635 MPa), Inconel alloy 718 (725 MPa), Waspaloy (760 MPa), and Astroloy (842 MPa)[8]. Obviously, the use of higher strength materials might permit the use of thinner disks, thus saving weight and improving engine performance, although any change in fracture tourghness must also be considered.

Advanced high thrust to weight aircraft gas turbine engines require[9] large diameter turbine disks fabricated from highly alloyed superalloys such as Astroloy. Fabrication of these disks by conventional ingot metallurgy (I/M) results in severe alloy segregation due to the high alloy content and slow solidification times inherent in producing large diameter ingots. Conventional forging of these alloys is therefore very difficult. The uniformity of mechanical properties and microstructure of these disks is also affected. Powder metallurgy (P/M) can result in a more homogeneous product and can resolve many problems observed with conventionally processed material.

1.1 Powder Metallurgy Processing

There are essentially two methods of manufacturing disks, the various stages in both processes are as following[10]:

Conventional (I/M): ingot → billet → forge → machine

Powder (P/M): ingot / direct → powder → consolidate → (forge) → machine

The conventional method begins with a cast ingot prepared by vacuum induction melting (VIM), subsequent vacuum arc remelting (VAR) and casting. This material is drawn down to billet by mechanical working from which forging multiples are sectioned. A series of forging operations reduce such a section to the general shape of the required disk. Figure 1-1[11] shows the microstructure of I/M Astroloy.

The second production route is schematically shown in Figure 1-2[12]. It begins by reduction of the alloy to powder form, either by remelting ingot or producing a (virgin) melt directly and then fragmenting a stream of metal into small droplets. Reconsolidation of the powdered alloy to the desired preform shape can be accomplished by several methods[10]. These include extrusion and forging, hot isostatic pressing (HIP), and hot isostatic pressing plus forging (H+F).

In general, for low carbon (LC) Astroloy alloy, the powder production method is inert gas (argon) atomization[9], which can overcome the oxidation of powders which occurs with conventional P/M techniques, which leads to poor tensile and rupture ductility. Figure 1-3[13] shows typical LC Astroloy powder which was prepared by argon atomization.

There are several methods of consolidation as summarized in Table 1-1[14] for P/M LC Astroloy. Each method contains a HIP process.

The basic method for producing HIP shapes is quite simple, as illustrated in Figure 1-4[15]. A container is filled with powder, outgassed, sealed and placed in an autoclave, where it is subjected to pressure at a high temperature. After consolidation the container is removed and the shape proceeds through the normal inspection, heat-treatment, and machining procedures. The consolidated preform is shown in Figure 1-5[9]. A microstructure typical of an Astroloy preform made by HIP and H+F are shown in Figure 1-6[16] and Figure 1-7[16]. The microstructure of the H+F Astroloy is more complicated than that of HIP Astroloy in three respects[17]:

(1) the forging and subsequent heat treatment produces some fine recrystallized grains in the area of the large grain boundaries. The small recrystallized grains give a "necklace" microstructure (See Figure 2-18 also). This "necklace" Astroloy is one of the best high performance Ni-base superalloys.[47]

(2) moving grain boundaries in the recrystallization process have transformed the γ' not in solution at the forging temperature into large 0.5 to 3 μm particles at the boundaries of the γ grains.

(3) the forging operation has left a stable subgrain structure in the large unrecrystallized grains.

From above, we can find that aircraft engine producers were attracted towards P/M superalloys for two reasons. First, it was thought that the improved homogeneity of consolidated powder billets would offer more uniformity in the final product than cast (I/M)

billets. Second, it was recognized that P/M offered a potential for low cost near net shape manufacture of components such as disks using hot isostatic pressing.

1.2 Chemical composition and Element Function

Since the development of superalloys was spurred by the need of aircraft and industrial gas turbine designers to increase the thermal efficiency of their engines by continuously raising the gas inlet temperature and thereby also increasing the metal temperatures, the results of this development have led to alloy chemistry and processing developments with the goal of utilizing all the strengthening mechanisms known today. P/M LC Astroloy is one of these advanced superalloys, which is used mainly as aircraft turbine disks. The elements which are contained in this alloy (Table 1-2)[18] can be divided into different groups depending on their contribution to strengthening and corrosion resistance[19].

(1) Matrix-class elements —— solid-solution strengthening

The nickel-base alloys have a high tolerance to alloying elements, with preservation of the face-centred cubic (F.C.C.) structure up to 0.8 Tm (where Tm is the melting point). Among the elements contained in Astroloy, Cr, Co, Mo, Ti and Al can contribute to solid- solution strengthening of the γ matrix, i.e., provide high resistance to deformation of the alloy matrix. The main purpose of chromium, however, is to improve corrosion properties, and aluminium is mainly known as a precipitation-strengthening element.

(2) γ'-phase-forming elements —— precipitation strengthening

Although aluminium and titanium serve as potent solid-solution strengtheners in superalloys, their main function is to combine with nickel to form the γ' precipitate, which provides the main strength to precipitation-hardened superalloys such as LC Astroloy.

The γ' phase has an F.C.C. structure [$Ni_3(Al,Ti)$] and a lattice constant which shows only small deviation from that of the matrix (less than 1.5%). Coherence between the two phases is maintained by tetragonal distortion. A consequence of this coherency is the easy homogeneous nucleation of the precipitate, and because of the low value of interfacial energy, a long-term stability at elevated temperature.

Cobalt increases the structural stability of Astroloy at elevated temperatures by raising the solvus temperature of γ'[19].

(3) Carbide-forming elements —— reduction of grain boundary sliding

Carbides in nickel-base superalloys form mostly at the grain boundaries. The carbide formers are chromium, molybdenum and titanium in Astroloy. The role of carbide in superalloys results in two competing effects on high temperature mechanical properties: carbides dispersed at grain boundaries have a beneficial effect on rupture strength by reducing grain-boundary sliding, while carbides of certain morphologies can have adverse effects on ductility. There is also an undesirable chemical effect due to the removal of carbide forming elements from the matrix surrounding the grain boundary.

There are three basic types of carbides in Astroloy. MC carbide which forms first during solidification is coarse and appears

both at grain boundaries and within the matrix of the solidified alloy. It can transform at lower temperatures to the more stable $M_{23}C_6$ carbide. $M_{23}C_6$ carbides can be discontinuous blocky grain-boundary precipitates and are mainly beneficial in this form because they prevent grain-boundary sliding. They can have very detrimental effects on ductility if they form continuous brittle grain-boundary films. M_6C carbides have effects on mechanical properties similar to those produced by $M_{23}C_6$, except that they are more stable at high temperature.

The MC carbides can be transformed into the lower carbides by following metallurgical reactions[20]:

$$MC + \gamma \rightarrow M_{23}C_6 + \gamma'$$

$$MC + \gamma \rightarrow M_6C + \gamma'$$

These reactions are considered to be beneficial, and they are made use of during heat treatment to form discontinuous grain-boundary precipitates. The γ' precipitate which is another reaction product forms an envelope around the carbides, making the grain-boundary layer more ductile.

In LC P/M Astroloy the carbon content has been decreased to a very low level to prevent prior particle boundary (PPB) precipitation[21].

(4) Grain-boundary-active elements —— enhancement of creep strength and rupture ductility

Small additions of boron and zirconium significantly enhance creep properties and rupture ductility. Although the reasons for these improvements are not entirely clear, it is believed that these

elements, because their atomic size, deviate markedly from that of the matrix, segregate to grain boundaries, filling vacancies and reducing grain-boundary diffusion.

Typical Ni-base superalloys may be hardened by γ' precipitation as sketched in Figures 1-8[22]. The γ' in the first generation Ni-based alloys generally was spheroidal, whereas, in later it was cuboidal. The composition of Astroloy is close to that of N-115 alloy.

1.3 Heat Treatment and Microstructure

The heat treatment of conventional cast plus wrought Astroloy forgings consists of a partial solution treatment followed by a two step stabilization and a two step age. The heat treatment cycle is[23]:

1115°C ($\sim$ 15-20°C below the γ' solvus)/4 hrs/315°C/salt quench

+870°C / 8 hrs/air cool

+980°C / 4 hrs/air cool

+650°C /24 hrs/air cool

+760°C / 8 hrs/air cool

The first part of the two-step stabilization (870°C/8 hrs/air cool) is designed to precipitate grain boundary $M_{23}C_6$ carbides and the second part (980°C/ 4 hrs/air cool) is to coarsen these $M_{23}C_6$ carbides, without causing the formation of films. The two-step age (650°C/24 hrs/air cool + 760°C/8 hrs/air cool) is used to maximize the number of γ' particles and minimize their spacing. Conventionally cast and

forged Astroloy contains a high degree of segregation due to the high alloy content and slow solidification times inherent in producing large diameter ingots. The four-step heat treatment is designed to minimize the effects of segregation present in the forgings.

Since HIP'ed LC Astroloy is more homogeneous and has less carbides than cast and wrought Astroloy, a two-step stabilization followed by a two-step age may not be necessary. To determine the effects of varying heat treatment on the consolidations, the compacts were partial solution treated at 1115°C/4 hrs/fan air cool and sectioned by Mark T. Podob[23]. One half received the two-step stabilization and two-step age as outlined above. The other was stabilized and aged at 982°C/8 hrs/air cool + 760°C/8 hrs/air cool. After stabilization and aging, there were no apparent microstructure differences between them[23].

The grain size in LC Astroloy increases with HIP temperature, as may be seen from Figure 1-9[10]. The γ' size increases with aging temperature as shown in Figure 1-10[25]. Extraction replication, as an aid in phase identification indicated that both $M_{23}(B,C)_6$ and MC occur as the carbides phases and M_3B_2 as the boride phase present. $M_{23}(B,C)_6$ was extracted as thick particles (Fig. 1-11)[23].

1.4 Mechanical Properties

Astroloy is a disk material which operates in the intermediate temperature range (550-650°C). Its major properties are high yield and tensile strengths combined with high low-cycle fatigue

and creep strengths[24,26]. The mechanical properties will depend upon alloy composition and heat treatment together with grain size, grain shape, dislocation substructure, and the size, morphology and distribution of γ' and carbide precipitates, all of these in turn depend upon the processing sequence employed.

Figure 1-12[27] gives a tensile property comparison among the different alloys at various temperatures. Figure 1-13[28] shows the result of creep fracture tests of a number of superalloys at 704°C. The results are plotted in terms of time to failure versus the initial stress intensity at the tip of the fatigue crack. Floreen[28,29] has investigated the question that is whether or not the creep crack growth process can be characterized by the stress intensity parameter (K) in a study of Inconel 718 in the temperature range from 595 to 704°C. In this study center notched specimen were used, it was concluded that creep cracking occurred with only a small amount of creep strain at the crack tip and that stress intensity adequately characterizes stresses and strains in the region of the crack tip. For superalloys that are used at high temperature after being heat treated to high toughness and ductility, it must be demonstrated experimentally that K adequately describes the creep crack growth process. Creep crack growth rate data for these alloys are shown in Figure 1-14[29]. Once again a large difference exists between the various alloys.

Since the P/M process substantially minimizes the segregation in alloys, the mechanical properties of P/M Astroloy are better than those of I/M Astroloy, as shown by the data in Figure 1-15[9], tensile strengths are approximately 1-15 ksi over conventional Astroloy

requirements at the temperature of 70°F (21°C) and 1400°F (760°C), both creep- [1300°F (704°C), 74 ksi] and stress-rupture [1400°F (760°C), 85 ksi] strength were also in excess of conventionally processed Astroloy requirements, as shown by Figure 1-16[9]. Low cycle fatigue (LCF) properties of Astroloy are shown in Figure 1-17[9]. The creep and LCF properties of Astroloy will be discussed in 2.1.1 and 2.1.2.

CHAPTER 2: FATIGUE CRACK PROPAGATION AT HIGH TEMPERATURE IN ASTROLOY

2.1 Deformation and Fracture Mechanisms

2.1.1 Creep

Creep is a process by which plastic flow occurs when a constant stress is applied to a metal for a prolonged period of time. Figure 2-1[30] is a typical creep curve, where ϵ_o is the initial strain which follows the application of the load. Stage I is a transient creep region, where the creep rate decreases with time according to $\dot{\epsilon} = \beta t^{1/3}$. Slip within grains and along grain boundaries produces this deformation. At this stage, the effect of deformation strengthening is larger than the effect of recovery softening. Stage II is the steady-state region. The creep rate is constant, with $\epsilon = kt$. In this region, the effect of deformation strengthening is equal to the effect of recovery softening. Stage III is an accelerated region. The creep rate increases with time and when the crack length reaches a critical value, creep failure occurs.

There are four mechanisms of deformation during the creep process[31]:

(1) the glide of dislocations producing slip;

(2) the climb of dislocations leading to sub-grain formation;

(3) the sliding of grain boundaries;

(4) the diffusion of vacancies.

A formula to express the creep crack growth rate of a spherical cavity ahead of a crack has been derived by DiMelfi and Nix[32]. The result of their calculation is:

$$\frac{1}{C} \cdot \frac{dC}{dt} = A\left[\frac{2}{\sqrt{3}}\right]^{n-1} \left[\frac{3K}{2n\sqrt{2x}}\right]^{n} x^{-n/2}$$

where A is a constant, C is the cavity diameter, n is the exponent in the creep equation, X is the distance ahead of the crack and K is the stress-intensity factor.

If it is assumed that the creep crack growth is the result of a cavitation process and that the creep crack growth rate is proportional to the right-hand side of DeMelfi's equation, and if x is identified with grain size, then DeMelfi's equation implies the following:

$$da/dt = B\ (\frac{K}{D})^{n}$$

where B is a constant and D is grain diameter. The data presented in Figure 1-14 has been plotted using this correlation. The fact that a good correlation is obtained for this wide range of materials has been interpreted to imply that grain size is the primary variable in determining the creep crack growth rate.

Figure 2-2[33] shows the results of constant load creep crack growth rates at 765°C, 725°C, 700°C and 655°C in HIP'ed Astroloy. A detailed fractographic investigation[33] of the creep growth specimen shows a completely intergranular fracture path (Figure 2-3.)

But creep effects need not always give rise to a more rapid rate of cracking. A microcreep effect at the crack tip could lead to crack tip blunting, which would effectively decrease the stress in the

region of the crack tip. This mechanism could lead to a decreasing crack propagation rate with increasing temperature.

2.1.2 Low and high cycle fatigue

Fatigue can be classified into two categories: low-cycle fatigue (LCF) and high-cycle fatigue (HCF). For LCF, plastic strain predominates and ductility controls performance. For HCF, elastic strain dominates and strength controls performance. A complete S-N curve may be divided into two portions: the low-cycle range and the high-cycle range. There is no sharp dividing line between the two, we might arbitrarily say that 0 to about 10^6 or 10^7 is low cycle and from about 10^6 cycles to 10^7 or higher is high cycle. The S-N curve of I/M and P/M Astroloy are shown in Figure 2-4[9], the lower lives for P/M Astroloy coincide with typical lives for conventional Astroloy at high alternating stress levels, while at lower alternating stress, even the minimum powder disk lives were well above typical conventional properties.

High cycle fatigue tests therefore consist of applying an alternating stress, S_a, to the specimen until fracture occurs and measuring the number of elapsed cycles that were required to cause this fracture. Figure 2-5[34] summarizes the definitions of the most basic stress and parameters employed in "high-cycle" fatigue.

Low cycle fatigue is strain-controlled fatigue and it considers the strain amplitudes acting at the root of the notch. Low cycle fatigue tests performed at different applied strain amplitudes

permit the achievement of a reliable strain-life diagram (See Figure 2-6)[34]. In this figure, the total strain range $\Delta\epsilon_t$ has been decomposed into an elastic strain $\Delta\epsilon_e$ and plastic strain $\Delta\epsilon_p$. The strain amplitudes are therefore:

$$\frac{\Delta\epsilon_t}{2} = \frac{\Delta\epsilon_e}{2} + \frac{\Delta\epsilon_p}{2}$$

For the higher amplitudes and shorter lives, the plastic strain component dominates the fatigue behavior. At low amplitudes and long lives, it is the elastic strain component which dominates.

Paris and Erdogan were the first to propose that the crack growth rate, da/dN, was related to ΔK, stress intensity factor, through the empirical relationship:

$$da/dN = C\Delta K^n$$

where C and n are material constants. This equation describes a linear region of slope n on a log-log plot as shown for region B in Figure 2-7[34]. As this figure indicates, the Paris relationship is only applicable for a certain range of ΔK. When ΔK becomes too high and K_{max} approaches K_c, the critical value, a rapid acceleration in crack growth occurs (region C in Figure 2-7). As well, when ΔK is decreased below a certain value, the crack growth rate decelerates considerably and there is a threshold value ΔK_{th} below which the crack can be considered as remaining dormant (region A in Figure 2-7). The fatigue fracture mechanisms and influencing factors for the different regions are also shown in Figure 2-7.

Several fracture mechanisms have been proposed for high temperature fatigue as follows:

(1) Deformation induced stacking faults in P/M Astroloy are the dominant fatigue fracture mechanism at high temperature[35].

(2) Figure 2-8[36] gives the diffusion model for fatigue crack propagation mechanism at high temperature. In Figure 2-8(a), under creep condition, there is only a tension stress. A lot of cavities form by diffusion along grain boundaries,the region near the crack tip is strain induced so the cavities get larger. When a compressive stress or cyclic stress (fatigue) has been applied, as shown in Figure 2-8(b), the crack tip resharpens and leads to a large displacement of the crack tip, which meets the cavities in front of it, advancing the crack.

(3) When the cyclic stress was applied to the metal, the grain boundaries will slide, especially at high temperature, a microcrack might be formed at a triple-junction, which is a boundary intersection of three grains. When the crack tip meets these microcracks, the crack advances[37].

(4) The strain-range partitioning approach developed by Manson[38] is based on the belief that the high temperature low cycle fatigue (HTLCF) resistance is degraded as a result of essentially creep deformation and creep damage processes interacting with cyclic deformation.

(5) Coffin[39] regarded the HTLCF life as being governed by a combination of cyclic deformation processes and environmental attack. Figure 2-9[36] shows an oxygen film model. Under the effect of creep and fatigue, when the film breaks, the

grain boundary and matrix will be attacked, then the crack advances.

(6) Powder metallurgy materials often suffer from premature failure associated with non-metallic inclusions[40] and some failure sites were observed at prior particle boundary (PPB) precipitation[41].

Most investigations have shown that the fracture mode is transgranular at low and moderate temperatures[40,41] in LC Astroloy.

2.1.3 Creep fatigue interaction and crack propagation models

Creep fatigue interaction is a special phenomenon that can have a detrimental effect on the performance of metal parts or components operating at elevated temperatures. When temperatures are high enough, both creep strains and cyclic (i.e., fatigue) strain can be present; interpretation of the effect that one has on the other becomes extremely important. For example, it has been found that creep strain can seriously reduce fatigue life. Creep fatigue interaction is a problem that designers of elevated temperature components must deal with to provide reliable service within the creep range[42].

Creep fatigue crack propagation is common to all classes of structural alloys at temperatures where creep rupture is possible. At these temperatures, fatigue is characterized by viscoplasticity and by a significant effect of diffusion which involve principally cavitation and environment attack at grain boundaries. High temperature implies

time dependent strain, diffusion and at least the possibility of creep damage.

Manson[43] has explained the influence of strain-temperature-time phase relationship on the fracture mechanism in low cycle fatigue and given the modes of inelastic strain for microstructural mechanisms. Manson suggested that the high temperature stress relaxation is accompanied by grain boundary sliding. Since the grain boundary sliding stress is assumed to be lower than the flow stress for transgranular slip, when the direction of strain is reversed at low temperature, the flow stress is less than the stress required for grain-boundary sliding. Repeat cycles then accumulate grain boundary shear in tension balanced by compressive plastic strain. At some point this unreversed sliding exceeds the ability of the grain boundary to conform and triple grain junction cracking results.

Damage modes can be represented schematically as limits of an interaction (See Figure 2-10)[36].

A study[33] of creep fatigue environment interaction in LC Astroloy from 650°C to 760°C showed that the acceleration of creep cracking following pure fatigue was observed for the sequential fatigue- creep crack growth tests. Figure 2-11[33] shows the effect of creep on fatigue crack propagation rate.

To describe the fatigue crack growth process in Astroloy, the Paris equation, $da/dN = C(\Delta K)^n$ has been used by Stoloff[40] and the constants found for different conditions in air:

$$1 \text{ Hz}, \quad C = 1.38 \times 10^{-12} \qquad n = 4.0$$

$$20 \text{ Hz}, \quad C = 2.24 \times 10^{-13} \qquad n = 4.3$$

Saxena[44] proposed the new model for fatigue crack growth rate in Astroloy.

$$da/dN = 6.05 \times 10^{-8} (\Delta K)^{2.63} + 1.93 \times 10^{-8} (\Delta K)^{3.46} \sqrt{t_h}$$

where ΔK is stress intensity factor, t_h is hold time during fatigue. Wallace[45] gave an empirical model:

$$\log da/dN = C_1 \sinh\{C_2 \log \Delta K + C_3\} + C_4$$

where C_1 is a material constant, and the other coefficients are functions of load ratio, temperature and frequency which are obtained by from statistical regression analysis.

Astroloy alloys generally are considered microstructurally stable at the temperatures for which they are employed as disks[46]. If they are exposed for prolonged times at temperatures that exceed about 650°C, the strengthening phases may coarsen slightly. However, unless the alloys are operated at temperatures well into or above their aging temperature ranges, no significant microstructure effects will be noted. Carbide precipitation at dislocations may be significant when operating times at 480 to 650°C exceed 10,000 hours. At higher temperatures (725-850°C), microstructural changes more readily occur with time. Furthermore, when stress is applied, the changes may be accelerated. The principal changes are: (a) breakdown of primary carbides; (b) agglomeration of primary geometrically close-packed (gcp) strengthening phases such as γ', and; (c) formation of topologically close-packed (tcp) phases, such as sigma, Laves and mu.

The microstructure of P/M Astroloy after low cycle fatigue is shown in Figure 2-12[35]. Fractographs of fatigue initiation and propagation in Astroloy are shown in Figure 2-13[41] and 2-14[41].

Deformation in Astroloy was more homogeneous than that in Waspaloy (see Figures 2-15 and 2-16)[17]. Well defined slip bands, such as those in Figure 2-15 cutting through the large aging γ' particles, were not as frequently seen. This grain was in a specimen of HIP Astroloy cycled with $\Delta\epsilon/2 = 2\times10^{-4}$. A more typical deformed grain in the same specimen is shown in Figure 2-16. Here the difficulty the dislocations experience in cutting the large γ' precipitates is clearer. The dislocations are jammed into the matrix between the large γ' particles producing a cell-like appearance.

The dislocations in Astroloy are mostly paired, unlike in Waspaloy where dislocations travel singly. This is seen readily in Figure 2-15. This pairing, even in the matrix between the particles, appears to indicate that the dislocations are cutting the fine 0.02 to 0.05 μm diameter γ' particles in the matrix, though they may be having difficulty cutting the large γ'. When ordinary glissile pairs of dislocations cut the γ' in Astroloy (see Figure 2-17[48]), the dislocations appear in pairs even in the γ matrix between the γ' precipitates. The passage of two dislocations restores order to the $L1_2$ ordered structure of γ'. The passage of only a single dislocation produces a high energy antiphase boundary.

2.2 Factors Influencing Fatigue Crack Propagation

2.2.1 HIP and heat treatment

Fatigue crack propagation behaviour is sensitive to microstructures in Astroloy [49], therefore it is affected by the processing

histories of the components. Figure 2-18[50] shows the range of microstructures which in principle can be obtained in P/M superalloys by various thermomechanical processing (HIP, forging, heat treatment) techniques and the effect which these microstructures will have on the dynamic mechanical properties at various temperatures. The microstructure of a P/M superalloy is determined by HIP and heat treatment.

Figure 1-9 shows that grain size increases with HIP temperature. Low aging temperatures produce fine γ'. Experiments have proven that fine gamma prime (γ'), large grain size is beneficial to fatigue crack propagation resistance (see Figure 2-19[25]), because fine γ' leads to a coarse planar deformation mode. Decreasing grain size promotes grain boundary failure which is due to the increased grain boundary volume, for it dilutes effectively the composition in these elements segregated to the grain boundaries such as B and Zr. B is effective in reducing the susceptibility of Ni to environment embrittlement at high temperature.

2.2.2 Testing temperature

From Figure 2-2, we find that the creep crack propagation rates increase with temperature in Astroloy. This is because the activation energy for environmental interactions at elevated temperature is higher. There would come a point at which oxidation or another crack tip environment interaction would become the dominant factor leading to an increased fatigue crack propagation rate. An alternative method of examining the effect of temperature for nickel-

based superalloys is shown in Figure 2-20[51], crack growth rates at a fixed ΔK (in this case, 33 MPa$\sqrt{m}$) are plotted as a function of reciprocal temperature for a variety of nickel-based superalloys. Clearly the rate dependence at low temperature is much lower than at high temperatures. Figure 2-20 also shows as a dashed line scatterband the data normalized with respect to the elastic modulus. This is included in order to give some insight into the factors governing the temperature dependence of fatigue crack propagation. It is proven[51] that the crack growth rates are inversely proportional to fatigue flow stress and elastic modulus. As shown in Figure 2-20, the normalized curves do not increase as rapidly as the original curves, which indicates that the drop in flow stress with temperature may be making a contribution, particularly at the high temperatures.

2.2.3 Variable amplitude loading [52-56]

In the mechanical load-time history acting on a component in service, load is virtually always of the variable amplitude variety and only rarely of the type known as constant amplitude loading. Variable amplitude loading should therefore be the system of choice in the majority of fatigue tests.

The prediction of fatigue crack growth rate under variable amplitude loading is complex, especially when the retardation or acceleration effects caused by overload and underload are non-negligible. Research has shown that a thorough understanding of the effect of various variables on the fatigue crack propagation under

variable amplitude load fluctuation is essential for the development of accurate predictive methods of assessing the fatigue life of engineering structures. Although the effects of variable amplitude loading on fatigue life are presently not well established, the fracture mechanics approach to fatigue crack propagation under these conditions appears to be the most promising.

Between the extremes of a simple constant amplitude loading and a complex random stress history, there is a multitude of patterns of varying complexity which can be described by either analytic expressions or numerical techniques. The first step in doing so is to characterize the stress or strain fluctuations in a manner that is suitable for further study, the use of techniques based on probability theory being perhaps the most appropriate.

The stress or stress amplitude spectrum for a particular location in a component may be defined in terms of the frequency of occurrence of the maximum peak stress or stress amplitudes, respectively.

Several investigators have observed that changes in cyclic load amplitude may result in either retarded or accelerated fatigue crack growth rate.

Figure 2-21(top)[57] presents a schematic of a crack growth curve, crack length (a) versus number of applied fatigue cycles (N), illustrating the common effects of a single overload on previously unretarded crack growth. When the crack growth produced by constant load amplitude fatigue is interrupted by an overload, crack growth accelerates corresponding to the overload. Thereafter, the rate of

crack propagation quickly decelerates, and after a small number of subsequent fatigue cycles the rate of crack growth achieves a minimum. This deceleration to a minimum rate of crack propagation is known as delayed retardation and the period of delayed retardation is defined as the number (N_{DR}) of post-overload fatigue cycles required to achieve the minimum crack growth rate. Following delayed retardation, crack growth continues at a near minimum rate for an extended period, and the exhaustion of the retardation process is marked by an acceleration of crack growth to regain the unretarded rate. The total period of crack retardation, N^*, is defined as the number of cycles during which crack growth rate is retarded following an overload application. The nature of the transient crack propagation behaviour that results following an overload is further revealed by differentiating the crack growth curve, Figure 2-21 (top), to give crack propagation rate, da/dN, as a function of N, Figure 2-21 (bottom).

Wei and Shih[58,59] studied the effect of delay, or retardation in the rate of fatigue crack growth, produced by load interactions in variable amplitude loading in order to predict the fatigue live and/or inspection intervals for a mill annealed Ti-6Al-4V alloy. This investigation showed that fatigue crack growth delay is strongly dependent on all loading variables, eg. the ranges of the stress intensities, their ratio and the number of constant amplitude cycles between the high tensile load cycles.

The explanations for delay phenomenon are residual stress, crack closure, or a combination of these mechanisms. A crack tip geometry model advocates that high tensile load cycles cause crack tip

blunting which in turn causes retardation in fatigue crack growth at the lower load fluctuations until the crack is resharpened. The residual stress model suggests that the application of a high tensile load cycle forms residual compressive stress in the crack tip vicinity that reduces the rate of fatigue crack growth. The crack closure model postulates that the delay in fatigue crack growth is caused by the formation of a zone of residual tensile deformation left in the wake of a propagating crack that causes the crack to remain closed during a portion of the applied tensile load cycle. Consequently, fatigue crack growth delay occurs because only the portion of the tensile load cycle that is in excess of the crack-opening level is effective in extending the crack.

Many complex cycle by cycle models have been developed and proposed in the literature to take these factors into account. Unfortunately, these models require the knowledge of the order of appearance of the peak and valleys of the loading history, information which is not always available. In fact service loadings are most of the time available in the form of amplitude distributions rather than waveform signals or succession of peak and valleys. Moreover, in an ASTM round-robin investigation using a flight simulation loading for which the cycle interaction effects are expected to be important, a simple linear accumulation model produced surprisingly good predictions as compared to much more complex models[54].

This simple model can be expressed as

$$\Delta K_{eq} = [\frac{1}{K} \sum_{i=1}^{K} \Delta K_i^n]^{1/n}$$

where ΔK_i is the individual consecutive ranges of stress intensity factor (or half-cycles), n is the Paris law exponent and ΔK_{eq} is intended to replace ΔK in the Paris law equation:

$$da/dN = C[\Delta K_{eq}]^n$$

On the other hand, variable amplitude tests are specific to the loading history employed and cannot be directly used for a different loading history.

The amount of retardation due to tensile overload decreases as temperature increases. Furthermore, the magnitude of retardation exhibited at the higher temperature was found to be relatively small for overload values generally exhibited in a turbine disk load spectrum. Thus retardation effects may not be as significant at high temperature as at intermediate temperature where fatigue crack retardation may be more pronounced.

2.2.4 Specimen geometries for fatigue crack propagation

Selection of a fatigue crack propagation test specimen is usually based on the availability of the material and the types of test systems and crack monitoring devices to be used. Any specimen configuration with a known stress intensity factor solution can be used in fatigue crack growth testing, assuming that the appropriate equipment is available for controlling the test and measuring the crack dimensions. These specimens can be divided into two main classes[1], specimens containing through cracks, where the crack length is constant through the thickness of the testpiece, and specimens containing

part-elliptical cracks. The former class includes[60] the compact tension specimen, the keyhole specimen, the single edge cracked specimen, the double edge cracked specimen, the centre cracked specimen, the notched specimen, and the single edge cracked bending specimen. The latter class includes the corner crack specimen, the surface cracked tensile specimen, and the surface cracked bending specimen. The most widely used types of specimens for fatigue crack propagation are the centre cracked tensile specimen (CCT), the compact tension specimen (CT), and the corner crack specimen (CC). Figure 2-22(a)[42] shows the CCT specimen geometry, while Figure 2-22(b)[60] shows the geometry of the CT specimens, which is one of the most popular for crack propagation. Figure 2-22(b) also shows the variation of normalized stress intensity with normalized crack length for this specimen, based on:

$$K = \frac{YP}{BW^{\frac{1}{2}}}$$

where P is the load applied to specimen,

$$Y = [439.20\ (a/w)^{\frac{1}{2}} - 294.2(a/w)^{3/2} + 1118(a/w)^{5/2} - 1842(a/w)^{7/2} + 1159(a/w)^{7/2}$$
$$11159(a/w)^{9/2}$$

Figure 2-22(c)-1[2] shows the geometry of the CC specimen. The initial notch is introduced by 'nicking' one corner of the specimen to simulate the growth of quarter circular cracks in engine components. Figure 2-22(c)-2[60] shows the variation of normalized stress intensity with normalized crack length for quarter-circular cracks in the corner crack specimen. The CC specimen is best suited for obtaining crack propagation data for engine disk applications, for it simulates the

typical 'non-through' crack geometries such as corner and surface cracks identified as critical in most engine disc applications.[1]

Figure 2-23[61] shows the difference of fatigue crack propagation rates between CT and CC specimens under 200°C, where alloy B is a P/M nickel-base superalloy. The corner-crack propagated progressively slower with increasing ΔK than expected from the CT specimen behaviour for $\Delta K \geq 25$ $MNm^{-3/2}$. This difference was related to the ratio of plane stress to plane strain crack growth along the crack front, and was accentuated at 200°C as a result of a change in fatigue crack growth mechanisms at this temperature under plane stress conditions.

2.2.5 Other factors

Frequency: The fatigue crack propagation rate, da/dN, decreases with increasing cycling frequency in Astroloy (see Figure 2-24[40]). Neglecting environment effects the range of the crack tip displacement decreases with frequency increase because a higher effective flow stress is required at high strain rate. The effect of environment and creep tend to be minimized as the test frequency is increased. The lower the frequency, the larger the plastic zone size and the faster the crack propagation rate.

Environment: Crack propagation rates are higher in air than in argon for Astroloy (see Figure 2-25[40]). From the point of environment-controlled fracture mechanisms (see p.18), the effect of environment can often promote fatigue crack propagation, but it need

not always lead to more rapid crack propagation. It has been proposed that oxidation products could form a thin film in the crack tip region and prevent crack resharpening during the unload portion of the cycles. If the stresses are sufficiently low, the oxidation products in the crack tip region will not be cracked and an elevation of the threshold ΔK can result.

Hold time: Comparing with pure fatigue testing, holding the specimen at peak stress, increased the fatigue crack propagation rate (Figure 2-26[40]). The mechanism responsible for this increase however, was not clearly identified. When the load ratio R was increased, the fatigue crack propagation rate is also increased.

CHAPTER 3: CRACK LENGTH MEASUREMENT TECHNIQUES [2,34,62-66]

Crack length measurement is very important in fatigue testing because of the effect on the accuracy of fatigue life prediction. In the early stages of the development of crack length measurement techniques, optical and fracture surface observations were the main methods available to research workers in the field of fracture and fatigue. Since the 1960's techniques such as the compliance methods, potential difference, acoustic emission and ultrasonics have been used for the detection and measurement of crack extension during fracture and fatigue. More recently new techniques such as back face strain measurement and a.c potential difference methods have become available. Crack length measurements are required not only for the measurement of the propagation rate da/dN, but also for the calculation of the applied value of ΔK. Different techniques are available each presenting inherent advantages and disadvantages.

3.1 Optical Method

The optical method largely relies on the use of travelling microscopes or telescopes. Crack length measurement is often aided by markings etched or scribed on the specimen surface without necessitating the interruption of the test. It is a method which can be easily employed at room temperature in air or in other clear environments. The method is relatively inexpensive, does not require calibration, and does not require the specimen to behave in a linear

elastic manner. This method, however, measures the surface crack length only, not the interior crack length and it is time consuming, not amenable to automation and requires the specimen surface to be accessible and in a well polished condition.

3.2 Eddy Current Method

This crack length measurement technique uses an eddy current probe positioned adjacent to the crack surface to produce an electrical signal indicating the crack. A second probe unaffected by the crack is employed for reference comparison. The disequilibrium voltage between the two receivers is fed into a comparator. It has been used for centre cracked sheets but should be adaptable to other geometries. The method can easily be incorporated in automatic crack length detecting systems. This technique is expensive and only produces surface measurements.

3.3 Strain Gauge Filament Method

Electrically conducting wires are attached to the specimen in such a way that they are broken by an advancing crack thereby producing stepwise changes in resistance. It is a convenient method to employ and used for all specimen geometries. Very low costs are involved and the method is easily adapted for automatic crack length measurement. But only surface measurements are produced and the technique is not well suited to high temperature and aggressive environments.

Difficulties may arise in the location of the gauges and in ensuring that the filament is always broken by the passage of the crack tip and only the crack tip.

3.4 Ultrasonic Method

The ultrasonic method involves the transmission and reception of a pulsed ultrasonic beam intersected by a crack. The transducer employed is positioned slightly ahead of the crack and as soon as the echo reflected from the crack attains a preset maximum threshold, the automatic displacement of the transducer is triggered. This displacement stops as soon as the echo decreases below a preset minimum threshold. Crack profiles of embedded cracks can be obtained using the ultrasonic method. Incorporation in automatic systems is relatively easy and non-metals can also be studied. Relaxation from linear elastic behaviour is readily accommodated and accuracies of ±0.2 mm can be achieved. The probe displacement variation does not require calibration and the time-of-flight variation is simply calibrated and very versatile. Ultrasonic methods are not well suited to small, thin specimens. The methods are expensive and have not yet been developed for high temperature or aqueous corrosion studies.

3.5 Acoustic Emission Method

Acoustic emission involves the attachment of a sensing transducer to the test piece which oscillates at its resonant frequency

on receiving elastic stress wave from sources of deformation. The detected emissions are then amplified, selectively filtered and conditioned and then counted either on a periodic basis as a rate of emission or as a cumulative total. The method is adaptable to any specimen geometry. The technique is capable under many circumstances of resolving details of continuous cracking processes with higher sensitivity than other methods particularly during tests on high strength materials under constant load. Acoustic emission equipment is expensive and sophisticated. The filtering of extraneous noise from the testing machine and grips etc. may prove to be tedious and difficult. The correlation of emissions with crack length is poor unless the equipment is capable of measuring the energy associated with the emissions. The signals are material and mechanical/thermal treatment sensitive and tend to be less prolific in lower strength materials.

3.6 Compliance Methods

(1) Crack opening displacement (COD)

The basis is to measure the COD usually between points along the loading line or, in the case of bend and wedge opening specimens at the front face. A COD extensometer is attached to the lips at the crack mouth and produces an electrical voltage which is proportional to the value of δ(COD). For high temperature testing, extension arms may be used to transfer the displacements to regions of lower temperature where conventional gauges may be used. The cost of the method depends

on the application and ranges from low cost in room temperature air to moderately expensive in high temperature aggressive environments. The specimen does not have to be visually accessible and can provide an "average" crack length figure where crack front curvature occurs. The method is easily incorporated in automatic crack length measurement systems. But separate calibration tests may be necessary in some cases. Clip gauges and, to a lesser extent, transducers are not very robust. The COD technique is only applicable to specimens where reversed plasticity effects are small. Because the large reversed plasticity will change the effective modulus during the test, it will lead to errors in crack length or load.

(2) Back face strain (BFS)

Strains are measured on the back face (i.e. uncracked ligaments) of CT, or T type wedge opening loading (WOL) specimens[66] by strain gauges or possibly clip gauges or transducers in large test pieces. A specimen calibration is required and this method provides an average measurement of crack length. The cost depends on the particular application and ranges from very inexpensive in room temperature air test to moderately expensive in high temperature aggressive environments. The BFS technique shows excellent characteristics for incorporation in automatic systems. The method can be used in conjunction with a relatively inexpensive device for maintaining constant K conditions during crack growth in CT and T type WOL specimens. But the technique should only be applied to specimens where time dependent, time independent and reversed plasticity effects are small.

(3) Crack tip strain

The strain close to but behind the crack tip is measured using surface mounted strain gauges. The method is only suitable for bend specimens. The initiation of crack growth is detected even in the presence of large scale plasticity. The cost of the method depends on the particular application but is usually a low cost item. The method is only of limited value in crack length measurement and problems occur in thick specimens where events on the surface of the specimen do not reflect crack growth in the interior. Although large scale plasticity is tolerated, the onset of general yielding may make interpretation difficult.

3.7 Potential Drop Methods

The last method which will be considered is based on the fact that the specimen cross sectional area is reduced as the crack propagates, resulting in a change in the electrical resistance of the specimen. A constant direct or alternating current is passed through a specimen in such a way that a change in crack length alters the potential difference of suitably placed contact points, usually in the vicinity of the crack tip. The method is suitable for all test piece geometries.

The potential drop (PD) technique is a widely accepted method of monitoring crack initiation and growth in controlled laboratory tests, which provides a total measurement, including crack front curvature and fulfills the requirements of a high degree of accuracy and

repeatability for data acquisition.[1,2,67] The PD technique has proven to be particularly valuable in tests where inelastic deformations or creep occurs because the calibration of the technique does not rely on elasticity theory and also offers a virtual independence from the applied loading cycle thus allowing various mission spectrum loading sequences to be employed.[67] This also allows for changes in test parameters to be implemented without stopping the test. The technique is suitable for any crack geometry, especially for surface crack and the PD system is highly stable and well suited for automatic control and long term, high temperature testing.[1,2,71,73,74] There are two types of PD techniques employed for crack length measurement[1,67,72]; the alternating current (ac) and the direct current (dc) method. Although the ac method has been reported to offer higher sensitivity and improved accuracy over the dc method, it is much more complex and difficult to implement and the equipment required is more elaborate. The dc PD technique was the technique selected for this test program.

3.7.1 ac potential drop

The calibration for different specimen geometries is simple since there is a linear relationship between output and crack length and there is no specimen size dependence. The method does not require any delicate instrumentation to be attached to the specimen. Some relaxation from linear elastic behaviour is easily accommodated. Incorporation in automatic systems is simple and average crack length

values can be produced. The technique is capable of high sensitivity. By comparison with the dc method, a strong advantage of the ac system is its suitability to large test pieces and to surface cracks in specimens and structures. But moderately high cost is involved with the ac technique. Connecting wires have to be carefully placed and must not be moved during tests because of lead interaction effects. Although considerable improvements have recently been made, there is a requirement for high stability in the electronic and long term stability may be difficult to achieve. Bridging of crack surface by corrosion products may produce erroneous crack length readings. Electrical insulation of specimens is required.

3.7.2 dc potential drop

This system does not require any delicate instrumentation to be attached to the specimen and moderately low costs are involved. The technique is simple, robust and advanced electronics are not necessary. Average crack length values can be produced and the method is well established for certain specimen sizes and geometries. The system is highly stable and well suited for automatic control and long term, high temperature testing. Small relaxations from linear elastic behaviour are easily accommodated. Some theoretical calibrations are available but the relationships between PD and crack length are relatively complex and it is more usual to carry out calibration tests. The method can not distinguish between crack extension and changes in the external dimension of the specimen such as would occur during general

yielding. There is some uncertainty in stress corrosion and corrosion fatigue studies over the possible interface with electro-chemical conditions adjacent to the crack tip. For decreasing ΔK/constant COD tests, the crack faces may short electrically thus producing an underestimate of crack length. In some cases the loading grips may have to be electrically insulated from the test machine. Thermal electromotive force (emf) may cause problems and the dc method is not suitable for large specimens. The details of the dc method are further explained in the following section.

3.7.2.1 The principle of dc PD technique

The principle of the dc PD technique requires that a constant current be applied through the specimen which is being tested. As the crack grows, the cross sectional area through which the current can flow is decreased and then the electrical resistance of specimen (R) is increased according to the equation:[2,67]

$$R = \frac{\rho L}{A}$$

where ρ is the material resistivity which is a constant under the same temperature, L is the length of current travel which is increased during the test and A is the cross sectional area available for current flow. When a constant current (I) is maintained through a body of increasing resistance, the voltage drop or PD (V) across that body is governed by Ohm's law:[1,2]

$$V = IR$$

The increase of voltage from the increase of resistance should therefore reflect the increase of crack length in the test specimen and

the PD can then be measured and calibrated as a function of crack length.

3.7.2.2 dc PD technique systems

A possible set-up for fatigue testing and crack length measurement system is shown in Figure 4-1.[2] Since metals are excellent conductors of electricity, relatively high current was necessary to obtain a reasonable signal to noise ratio in the dc method. This high current however, causes heating in the current leads and the lead specimen junctions which not only affects the resistance of the leads but causes a thermal emf problem.[73,74] These problems can be minimized by employing a pulsed current system.[2,67] In such a system, the current is only turned on for the data acquisition sequence, typically involving 2 seconds for stability and 1 second for data acquisition at high temperature, so that the leads and junctions do not have time to heat up appreciably.

In order to eliminate the temperature effects, current variation, thermoelectric effects and drift of the system, a reference voltage is measured. The reference voltage can be measured at a location far from the crack or on a separate piece of identical material located in the same testing environment.[2,68]

A computer is used in this application for both control of the test and data acquisition, for it overcomes the problems of labour which is time consuming and also promotes the sensitivity and accuracy of the measurement system.[2]

In order to enhance the accuracy of the technique, the computer was programmed to stop cycling and maintain a maximum load plateau during data acquisition which overcomes any closure effects at the crack tip and magnetic-mechanical effects during cycling.[1,67]

Based on the method described above, the ratio γ is

$$\gamma = \frac{(V_{on}-V_{off})_{notch}}{(V_{on}-V_{off})_{reference}}$$

where the V_{on} and V_{off} are the voltages during current on and off, respectively. The ratio γ is material and specimen size independent and is just dependent on the location of both the current input leads and the voltage measuring probes and on the crack geometry.

The optimal position of the voltage probes is located on cross corners of the notch and specimen edge and as close to the notch as possible, since the voltage probes in the above position are insensitive to small errors in positioning providing the maximum increase in voltage over other locations. The selection of an optimum position for the current leads is arbitrary. It was decided to follow the recommendations of the AGARD cooperative test programme procedures which located the current leads on the top and bottom edges at the load line.[67,73]

3.7.2.3 Calibration

The application of potential drop methods is totally dependent on an accurate calibration relating output voltage to crack length. There are a lot of methods for this purpose, such as

theoretical, analogue and experimental methods, etc.[1,2,67,69,70,73,74]

Theoretical calibrations are based on the solution to Laplace's equation which relates the current flow and is a time independent heat flow equation for specific boundary conditions of a given test piece geometry where for a strip of metal of constant thickness and width containing a transverse crack. For a homogeneous specimen in which the current flows only in the plane of the specimen then the steady electrical potential V and at a point (x,y) is given by

$$\frac{\partial V^2}{\partial x^2} + \frac{\partial V^2}{\partial y^2} = 0$$

Analogue method is based on the pattern of electrical potential distribution and current flow in a specimen depending only on its profile. A 2D slice through the specimen may be conveniently modelled by a sheet of aluminium foil cut to the same geometry as the test piece. A stable current is passed through the foil, the foil is slit in small increments with a scalpel to simulate a crack extending from the notch. After each increment the crack length is measured with a travelling microscope and the corresponding potential drop is read using a digital voltmeter (DVM) capable of 1 μV resolution.

Experimental calibration curves have been obtained by measuring the electrical potential difference: (1) across machined slots of increasing length in a single test piece by employing the travelling optical microscope; (2) across a growing fatigue crack where the length of the crack to each point of measurement is marked on the fracture surface by a single overload cycle or by a change in mean stress, or;

(3) across a growing fatigue crack in a thin specimen where the length of the crack is measured by surface observation. In the third case, the calibration curve can be obtained by drawing a straight line through two data points. The first marking is obtained by heat tinting, the second marking is the clearly distinguishable transition line between the fatigue and overload areas.[2]

Table 3-1[34] summarizes the principal characteristics of the different techniques available for measuring crack lengths.

CHAPTER 4: EXPERIMENTAL PROCEDURES

Fatigue crack propagation rate tests were carried out at room temperature and 650°C on corner crack Astroloy specimens under five loading conditions. A dc-PD technique was used to measure crack length.

4.1 Test Apparatus

A general schematic of the high temperature fatigue test rig is shown in Figure 4-1. Figure 4-2 shows the LCF apparatus with the specimen and Figure 4-3 shows the LCF apparatus with the furnace. In this design, the apparatus consisted of a computer controlled servo-hydraulic load frame system; a furnace; grips; cooling coils; thermo-couples; temperature controllers; a DC power supply; amplifiers and PD wires. A direct current potential drop (dc-PD) technique was used for crack length measurement (see Figure 4-4).

A closed loop, hydraulic driven, servocontrolled MTS test system was used for all tests which was interfaced to a PDP 1134 computer. The computer was used to: (1) generate load command signals and frequencies; (2) define statements to turn the DC power supply on and off at certain times; (3) obtain through the analogue to digital (A/D) data acquisition system voltage readings from the specimen and the reference specimen at timed intervals, and store them on a hard disk.

In fatigue tests, a load frame is required for reacting forces applied to the specimen and to support the specimen and sensors. Provisions are made to assure convenience in mounting the specimen and auxiliary equipment such as environmental chambers. A load frame usually takes the shape of a rigid closed box structure providing good stiffness, minimum weight and a resulting high resonant frequency[75]. For this work, an MTS 311.11 load frame was used which consists of four vertical columns that join a movable crosshead and a fixed platen, with a force rating of 250 kN.

A three zone electric muffle furnace (Marshall), shown in Figures 4-1 and 4-3, was used for heating. Electrical resistance coils embedded in refractory mouldings define the shape of the heated space. The heater assembly is encased in refractory insulation. In order to compensate and obtain a uniform central temperature, there are three coils in the furnace, defining a central zone and two outer zones. The furnace is a split type which consists of two longitudinally divided half cylinders hinged together. A furnace of this design provides a high degree of access to the specimen-grip-PD system and is available in a variety of ratings governed primarily by the bore and heated length. The furnace can operate up to 980°C (1800°F). At the top and bottom of the furnace openings, 902 Precision Machinable ceramic plates were used to seal the ends of the furnace during testing. The maximum continuous service temperature for the ceramic plates is 1150°C. Temperature control and measurement was achieved using OMEGA series 6100 temperature controllers and an OMEGA model 660 temperature indicator (see Figure 4-5). Three K-type thermocouples were located at

the top, center and bottom zones of the furnace (they are shown in Figure 4-5) through McDaniel ceramic tubes. The temperature indicator was wired in parallel with the center thermocouple.

A set of long grips were used for this work (see Figure 4-6). These grips were made of Nimonic 105, a nickel based superalloy. Two 6.5 mm diameter water cooling coils, made of copper, were wound around the upper and lower grip ends to reduce the temperature in the grips and to protect the load cell.

Crack lengths were measured using a dc-PD system. The system includes (1) a Sorensen power supply, which was used as a constant current source with an output capability of 0 to 25 amps at 0 to 10 volts d.c.; (2) three amplifiers, Pacific model 8255, which were used to amplify the voltage readings into the 0 to 10 volt range. The first amplifier was connected in series with the second to increase the gain of the specimen signal, the third was used for the reference signal. The amplified analog voltages were then fed through analog to digital converters to a PDP 1134 computer; and (3) the voltage drop wires which connected the specimen to the amplifier wires, were made of titanium and had diameters of 0.005 inches (0.1275 mm). The d.c. current used for crack length measurement was 23 amperes with initial voltage values of 180~200 μV at 600°C.

4.2 Testing Material

The material used in this investigation was taken from an RB-211 high pressure turbine disc supplied by Rolls Royce PLC which was

HIP'd P/M Low Carbon (LC) Astroloy (see Chapter 1). Figure 4-7 shows the as-received RB-211 fan disc material. The chemical composition of as-received Astroloy is given in Table 4-1. A typical material was heat treated at 1093°C for 4 hours and fan air cooled, aged at 650°C for 24 hours, air cooled and aged at 760°C for 8 hours and air cooled. The mechanical properties of the material are listed in Table 4-2[18].

In order to investigate the FCP behavior at different orientations, the material was cut in three directions: (1) BT; Bore-Tangential; (2) BA: Bore-Axial, and (3) WR: Web-Radial. Figure 4-8 shows the specimen orientations and locations in the disc.

4.3 Loading Conditions

The test program was divided into two sections: "baseline" tests and "verification" tests. Baseline tests were used to obtain the fatigue crack propagation rates at constant amplitude with or without dwell times. Verification tests were used to determine the effect of minor cycles upon the fatigue crack propagation behaviour.

The waveforms used for the baseline tests were ramp waveforms with 0, 10 and 100 second dwell times at maximum load as shown in Figures 4-9, 4-10 and 4-11. The waveforms used for verification tests consisted of 450 and 900 minor cycles with 0.05 and 0.1 minor cycle load range ratios on 100 second dwell time at maximum load (see Figures 4-12 and 4-13). For all of the tests, the R or load ratio of the major cycle was 0.1.

4.4 Crack Length Measurement

Crack lengths were measured by a dc-PD method with a resolution of approximately 0.05 mm. A schematic of the dc-PD system used in this work is shown in Figure 4-4.[2,77] In order to ensure that the voltage rise due to the increase in crack length was the dominant measurement, a large current must be applied through the specimen. This large current if continually applied would cause heating in the current leads and the load-specimen junctions. This problem was solved by employing a pulsed current system.[67] The current is turned on for six seconds which allows the current to stabilize before data acquisition.

In order to enhance the accuracy of the technique, the computer was programmed to stop cycling and maintain a maximum load level during data acquisition, as seen in Figure 4-14. In order to eliminate the effects of current variations and temperature upon voltages during the test, a reference potential is required from a dummy specimen. The dummy specimen is connected in series with the current supply. The reference was made from Ti-6Al-4V, with the same corner crack (CC) geometry as the test specimen.

The current in and out positions were located at the ends of the grips. The PD wires were located at each side of the notch and as close to the notch as possible (see Figure 4-15). By ensuring that the wires are welded at the same locations for each test one enhances reproducibility, decreases sensitivity to placement error and provides the maximum increase in voltage over other locations.[67]

Each set of voltage readings consisted of current-off and current-on values for the reference and the specimen potential, respectively. In order to compensate for voltage fluctuations, the current-on minus the current-off values were used for measurement purposes. For each measurement, 20 data sets were obtained and averaged to obtain mean values. A calibration curve was determined by drawing a straight line[2] through two known sets of voltage and crack lengths. The data sets used for this calibration curve were the initial notch length and the final fatigue crack length, shown in Figure 4-16. Therefore, the formula for the line can be obtained using:

$$y = mx + b \qquad (4\text{-}1)$$

where y is voltage, x is crack length, m is slope of the line and b is the intersection point on the y axis. Hicks and Pickard[69] investigated the calibration methods of the PD technique in the corner crack specimen and compared the results of analytical and finite element methods (see Figure 4-17). Figure 4-17 shows the effect of the PD probe's distance from the centreline (Z) of the notch. In the tests, Z = 0.08 to 0.20 mm were measured. It is imperative to note that the tests were always stopped before an overload failure occurred in order that the final fatigue crack length and associated voltage could be accurately measured.[2] The optical measurement of the final crack length on the fracture surface was determined by taking the average of five readings; one at each side surface of the specimen (the surface crack length), and another three at angles of 22.5°, 45° and 67.5° with respect to one of the side surfaces.

4.5 Software Control

An MTS control system linked to a PDP 1134 computer was used to generate the command waveshape, the data acquisition and the dc PD control. The application program was written using a high level modified BASIC language specifically for mechanical testing purposes. A flow chart of the program is shown in Figure 4-18 and the software subroutines are listed in Appendix A. The general organization of the program can be divided into three main sections:[76] function generation, dc-PD control, and data acquisition.

For function generation, an FG call in software activates the hardware segment generator in the MTS 433.50 interface providing the repeats frequency. The tests were conducted using a series of ramp waveshape segments tied together to produce the desired sequences.

The dc-PD control portion of the program was used to control current-on and current-off for data acquisition. It consists of a RELAY call for current on and off. The MTS 433.50 interface uses a reed relay circuit to activate the D.C. power supply.

The data acquisition is done by means of the A/D subsystem in the MTS 433.50 interface. The test program defines the channels and sample rates which are to be recorded during the appropriate time interval. The data acquisition routine consists of TIME, DACQ, START, QUIT calls. The TIME call sets the time interval of data acquisition. The DACQ call is used to determine the type of data to be acquired, to define the selected analog to digital channels of the MTS 433.50 interface and to choose the number of clock interrupts to elapse between the

taking of data. START, QUIT calls were used to start and stop the action of data acquisition.

The number of elapsed cycles was counted using a subprogram which accumulated the elapsed numbers as a function of the number of repeats in FG routine.

4.6 Data Processing

When fatigue crack propagation occurs in the specimen, the cross section of the notch plane is decreased which leads to the voltage between the PD wires increasing. At the conclusion of the test, a curve of increasing voltage, V, versus cycles, n, was obtained. The voltage values where converted to crack length values using the compliance curve described in Section 4.4. Therefore, a curve of 'a' versus 'N' was drawn from V-N and a-v data. Crack growth rates were calculated by dividing the change in crack length by the number of elapsed cycles during this change. The corresponding ΔK values were calculated from the average crack length, $\bar{a}$, and the stress applied on the remaining section:[68]

For $\bar{a}/w < 0.2$:

$$\Delta K = 1.16 \frac{2}{\pi} \Delta\sigma\sqrt{\pi\bar{a}} \qquad (4\text{-}2)$$

For $\bar{a}/w > 0.2$

$$\Delta K = \{1.12-0.13(\bar{a}/w)+1.84(\bar{a}/w)^2+0.11(\bar{a}/w)^3+0.8(\bar{a}/w)^4\}\frac{2}{\pi} \Delta\sigma\sqrt{\pi\bar{a}} \qquad (4\text{-}3)$$

$$\Delta K = K_{max} - K_{min} \qquad (4\text{-}4)$$

where ΔK is the change in stress intensity at the crack tip and w is the width of the specimen.

4.7 Fractography and Microstructure Characterization

For all loading conditions, the fracture surface were observed using either a JEOL JSM 820 or 840 Scanning Electron Microscope (SEM). The initial notch and final crack lengths were measured and fracture modes at different ΔK values were investigated. The crack propagation rates were determined from the spacings of the striations on the fracture surface and compared with calculated values.

Selected specimens were sectioned at right angles to the loading axis, polished and etched for microscopic examination. The morphology and the distribution of precipitates and grain boundaries were observed. To produce grain contrast, a solution of 5 grams of $CuCl_2$, 100 ml of ethanol and 100 ml of HCl was used as an etchant. In order to find the secondary crack propagation modes and paths, selected specimens were sectioned diagonally, mounted, polished and etched.

CHAPTER 5: EXPERIMENTAL RESULTS

The raw data obtained from the fatigue crack propagation tests consisted of PD values (V) for given numbers of cycles or major cycles in the case of tests with major and minor cycles. This number of cycles or major cycles N can also be considered to be equivalent to a similar number of flights. From the known relationships between V-N and V-a, the crack lengths (a) versus the numbers of flights (N) were obtained. Then, the crack propagation rates (da/dN) versus the change in stress intensity, Δk, were plotted for each specimen and the data were fitted by the Paris and the Weibull curve fitting models. The numbers of flights to failure for several stress ranges were obtained by using the critical stress intensity (K_{IC}) for this material and the Paris coefficients (n and c) for each test condition.

Fractographic analyses for each test specimen were performed. Secondary crack morphology and microstructural analyses were carried out for the room temperature and 650°C specimens.

5.1 Calibration Curves

The calibration curves which represent the voltage change (Vc) from dc-PD technique as a function of crack length (a) for each specimen are shown in Figures 5-1 to 5-7. These curves were obtained by drawing a straight line through two known pairs of voltage drop and crack length data. These two points corresponded to the initial notch and final crack lengths. The tests were always stopped before an over-

load failure occurred in order that the final crack length and associated voltage drop could be accurately measured. The optical crack lengths on the fracture surfaces were determined by taking the average of five readings: two at the side surfaces of the specimen, and the other three at angles of 22.5°, 45° and 67.5° with respect to one of the lateral surfaces (see Figure 4-16). The crack lengths were somewhat (up to 1mm) shorter at the lateral surfaces (0° and 90°).

Since the initial notches in the corner cracked specimens are small and variable, it is not feasible to normalise the potential changes to the initial potential value. Hence the final average crack length on the specimen is measured and the data are normalised with respect to the remote potential gradient, V(RG), where

$$V(RG) = \frac{V_F - V_I}{a_F - a_I} \qquad (5\text{-}1)$$

a_I and V_I are the initial notch length and voltage change, a_F and V_F are the final crack length and voltage change. The calibration curve is a plot of $V_c/W \cdot V(RG)$ versus a_c/W. The equation of the calibration curve, which is a straight line, is assumed as follows:

$$y = mx + b \qquad (5\text{-}2)$$

where y is $V_c/W \cdot V(RG)$ and x is a_c/W. Thus the calibration curve takes the form of:

$$\frac{V_c}{W \cdot V(RG)} = \frac{a_c}{W} + \frac{a_F V_I - a_I V_F}{W(V_F - V_I)} \qquad (5\text{-}3)$$

where W is specimen width. The relationship between potential drop measured (V_c) across the crack radius (a_c) is:

$$V_c = \frac{V_F - V_I}{a_F - a_I} a_c + \frac{a_F V_I - a_I V_F}{a_F - a_I} \qquad (5\text{-}4)$$

Table 5-1 gives the loading sequence type and the values of calibration curve parameters, a_I, V_I, a_F, V_F, V(RG), $(a_F V_I - a_I V_F)/W \cdot (V_F - V_I)$, for each test specimen.

5.2 FCPR Expressions

5.2.1 Data Processing

The da/dN data were obtained by using a secant method[78] which is based on the plot of crack lengths (a) versus the corresponding numbers of flights (N). These plots are shown in Figures 5-8 to 5-14 for each test specimen. Two neighbouring data of crack length were taken (a_i,a_{i+1}) and the da/dN was obtained by following form:

$$da/dN = \frac{\Delta a}{\Delta N} = \frac{a_{i+1} - a_i}{N_{i+1} - N_i} \qquad (5\text{-}5)$$

where N_i and N_{i+1} are numbers of flights corresponding the crack lengths a_i and a_{i+1}.

The Δk values were calculated using the expressions described in section 4.6 where the crack lengths (a) took the average crack lengths between two neighbouring data. It takes the form of:

$$\bar{a} = \frac{a_i + a_{i+1}}{2} \qquad (5\text{-}6)$$

where $\bar{a}$ is the average crack length.

The crack propagation data are presented in tabular form for each specimen in Tables 5-2 to 5-8.

5.2.2 Paris Relation and Coefficients

Paris and Erdogan were the first to propose that the FCPR(da/dN) was related to stress intensity factor ΔK in 1963,[79] through the emprical relationship:

$$da/dN = c(\Delta K)^n \qquad (5\text{-}7)$$

where 'c' and 'n' are material constants for given values of temperature, frequence and load ratio. This equation describes a linear region of slope 'n' on a log-log plot, or region II.

The method used for the regression of the da/dN-ΔK data to obtain the Paris relationship was the least-squares method. In this method, the distances of the data point from the regression line are calculated. Their square values are summed and the regression line found which minimizes this sum. We assume that the equation of the regression line is:

$$y = a + bx \qquad (5\text{-}8)$$

where 'a' and 'b' are unknown constants. For example, there are five data sets for the regression, the coordinates of these five data are (x_1,y_1), (x_2,y_2), (x_3,y_3), (x_4,y_4) and (x_5,y_5), respectively. The distances from the data to the regression line are d_1, d_2, d_3, d_4 and d_5, respectively, where (from equation 5-8):

$$d_i = y_i - (a + bx_i) \qquad (5\text{-}9)$$

The least-squares regression line is obtained by so choosing 'a' and 'b' such that:

$$d_1^2 + d_2^2 + d_3^2 + d_4^2 + d_5^2 = \sum_{i=1}^{5} d_i^2 \qquad (5\text{-}10)$$

is a minimum. Based on this principle, we get:

$$\sum_{i=1}^{n} d_i^2 = \sum_{i=1}^{n} [y_i - (a+bx_i)]^2 = \sum_{i=1}^{n} (y_i - a - bx_1)^2$$

$$= \sum_{i=1}^{n} (y_i^2 + a^2 + b^2x_i^2 - 2ay_i - 2bx_iy_i + 2abx_i)$$

$$= \sum_{i=1}^{n} y_i^2 + na^2 + b^2 \sum_{i=1}^{n} x_i^2 - 2a \sum_{i=1}^{n} y_i - 2b \sum_{i=1}^{n} x_iy_i + 2ab \sum_{i=1}^{n} x_i$$

If we complete the square, first on 'a', then on 'b', we get:

$$\sum_{i=1}^{n} d_i^2 = n[a-(\bar{y}-b\bar{x})]^2 + (\sum_{i=1}^{n} x_1^2 - n\bar{x}^2) \left[b - \frac{\sum_{i=1}^{n} x_iy_i - n\,\bar{x}\,\bar{y}}{\sum_{i=1}^{n} x_i^2 - n\bar{x}^2}\right]^2$$

$$+ \sum_{x=1}^{n} y_i^2 - n\,\bar{y}^2 - \frac{\left(\sum_{i=1}^{n} x_iy_i - n\,\bar{x}\,\bar{y}\right)^2}{\sum_{i=1}^{n} x_i^2 - n\,\bar{x}^2} \qquad (5\text{-}11)$$

where $\bar{x}$ and $\bar{y}$ are the sample means of the x's and y's. Obviously,

$\sum_{x=1}^{n} d_i^2$ is minimized if:

$$b = \frac{\sum_{i=1}^{n} x_iy_i - n\,\bar{x}\,\bar{y}}{\sum_{i=1}^{n} x_i^2 - n\,\bar{x}^2} \quad \text{and} \quad a = \bar{y} - \overline{bx} \qquad (5\text{-}12)$$

Thus, the equation of the regression line can be obtained. In this study, 'b' is the Paris coefficient 'n' and 'a' is the Paris coefficient 'c'.

The FCPR's as a function of stress intensity factors for the seven tests can be seen in Figures 5-15 to 5-21 with the Paris lines superimposed. Table 5-9 provides a summary of the Paris coefficients for each specimen.

5.2.3 Weibull Equation and Coefficients

Since the Paris relation of the form $da/dN = c\ (\Delta K)^n$ does not account for the two extreme regions (region I and II) in the FCPR data, a four parameter Weibull analysis was undertaken to fit the FCPR data in the three regions. The form of the equation is given as follows:[80,81]

$$da/dN = e + (v-e)\left[-\ln\left(1 - \frac{\Delta K}{K_b}\right)\right]^{1/S} \qquad (5\text{-}13)$$

where 'e' is the threshold parameter, K_b is the stress intensity value where da/dN is indefinitely large, 'v' is the characteristic value and 's' is the shape parameter. This equation can represent two extremes of FCP referred to as the threshold region (region I) and the region of instability (region III). In the region of instability, the maximum ΔK for FCP is limited by the material's fracture toughness through the parameter K_b. When da/dN increases, the $\Delta K/K_b$ term goes to 1, the $-\ln (1 - \Delta K/K_b)$ term thus increases rapidly at the onset of fast fracture. In the threshold region, da/dN is zero and Δk_{th} takes the form of:

$$\Delta K_{th} = K_b \{1 - \exp [- (\frac{e}{e-v})^s]\} \qquad (5\text{-}14)$$

In order to determine the four Weibull parameters, the method of least-squares curve fitting, described in Section 5.2.2 was used. The following steps are followed to obtain the parameters of Weibull equation:

(1) K_b is the stress intensity value where da/dN becomes indefinitely large. For the present material, K_b was estimated to be approximately 130 MPa$\sqrt{m}$ for room temperature and 120 MPa$\sqrt{m}$ for 650°C from the curve-fitting procedure.

(2) For least-squares fitting, the following quantity must be minimized:

$$D = \sum_{i=1}^{n} \{ \frac{da_i}{dN_1} - e - (v-e) [-\ln (1 - \Delta K/K_b)^{\bar{s}}] \}^2 \qquad (5\text{-}15)$$

where 'n' is the number of data points. This equation was solved by determining the quantities $\frac{\partial D}{\partial e}$ and $\frac{\partial D}{\partial (v-e)}$, and setting these values equal to zero. The resulting solutions obtained were as follows:

$$v-e = \frac{\Sigma x_i y_i - \frac{(\Sigma x_i)(\Sigma y_i)}{n}}{\Sigma x_i^2 - \frac{(\Sigma x_i)^2}{n}} \qquad (5\text{-}16)$$

$$e = \frac{1}{n} [\Sigma y_i - (v-e) \Sigma x_i] \qquad (5\text{-}17)$$

where $y_i = da_i/dN_i$ and $x_i = [-\ln(1-\Delta K_i/K_b)]^{\frac{1}{s}}$

(3) Choose the parameter 's' from a range of S_i to S_f and maximize the value of the correlation coefficient. In this study, the 's' values ranged from 0.5 to 1.

(4) Using constant values of x_i and y_i, the values of 'e' and 'v' can be obtained from equations 5-16 and 5-17.

The Weibull equation coefficients for each specimen are reported in Table 5-10 and the FCPR's as a function of stress intensity for the seven tests are shown in Figures 5-22 to 5-28 with the Weibull lines superimposed.

5.3 Applied Stresses Versus Numbers of Flights to Failure

For most structural materials, the tolerable critical flaw sizes are much larger than any initial undetected flaws. However, for structures subjected to fatigue loading, these initial cracks can grow throughout the life of the structures. Thus, an overall approach to preventing fracture or fatigue failures assumes that a small flaw of certain geometry exists after fabrication. This flaw can either cause brittle fracture or grow by fatigue to a critical size, a_{cr}. For design purposes, the numbers of flights (or cycles) required to grow a initial flaw (a_o) to a critical crack (a_{cr}) must be greater than the design life of the structures.

In order to obtain the relationship between applied stresses and the numbers of flights to failure, two material parameters must be known: the stress intensity at the critical value, K_{IC}, and the da/dN vs ΔK relationship. The following steps are then followed:

1. An initial flaw size, a_o, is assumed. It is equal to 0.2 mm for our corner cracked tests.

2. The final critical crack size, a_{cr}, was calculated using the form:

$$\Delta K_{IC} = \left\{1.12-0.13\left(\frac{a_{cr}}{W}\right)+1.84\left(\frac{a_{cr}}{W}\right)^2+0.11\left(\frac{a_{cr}}{W}\right)^3+0.8\left(\frac{a_{cr}}{W}\right)^4\right\}\cdot\frac{2}{\pi}\cdot\Delta\sigma\cdot\sqrt{\pi a} \qquad (5\text{-}18)$$

where K_{IC} is the critical stress intensity, 130 MPa$\sqrt{m}$ at room temperature and 120 MPa$\sqrt{m}$ at 650°C. W is the specimen width-10 mm for the corner crack specimen. $\Delta\sigma$ is the stress range,

$$\Delta\sigma = \sigma_{max} - \sigma_{min} \qquad (5\text{-}19)$$

3. A crack growth integration is performed between a_o and a_{cr} using the Paris relationship described in section 5.2.2 to obtain the numbers of flights to failure, N_f, for a given $\Delta\sigma$, where:

$$N_f = \int_{a_o}^{a_{cr}} \frac{da}{c(\Delta K)^n} \qquad (5\text{-}20)$$

These results are of particular interest because the da/dN vs ΔK relationships have been determined for two temperature regions and different load sequences.

4. The data is then plotted in graphical form as N_f vs $\Delta\sigma$ as shown in Figures 5-29 to 5-35 for specimens BT1 to BT10, respectively.

Table 5-11 reports the calculated N_f values at different load level values for each test specimen.

5.4 Temperature Effects

The tests of specimens BT1 and BT7 were carried out with the same loading sequence, loading sequence type 1 (see Figure 4-10), which is a trapezoidal load waveform with 10 seconds of hold time at maximum load per cycle. BT1 was tested at room temperature and BT7 was tested at 650°C.

The crack lengths vs the numbers of flights for specimens BT1 and BT7 are shown in Figures 5-8 and 5-13. From these figures, one observes that room temperature test has a much longer life than high temperature test (650°C) to approach a same crack length. For example, specimen BT1 took 11500 flights to arrive at a 2 mm of crack length, and specimen BT7 took 2680 flights to arrive at the same crack length.

Figure 5-36 compares the fatigue crack propagation rate (FCPR) between room temperature test (BT1) and high temperature test (BT7). High temperature fatigue test shows a higher FCPR than room temperature test, especially at lower da/dN rates or ΔK values. For example, the FCPR in the high temperature test is approximately 8.2 times greater than that in the room temperature test when the 24 $MPa\sqrt{m}$ of the ΔK value. The difference of FCPR between room and high temperature decreases with increasing the Δk values. For example, the FCPR at high temperature are approximately 4.1 and 2.1 times greater than that at room temperature under the 45 and 70 $MPa\sqrt{m}$ of the ΔK values, respectively. When the da/dN is 8.3×10^{-6} m/cycle where the value of ΔK is approximately 100 $MPa\sqrt{m}$, the FCPR of room and high temperature converges together.

When comparing the numbers of flights to failure of the specimens BT1 and BT7 for a given load level, one can find that the room temperature test has a much longer life than the high temperature (650°C) test (see Figures 5-29 and 5-34). For example, at a load level of 90 kN the numbers of flights to failure for the room temperature test is 17543 compared to 2727 for the high temperature test.

5.5 Hold Time Effects

The tests on specimens BT2, BT7 and BT5 were carried out with loading sequence types 2, 1 and 3 under 650°C (see Figures 4-9, 4-10 and 4-11), which corresponds to a trapezoidal load waveform with 0, 10 and 100 seconds of hold time at maximum load per cycle, respectively.

The crack lengths vs the numbers of flights for specimens BT2, BT7 and BT5 are shown in Figures 5-9, 5-13 and 5-11 respectively. From these figures, one finds that the specimen with no hold time took a much larger number of flights to arrive at the same crack length than the specimens with 10 and 100 seconds of hold time. The specimen with 10 seconds of hold time took the least number of flights to arrive at a given crack length. The effect however is more pronounced between 0 and 10 seconds than between 10 and 100 seconds of hold time. For example, the number of flights for specimens BT2, BT7 and BT5 are approximately 8300, 3000 and 3800 flights to arrive at a crack length of 2.5 mm.

Figure 5-37 shows the effects of hold time on FCPR. The data indicates that the FCPR increased with increasing hold time for short

hold times with no significant difference on FCPR when the hold times were 10 or 100 seconds for this material. For example, the FCPR's of specimens BT2, BT7 and BT5 are approximately 9.31×10^{-7}, 1.7×10^{-6} and 1.75×10^{-6} m/cycle respectively when the $\Delta K = 45$ MPa$\sqrt{m}$.

When looking at this data as the number of flights to failure, specimens BT2, BT7 and BT5 are 4176, 2727 and 2398 flights respectively at a load range of 90 kN.

5.6 Minor Cycle Load Range Ratio Effects

Specimens BT5 and BT4, BT10 and BT6 were tested at 650°C with loading sequence types 3, 5 and 4 (see Figures 4-11, 4-13 and 4-12). All of these tests were carried out with a trapezoidal waveform with 100 seconds of hold time at maximum load per cycle. There were no minor cycles during the 100 seconds of hold time for specimens BT5 and BT4 (0 minor cycle load range ratio tests). There were 900 minor cycles with 0.05 minor cycle load range ratio, and 450 minor cycles with 0.1 minor cycle load range ratio on 100 seconds of hold time for specimens BT10 and BT6, respectively.

The crack lengths vs the numbers of flights for specimens BT5, BT10 and BT6 are shown in Figures 5-11, 5-14 and 5-12. From these figures, it is seen that the larger the minor cycle load range ratio the shorter the life. The effect however is more pronounced between 0.1 and 0.05 than between 0.05 and 0 minor cycle load range ratio. For example, the numbers of flights for specimens BT5, BT10 and BT6 are

3590, 3410 and 2550 respectively, to arrive at a crack length of the 2 mm.

The FCPR's for the 0 and 0.05 minor cycle load range ratio tests are very similar for a given ΔK value. The FCPR for the 0.1 minor cycle load range ratio test is approximately the same as the 0 and 0.05 minor cycle load range ratio tests when the ΔK values of the major cycle are less than 35 MPa$\sqrt{m}$ (see Figure 5-38). When the ΔK values of the major cycle are greater than 35 MPa$\sqrt{m}$, the FCPR for the 0.1 minor cycle load range ratio test increases at a faster rate than the 0 and the 0.05 minor cycle load range ratio tests with increasing ΔK values. These results therefore indicate that there was no effect of minor cycle on the FCPR when the minor cycle load range ratio was less than 0.05. There are effects of minor cycle on FCPR when the minor cycle load range ratio is 0.1, especially when the ΔK values of the major cycle are greater than 35 MPa$\sqrt{m}$. For example, the FCPR for specimens BT4, BT10 and BT6 are 5.5×10^{-7}, 5.2×10^{-7} and 6.1×10^{-7}m/cycle, respectively, at a ΔK value of 27 MPa$\sqrt{m}$. When the ΔK value increases to 45 MPa$\sqrt{m}$, the FCPR for specimens BT4, BT10 and BT6 are 1.57×10^{-6}, 1.68×10^{-6} and 3.5×10^{-6} m/cycle, respectively.

Figures 5-31, 5-35 and 5-33 show the numbers of flights to failure at different load levels for the 0, 0.05 and 0.1 minor cycle load range ratio tests. For example, the numbers of flights to failure for specimens BT4, BT10 and BT6 are 2673, 2715 and 2034 flights respectively at a load range of 90 kN.

5.7 Fractography and Microstructure

5.7.1 Fractography

The fracture surfaces of all the test specimens were observed by scanning electron microscopy. For all specimens, the fractographic aspects changed from strongly crystallographic cracking at low stress intensity (ΔK) to fatigue striations at intermediate ΔK, with these striations changing from crystallographic to non-crystallographic with increasing ΔK. At high ΔK values, many dimples appeared, which gives the fracture surface a partially ductile cracking aspect. Crack deviation and blunting lines with a spacing approximately equal to the macroscopic FCPR were observed on stereomicrography pairs and the observations of matching surfaces. Striation-like features with interstriation spacings which are much smaller than the macroscopic FCPR were also observed and should correspond to slip band traces within the region of propagation by crack tip stretching.

Room Temperature Fracture Surface Morphology:

The typical fatigue fracture morphology for the room temperature test (specimen BT1, 10 seconds of hold time with constant load amplitude) is shown in Figure 5-39. For the ΔK values less than 15 MPa$\sqrt{m}$, highly crystallographic fractures were observed. Figure 5-39a illustrates an example found on the fracture surface near the notch where the crack length is 0.2 mm and the FCPR is 5×10^{-9} m/cycle. In this figure, linear and parallel ridges are orientated at random angles to the macroscopic propagation direction and smooth

planar microfacets separated by rough steps are observed. The fracture mode at this ΔK value is trangranular which can be characterized by the presence of a high density of small planar facets. The edges of the facets appear very angular and jogged, which suggests separation by a brittle cracking process. Figure 5-39b shows the fracture morphology under the same ΔK value at lower magnification. Careful measurement indicated that the average spacing between fine facets is approximately 0.2 μm. The macroscopic crack propagation rate measured by employing the dc-PD technique is approximately 5×10^{-9} m/cycle (or 0.005 μm/cycle). This rate is 40 times lower than the measurement from the microfacets, which indicates either that each microfacet corresponds to a number of fatigue cycles or each microfacet is produced discontinuously in a single cycle but not at every cycle.

Figure 5-39c shows the fatigue crack surface morphology at a ΔK value of 35.5 MPa$\sqrt{m}$ where the crack length is 1.2 mm. Fatigue striations are observed which have a crystallographic aspect, since they changed orientation from grain to grain. The fracture mode is transgranular in the regions of large grains with some intergranular cracking in the regions of small grains. Well formed non-crystallographic fatigue striations are clearly observed with transgranular features (Figure 5-39d) for a ΔK of 46.5 MPa$\sqrt{m}$ and a crack length of 1.8 mm. The microscopic FCPR'S determined from striation spacing measurements are approximately 2.5×10^{-7}m/cycle and 4.2×10^{-7} m/cycle for Figures 5-39c and 5-30d, respectively. The macroscopic FCPR's determined from the dc-PD measurements are approximately 2.4×10^{-7} m/cycle and 4.3×10^{-7} m/cycle for the 1.2 and

1.8 mm crack lengths, respectively. Good agreement therefore exists between the FCPR's measured macroscopically and microscopically. This indicates that one load cycle corresponds to one fatigue striation and that fatigue crack propagation occurs continously at the intermediate ΔK values.

Figure 5-39e shows a pair of stereofractographs at a ΔK value of 89 $MPa\sqrt{m}$ where the crack length is 3.9 mm. The fracture surface is now more complex than at the lower ΔK values. Dimples indicating ductile microvoid formation at some of the precipitates can now be observed. Employing a stereoviewer and matching surface observations, crack deviation can be observed. The spacings between these deviation lines are in good agreement with the corresponding macroscopic FCPR. For example, the average spacing of deviation lines is approximately 5 μm (5×10^{-6} m/cycle) and the FCPR from dc-PD is approximately 4.9×10^{-6} m/cycle at the 89 $MPa\sqrt{m}$ ΔK value. Therefore the deviation lines replace fatigue striations at the high ΔK values. Between these deviation lines striation-like features are present. These are crystallographic and change orientation from grain to grain and correspond to slip traces and not to fatigue striations.

High Temperature (650°C) Fracture Surface Morphology

Figures 5-40 are SEM photographs of specimen BT4 which was tested under type 3 load sequence (100 seconds of hold time at maximum load with constant load amplitude) at 650°C. Figure 5-40a shows the fracture surface morphology near the threshold region where the ΔK value is 13 $MPa\sqrt{m}$ and the crack length is 0.2 mm. This figure presents

both areas of small and large grains, with the areas of large grains appearing to be more dominant in the lower half of the figure. These areas of large grains appear relatively flat and present river lines, some of which are finely serrated. A higher magnification micrograph of one of these regions is presented in Figure 5-40b. Fine crystallographic striation- like features are present. The alternating lighter and darker lines indicate that on a microscopic scale the fracture surface has a 'hill and valley' aspect, made up to two alternating orientations of crystallographic microfacets. The striation-like features correspond to the sites at which pairs of microfacets of different orientations meet at a crest or in a valley. The regions of the small grains present some intergranular cracks that follow the grain boundaries and dimples on some of the ridge (or river) line features (see Figure 5-40c).

The fracture morphology at 650°C in the near threshold region is seen to favour large crystallographic facets in the large grains. These facets are made up of two alternating sets of finer crystallographic microfacets. However, in the region of the small grains there appears to be some intergranular cracking. Testing at room temperature in the near threshold region produces many different orientations of small microfacets in both the large and small grains. Some secondary cracks are also seen, especially in and near the regions of intergranular cracking.

At intermediate ΔK values, the fatigue striations formed at high temperature were poorly defined and less often observed in comparison to those for the room temperature test. Figure 5-40d shows

the fatigue striations morphology when the ΔK value is 50 MPa$\sqrt{m}$ and the crack length is 2.2 mm. Similar to the room temperature results, there is good agreement between the macroscopic and microscopic FCPR at intermediate ΔK values. For example, the microscopic FCPR from Figure 5-40d is approximately 1.6×10^{-6} m/cycle and the macroscopic FCPR from the dc-PD technique is approximately 1.65×10^{-6} m/cycle.

Figures 5-40e are a pair of stereographs which show the fracture morphology at a high ΔK value (99.5 MPa$\sqrt{m}$, with a crack length of 4.5 mm). From the stereographic observations, it is seen that the fracture surface is very rough at the high ΔK values. The relatively featureless regions which tend to start and stop at bands of dimples correspond to zones of stretched crack tip blunting. The spacings between the blunting lines, where the zones of crack tip stretching end, are in good agreement with the macroscopic FCPR. This indicates that those blunting lines correspond to the positions of crack arrest after each cycle. The fracture region for each load cycle (or between two neighbouring blunting lines) consists of two portions. The first is the fatigue region where the increasing ΔK portion of the load cycle reinitiates crack propagation. Dimples are often present in this region. The second portion is the crack tip stretching region which forms largely during the hold time period. The relative widths of the fatigue and stretching region can be used to estimate the individual influence of the increasing ΔK and constant ΔK or hold time affect on FCPR. Since the test of specimen BT2 (constant amplitude without hold time) was stopped at a lower ΔK value of approximately 65 MPa$\sqrt{m}$,

comparison of these observations with those for no hold time must be done with care.

Figure 5-41 shows the fracture surface morphology of specimen BT6 which was tested under the type 4 load sequence (450 minor cycles with 0.1 minor cycle load range ratio during 100 seconds at maximum load level) at 650°C. In Figure 5-41, the ΔK value is 56 MPa$\sqrt{m}$ and the crack length is 2.6 mm. From Figure 5-41a, it is seen that the block-striations corresponding to the major cycles are clearly observed in the regions of the large grains and less clearly observed in the regions of the small grains. The interstriation spacing varies but generally appears somewhat finer in the region of the small grains. Some intergranular cracking is seen in the region of small grains, with secondary cracks present on the fracture surface in these regions. A higher magnification micrograph of a region in a large grain is shown in Figure 5-41b. The fracture surface consists of two portions for each major load cycle. The first is the flatter portion presenting a number of fine striation-like features (approximately 20 to 30 appear visible at this magnification) corresponding to the minor cycle crack propagation. The second is a rough region caused by major cycle propagation which results in two pronounced striation lines with the material between these lines appearing higher (Figure 5-41b) or lower (Figure 5-41c) than the minor cycle portion. The region between these two pronounced striation lines at times can be seen to present finer striations similar to those in the region of minor cycle propagation. Serrated river or ridge lines are also observed. These often start or stop or jog along the second or further of the two striation lines

associated with the major cycles. Some of the river lines also present jogs within the region of minor cycle propagation, with the jog at times parallel to the fine striations. The average width of the flatter region is approximately 3.5 times greater than that of the rougher region in Figure 5-41b (ΔK value of 56 MPa$\sqrt{m}$). At the same ΔK value, the macroscopic FCPR for this test is 4.6 times greater than that for the no-hold time test (specimen BT2). This good agreement indicates that the fracture analysis can estimate the FCPR under minor load cycle tests and find the minor load cycle effect on FCP behaviour.

For the fatigue test carried out with a 0.05 minor load cycle range ratio test (specimen BT10), the striations for the major cycle were clearly observed but were not separated by a flat region of minor cycle propagation (see Figure 5-42). For this test, the minor cycles did not accelerate macroscope FCPR compared to a test with a constant load hold time (specimen BT2).

5.7.2 Secondary Cracking Observations

In order to obtain further information on the fatigue crack propagation characteristics for this material, metallographic sections were prepared perpendicular to the fracture surface and making an angle of 45° with the specimen surfaces. The position of the crack tip at various intervals and secondary cracks are shown in Figure 5-43 for room (5-43a) and high (5-43b) temperature tests. The crack propagation macroscopically is in the plane normal to the stress axis, but micro-

scopically the propagation path is affected by the microstructure. The effect of the microstructure is seen from the zigzag crack path, which depends on the grain size. For both room and high temperature tests, the fracture modes of the secondary cracks are transgranular in the large grains and intergranular in the small grains. Microcavities were observed near the fracture surfaces for the specimen tested at high temperature. Figure 5-43c shows the secondary crack morphology at high temperature under high magnification. Arrow A indicates a secondary crack following a grain boundary near the fracture surface.

5.7.3 Microstructure Observations

Figure 5-44 shows the morphology of the microstruture for the test material at low magnification. It consists of large grains surrounded by small grains, which is usually referred to as a duplex or 'necklace' structure. The average grain sizes are 8 to 10 μm and 30 to 40 μm for small and large grains, respectively.

The grain and grain boundary morphology of the alloy, as received, after room and high temperature testing are shown in Figures 5-45a, 5-45b and 5-45c, respectively. No significant difference in microstructure was observed between these different specimens. Some 'twin' grain boundaries appear present in these figures. Figure 5-45d shows more details of 'twin' grain boundaries at high magnification. Three sizes of gamma prime (γ') precipitates are observed. Coarse γ' precipitates are present at grain boundaries and triple points, while fine γ' precipitates are observed in both the small and large grains.

Figure 5-45e shows that the intermediate size γ' precipitates are present only in the large grains. Some carbides are observed both at the grain boundaries and within the grains. These different phases were identified by employing an Energy Dispersive Spectrometer (EDS), comparing the relative peak heights for elements with respect to that expected. The spectra obtained for the matrix (γ), the γ' precipitates and the carbides are shown in Figures 5-46 to 5-48, respectively.

CHAPTER 6: DISCUSSION

6.1 Fractographic Morphology for Room and High Temperature Tests

For the room and high temperature (650°C) tests with 10 seconds of hold time, crystallographic cracking consisting of smooth planar facets and parallel tear ridges or river lines was observed in the crack initiation region where FCPR's are near threshold. The fractographic aspect was very strongly crystallographic for the test at room temperature with many small facets (microfacets) present (see Figures 5-39a and 5-39b), while the test at 650°C produced crystallographic cracking with considerably larger facets (see Figures 5-40a and 5-40b). For the room temperature tests, the transgranular cracking occurred both in the large and small grain regions near the initiation zone, while the test at high temperature produced transgranular cracking in the large grain regions and some intergranular cracking in the small grain regions. It is believed that these differences in the fracture surface morphology were caused by the effects of environment.

These crystallographic aspects are related to the influence of microstructure on crack propagation. The crystallographic fracture surfaces have been described as crystallographic decohesion, decohesion along slip planes or quasi-cleavage[82]. Three factors strongly influence the cracking properties in this region. These are the microstructure, the R-ratio and the environment. Previous studies indicated that the facets are generally identified as low index planes.

Bailon et al[82,83] and Dickson et al[84] have investigated the fracture surface morphology at and near the threshold regions for face centered cubic alloys such as 2024 aluminium alloy, 316 astenitic stainless steel, and 70-30 alpha-brass. They concluded that the transgranular cracking at the threshold region occurred generally in the <110> or the <100> directions along planes usually with average orientations close to the {100} and occasionally close to the {110}. They also found that on a fine scale the facets were along the {111} planes and the fine serration on tear ridges or river lines were along two <110> directions. This cracking crystallography was explained by the occurrence of fine scale microscopic decohesion in an alternating manner on two or more sets of {111} slip planes. In the present work, the orientations of the microfacets and the river lines have not been identified. Such identification requires the use of techniques such as etch pitting. The fracture surface morphology of this work, however, appears similar to that observed in these previous studies and, therefore, suggests that similar results would be obtained.

At values of ΔK somewhat higher than the threshold, transgranular cracking with crystallographic fatigue striations which changed direction from grain to grain were found in the large grain regions for both test temperatures. The regions of small grains showed more intergranular cracking at high temperature than at room temperature. Two basic mechanisms for cracking are applicable to this ΔK region. The first[85-88] is the alternate slip mechanism with the crack plane bisecting the angle between the two active slip planes which meet at the crack front. Crack propagation occurs as a result of

localized slip in the crack tip region. The second[89] is due to the formation of fatigue striations, which involves a combination of brittle damage and ductile slip decohesion mechanisms. Intergranular cracking at low crack growth rates is known to occur when the cyclic plastic zone at the crack tip is similar to the grain size. The cracking will generally be entirely intergranular. Transgranular cracking would occur, if the plastic zone size is larger or smaller than the grain size. Intergranular cracking can also be caused by an environmental effect since such cracking generally involves reduction the grain boundary cohesive strength. Previous work has indicated that the occurrence of intergranular cracking at low da/dN is an environmental effect[90-92].

In the intermediate ΔK regions, non-crystallographic transgranular fatigue striations were observed in the large grain regions at both test temperatures. A mixed fracture mode (transgranular and intergranular) was found in the small grain regions. The amount of intergranular cracking was considerably less than in the near-threshold ΔK regions. This indicates that the environmental effect is reduced with increasing ΔK values. The mechanisms for the formation of the striations should then be crack blunting in the load increasing portion[93,94] and crack resharpening in the load decreasing portion. Since the stress intensity is increased by either an increase in the crack length or in the applied ΔK, slip begins to occur near the crack tip on planes other than the primary plane and the slip is less localized. Plastic blunting occurs because this multiple slip induces crack propagation by shear deformation on planes oriented roughly at

45° to the plane of the crack. The best way of observing blunting lines is by employing stereography and observing matching fracture surfaces.

For the test at 650°C, the fracture surface at intermediate and high ΔK's also presented dimples in the grain boundary regions associated with the small grains. Microvoid nucleation at the crack tip can be expected to occur when the crack tip plastic strains are sufficiently high.

The good agreement between the FCPR microscopically determined from the measurement of striation spacings and that determined macroscopically from the dc-PD technique indicates that one fatigue striation corresponds to one load cycle at intermediate ΔK values. This result shows that a continuous fatigue cracking mechanism occurred at these intermediate ΔK values.

At high ΔK values the fatigue striations disappeared and the fracture surfaces became rougher and presented a 'hill and valley' aspect. In the large grain regions, there were a number of parallel striation-like markings between the successive peaks. These markings corresponded to slip traces. Observations of stereographic pairs of matching regions showed that the fractographic features generally interlocked quite well with only a few signs of a small amount of blunting. There was, however, crack deviation associated with the major cycles. The major cycles at times appeared marked by intergranular secondary cracking in the regions of the small grains and quite pronounced steps on the fracture surfaces in the regions of the large grains. The intergranular cracks in the regions of the small

grains were present within valleys on the fracture surface and were absent on the crests on the opposite surface. The cracking in the large grain regions was always transgranular.

In the small grain regions, there was more transgranular cracking at high ΔK than at low ΔK for both temperatures. More dimples and less striation-like features were observed on the fracture surfaces produced at high temperature. These observations suggest that the time- dependent effects are more pronounced in the high temperature tests.

Some flat, apparently crystallographic fracture facets were found at both temperatures in the large grains. Bands of dimples corresponded to some of the crack arrest sites near interfaces between regions of large and small grains and were associated with the coalescence of voids around grain boundary precipitates in the regions of the small grains.

The extensive plastic flow around the grain boundary carbides led to strain gradients at the carbide-matrix interface which resulted in decohesion between the carbide particles and the matrix. More striation-like features between the crack arrest marks were observed for the room temperature test and their apparently crystallographic aspect indicated that they were produced by slip deformation. Some non- crystallographic shear at the crack tip was observed at the high temperature test which can be associated with a plastic zone size much larger than the grain size during the hold time, possibly with some microvoid growth and coalescence also involved. That more crystallographic slip was found for the room temperature test and some

non-crystallographic shear was found for the high temperature indicates that the crack tip plastic strains are more pronounced at high temperature.

6.2 High Temperature FCPR Behaviour

The tests on specimens BT1 and BT7 were carried out at room temperature and 650°C, respectively, employing the type 1 (see Figure 4-10) loading sequence, which included 10 seconds of hold time at maximum load. Figure 5-37 compares the FCPR for these two tests. It is seen that the high temperature test resulted in a higher FCPR for a given ΔK value than the room temperature tests, and that the difference in FCPR decreased with increasing ΔK values.

High temperature fatigue crack propagation is a very complex process. In general, the temperature dependence of the FCPR can be separated into two different crack propagation processes:

(1) a purely cyclic dependent crack propagation process which is essentially a fatigue damage process and is controlled by material properties, applied stress, test temperature and specimen geometry;

(2) a time-dependent process which can be influenced by environmental effects and creep effects or a combination of the two. Time-dependent crack propagation can be strongly influenced by the test temperature, and by changes in microstructure or in microstructural properties, such as the grain size, the grain morphology and the relative strength of the grains and grain boundaries.

Fatigue crack propagation which occurs in a process zone in the region of the crack tip involves cyclic plastic deformation mechanisms such as the slip of dislocations. Creep damage is essentially an internal failure process which occurs by the initiation and growth of grain boundary cracks or cavities. Environmental effects include oxidation attack of the grain boundaries intersecting the crack tip surface and oxidation of the material ahead of the crack tip. The crack propagation during high temperature tests therefore may involve:

(1) only fatigue cracking if the relative extent of cavitation and the influence of environment are negligible;

(2) creep/fatigue interactions if there is a significant interaction between the fatigue crack propagation and internal cavitation or intragranular cracking;

(3) mainly time-dependent propagation if cavity development or grain boundary oxidation occur at a significantly more rapid rate than the fatigue crack propagation process.

The FCPR at high temperature is higher than that at room temperature which can be explained by a time-dependent contribution at high temperature. Such time-dependent processes include environmental interaction, dislocation climb and cross slip, grain boundary sliding, and other microstructural instabilities. FCPR at high temperature, especially at low and intermediate ΔK values can be accelerated by the following environmental effects:

(1) cracking occurring atom by atom at the tip of the crack as soon as oxygen molecules arrive;

(2) formation of an oxide at the crack tip with the cracking then occurring in the oxide or at the matrix-oxide interface;

(3) diffusion of oxygen into the metal ahead of the main crack, the last of which can promote a subsurface crack that later links up to the main crack;

(4) creep effects such as grain boundary sliding or the initiation, growth and coalescence of microcavities.

The fracture surface was flatter at high temperature for both low and intermediate ΔK values and there were more intergranular crackings in the small grain regions for high temperature at all ΔK values (except very high ΔK values). These observations therefore indicate that the environmental and perhaps creep effects play an important role during the FCPR process at high temperature at low and intermediate ΔK values.

The difference in FCPR between room and high temperature decreased with increasing ΔK values which can be explained by the reduced time available for such effects with increasing ΔK and da/dN values at high temperature. Creep effects however can also be less pronounced at high da/dN values, since grain boundary sliding is less important at high ΔK values[95]. The amount of oxide on the fracture surface decreased with increasing ΔK and the amount of intergranular cracking for the high temperature tests also decreased with increasing ΔK values. These observations indicate that the environmental and creep effects were reduced with increasing ΔK values. The fracture surfaces were considerably smoother at high temperature than at room temperature at lower or intermediate ΔK values. Crack closure effects

are particularly important under these conditions. Therefore, a decreased effect of roughness-induced crack closure may partly be responsible for the more rapid crack propagation at high temperature for low ΔK values.

It is difficult to separate the individual contribution of the environment from the creep time-dependent effects in high temperature tests. Some researchers claim that the environment is solely responsible; others claim that creep is responsible; yet a third group considers that both creep and environment are important with their relative influence depending upon the cycling frequency. Performing tests under vacuum at room temperature and 650°C can resolve this question. From such tests, the effects of creep which are caused by increasing temperature can be distinguished, and the amount of intergranular cracking in small grain regions and the transgranular fracture features in large grain regions can also be identified from the observation of fracture surfaces. Comparing these results with the present work, the relative influence of environment and creep associated with increasing temperature could be determined and such results would be very helpful in understanding the fracture mechanisms at high temperature for this material.

6.3 Influence of Hold Time on FCPR Behaviour

Figure 5-37 shows the influence of hold time on FCPR at 650°C. Specimens BT2, BT7 and BT5 were tested with hold times of 0, 10 and 100 seconds respectively at the maximum load level. From this

figure, the longer the hold time the higher is the FCPR. The influence, however, is more pronounced from 0 to 10 seconds than from 10 to 100 seconds of hold time where the influence observed was slight. The difference of FCPR between 0 and 10 seconds of hold time increased with increasing ΔK values.

The influence of hold time on FCPR at high temperature may depend either on the environmental influences or on the creep contribution or on both effects. The influence of hold time should also depend on the stress intensity during the hold time period with respect to a threshold stress intensity. Since in the present study, the hold time accelerated the FCPR, the stress intensity during the hold time was greater than this threshold value.

The longer the hold time the higher is the FCPR. This may be related to the environmental and creep damage influence during the hold time period. The hold time effects also can be considered a frequency effect. The decrease in frequency as a result of the hold time allows for the conversion of part of the elastic strain to a plastic strain, and perhaps to an anelastic strain. This increase in the plastic strain range can cause the decrease of the fatigue life and cause stress relaxation in the crack tip region. This stress relaxation results from the creep damage in the specimen interior that can result in cavities on grain boundaries. These internal grain-boundary cavities can in turn interact with a propagating fatigue crack to result in an enhanced crack growth rate.

It is believed that the environmental and creep influences on FCPR are more pronounced in the hold time tests than in the test

without hold time, since the time at the maximum load level is a very important factor to cause both environmental and creep damage. For the no hold time test, the increase of the fatigue life was attributed to eliminating the effects of oxidation and creep. When comparing the fracture surfaces at the same ΔK values, there was more transgranular cracking in the regions of the small grains and there were no stretch zone aspects found for the test without hold time, although this test was only carried out to $\Delta K = 59.1$ mPa$\sqrt{m}$. These observations suggested that less environmental and creep effects occurred in the test without hold time.

That there is only a small difference in FCPR between 10 and 100 seconds of hold time may be related to oxidation and the creep deformation rate (CDR). The crack is propagated by cyclic and environmental influences if the CDR is low enough that creep deformation does not relax the stress field at the crack tip. The crack is propagated by cyclic, environmental and creep influences if the CDR is above a threshold level. However, if the CDR is high enough, blunting can occur at the crack tip which can relax the stresses in the crack tip region and arrest crack propagation in spite of environmental and cyclic influences.

The fracture surface for 100 seconds of hold time, when compared to the fracture surface for 10 seconds of hold time, showed much more intergranular cracking in the small grain regions and more crystallographic facets in the large grain regions. More intergranular cracking in the regions of small grains indicates that either environmental or creep effects or both are influencing the cracking in

these small grain regions. The more crystallographic cracking in the regions of large grains indicates that the environmental effect is more pronounced. A small amount of blunting on the fracture surfaces for all the tests indicates that the creep effect is less important than the environmental effect at this temperature. All these above factors would accelerate the FCPR.

The fracture surface for 100 seconds of hold time is rougher than for 10 seconds of hold time and this roughness was associated mainly with crack deviation produced by the major cycles. A small amount of blunting was also observed for 100 seconds of hold time. These aspects suggest that the major cycles are producing some retardation in the subsequent cracking during the hold time and that this retardation effect, which is similar to that which occurs after an overload, is more important in the case of a hold time of 100 seconds. Argon et al[96] have shown examples of cracks extending at 45° during creep crack growth in 304 stainless steel tested at 750°C resulting in subsequent crack tip shielding. The present fractographic results indicate that the main effect of the major cycles is to cause crack tip deviation possibly associated with shear or slip band cracking in the large grain regions, since the spacing between deviations corresponded to the macroscopic da/dN values. The crack tip shielding must result from these deviations and slow down the cracking during the hold time. The major cycles caused secondary cracking in small grain regions which also produced crack tip shielding. All of these effects would reduce the FCPR during the subsequent minor cycles.

The observations therefore indicate that there is a competition between two types of effects during the hold time period. Effects such as environmental and creep cracking which accelerate the FCPR and the retardation associated with crack tip shielding after the major cycles would reduce the subsequent FCPR. These two types of effects could be occurring competitively and this could explain the small difference in FCPR between 10 and 100 seconds of hold time. The fracture surfaces suggest that the accelerated cracking effects are more important for the 10 seconds of hold time and that the crack tip shielding and therefore retardation is more important for 100 seconds of hold time. Some of the previous work[97] showed that the FCPR can be decreased with increasing hold time in A-286 turbine discs material at 550°C. These results could also be explained if the major cycles for the longer hold time caused an increase in crack tip shielding which was more important than the increase in the time-dependent (environmental or creep) cracking.

Another possibility is that for the hold time tests, it is difficult to rupture the oxidation film at the crack tip since no cyclic effect exists during the hold time. The FCPR therefore can be reduced by the formation of an oxidation film at the crack tip. On the fracture surface of 100 seconds of hold time, more oxides were observed than that of 10 seconds. The thinner oxidation films associated with 10 seconds of hold time which formed at the crack tip may be easy to rupture which resulted in an accelerated FCPR. Such an effect can also explain the small difference of FCPR between 10 and 100 seconds of hold

time but cannot explain slower crack propagation for 20 seconds of hold time, as observed by Pishva[97] on A-286 alloy.

These results indicate that it would be useful to perform tests in Astroloy with shorter (2 or 5 seconds) or longer (600 seconds) hold times, which would provide better evidence concerning the contributions of creep, of crack tip oxidation and of crack tip shielding on the overall FCPR. Such results would improve our understanding of the effects of hold time at high temperature.

6.4 Influence of Minor Cycle Load Range Ratio on FCP Behaviour

Figure 5-39 shows the influence of the minor cycle load range ratio, which is defined as the ΔK_{minor} over K_{max}, on FCPR. Specimen BT5 was tested employing 100 seconds of hold time at the maximum load level, i.e. a minor cycle load range ratio of 0. Specimen BT10 was tested employing 900 minor cycles for each major cycle with a 0.05 minor cycle load range ratio and specimen BT6 was tested employing 450 minor cycles with a 0.1 minor cycle load range ratio. In both cases K_{max} for the minor and major cycles was the same value and the minor cycling took 100 seconds, which is similar to the hold time in the test without minor cycles (BT5). The results indicated that there was almost no difference of FCPR between the 0.05 (BT10) and the 0 (BT5) minor cycle load range ratio tests. Comparing the FCPR for the 0.1 minor cycle load range ratio test with that for the tests with ratios of 0 or 0.05, almost no difference in FCPR was found when ΔK_{major} values were less than 35 MPa$\sqrt{m}$. Above this value, the FCPR for the 0.1

minor cycle load range ratio test become increasingly more rapid than that for 0.05 or the 0 ratio tests with increasing ΔK_{major} values.

The FCPR with minor cycles at high temperature can be considered to consist of three contributions:

(1) the major cycle influence which can be considered equivalent to low cycle fatigue (LCF);

(2) the minor cycle influence or the high cycle fatigue (HCF) component;

(3) the time-dependent or creep-environmental influence.

LCF and time-dependent influences have already been discussed. Therefore, this section will focus on the influence of the minor cycles. When investigating the influence of HCF minor cycles on FCPR behaviour, two factors should be considered. One is the minor cycle load range ratio and the other is the number of minor cycles per major cycle.

In the present study, the LCF damage was greatest during the tests and minor HCF damage was not very significant until the stress intensity for the minor cycles, ΔK_{minor}, was at least greater than a certain value. This value is related to the threshold stress intensity at that load ratio, $\Delta K_{th\ minor}$, and the influence of environment. This means that the FCPR depends only on the major cycles and time-dependent effects if the ΔK_{minor} is less than the $\Delta K_{th\ minor}$, and on the major cycles, the minor cycles and the time-dependent effects if ΔK_{minor} is greater than the $\Delta K_{th\ minor}$. If ΔK_{minor} is sufficiently large, the minor cycles will contribute in an important manner to the crack propagation and the major cycles will be of lesser relative importance.

In the present study, the maximum range of ΔK_{minor} for the 0.05 minor cycle load range ratio test (BT10) is approximately 5.3 MPa$\sqrt{m}$. No influence of minor cycles on FCPR was found for this test. For the 0.1 minor cycle load range ratio test (BT6), the value of ΔK_{minor} is approximately 3.9 MPa$\sqrt{m}$ when the value of ΔK_{major} is 35 MPa$\sqrt{m}$, at which point the minor cycles started to contribute in a detectable manner to the FCPR. From these results, a certain ΔK value combination of ΔK_{minor} and ΔK_{major} must exist for each test at which time the minor cycles become active. It is suggested that minor cycles become active and influence the FCPR above their threshold value, under the appropriate stress ratio (R), cyclic frequency and major cycle range. For the 0.05 and the 0.1 minor cycle load range ratio tests, the load ratios for the minor cycles (R_{minor}) are 0.95 and 0.9, respectively. Since the minor cycles have negligible effect if their stress intensity range is below the threshold value of the material[98,99], the parameter ΔK_{onset} was introduced to the analysis of the minor-major cycle problem by Powell et al.[99,100]. The ΔK_{onset} is defined as the value of the total or overall stress intensity range associated with the combined major and minor cycles at the point where the minor cycles become active. The ΔK_{onset} is expressed as follows:

$$\Delta K_{onset} = \left(\frac{2+Q}{2Q}\right) \Delta K_{th\ minor} \qquad (6\text{-}1)$$

where $Q = \Delta K_{minor}/\Delta K_{major}$. This equation follows from the basic definitions from the basic definitions of the parameters it contains. For the 0.1 ratio test Q = 1/9 and for the 0.05 ratio test Q = 1/18.

$\Delta K_{th\ minor}$ is the threshold stress intensity value for minor cycles which is or can be a function of minor cycle load ratio, minor cycle load range ratio, major cycle load ratio, minor cycle frequency and time-dependent environmental effects. The fatigue threshold values for the minor cycle ($\Delta K_{th\ minor}$) will not be known exactly due to the material variability, the influence of crack length and shape, crack closure, prior cyclic loading history and other variables. Even when such variables are carefully controlled, and this is far from simple, experimental errors must still be expected, since the values of $\Delta K_{th\ minor}$ are very small.

Therefore, it is suggested from the results of the 0.05 ratio test that the $\Delta K_{th\ minor}$ is equal to 5.3 MPa$\sqrt{m}$ when the ΔK_{major} is at a maximum value (106 MPa$\sqrt{m}$) during the test.

This means that the ΔK_{onset} for the 0.05 ratio test should be larger than the ΔK_{onset} at which the $\Delta K_{th\ minor}$ is 5.3 MPa$\sqrt{m}$. From this suggestion we have:

$$\Delta K_{onset} > (2+\frac{1}{18})/\frac{2}{18} \times 5.3 = 98\ \text{MPa}\sqrt{m}$$

This value indicates that the ΔK_{onset} for the 0.05 ratio test should be larger than 98 MPa$\sqrt{m}$. This point is consistent with Fig. 5-39, in which the macroscopic FCPR results showed that there was no influence of minor cycles, even when the ΔK_{major} was 95 MPa$\sqrt{m}$.

For the 0.1 ratio test Q = 1/9 and $\Delta K_{th\ minor}$ is 3.9 MPa$\sqrt{m}$ (since the minor cycles became active when ΔK_{major} was 35 MPa$\sqrt{m}$ from the observation of Fig. 5-39). Therefore:

$$\Delta K_{onset} = (2+\frac{1}{9})/\frac{2}{9} \times 3.9 = 37.1 \text{ MPa}\sqrt{m}$$

This result is close to the macroscopic result from Fig. 5-39 (35 MPa$\sqrt{m}$). The difference between the calculated value (37.1 MPa$\sqrt{m}$) and the macroscopic result (35 MPa$\sqrt{m}$) is due to the fact that ΔK_{onset} is not ΔK_{major}. ΔK_{onset} is defined as a total stress intensity range associated with combined major and minor cycles. It should be slightly higher than ΔK_{major}. The minor cycle effects increased with increasing ΔK_{major} since ΔK_{minor} increased with increasing ΔK_{major}.

Another method to analyse the minor cycle's influence in major-minor cycle tests is the superposition method. This method suggests there is always an influence of minor cycles if ΔK_{minor} is above ΔK_{th}. At very low ΔK_{minor} values, the influence of minor cycles is however so small that it can be neglected, since their contribution is much less than that of the major cycles. This is also the case if ΔK_{minor} is less than ΔKth_{minor} for the applicable R-ratio and where the contribution of ΔK_{minor} should be clearly negligible. Figure 6-1 shows that linear summation of FCPR where the FCPR can separated as follows:

$$(\frac{da}{dN})_{total} = \frac{da_{major}}{dN_{major}} + \frac{nda_{minor}}{dN_{minor}} \qquad (6-2)$$

where n is the number of minor cycles per major cycles. Therefore, the FCPR for minor cycle load range ratios 0.1 and 0.05 are:

$$\frac{da_{minor}}{dN_{major}} = \frac{450\ da_{minor}}{dN_{minor}} \qquad (6-3)$$

and

$$\frac{da_{minor}}{dN_{major}} = \frac{900\ da_{minor}}{dN_{minor}} \qquad (6\text{-}4)$$

These FCPR's for the sum of the minor cycles during each major cycle should be added to the corresponding rate for the ΔK_{major} value. In Fig. 6-1, 'A' is associated with applied major cycles and corresponds to the experimental curve with 100 seconds of hold time; 'B' is the experimental curve for the tests with minor cycles; and 'C' represents the effects of the minor cycles da_{minor}/dN_{major} and is obtained by subtracting A from B.

The use of fatigue threshold values and the linear summation rule to predict the onset of minor cycle damage and FCP under major-minor cycling assumes that there is no interaction between the major and minor cycles. Whether an interaction influence of the major and the minor cycles existed could be determined if tests had also been carried out employing only minor cycles (R = 0.9 and 0.95). Tests to determine the amount and extent of interaction can be suggested for a future study.

The fracture surface observation showed that the fractographic aspects for the 0.05 minor cycle load range ratio test were similar to those for the 100 seconds of hold time test at similar ΔK_{major} values. These fractographic aspects (the 0 load range ratio or 100 seconds of hold time) have been described and discussed in section 6.1 for the different ΔK values. For the 0.1 load range ratio test, the fracture surface aspects were similar to the 0.05 and 0 load range ratio tests when ΔK_{major} was less than 35 MPa$\sqrt{m}$. These results

indicated that, below this value of ΔK_{major}, the crack propagation process was essentially associated with the major cycle crack propagation. When the ΔK_{major} value was larger than 35 MPa$\sqrt{m}$, the combined major and minor cycles gave rise to the development of block striations in the regions of large grains. These block striations consisted of two portions for each major cycle. One appeared as two valley-hill-valley lines which initially were suspected to be associated with the unloading portion of the previous major cycle and the loading region of the present major cycle. Some finer striation lines were present between these two pronounced lines. The other portion of the block striations appeared as flat facets within the large grains with serrated river lines and fine striation-like features. The fine striations appeared much less numerous than that of the total number of minor cycles per major cycle. The $(da/dN)_{minor}$ is approximately 5×10^{-6} m/cycle measured from the microscopic interstriation spacing and 1×10^{-8} m/cycle estimated from the macroscopic.

The macroscopic propagation rate associated with the minor cycles is in the range where the average da/dN is generally larger than the interstriation spacing. The fracture morphology for this portion appears similar to that in the region with low values of ΔK_{major}.

Stereographic observations on matching surface indicated that the two pronounced striations at the start of each block of striations in the regions of large grains was associated with some crack retardation or crack deviation effect associated with the loading portion of the major cycles. The loading portion of the major cycle

caused the crack plane to deviate. The minor cycles initially caused the crack to continue propagating along this path inclined to the average fracture surface. The second pronounced line corresponded to the reinitiation of a crack along approximately the prolongation of the same plane on which cracking occurred before the major cycle. The remaining number of minor cycles propagated the crack along this plane which produced the flatter portion on the fracture surface.

Secondary cracks which are only observed on one of the matching surfaces, mixed crack aspects (transgranular + intergranular) and less pronounced block striations were observed in the regions of small grains. These fractographic observations suggest that the spacing between block lines in this region is slightly smaller than in the regions of large grains. This result suggests that the FCP is faster in the large grain regions than in the small grain regions. This should be caused by the influence of environment, since the environmental effect can promote the FCP associated with some crystallographic cracking in the regions of large grains.

The fractographic observations on matching fracture surfaces for the test with minor cycles (see Fig. 6-2 and 6-3) suggest that the load-increasing portion of the major cycles at high ΔK_{major} causes the crack to deviate. This suggests that for the tests with hold time, the portion of da/dN produced during the load-increasing portion corresponds to the crack deviation regions on the fracture surface and the da/dN produced during the hold time corresponds to the flatter regions between these inclined zones. The roughly similar sizes of the inclined zones and the flat zones in the large regions are then

consistent with the hold time approximately doubling the FCPR at high ΔK.

For high values of ΔK_{major} (larger than 75 MPa$\sqrt{m}$) in the test of 0.1 minor load range ratio, the block striations disappeared and crystallographic facets were observed in the regions of large grains. Microvoid coalescence was associated with this high propagation rate regime. These features are similar to those reported by others[101-103] except that crystallographic cracking was more in evidence in the present study. Previously, Powell and Duggan[104] found that cyclic cleavage (crystallographic-like) was the predominant mode of crack propagation found in all specimens subjected only to minor cycles (no hold time R = 0.9) in Ti-6Al-4V material. This indicates that some of the crystallographic facets at the high ΔK values for the 0.1 load range ratio test could be caused by the minor cycles as the minor cycles become active in this ΔK region. Ward-Close and Beevers[105] investigated the effects on propagation rates when both cyclic cleavage and fatigue striations were present. They showed that propagation rates due to cyclic cleavage were much higher than those due to striated crack growth (about ten times). This result is similar to the present study where the crack deviation lines, which indicate the position of the crack front after each major cycle at high ΔK, disappeared when they met crystallographic facets larger than the spacing between the deviation lines. A more detailed investigation of fracture surface morphology in this material, including a comparison with that obtained on specimens which would be subjected only to the minor cycles is suggested as a topic for a future study.

Powell and Duggan[99] also investigated the effect of the number of minor cycles on the FCPR in Ti-6Al-4V material with CT specimens. They found that the minor cycle damage becomes dominant when the number of minor cycles was over 1000 with a 0.1 minor cycle load range ratio. In the present study, the influence of the number of minor cycles on FCPR was not studied. This influence should depend on the material properties, the ΔK_{minor}, the minor cycle load range ratio and possibly the specimen geometry.

After understanding that both ΔK_{minor} and ΔK_{onset} are important factors in FCP, a comparison with crack growth rates and fractographic features in tests subjected only to the minor cycles can be suggested to investigate the influence of minor and major cycle interactions. This influence was not considered in the present study. It is particularly important to establish whether the major cycles cause crack retardation effects during the minor cycling and what factors control these retardation effects. Tests with different numbers of minor cycles at the same minor cycle load range ratio are suggested to investigate the influence of the number of minor cycles on FCP behaviour. The tests in which an overload is employed during the minor cycles can also be suggested as potentially useful to evaluate the interaction of minor and major cycles. The results of such tests should be useful in better understanding the influence of the minor cycle effect.

6.5 Influence of Microstructure on FCP Behaviour

The HIP parameters and heat treatment regime for the test materials have been described in section 4.2. Some investigators[106] have found that there are strong influences of microstructure on FCP behaviour at high temperature for Ni-based superalloys (IN718). A necklace microstructure, which essentially consists of large grains surrounded by a string of finer recrystallized grains, was observed in this material with approximately 40% of the volume consisting of the fine, recrystallized grains. This microstructure is generally considered to offer better LCF properties than other microstructures at high temperature, because the large grains reduce the creep rate (see Section 2.1) and the small grains have a high resistance to FCP[107]. Figure 5-41 shows that the spacings between crack arrest marks are larger in the regions of large grains than in those of small grains. The fractographic observations show that the small grains tend to favor intergranular cracking and the large grains transgranular cracking. This mixed fracture mode could enhance the resistance to FCP at high temperature. The regions in which the fatigue crack propagation is slower should at least slow down the propagation rate in the regions of faster propagation. The intergranular cracking in the regions of small grains also tends to result in some secondary cracking. This effect can reduce the local effective value of ΔK.

In the present study, it is found that recrystallized grains had nucleated in the region of "hard particles" (for example carbides) or coarse γ'. These observations indicate that the achievement of the

necklace structure is governed by the coarse primary γ' precipitate distribution. The coarse γ' particles control the recrystallization nucleation at the grain boundaries and can also inhibit the growth of the necklace microstructure by a pinning effect on the grain boundaries in the recrystallized region. Moreover, coarse γ' distribution determines the grain size of the fully recovered microstructure.

Carbides, which should be primary MC or secondary $M_{23}C_6$, were found at the grain boundaries. Two competing effects of carbides on FCP at high temperature can exist. The first is that carbides dispersed at the grain boundary have a beneficial effect on the creep rupture strength by reducing grain boundary sliding. The second is that the carbide formation may have removed the carbide forming elements from the matrix surrounding the grain boundary. A precipitate-free zone (PFZ) therefore would be formed surrounding the grain boundaries. If such zones become wide or much weaker than the matrix, deformation would concentrate in these zones resulting in early failure. Wallace et al[108] have shown that carbides usually can cause brittle crack propagation at high temperature. Wallace et al[109,110] also found that $M_{23}C_6$ precipitation during subsequent aging caused interparticle fracture with severe loss of tensile and stress-rupture ductility in 713 LC compacts. In the present study, carbides were found on the intergranular facets which suggest that these carbides contributed to the intergranular cracking.

From the fracture surface observations, however, the FCPR is slightly faster in the regions of large grains than in the regions of small grains at the high ΔK values. This result could possibly be

related to the influence of environment which can cause some brittle (crystallographic) cracking in the regions of large grains. Some of the crystallographic fracture surface morphology in the large grain regions at high ΔK values could be caused by such brittle cracking and this effect would accelerate the FCPR. This faster cracking in the large grain regions also indicates that the creep influence is not very significant in these tests, since the small grain regions should be less resistant to creep than the large grain regions. If the effect of hold time and minor cycle was predominantly a creep-fatigue effect, higher FCPR would be expected in the regions of small grains than in the regions of large grains.

CHAPTER 7: CONCLUSIONS

(1) The dc-PD technique was successfully employed to measure the crack length during fatigue crack propagation for corner cracked specimens at both room and high temperature (650°C).

(2) The FCPR data of corner cracked specimens can be expressed by the Paris relation and by the Weibull equation in a log-log plot. The Weibull analysis can successfully represent the three regions of FCP.

(3) The log da/dN - log ΔK fatigue crack propagation curve of Astroloy at 650°C is higher than at room temperature, with the difference between the curves decreasing with increasing ΔK. The fracture surface observations show:

   (a) transgranular cracking with some crystallographic aspects in the regions of large grains,

   (b) some intergranular cracking with secondary cracks in the regions of small grains,

   (c) more intergranular and secondary cracking at 650°C.

Since the difference in FCPR is smaller at higher ΔK and decreases with ΔK, these differences cannot be explained by crack closure effects. At 650°C, more important corrosion-product induced crack closure would be expected. As well, the fracture facets at low ΔK were also larger for the test at 650°C, which should also have produced more roughness induced crack closure in the test. The results therefore indicate that the differences between the FCPR at room temperature and 650°C are mainly associated with

time-dependent contributions at 650°C. The lower amounts of fracture surface oxidation and of intergranular cracking with increasing da/dN values qualitatively agree with the decreasing difference in FCPR. This suggests that the environmental and crack deviation effects played a more important role than the creep effects for the high temperature tests. These observations also suggest that the transgranular cracking in the regions of large grains occurs more rapidly than the intergranular cracking in the small grain regions. The difference between the FCPRs at room temperature and at 650°C decreases with increasing da/dN. This appears to be primarily associated with a decreasing influence of the environment. In general, the results suggested that the accelerated FCPR at 650°C was mainly the result of environmentally assisted cracking.

(4) Increasing the hold time at K_{max} during the test at 650°C from 0 to 10 seconds, increases the FCPR in Astroloy. A further increase of hold time to 100 seconds did not significantly increase the FCPR further. While increasing the hold time increases the influence of the time-dependent effects, the fractographic observations indicated that increasing the hold time to 100 seconds resulted in more pronounced crack deviations on the fracture surface, which can decrease ΔK_{eff} and compensate for the increase time available for the time-dependent contribution to the cracking process.

(5) The influence of minor cycles on FCPR was only observed in the 0.1 minor cycle load range ratio test for $\Delta K_{major} > 35$ MPa$\sqrt{m}$. This

result should be related to the threshold value of the minor cycle, ΔKth minor, which depends on:

(a) the R-ratios of the minor and major cycles,

(b) the minor cycle frequency,

(c) the shape and length of the crack,

(d) any cyclic effects which influence the fracture of oxide film at the crack tip.

The clear block-striations with two pronounced lines per major cycle, the striation-like features between these two pronounced lines, the flatter regions with striation-like features after the block-striations, and of the stronger crack deviation for $\Delta K_{major} > 35$ MPa$\sqrt{m}$ indicated that crack deviation occurred after the load-increasing portion of the major cycle and that the minor cycle propagation initially followed the deviated crack. These observations also suggested that the crack then reinitiated on a plane close to the initial fracture plane and that there were interaction effects between the minor and major cycles.

8. REFERENCES

1. M.D. Raizenne, W. Wallace, "Review of Methods for Crack Growth Testing in Gas Turbine Engine Disk Materials", to be published.
2. A.J.A. Mom, M.D. Raizenne, "AGARD Cooperative Test Programme on Titanium Alloy Engine Disc Material", AGARD-CP-393, 1985, p 9.
3. J.A. Harris, C.G. Annis, M.C. Vanwanderham, D.L. Sims, "Engine Component Retirement for Cause", AGARD-CP-317, Jan. 1982.
4. R.J. Hill, W.H. Reimann, J.S. Ogg, "A Retirement-for-Cause Study of an Engine Turbine Disk", Nov. 1981, AFWAL-TR-81-2094.
5. C.F. Harrison, "Recorder's Report of final Discussion", AGARD-CP-393, 1985.
6. C.T. Sims, W.C. Hagel, "The Superalloys", J. Wiley Co., New York, 1972. p 6.
7. G.H. Gessinger, "Powder Metallurgy of Superalloys", London; Boston; Butterworths, 1984, p 165.
8. See Reference 6, p 17.
9. D.J. Evans, "Powder Metallurgy processing of Astrology Turbine Disks", Modern Developments in Powder Metallurgy, Vol. 8, 1974, pp 473-490.
10. M.J. Blackburm, "Production of Components by Hot Isostatic Pressing of Nickel-Based Superalloy Powders", Metals Technology, Aug. 1977, pp 388-395.
11. "Metals Handbook", American Society for Metals, Metals Park, Ohio 44073, Ninth Edition, Vol. 9, p 320.

12. J.A. Dominque et al., "Advances in Understanding Powder Superalloys - A Sequel", P/M Aerospace materials, Nov. 1984.

13. T.C. Lu et al., "The Influence for Powder Characteristics on the HIP Behaviour of Low Carbon Astroloy" P/M Aerospace Materials, Vol. II.

14. See Reference 7, p 149.

15. R.D. Mclntyre, "Superalloys - More Super than Ever", Mater. Eng., Jan. 1982, 95, (1), pp 36-43.

16. N.A. Wilkinson, "Technological Considerations in the Forging of Superalloy Rotor Parts", Metals Technology, July 1977, pp 346-359.

17. R.V. Miner, "Fatigue and Creep — Fatigue Deformation of Several Nickel-Based Superalloys at 650°C", Metall. Trans. A, Oct. 1982, 13A(10), pp 1755-1765.

18. Ladish Co. Rolls Royce Ltd., "Mechanical Property and Structure Evaluation of the RB-211 High Pressure Turbine Disc", 1982.

19. "Superalloys: Source Book", M.J. Donachie, Jr. ed., ASM Metals Park, Ohio, 1984.

20. See Reference 7, pp 4-6.

21. R. Thamburaj et al., "Prior Particle Boundary Precipitation in P/M Superalloys", Modern Developments in P/M, Vol. 15-17, 1985, pp 635-673.

22. See Reference 19, p 102.

23. M.T. Podob, "Effect of Heat Treatment and Slight Chemistry Variations on the Physical Metallurgy of HIP LC Astroloy Powder", Modern Developments in P/M, Vol. 11, 1977, pp 25-44.

24. M. Carol, "Microstructure - Property Relationship in some Ni-based Superalloys", Thesis of Master on Applied Science, Dept. of Metal. Eng., Ecole Polytechnique de Montréal, Aug. 1986.

25. J. Gayda et al, "The Effect of Microstructure on 650°C Fatigue Crack Growth in P/M Astroloy, Metall. Trans. A., Nov. 1983, 14A, pp 2301-2308.

26. See Reference 7, p 132.

27. M.J. Weaver, "Powder Metallurgy and the Aerogas Turbine Engine", Powder Metall. 1984, 27 (3), pp 141-146.

28. S. Floreen, "High-Temperature Crack Growth Structure — Property Relationships in Nickel-Base Superalloys", taken from "Creep-Fatigue-Environment", The Metallurgical Society of AIME, New York, 1980, pp 112-128.

29. S. Floreen et al, "A Critical Strain Model for the Creep Fracture of Nickel Base Superalloys", Metallurgy Transactions, Vol. 7A, No. 8, Aug. 1976.

30. V. Lupic, "Creep: Introduction and Phenomenology ", Creep and Fatigue in High Temperature Alloys, 1981.

31. R.E. Smallman, "Modern Physical Metallurgy", Fourth Edition, London; Boston: Butterworths, 1985.

32. R.I. DiMelfi et al., "The Stress Dependence of the Crack Growth Rate During Creep", International Journal of Fracture, Vol. 13, No. 3, 1977.

33. R.M. Pelloux, J.S. Huong, "Creep-Fatigue-Environment Interactions In Astroloy", taken from "Creep-Fatigue-Environment", The Metallurgical Society of AIME, New York, 1980, pp 151-164.

34. J.P. Bailon and J.I. Dickson, "Fatigue: Testing and Meaning", Workshop on Fatigue, V International Congress on Experimental Mechanics, June 10-15, 1984, Montréal.

35. A.J. Huis, "Microstructure of Plastically Deformed Ni-Base Superalloy", Strength of Metals and Alloys, Vol. 1, 1985, pp 411-416.

36. C.H. Wells, "High Temperature Fatigue", Fatigue and Microstructure, ASM Materials Science Seminar, Metals Park, Ohio, 1978.

37. J. Bressers et al., "Fatigue Dominated Damage Processes", High Temperature Alloys for Gas Turbines and Other Applications, 1986: Proceedings of A Conference Held in Liége, Belgium, edited by W. Betz, D. Reidel Publ. Co.

38. S.S. Manson, "Fatigue at Elevated Temperatures", ASTM STP520, 1973, pp 744-782.

39. L.F. Coffin, "Fatigue at Elevated Temperatures", ASTM STP520, 1973, pp 5-34.

40. N.S. Stoloff, "Fatigue Crack Growth and Low Cycle Fatigue of Two Nickel-Base Superalloy", N84-10267, 16 Sept. 1983.

41. J. Gayda et al., "Fatigue Crack Initiation and Propagation in Several Nickel-Base Superalloys at 650°C", Int. J. Fatigue, July 1983, 5(3), pp 135-143.

42. See Reference 11, Vol. 8, Mechanical Testing.

43. S.S. Manson, "Time-Dependent Fatigue of Structure Alloys", ORNL-5073, Oak Ridge, 1977.

44. A. Saxena, "A Model for Predicting the Environment Enhanced Fatigue Crack Growth Behaviour at High Temperature", Thermal and Environment Effects in Fatigue [proc. conf.], 1983, PVP-Vo 71, pp 171-183.

45. R.M. Wallace, "Application of Fracture Mechanics at Elevated Temperature", Report AFML-TR-76-176, 1976.

46. (11), Vol. 3, p 223-227.

47. M. Jeandin, "Necklace Structure Obtained by Forging Astroloy Supersolidus-Sintered Preforms", Journal of Materials Science, 17, 1982, pp 2902-2910.

48. J. Bressers, "Time Dependent Low Cycle Fatigue of PM Astroloy at 1003K", High Temperature Alloys for Gas Turbines 1982 [Proc. Conf.], pp 597-609.

49. J.E. Coyne, "Microstructural Control in Titanium and Nickel-Base Forgings: An Overview", Metals Technology, July 1977, pp 337-345.

50. See Reference 7, p 329.

51. G.J. Lloyd, "High Temperature Fatigue and Creep-Fatigue Crack propagation: Mechanics, Mechanisms and Observed Behaviour in Structural Materials", taken from "Fatigue at High Temperature", edited by R.P. Skelton, Applied Science Publishers Ltd., London and New York, 1983, p 215.

52. D. Schütz, "Variable Amplitude Fatigue Testing", AGARD. LS-118, Fatigue Test Methodology, 1982.

53. J.W. Provan, "Introduction to Fracture and Fatigue Concepts", Fatigue Theory and Testing, Department of Mechanical Engineering, McGill University, 1984.

54. F.G. Hamel et al., "Fatigue Crack Rate Under Variable Amplitude Loading Predicted by a Simple Cumulative Damage Parameter", Fatigue 1984.

55. R.P. Wei, "Delay in Fatigue Crack Growth", Int. J. Fracture, 10, 1974, ASTM STP 595, 1976.

56. D.E. Macha, "Fatigue Crack Growth Retardation Behaviour of IN-100 at High Temperature", Eng. Fracture Mechanics.

57. J.M. Larsen et al., "Observation of Crack Retardation Resulting from Load sequencing characteristic of Military Gas Turbine Operation", ASTM STP 714, 1980, pp 91-107.

58. R.P. Wei, "Delay in Fatigue Crack Growth", Int. J. Fracture, 10, 1974.

59. R.P. Wei et al., "Influences of Chemical and Thermal Environments of Delay in a Ti-6Al-4V Alloy", ASTM STP 595, 1976, pp 113-120.

60. A.C. Pickard, "The Application of 3-Dimensional Finite Element Methods to Fracture Mechanics and Life Prediction", EMAS, 1986, pp 117-178.

61. C.W. Brown et al., "Fatigue Growth of Surface Cracks in Nickel-Base Superalloys", Int. J. Fatigue, April 1982, pp 73-81.

62. C.J. Beevers et al., "The Measurement of Crack Length and Shape During Fracture and Fatigue", 1980.

63. S.J. Hudak et al., "Fatigue Crack Growth Measurement and Data Analysis", ASTM STP 738, 1981.

64. G. Summer et al., "Technique for High Temperature Fatigue Testing", 1983.

65. H. Policella et al., "Mesure de Longueur de Fissure, Deformation et Endommagement par Une Technique de Potentiel Electrique", AGARD, CP-393.

66. C.E. Richards, W.F. Deans, "The Measurement of Crack Length and Load Using Strain Gauges", taken from "The Measurement of Crack Length and Shape During Fracture and Fatigue". Edited by C.J. Beavers, EMAS Ltd. West Midlands, United Kingdom. 1980.

67. G.F. Aker, T. Tereada, "The Calibration and Implementation of the Direct Current Potential Drop Technique On CT Specimen", NRC-Laboratory Technical Report, LTR-ST-1599, 1986.

68. A.J.A. Mom, "Working Document for the AGARD Cooperative Test Programme On Titanium Alloy Engine Disc Material", NLR TR 84022L, 1984.

69. M.A. Hicks, A.C. Pickard, "A Comparison of Theoretical and Experimental Methods of Calibration the Electrical Potential Drop Technique for Crack Length Determination", Int. Journ. of Fracture 20, 1982, pp 91-101.

70. A.E. Carden, "A Critical Evaluation of Fatigue Crack Growth Measurement Technique for Elevated Temperature Applications", BULLETIN 283, 1983, ISSN 0043-2326.

71. A.C. Pickard, C.W. Brown, M.A. Hicks, "The Development of Advanced Specimen Testing and Analysis Techniques Applied to Fracture Mechanics Lifing of Gas Turbine Components",

72. R.P. Wei, R.L. Brazill, "An Assessment of A-C and D-C Potential Systems for Monitoring Fatigue Crack Growth", ASTM. STP 738, 1981, pp 103-119.

73. "The Measurement of Crack Length and Shape During Fracture and Fatigue", Edited by C.J. Beevers, pp 85-284.

74. "Advances in Crack Length Measurement", Edited by C.J. Beevers, pp 97-252.

75. S. R. Swanson, "Handbook of Fatigue Testing", ASTM STP 566, 1974.

76. M.D. Raizenne, "An MTS Basic 770 Computer Program for Automated Fatigue Crack Growth Rate Testing", NAE-NRC Laboratory Technical Report, LTR-ST-1538, 1986.

77. A.J.A. Mom, M.D. Raizenne, "AGARD Engine Disc Cooperative Test Programme", NLR MP 86045 U, December 1987.

78. P.C. Paris and F. Erdogan, "A Critical Analysis of Crack Propagation Laws", Trans. ASME, J. Basic Eng., Vol. 85, No 4, 1963, p. 528.

79. 1984 Annual Book of ASTM Standards, Section 3, E-647-83, p. 711.

80. G.E. Bowie and D.W. Hoeppner, "Numerical Modeling of Fatigue and Crack Propagation Test Results", Nuclear Metallurgy Proceedings of the 1976 International Conference Simulation for Materials Applications, Vol. 20, Part 2, p. 1171.

81. P.M. Sooley and D. McCammond, "Low Cycle Fatigue Life and Fatigue Crack Growth Behaviour of Ti6A1-4V Disc Material", Dept. of Mechanical Eng., U. of Toronto, Contractors Report, series 86-31.

82. J.P. Bailon, P. Chappuis, J. Masounave and J.I. Dickson, "Fractographic Aspects near the Threshold in Several Alloys", Fatigue Thresholds, Vol. 1, 1981, p.227.

83. J.P. Bailon, J.I. Dickson and Li Shiqiong, "Relationship Between Fractographic Features and Fatigue Propagation Mechanisms At or Near the Threshold", Article invité accepté pour publication dans les comptes rendus du Symposium, Basic Mechanisms in Fatigue, April 1988, Brno, Techecoslovaquie.

84. J.I. Dickson, Li Shiqiong and J.P. Bailon, "An Explanation of the Fractography of Near-Threshold Fatigue in FCC Metals", Fatigue 87, p.759.

85. R.M. Pelloux, "Mechanism of Formation of Ductile Fatigue Striations", Trans. ASM, Vol. 62, 1969, p.281.

86. P.J.E. Forsyth and D.A. Ryder, "Some Results of the Examination of Aluminium Alloy Specimens Fracture Surfaces", Metallurgica, Vol. 63, 1961, p.117.

87. C. Laird and G.C. Smith, "Crack Propagation in High Stress Fatigue", Philosophical Magazine, Vol. 7, 1962, p.847.

88. P. Neumann, "New Experiments Concerning the Slip Processes at Propagating Fatigue Cracks, I and II", Acta Metallurgica, Vol. 22, 1974, p.1155.

89. C.A. Stubbington, "Some Observation on Air and Corrosion Fatigue of an Aluminium -7.5% Zinc -2.5% Magnesium Alloy", Metallurgica Vol. 68, 1963, p. 109.

90. See Reference 51, p. 187.

91. L.F. Coffin, "Damage Process in Time-dependent Fatigue - A Review", Creep-Fatigue-Environment Interaction, ed. R.M. Pelloux and N.S. Stoloff, AIME, 1980, p.1.

92. N. Marchand, "Thermal-Mechanical Fatigue Behaviour of High Temperature Alloys", Ph.D. thesis, MIT 1983.

93. C. Laird, "Fatigue Crack Propagation", ASTM STP 415, 1966, p.131.

94. J.C. Runkle and R.M. Pelloux, "Fatigue Mechanisms", ASTM STP 675, 1979, p.501.

95. A.K. Koul, P. Au, N. Bellinger, R. Thamburaj, W. Wallace and J.P. Immarigeon, "Development of a Damage Tolerant Microstructure for Inconel 718 Turbine Disc Material" Superalloys, Sept. 1988, eds. D.N. Duhl et al, p.3.

96. A.S. Argon, C.W. Lau, B. Ozmat and D.M. Parks, "Creep Crack Growth in Ductile Alloys", ed. K. Mitter, 1984, p.243.

97. S.M.R. Pishva, "Rejuvenation of Gas Turbine Discs", Masters thesis, 1988, Carleton University, Ottawa.

98. R.J.H. Wanhill, "Some Case Studies and the Significance of Fatigue Thresholds", Fatigue Thresholds, Fundamentals and Engineering Applications (EMAS, Warley, 1982) Vol. 2, p.953.

99. B.E. Powell and T.V. Duggan, "The Influence of Minor Cycles on Low Cycle Fatigue Crack Propagation", Int. J. Fatigue, Jan. 1982, p.4.

100. B.E. Powell and T.V. Duggan, "Predicting the Onset of High Cycle Fatigue Damage: an Engineering Application for Long Crack Fatigue Threshold Data", Int. J. Fatigue Vol. 8, No.4, 1986, p.187.

101. R.W. Hertzberg and W.J. Mills, "Character of Fatigue Fracture Surface Micromorphology in the Ultra-Low Growth Rate Regime",

Fractography-Microscopic Cracking Processes ASTM STP 600, 1976, p.220.

102. R.J. Bucci, P.C. Paris, R.W. Hertzberg, R.A. Schmidt and A.F. Anderson, "Fatigue Threshold Crack Propagation in Air and Dry Argon for a Ti-6Al-4V Alloy", Stress Analysis and Growth of Cracks. STP 513, 1972, p.125.

103. A. Yuen, S.W. Hopkins, G.R. Leverant and C.A. Rau, "Correlations Between Fracture Surface Appearance and Fracture Mechanics Parameters for Stage II Fatigue Crack Propagation in Ti-6Al-4V", Met. Trans. Vol. 5A 1974, p.1833.

104. B.E. Powell and T.V. Duggan, "Crack Growth in Ti-6Al-4V under the Conjoint Action of High and Low Cycle Fatigue", Int. J. Fatigue, Vol. 9, No.4, 1987, p.195.

105. P.E. Ward-Close and C.J. Beevers, "The Influence of Grain Orientation on the Mode and Rate of Fatigue Crack Growth in α-Titanium", Met. Trans. Vol. 11A, 1980, p.1617.

106. R. Thamburaj, T. Terada, A.K. Koul, W. Wallace and M.C. de Malherbe, "The Influence of Microstructure and Environment upon Elevated Temperature Crack Growth Rate in Inconel 718", Proc. Int. on Creep, Tokyo, Japan, April 1986, eds. D. Woodford et al., ASME/JSME, p.275.

107. M. Jeandin, "Necklace Structure Obtained by Forging Astroloy Supersolidus-Sintered Preforms", J. of Materials Science, Vol. 7, 1982, p.2902.

108. W. Wallace, H.B. Dunthorne and R.A. Sprague, "Microstructure and Mechanical Properties in a Turbine Disc Fabricated from Astroloy

Powder", Canadian Metallurgical Quarterly, Vol.13, No.3, 1974, p.517.

109. W. Wallace, W. Wiebe, E.P. Whelan, R.V. Dainty and T. Terada, "The Effect of Grain Boundary Structure on the Tensile Fracture Behaviour of Hot-Isostatically Pressed 713 LC Alloy Compacts", Powder Met. Vol. 16, (32), 1973, p.416.

110. R.T. Holt and W. Wallace, "Impurities and Trace Element in Nickel-Base Superalloys", Int. Met. Reviews, Vol. 21, 1976, p.1.

TABLES

No.	*Consolidation*	*Subsequent deformation*	*Microstructure*
1	HIP below γ′ solvus	(a) – (b) Isothermal forging below γ′ solvus	Fine grain recrystallized Fine grained
2	2-stage HIP below γ′ solvus	–	Fine grained, *no* MC at PPB
3	T/P + HIP below γ′ solvus	(a) – (b) Isothermal forging below γ′ solvus (c) Conventional forging	Very fine grained Fine grained Fine grained
4	HIP above γ′ solvus	(a) – (b) Isothermal forging above γ′ solvus (c) Conventional forging hot working hot work/warm work warm working	Increased grain size Necklace Coarse grains *Necklace* and fine grains Necklace and *fine grains*
5	HIP above boride solvus	(a) – (b) Isothermal forging below γ′ solvus	Coarse grains Mixture of fine grain + warm worked

TABLE 1-1

PROCESSING ROUTES USED OR SUGGESTED FOR P/M LC ASTROLOY AND THE MICROSTRUCTURES OBTAINED [14]

ELEMENTS	CONTENTS (WT %)
Carbon	0.01 ~ 0.35
Manganese	0.15 max.
Sulphur	0.015 max.
Phosporus	0.015 max.
Silicon	0.20 max.
Chromium	14.00 ~ 16.00
Cobalt	16.00 ~ 18.00
Molybdenum	4.50 ~ 5.50
Titanium	3.35 ~ 3.65
Aluminum	3.85 ~ 4.15
Boron	0.015 ~ 0.030
Zirconium	0.03 ~ 0.06
Tungsten	0.05 max.
Iron	0.50 max.
Copper	0.10 max.
Silver	5 ppm* *max.*
Lead	5 ppm *max.*
Bismuth	0.5 ppm *max.*
Nickel	Remainder

* ppm = 10^{-6}

TABLE 1-2

CHEMICAL COMPOSITION OF ASTROLOY ALLOY [18]

METHODE	PRELIMINARY CALIBRATION	LOCATION MEASURED	ENVIRONMENT					TYPE OF SPECIMEN	SENSITIVITY (mm)	MEASURING STEPS (mm)
			AIR			CORROSIVE				
			20°C	LOW TEMP.	HIGH TEMP.	20°C	HIGH TEMP.			
OPTICAL	No	Surface	+	0	±	+	0	All	0.005	0.5 recomm.
EDDY CURRENT	No	Surface	+	0	0	0	0	CT,KT,CCT	<0.05	0.1
ULTRASONIC	No	Volume	+	0	0	±	0	CT	0.03	0.1
CRACKING GAGES	No	Surface	+	+	0	±	0	All	0.2	0.2
CMOD GAGES	Yes	Volume	+	+	+	+	±	All	f(a/W)	continuous
BACK FACE STRAIN GAGE	Yes	Volume	+	+	0	+	0	CT,KT	f(a/W)	continuous
DROP VOLTAGE (electrical resistance)	Yes	Volume	+	+	+	0	±	All	0.01 to 0.05	continuous

Keys = + easy use; ± use with some caution; 0 = impossible to use.
KT = 3 point bending specimen.

TABLE 3-1

COMPARISON OF SOME EXPERIMENTAL TECHNIQUES FOR MEASURING CRACK LENGTHS [34]

Table 4-1

CHEMICAL COMPOSITION OF P/M LC ASTROLOY[18]

COMPOSITION (weight %) FOR ELEMENTS									
C	Mn	S	P	Si	Cr	Co	Mo	Ti	Al
0.027	0.01	0.02	0.05	<0.01	14.84	16.8	4.96	3.55	3.94
B	Zr	W	Fe	Cu*	Au*	Pb*	Bi*	Ni	
0.019	0.045	<0.05	0.04	<0.01	1.6 ppm*	0.3 ppm	<0.1 ppm	Balance	

*ppm = 10^{-6}

**Tramp elements*

Table 4-2

MECHANICAL PROPERTIES OF P/M LC ASTROLOY[18]

	0.2% YS (MPa)	UTS (MPa)	Elong. (%)	RA (%)
RT	1029	1448	23	28
650°C	945	1386	21	20

Stress-Rupture Properties:
760°C at 586 MPa

Rupture	Elongation
186.4 hrs.	13.0%

TABLE 5-1

CALIBRATION CURVES COEFFICIENTS

Specimen #	Loading sequence Type	a_I	V_I	a_F	V_F	V(RG)	$(a_F V_I - a_I V_F)/(V_F - V_I)$
		(mm)	(μV)	(μV)	(μV)	μV/mm	(mm)
BT1	1	0.22	191.56	5.62	2383.18	405.86	0.252
BT2	2	0.16	147.96	4.03	1877.32	446.86	0.171
BT4	3	0.20	190.28	4.49	2202.74	469.11	0.201
BT5	3	0.157	139.11	5.28	2385.44	438.48	0.160
BT6	4	0.16	145.58	4.72	2233.63	457.91	0.158
BT7	1	0.173	164.20	5.39	2499.82	455.55	0.182
BT10	5	0.14	146.31	4.47	2265.57	489.44	0.159

TABLE 5-2

FATIGUE CRACK PROPAGATION RATE DATA

FOR SPECIMEN BT1

MATERIAL: P/M LC ASTROLOY
SPECIMEN GEOMETRY: CORNER CRACK
TEST TEMPERATURE: ROOM TEMPERATURE
LOADING SEQUENCE TYPE: 1

P(MAX.): 90 kN
P(MIN.): 9 kN
MEASUREMENT TECHNIQUE: dc - PD
SMOOTHING TECHNIQUE: SECANT METHOD

OBS#	CYCLES	ΔV (μV)	a (mm)	a(AVG.) (mm)	ΔK [MPa√m]	da/dN (m/CYCLE)
1	0	191.56	.22			
2	0	269.23	.41	.455	22.7	.372E-07
3	2350	304.71	.50	.570	25.4	.567E-07
4	4850	362.23	.64	.710	28.4	.861E-07
5	6500	419.88	.78	.855	31.2	.123E-06
6	7700	479.72	.93	.985	33.6	.158E-06
7	8400	524.54	1.04	1.110	35.7	.187E-06
8	9150	581.33	1.18	1.245	37.9	.243E-06
9	9700	635.56	1.31	1.380	40.1	.281E-06
10	10200	692.65	1.45	1.520	42.1	.321E-06
11	10600	744.80	1.58	1.650	44.1	.400E-06
12	10950	801.59	1.72	1.785	46.0	.426E-06
13	11250	853.50	1.85	1.915	47.8	.518E-06
14	11500	906.08	1.98	2.040	50.1	.612E-06
15	11700	955.72	2.10	2.170	52.3	.682E-06
16	11900	1011.11	2.24	2.295	54.5	.736E-06
17	12050	1055.93	2.35	2.420	56.7	.935E-06
18	12200	1112.84	2.49	2.570	59.4	.105E-05
19	12350	1176.84	2.65	2.710	62.0	.118E-05
20	12450	1224.89	2.77	2.840	64.6	.153E-05
21	12550	1287.06	2.92	3.000	67.8	.164E-05
22	12650	1353.80	3.08	3.195	71.9	.222E-05
23	12750	1443.75	3.31	3.370	75.7	.241E-05
24	12800	1492.66	3.43	3.490	78.6	.253E-05
25	12850	1544.08	3.55	3.625	82.0	.290E-05
26	12900	1603.00	3.70	3.795	86.3	.388E-05
27	12950	1681.72	3.89	4.015	92.5	.500E-05
28	13000	1783.14	4.14	4.330	102.1	.748E-05
29	13050	1935.56	4.52	5.070	130.1	.220E-04
30	13100	2383.16	5.62			

TABLE 5-3

FATIGUE CRACK PROPAGATION RATE DATA

FOR SPECIMEN BT2

MATERIAL: P/M LC ASTROLOY
SPECIMEN GEOMETRY: CORNER CRACK
TEST TEMPERATURE: 650°C
LOADING SEQUENCE TYPE: 2

P(MAX.): 76.5 kN
P(MIN.): 7.65 kN
MEASUREMENT TECHNIQUE: dc - PD
SMOOTHING TECHNIQUE: SECANT METHOD

OBS#	CYCLES	ΔV (μV)	a (mm)	a(AVG.) (mm)	ΔK [MPa√m]	da/dN (m/CYCLE)
1	0	147.96	.16	.215	13.2	.426E-07
2	2600	197.42	.27	.315	16.1	.943E-07
3	3600	239.56	.36	.425	18.6	.153E-06
4	4400	294.27	.49	.550	21.2	.216E-06
5	5000	352.16	.62	.670	23.4	.263E-06
6	5400	399.18	.72	.785	25.4	.310E-06
7	5800	454.56	.85	.925	27.7	.406E-06
8	6200	527.05	1.01	1.105	30.2	.472E-06
9	6600	611.44	1.20	1.250	32.3	.548E-06
10	6800	660.41	1.31	1.370	33.9	.668E-06
11	7000	720.07	1.44	1.580	36.6	.700E-06
12	7400	845.13	1.72	1.790	39.2	.712E-06
13	7600	908.76	1.86	1.960	41.2	.101E-05
14	7800	999.38	2.07	2.175	44.5	.110E-05
15	8000	1097.88	2.29			
16	8300	1197.29	2.51	2.560	46.0	.974E-06
17	8400	1240.83	2.61			
18	9400	1561.24	3.32	3.390	50.9	.135E-05
19	9500	1621.51	3.46	3.510	52.8	.114E-05
20	9600	1672.62	3.57	3.650	55.0	.154E-05
21	9700	1741.38	3.73	3.790	57.5	.134E-05
22	9800	1801.46	3.86	3.945	60.3	.170E-05
23	9900	1877.31	4.03			

TABLE 5-4

FATIGUE CRACK PROPAGATION RATE DATA

FOR SPECIMEN BT4

MATERIAL: P/M LC ASTROLOY
SPECIMEN GEOMETRY: CORNER CRACK
TEST TEMPERATURE: 650°C
LOADING SEQUENCE TYPE: 3

P(MAX.): 85 kN
P(MIN.): 8.5 kN
MEASUREMENT TECHNIQUE: dc - PD
SMOOTHING TECHNIQUE: SECANT METHOD

OBS#	CYCLES	ΔV (μV)	a (mm)	a(AVG.) (mm)	ΔK [MPa√m]	da/dN (m/CYCLE)
1	0	190.28	.20			
2	0	206.70	.24	.290	17.1	.157E-06
3	700	258.18	.34	.400	20.1	.254E-06
4	1140	310.64	.46	.510	22.7	.374E-06
5	1420	359.73	.56	.620	25.0	.495E-06
6	1660	415.42	.68	.740	27.3	.580E-06
7	1860	469.65	.80	.850	29.4	.662E-06
8	2020	519.35	.90	.960	31.3	.952E-06
9	2140	572.97	1.02	1.150	34.3	.931E-06
10	2420	695.28	1.28	1.340	37.2	.105E-05
11	2540	754.15	1.40	1.475	39.2	.126E-05
12	2660	825.16	1.55	1.690	42.2	.138E-05
13	2860	954.80	1.83	1.895	44.9	.166E-05
14	2940	1016.97	1.96	2.030	47.2	.173E-05
15	3020	1081.88	2.10	2.180	49.6	.162E-05
16	3120	1157.66	2.26	2.370	52.7	.272E-05
17	3200	1259.64	2.48	2.590	56.5	.280E-05
18	3280	1364.73	2.70	2.760	59.5	.302E-05
19	3320	1421.40	2.82	2.890	62.0	.349E-05
20	3360	1486.92	2.96	3.030	64.6	.343E-05
21	3400	1551.28	3.10	3.160	67.2	.394E-05
22	3430	1606.67	3.22	3.120	70.5	.493E-05
23	3470	1699.12	3.42	3.480	74.0	.629E-05
24	3490	1758.11	3.54	3.605	77.0	.655E-05
25	3510	1819.60	3.67	3.745	80.3	.716E-05
26	3530	1886.77	3.82	3.910	84.5	.933E-05
27	3550	1974.34	4.00	4.105	89.9	.105E-04
28	3570	2072.53	4.21	4.280	94.9	.133E-04
29	3580	2135.06	4.35	4.420	99.2	.144E-04
30	3590	2202.72	4.49			

TABLE 5-5

FATIGUE CRACK PROPAGATION RATE DATA

FOR SPECIMEN BT5

MATERIAL: P/M LC ASTROLOY
SPECIMEN GEOMETRY: CORNER CRACK
TEST TEMPERATURE: 650°C
LOADING SEQUENCE TYPE: 3

P(MAX.): 85 kN
P(MIN.): 8.5 kN
MEASUREMENT TECHNIQUE: dc - PD
SMOOTHING TECHNIQUE: SECANT METHOD

OBS#	CYCLES	ΔV (μV)	a (mm)	a(AVG.) (mm)	ΔK [MPa√m]	da/dN (m/CYCLE)
1	0	139.10	.157			
2	0	140.57	.16	.225	15.1	.930E-07
3	1400	197.79	.29	.345	18.7	.277E-06
4	1800	246.33	.40	.465	21.6	.393E-06
5	2120	301.48	.53	.590	24.4	.512E-06
6	2360	355.33	.65	.715	26.9	.641E-06
7	2560	411.51	.78	.850	29.3	.861E-06
8	2720	471.91	.92	1.040	32.6	.880E-06
9	3000	579.99	1.16	1.230	35.6	.116E-05
10	3120	641.12	1.30	1.380	37.8	.130E-05
11	3240	709.33	1.46	1.515	39.7	.143E-05
12	3320	759.64	1.57	1.635	41.4	.157E-05
13	3400	814.72	1.70	1.770	43.2	.175E-05
14	3480	876.03	1.84	1.910	45.0	.173E-05
15	3560	936.55	1.98	2.060	47.6	.208E-05
16	3640	1009.52	2.14	2.235	50.5	.234E-05
17	3720	1091.59	2.33	2.420	53.5	.228E-05
18	3800	1171.40	2.51	2.635	57.2	.307E-05
19	3880	1279.06	2.76	2.885	61.8	.318E-05
20	3960	1390.74	3.01	3.180	67.6	.424E-05
21	4040	1539.62	3.35	3.475	74.0	.501E-05
22	4090	1649.47	3.60	3.725	79.8	.621E-05
23	4130	1758.35	3.85	3.970	86.1	.803E-05
24	4160	1863.93	4.09	4.185	92.1	.945E-05
25	4180	1946.80	4.28	4.390	98.3	.110E-04
26	4200	2043.58	4.50	4.560	103.9	.125E-04
27	4210	2098.30	4.63	4.700	108.7	.105E-04
28	4220	2163.94	4.77	4.860	114.7	.178E-04
29	4230	2241.98	4.95	5.115	124.9	.327E-04
30	4240	2385.42	5.28			

TABLE 5-6

FATIGUE CRACK PROPAGATION RATE DATA

FOR SPECIMEN BT6

MATERIAL: P/M LC ASTROLOY
SPECIMEN GEOMETRY: CORNER CRACK
TEST TEMPERATURE: 650°C
LOADING SEQUENCE TYPE: 4

P(MAX.): 85 kN
P(MIN.): 8.5 kN
MEASUREMENT TECHNIQUE: dc - PD
SMOOTHING TECHNIQUE: SECANT METHOD

OBS#	CYCLES	ΔV (μV)	a (mm)	a(AVG.) (mm)	ΔK [MPa√m]	da/dN (m/CYCLE)
1	0	145.58	.16			
2	0	171.84	.22	.280	16.7	.174E-06
3	680	226.00	.34	.425	20.6	.333E-06
4	1200	305.20	.51	.570	24.0	.438E-06
5	1480	361.32	.63	.690	26.4	.591E-06
6	1680	415.42	.75	.780	28.1	.770E-06
7	1760	443.63	.81	.840	29.2	.761E-06
8	1840	471.54	.87	.905	30.3	.838E-06
9	1920	502.26	.94	.975	31.5	.930E-06
10	2000	536.33	1.01	1.050	32.8	.952E-06
11	2080	571.20	1.09	1.115	33.8	.129E-05
12	2120	594.65	1.14	1.165	34.5	.112E-05
13	2160	615.16	1.19	1.210	35.3	.118E-05
14	2200	636.84	1.23	1.255	36.0	.117E-05
15	2240	658.34	1.28	1.315	36.8	.163E-05
16	2280	688.20	1.35	1.380	37.7	.156E-05
17	2320	716.78	1.41	1.440	38.7	.178E-05
18	2360	749.38	1.48	1.515	39.7	.182E-05
19	2400	782.79	1.55	1.595	40.8	.213E-05
20	2440	821.75	1.64	1.690	42.1	.253E-05
21	2480	868.03	1.74	1.795	43.6	.283E-05
22	2520	919.94	1.85	1.920	45.2	.345E-05
23	2560	983.20	1.99	2.080	48.0	.453E-05
24	2600	1066.19	2.17	2.280	51.1	.530E-05
25	2640	1163.28	2.38	2.515	55.1	.663E-05
26	2680	1284.74	2.65	2.820	60.5	.849E-05
27	2720	1140.27	2.99	3.210	68.3	.112E-04
28	2760	1646.18	3.44	3.780	81.3	.173E-04
29	2800	1963.22	4.13	4.425	99.4	.295E-04
30	2820	2233.62	4.72			

TABLE 5-7

FATIGUE CRACK PROPAGATION RATE DATA

FOR SPECIMEN BT7

MATERIAL: P/M LC ASTROLOY
SPECIMEN GEOMETRY: CORNER CRACK
TEST TEMPERATURE: 650°C
LOADING SEQUENCE TYPE: 1

P(MAX.): 85 kN
P(MIN.): 8.5 kN
MEASUREMENT TECHNIQUE: dc - PD
SMOOTHING TECHNIQUE: SECANT METHOD

OBS#	CYCLES	ΔV (μV)	a (mm)	a(AVG.) (mm)	ΔK [MPa√m]	da/dN (m/CYCLE)
1	0	159.32	.173			
2	0	204.87	.27	.295	17.3	.219E-06
3	200	224.53	.32	.335	18.4	.172E-06
4	400	239.92	.35	.390	19.8	.257E-06
5	680	272.23	.42	.460	21.5	.326E-06
6	880	301.48	.49	.520	22.9	.322E-06
7	1080	330.36	.55	.600	24.6	.462E-06
8	1280	371.82	.65	.695	26.5	.486E-06
9	1480	415.42	.74	.810	28.6	.642E-06
10	1680	473.01	.87	.950	31.1	.770E-06
11	1880	542.07	1.03	1.115	33.8	.862E-06
12	2080	619.44	1.20	1.130	36.7	.110E-05
13	2280	718.06	1.42	1.545	40.1	.126E-05
14	2480	830.90	1.67	1.825	43.9	.153E-05
15	2680	968.54	1.98	2.175	49.5	.198E-05
16	2880	1145.75	2.37	2.630	57.1	.258E-05
17	3080	1377.62	2.89	3.305	70.2	.415E-05
18	3280	1750.35	3.72	4.555	103.7	.835E-05
19	3480	2499.80	5.39			

TABLE 5-8

FATIGUE CRACK PROPAGATION RATE DATA

FOR SPECIMEN BT10

MATERIAL: P/M LC ASTROLOY
SPECIMEN GEOMETRY: CORNER CRACK
TEST TEMPERATURE: 650°C
LOADING SEQUENCE TYPE: 5

P(MAX.): 85 kN
P(MIN.): 8.5 kN
MEASUREMENT TECHNIQUE: dc - PD
SMOOTHING TECHNIQUE: SECANT METHOD

OBS#	CYCLES	ΔV (μV)	a (mm)	a(AVG.) (mm)	ΔK [MPa√m]	da/dN (m/CYCLE)
1	0	146.31	.14			
2	0	167.01	.18	.230	15.3	.131E-06
3	760	215.80	.28	.330	18.3	.211E-06
4	1240	265.33	.38	.440	21.1	.303E-06
5	1640	324.62	.50	.560	23.8	.403E-06
6	1920	379.82	.62	.665	26.1	.473E-06
7	2160	435.39	.73	.795	28.4	.629E-06
8	2360	496.94	.86	.930	30.7	.717E-06
9	2560	567.11	1.00	1.060	32.9	.771E-06
10	2720	627.50	1.12	1.200	35.1	.989E-06
11	2880	704.93	1.28	1.340	37.2	.991E-06
12	3000	763.18	1.40	1.475	39.1	.121E-05
13	3120	834.39	1.55	1.630	41.3	.133E-05
14	3240	912.49	1.71	1.765	43.2	.149E-05
15	3320	970.80	1.82	1.900	45.0	.197E-05
16	3400	1048.05	1.98	2.045	47.4	.156E-05
17	3480	1109.24	2.11	2.190	49.7	.201E-05
18	3560	1188.01	2.27	2.360	52.5	.226E-05
19	3640	1276.68	2.45	2.560	55.9	.274E-05
20	3720	1383.78	2.67	2.730	58.9	.308E-05
21	3760	1443.99	2.79	2.850	61.2	.304E-05
22	3800	1503.33	2.91	2.985	63.8	.376E-05
23	3840	1577.23	3.06	3.150	67.0	.449E-05
24	3880	1665.11	3.24	3.345	71.1	.507E-05
25	3920	1764.40	3.45	3.575	76.2	.647E-05
26	3960	1890.98	3.70	3.785	81.4	.830E-05
27	3980	1972.26	3.87	3.980	86.4	.111E-04
28	4000	2080.89	4.09	4.185	92.1	.122E-04
29	4015	2170.29	4.28	4.370	97.8	.195E-04
30	4025	2265.55	4.47			

TABLE 5-9

PARIS COEFFICIENTS

Specimen #	c	n
BT1	8.1915×10^{-13}	3.4450
BT2	7.6364×10^{-10}	1.8778
BT4	3.5458×10^{-10}	2.2173
BT5	5.2357×10^{-10}	2.1380
BT6	5.3179×10^{-11}	2.8430
BT7	3.9963×10^{-10}	2.1779
BT10	2.7632×10^{-10}	2.2836

TABLE 5-10

FOUR PARAMETER WEIBULL COEFFICIENTS

Specimen #	e	v	s	$B=k_b(MPa\sqrt{m})$
BT1	-1.08556×10^{-7}	2.87085×10^{-6}	0.50	130
BT2	-1.80917×10^{-7}	2.95805×10^{-6}	0.80	120
BT4	-3.01513×10^{-7}	5.25904×10^{-6}	0.73	120
BT5	-2.59800×10^{-7}	5.52684×10^{-6}	0.73	120
BT6	-2.00958×10^{-7}	1.40883×10^{-5}	0.48	120
BT7	-2.06578×10^{-7}	4.35131×10^{-6}	0.75	120
BT10	-1.57125×10^{-7}	5.72548×10^{-6}	0.64	120

TABLE 5-11

THE NUMBER OF FLIGHTS TO FAILURE
FOR VARYING LOAD LEVELS

	ΔP (kN) with R = 0.1							
Specimen #	90	81	72	63	54	45	36	27
BT1	17534	25239	37891	60051	102160	191490	413088	1112960
BT2	4176	5142	6483	8399	11289	15987	24400	42081
BT4	2673	3399	4443	6003	8778	12741	20937	39684
BT5	2398	3025	3921	5245	7323	10851	17525	32477
BT6	2034	2752	3857	5647	8763	14729	27792	62990
BT7	2727	3454	4495	6044	8487	12665	20634	38674
BT10	2715	3474	4574	6232	8890	13516	22537	43529

FIGURES

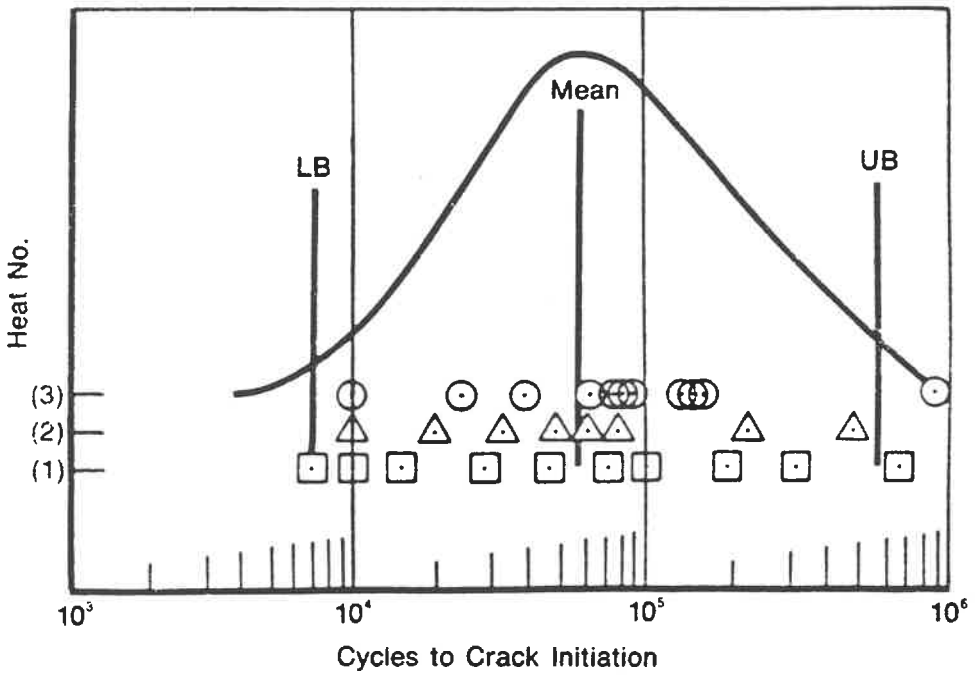

FIG. 1: SCHEMATIC OF CONSERVATIVE LIFING APPROACH (SAFE LIFE) [3]

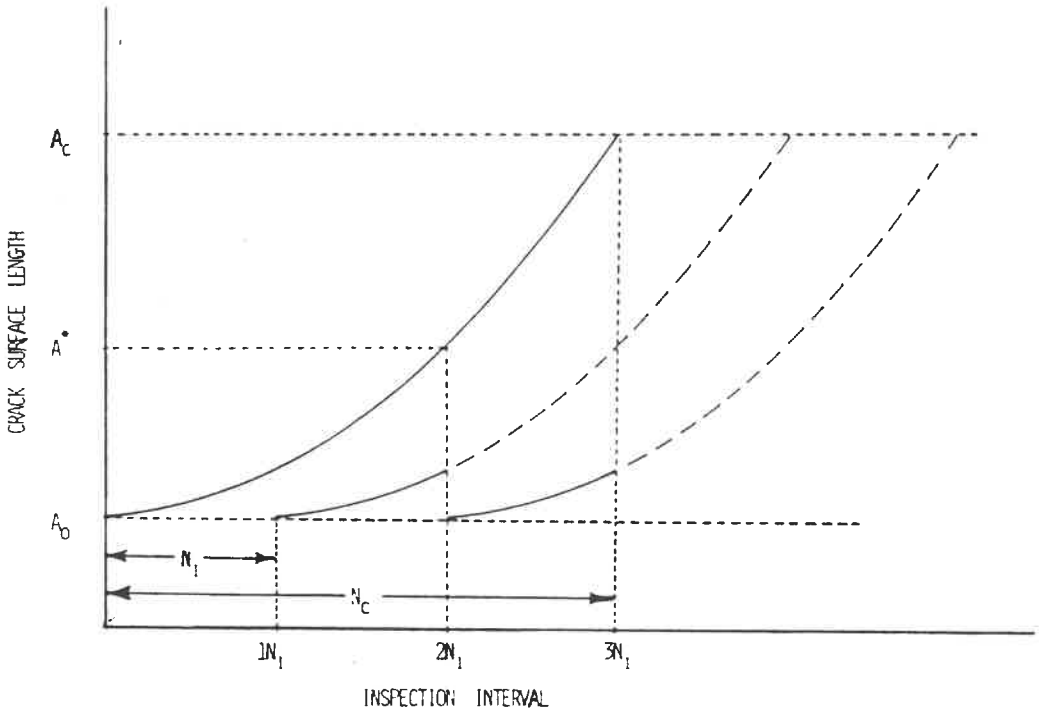

FIG. 2: SCHEMATIC OF RETIREMENT-FOR-CAUSE LIFING APPROACH [4]

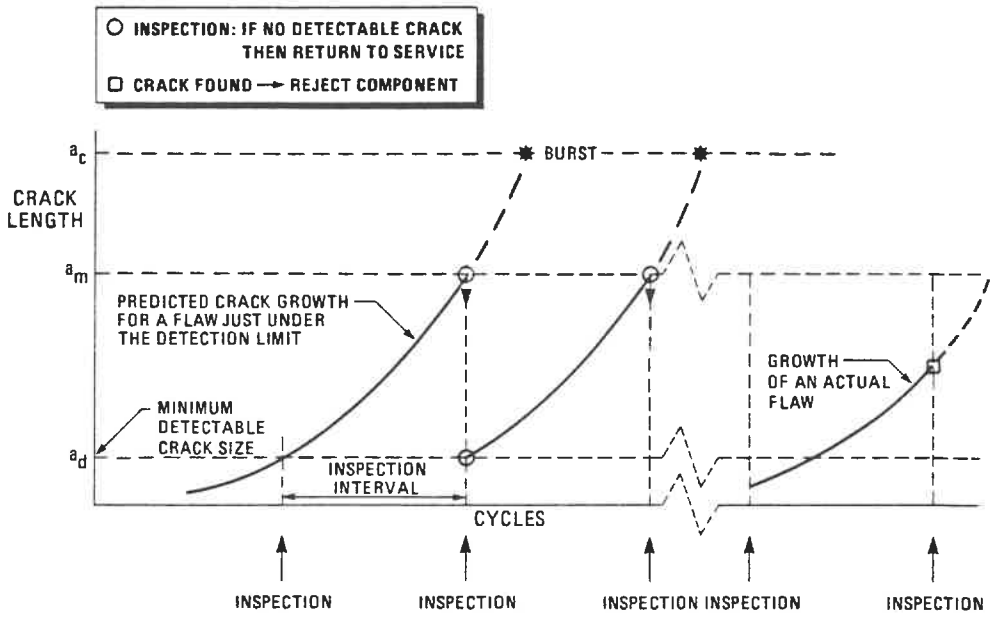

FIG. 3: SCHEMATIC OF DAMAGE TOLERANCE LIFING APPROACH [2]

(a) X 100 (b) X 10 000

FIG. 1-1: MICROSTRUCTURE OF I/M ASTROLOY [11]

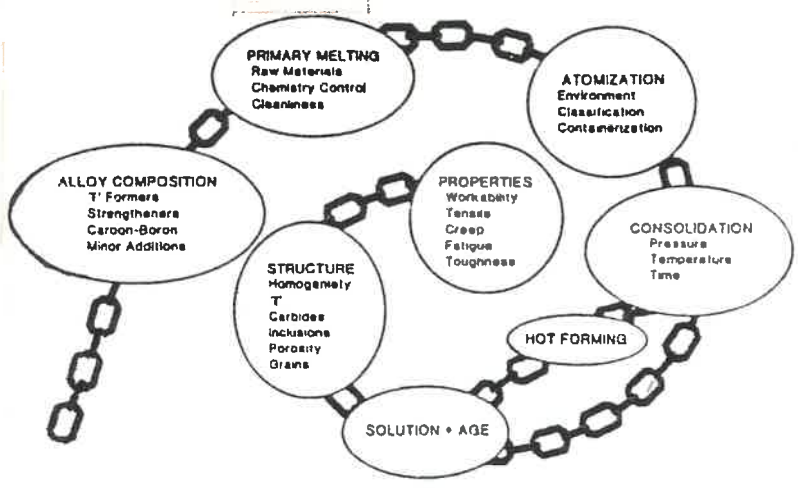

FIG. 1-2: CHAIN OF EVENTS IN P/M SUPERALLOY MANUFACTURING [12]

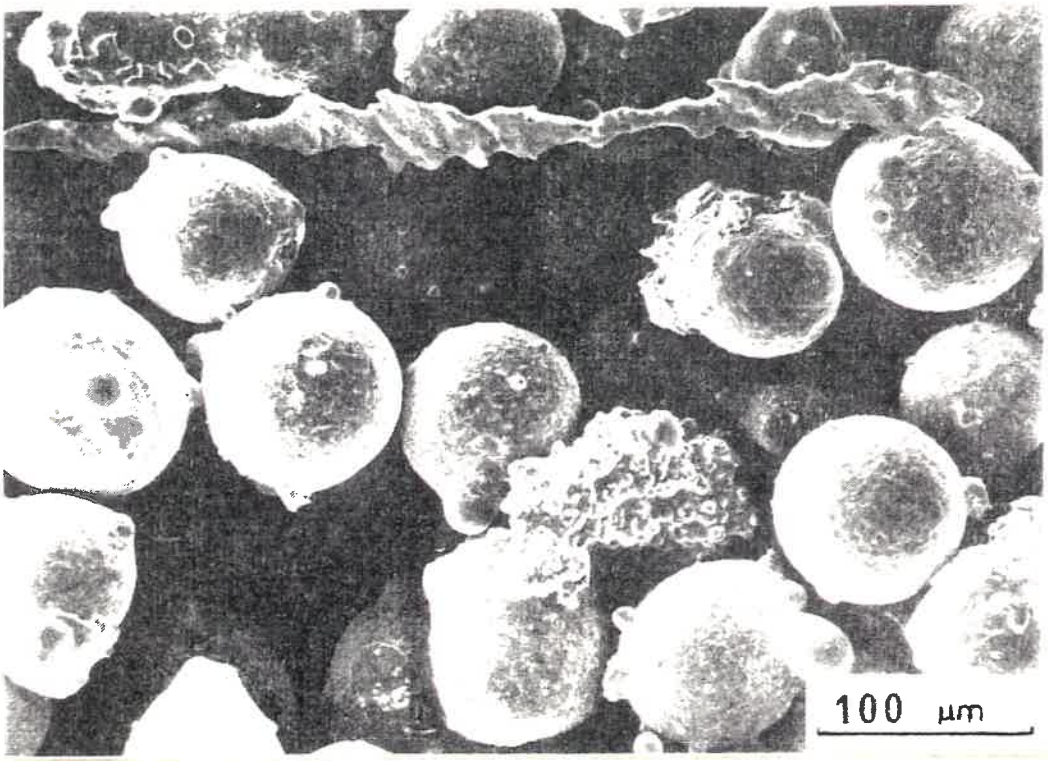

FIG. 1-3: ARGON-ATOMIZED POWDER OF ASTROLOY [13]

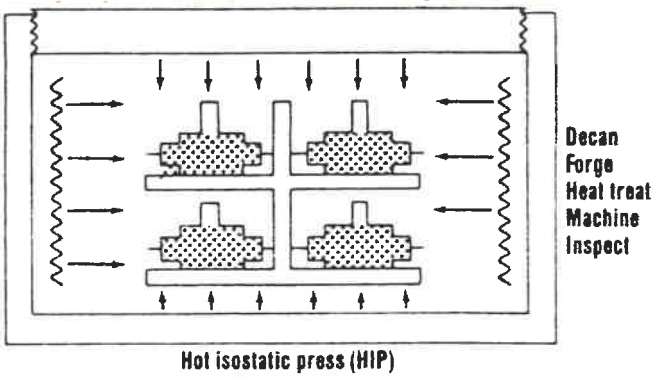

FIG. 1-4: HOT ISOSTATIC PRESS (HIP) PROCESSING [15]

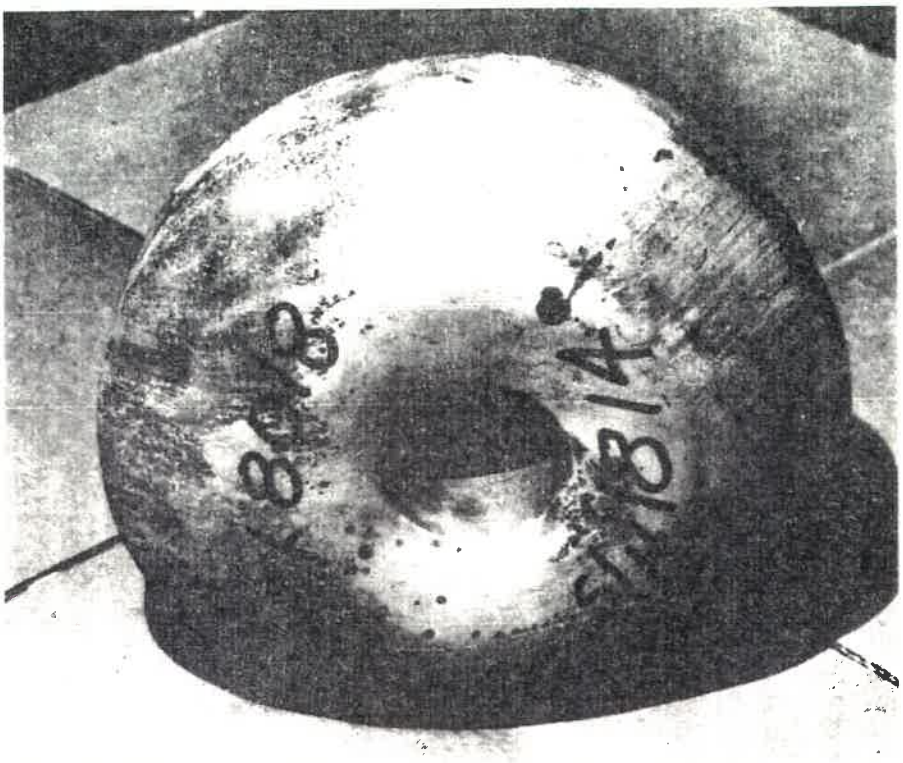

FIG. 1-5: ASTROLOY FORGING PREFORM AFTER HIP [9]

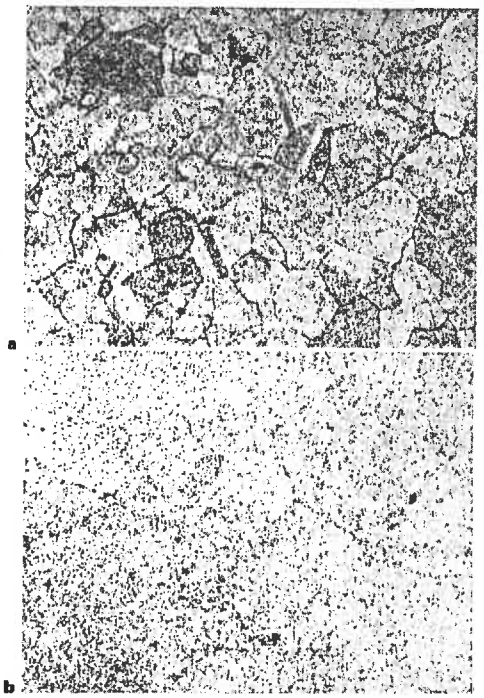

a ×100 ; *b* ×500

FIG. 1-6: TYPICAL MICROSTRUCTURE OF P/M ASTROLOY SUBJECTED TO HIP [16]

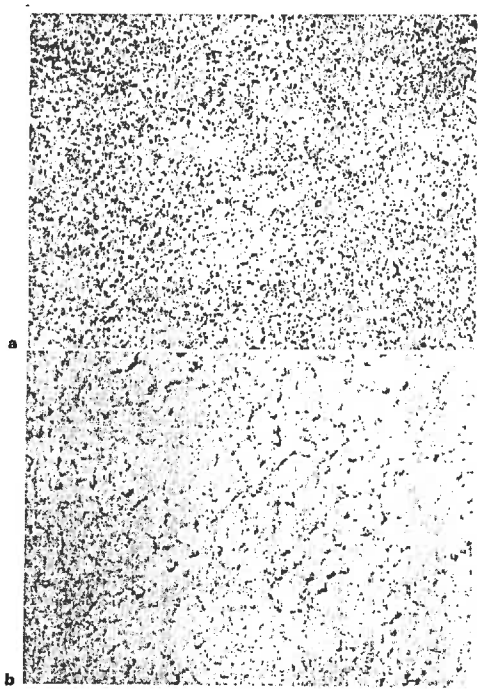

a ×100 ; *b* ×500

FIG. 1-7: TYPICAL MICROSTRUCTURE OF P/M ASTROLOY SUBJECTED TO HIP AND FORGED [16]

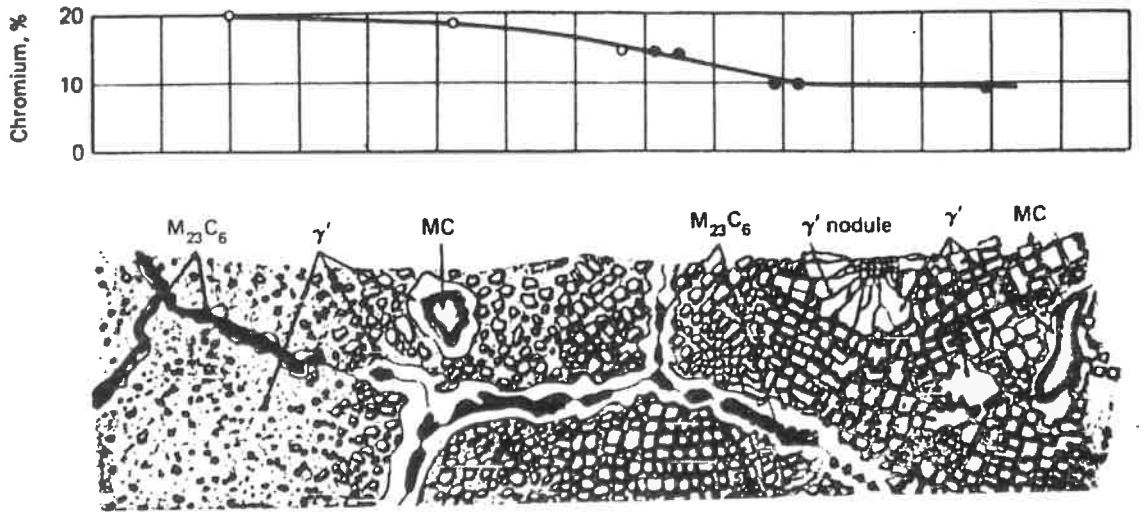

FIG. 1-8: QUALITATIVE DESCRIPTION OF THE EVOLUTION OF THE MICROSTRUCTURE AND CHROMIUM CONTENT OF Ni-BASE SUPERALLOYS [22]

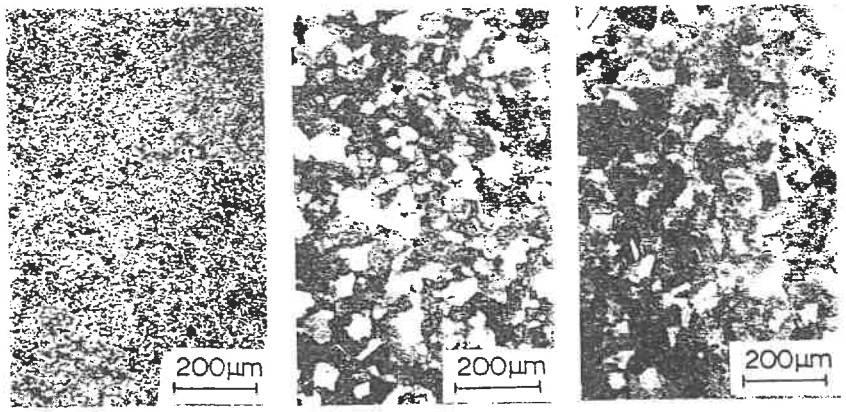

FIG. 1-9: MICROSTRUCTURES OF LC ASTROLOY AFTER HOT ISOSTATIC PRESSING AT (a) 1100°C (b) 1170°C (c) 1215°C [10]

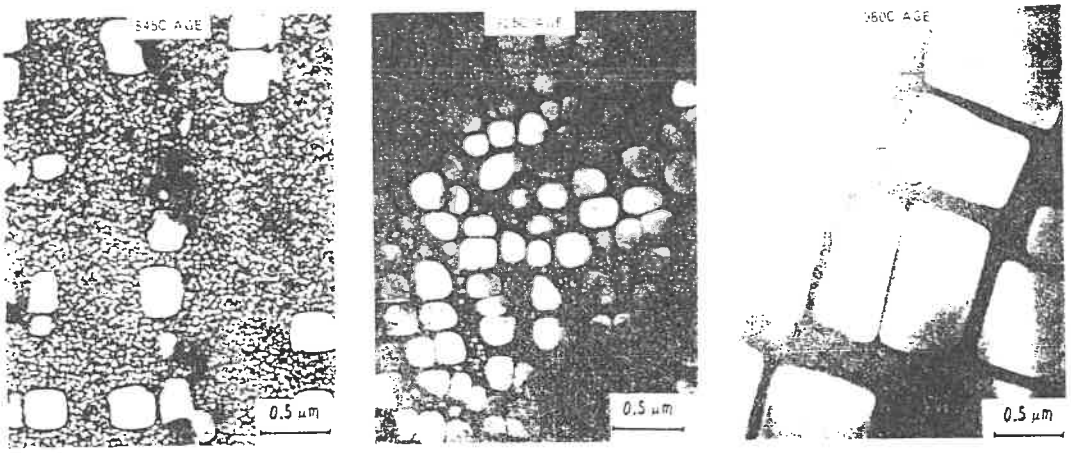

FIG. 1-10: DARK-FIELD TEM OF THE γ' DISTRIBUTION AS A FUNCTION OF AGING TEMPERATURE IN LC ASTROLOY [25]

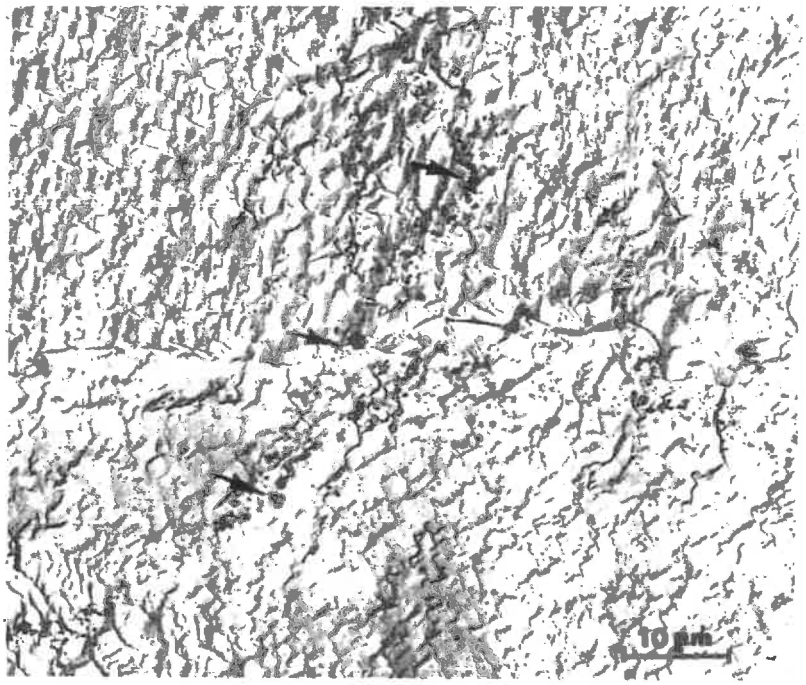

FIG. 1-11: ELECTRON MICROGRAPH OF EXTRACTION REPLICA MADE FROM ARGON-ATOMIZED POWDER LC ASTROLOY HIP'ED. ARROWS DENOTE MC AND M_{23} $(B.C.)_6$ PHASES EXTRACTED FROM GRAIN BOUNDARIES [23]

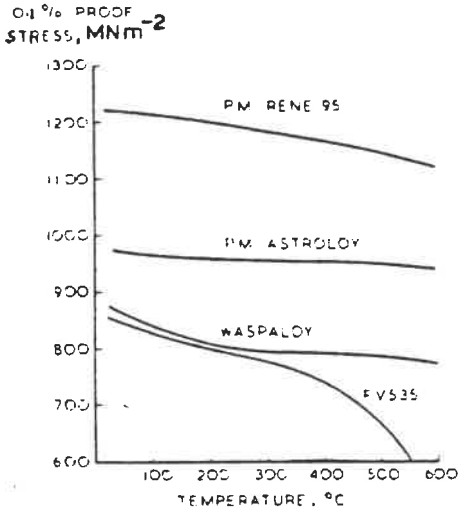

FIG. 1-12: COMPARISON 0.1% PROOF STRENGTH OF SELECTED TURBINE DISC ALLOYS IN DIFFERENT TEMPERATURE [27]

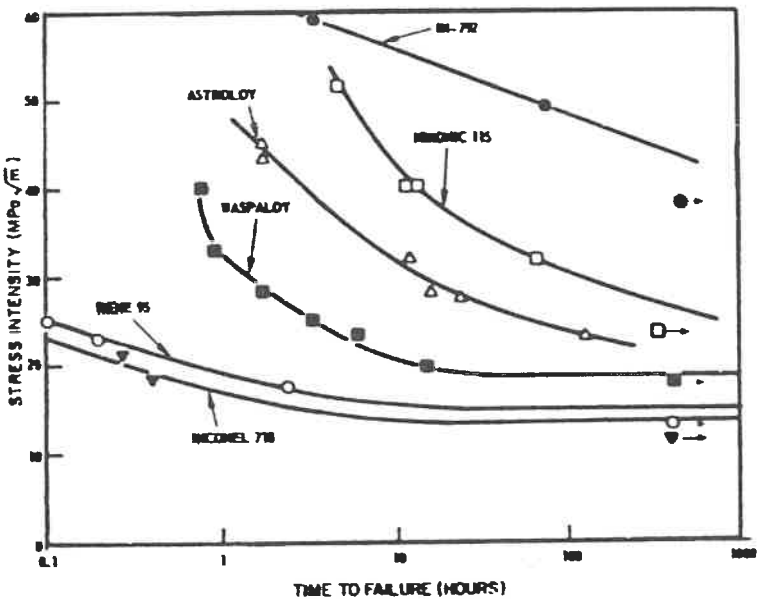

FIG. 1-13: TIME TO CREEP FRACTURE FAILURE VERSUS INITIAL STRESS INTENSITY IN SOME NICKEL-BASE SUPERALLOYS AT 704°C [28]

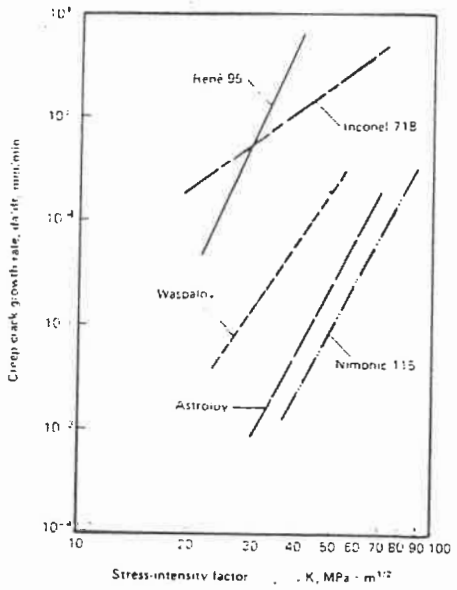

FIG. 1-14: CREEP CRACK GROWTH RATE DATA FOR VARIOUS SUPERALLOYS AT 704°C [29]

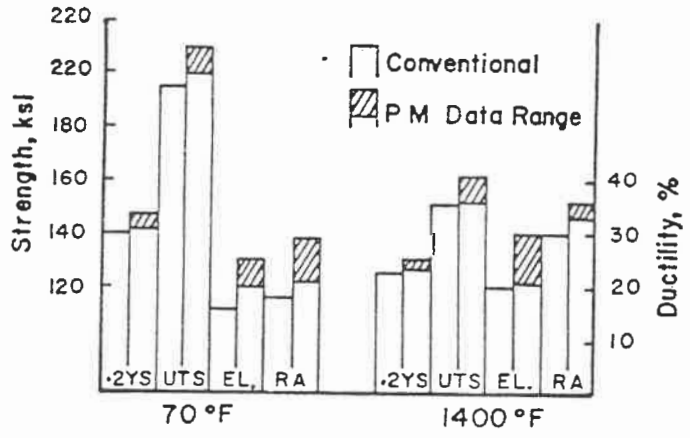

FIG. 1-15: TENSILE PROPERTIES OF CONVENTIONAL AND POWDER METALLURGY ASTROLOY DISKS [9]

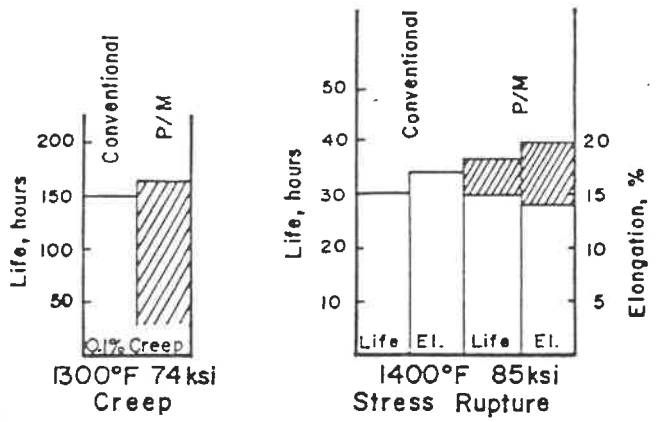

FIG. 1-16: CREEP-RUPTURE AND STRESS-RUPTURE PROPERTIES OF CONVENTIONAL AND POWDER METALLURGY ASTROLOY DISKS [9]

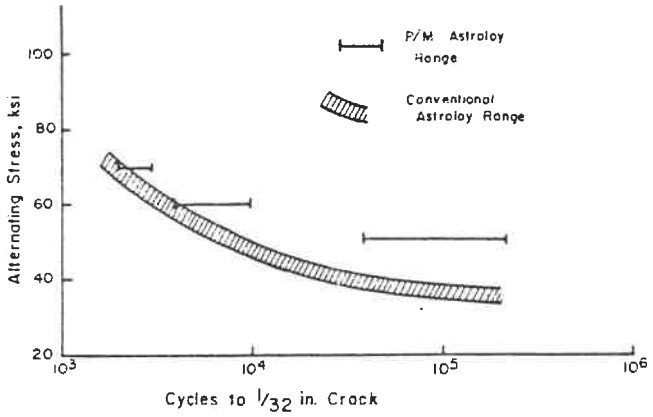

FIG. 1-17: NOTCHED LCF BEHAVIOUR OF POWDER METALLURGY ASTROLOY AT 1175°F [9]

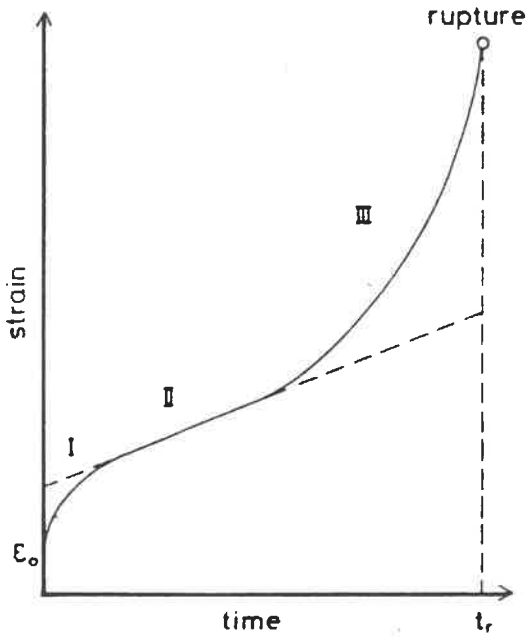

FIG. 2-1: TYPICAL CREEP STRAIN VERSUS TIME CURVE [30]

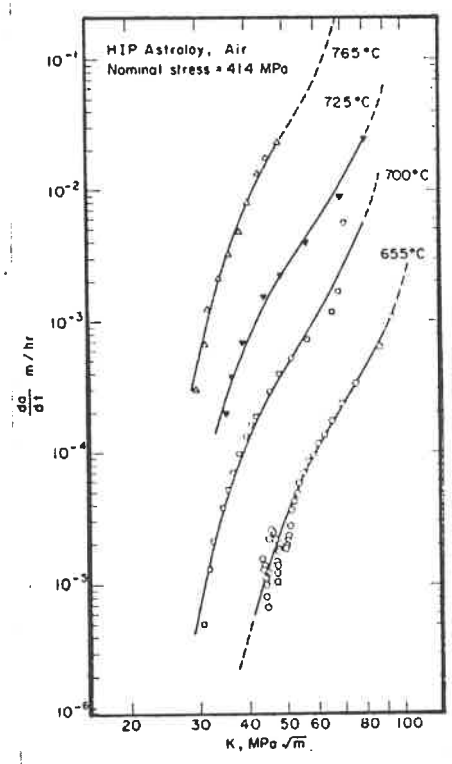

FIG. 2-2: CREEP CRACK GROWTH RATE VERSUS TEMPERATURE OF ASTROLOY [33]

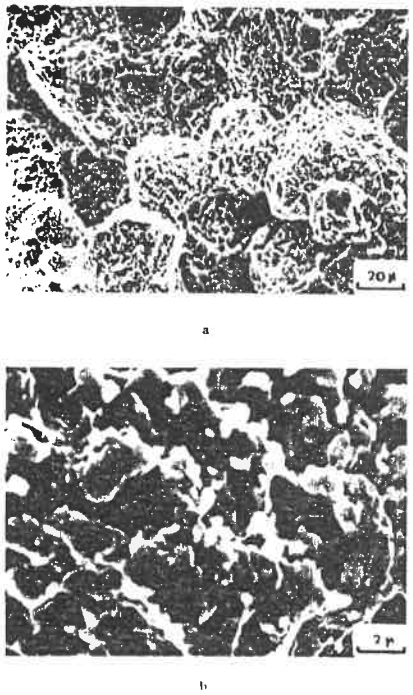

FIG. 2-3: TYPICAL INTERGRANULAR CREEP CRACK GROWTH FRACTURE SURFACE FEATURES OF ASTROLOY [33]

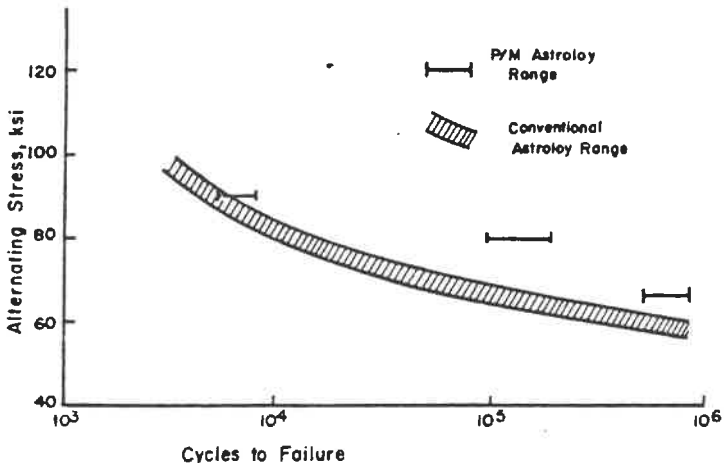

FIG. 2-4: SMOOTH LCF BEHAVIOUR OF P/M ASTROLOY AT 1175°F [9]

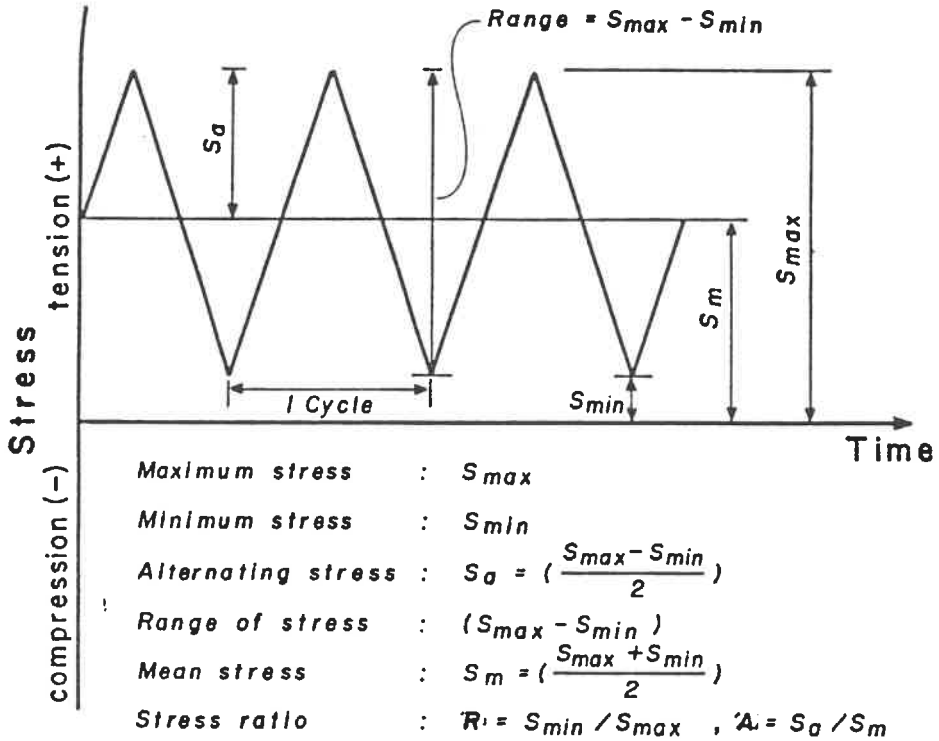

FIG. 2-5: NOMENCLATURE FOR CONSTANT AMPLITUDE LOADING [34]

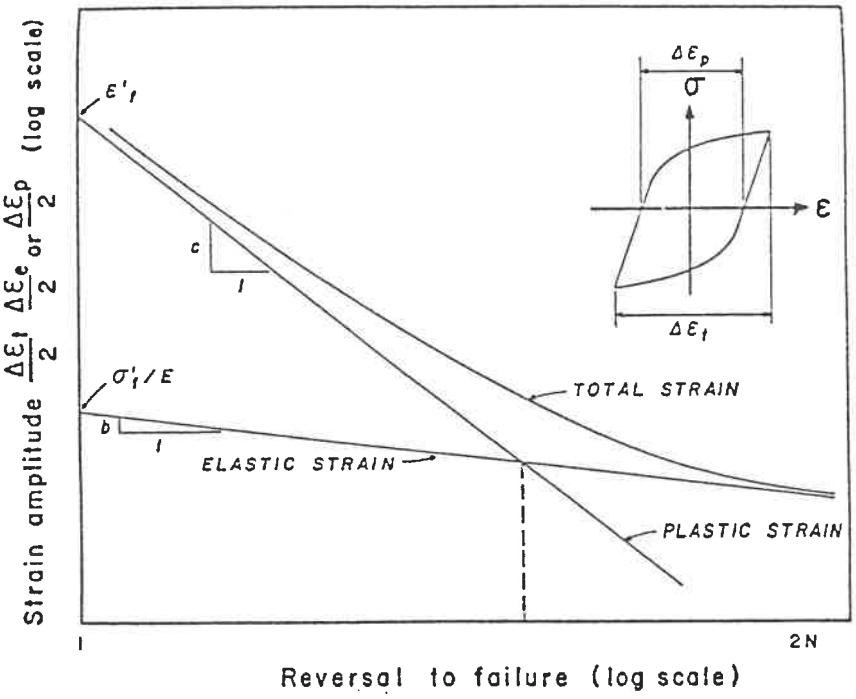

FIG. 2-6: SCHEMATIC STRAIN-LIFE CURVES SHOWING TOTAL ELASTIC AND PLASTIC STRAINS COMPONENTS [34]

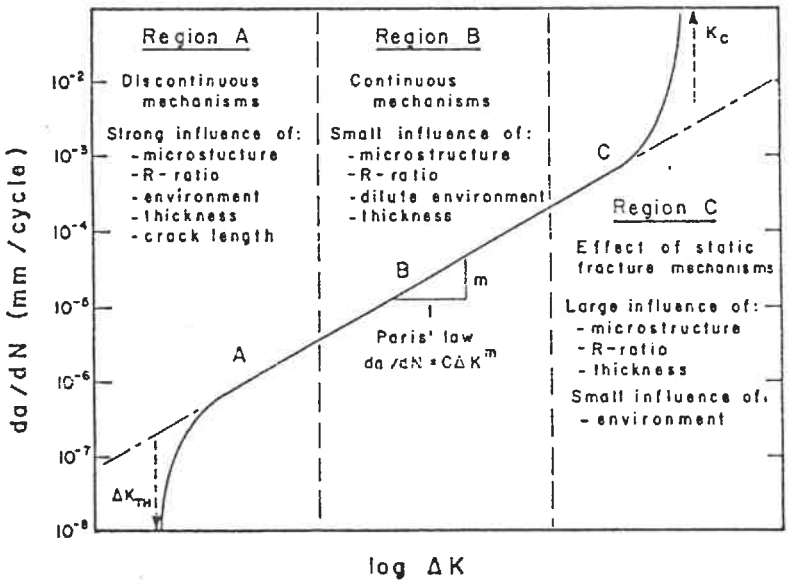

FIG. 2-7: SCHEMATIC SIGMOIDAL BEHAVIOUR OF FATIGUE CRACK GROWTH RATE VERSUS ΔK [34]

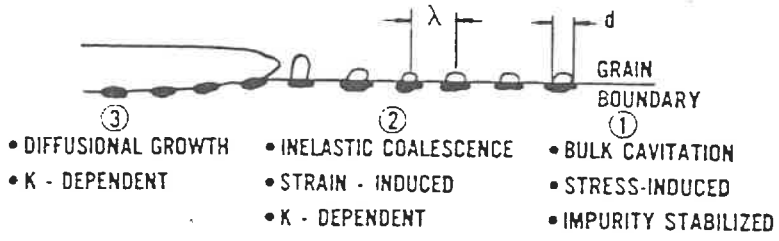

FIG. 2-8(a): SEQUENTIAL CREEP CRACK GROWTH MECHANISMS [36]

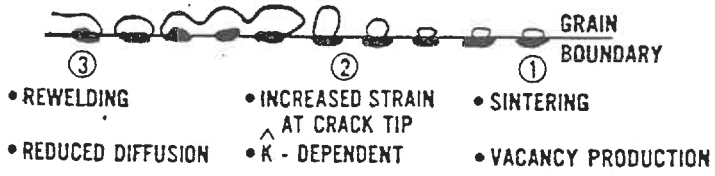

FIG. 2-8(b): EFFECT OF FATIGUE CYCLE ON MECHANISMS OF CREEP FRACTURE [36]

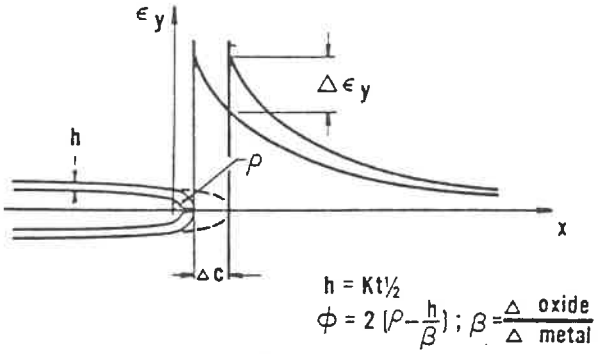

FIG. 2-9: FILM-FRACTURE MODELS OF ENVIRONMENTALLY ASSISTED CRACK PROPAGATION [36]

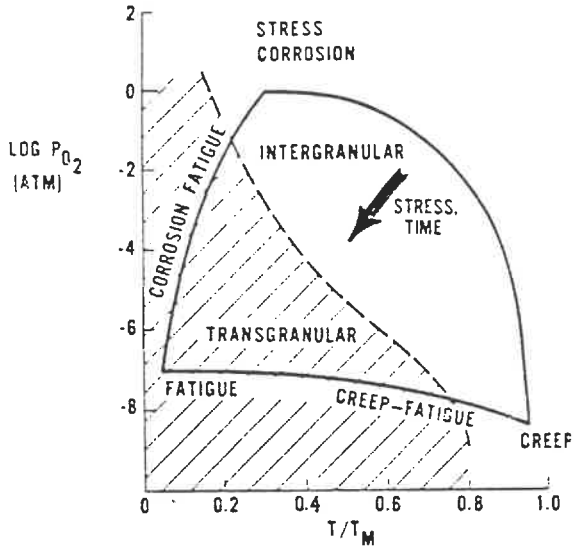

FIG. 2-10: SCHEMATIC INTERACTIONS AMONG CREEP, FATIGUE AND CORROSION [36]

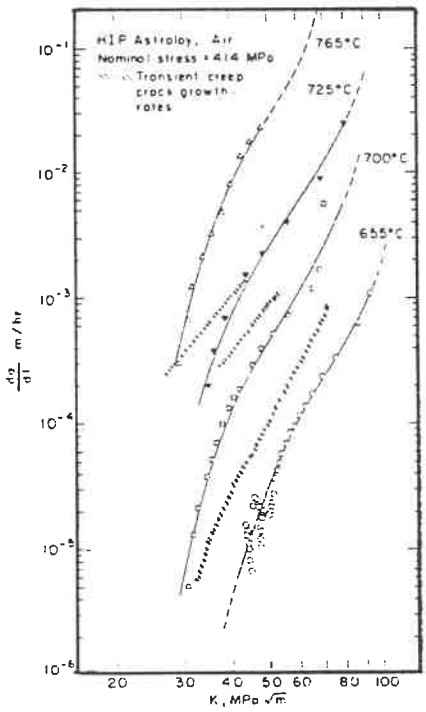

FIG. 2-11: CREEP CRACK GROWTH RATE DURING HOLD TIME UNDER SEQUENTIAL CYCLIC AND STATIC LOADING (HATCH MARKS) COMPARED WITH CONTINUOUS STATIC LOADING CREEP CRACK GROWTH RATE [33]

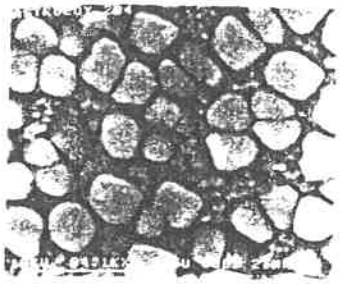

FIG. 2-12: MICROSTRUCTURE OF P/M ASTROLOY AFTER LCF AT 730°C [35]

FIG. 2-13: CLASSIC STAGE 1 FACETS (ARROW) ASSOCIATED WITH AN INTERNAL FATIGUE FAILURE IN H+F ASTROLOY[41]

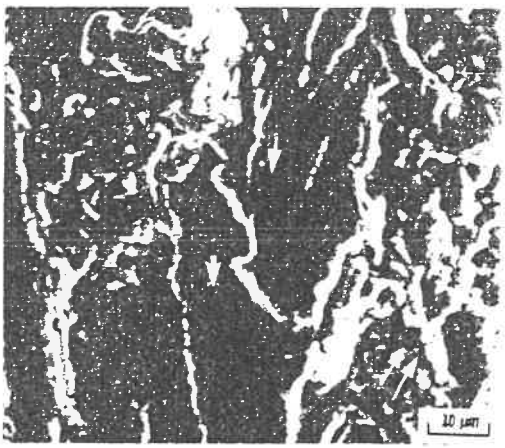

FIG. 2-14: CRACK PROPAGATION IN H+F ASTROLOY WAS TRANSGRANULAR (ARROW) IN THE COARSE GRAINS AND INTERGRANULAR (DOUBLE ARROWS) IN THE FINE RECRYSTALLIZED GRAINS[41]

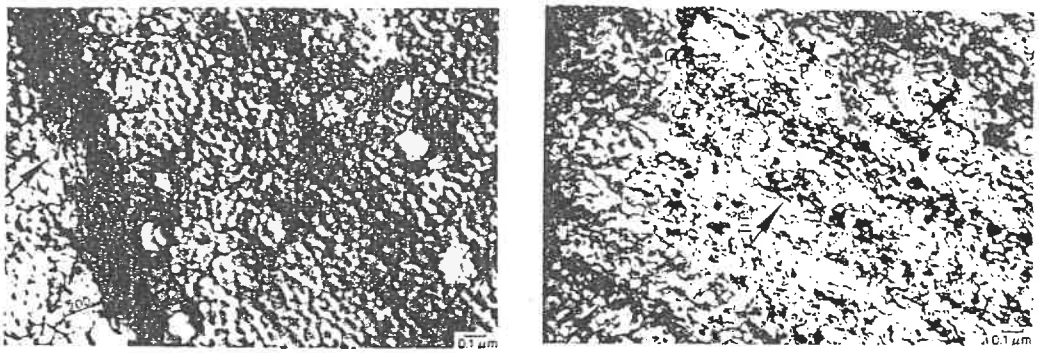

(a) $\Delta\epsilon/2 < 5 \times 10^{-5}$ (b) $\Delta\epsilon/2 = 1.7 \times 10^{-3}$

FIG. 2-15: SLIP BANDS (ARROWS) FORMED IN WASPALOY DURING FATIGUE[17]

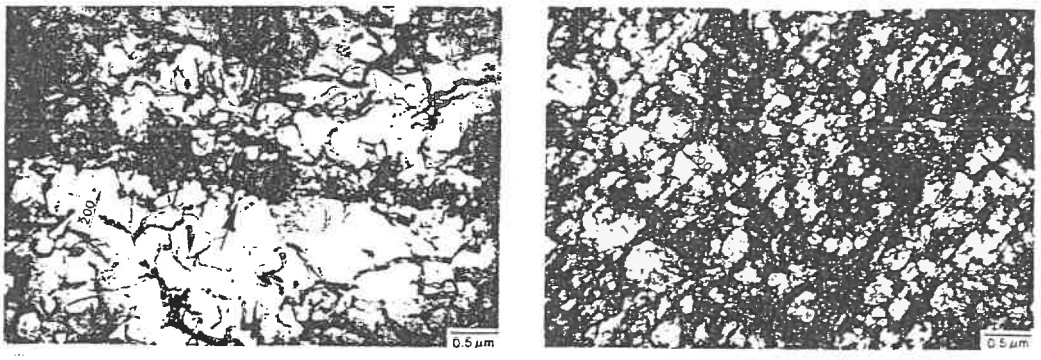

(a) ONLY A FEW SLIP BANDS (b) DEFORMATION WAS GENERALLY HOMOGENEOUS

FIG. 2-16: SLIP BANDS (ARROWS) FORMED IN ASTROLOY DURING FATIGUE[17]

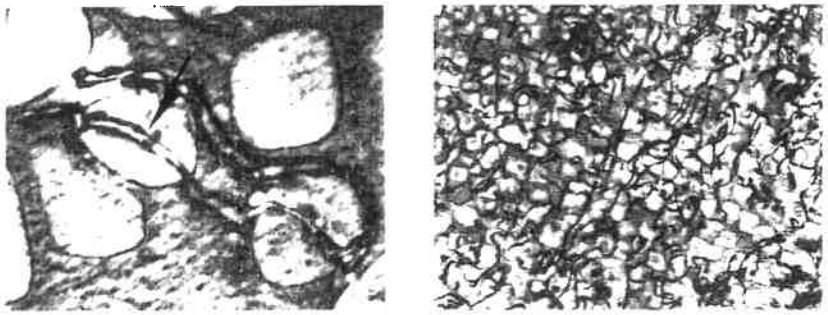

(a) $\epsilon t = 10^{-2}\ s^{-1}$ (b) $\epsilon t = 2 \times 10^{-6}\ s^{-1}$

FIG. 2-17: PAIRWISE CUTTING OF γ' PARTICLES BY DISLOCATIONS MOVING IN PLANAR SLIP [48]

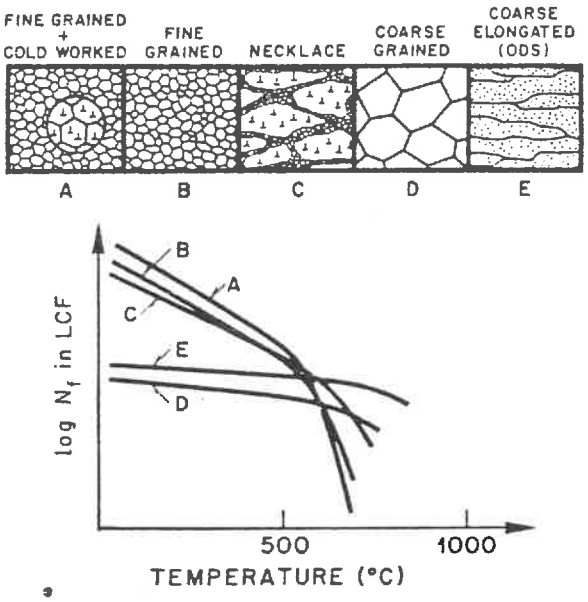

FIG. 2-18: RANGE OF POSSIBLE MICROSTRUCTURE IN P/M SUPERALLOYS AND THEIR EFFECT ON DYNAMIC MECHANICAL PROPERTIES [50]

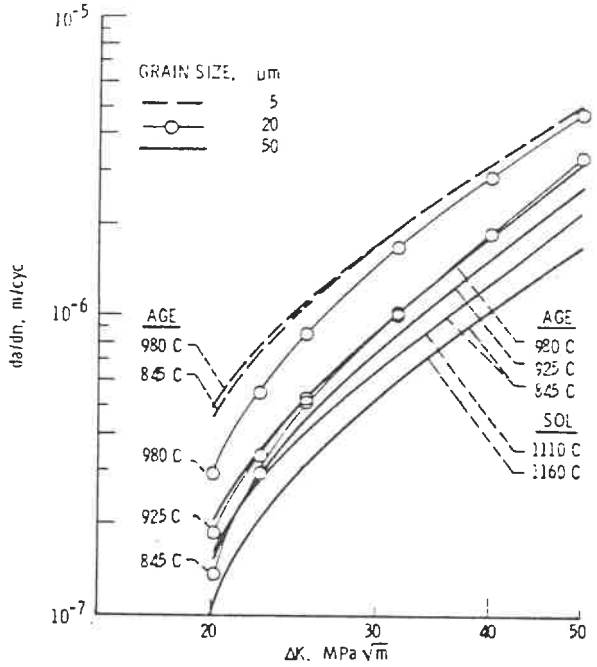

FIG. 2-19: FATIGUE CRACK GROWTH RATE FOR P/M ASTROLOY IN AIR AT 650°C [25]

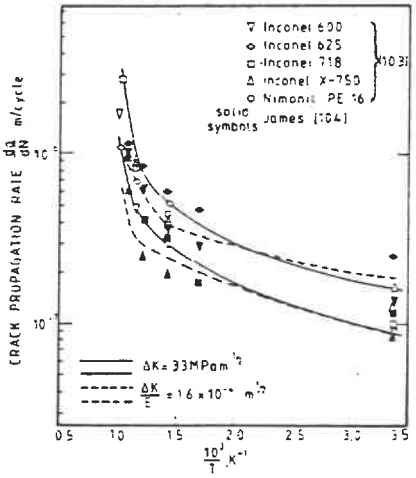

FIG. 2-20: THE TEMPERATURE DEPENDENCE OF FATIGUE CRACK PROPAGATION IN SELECTED NICKEL-BASE ALLOYS [51]

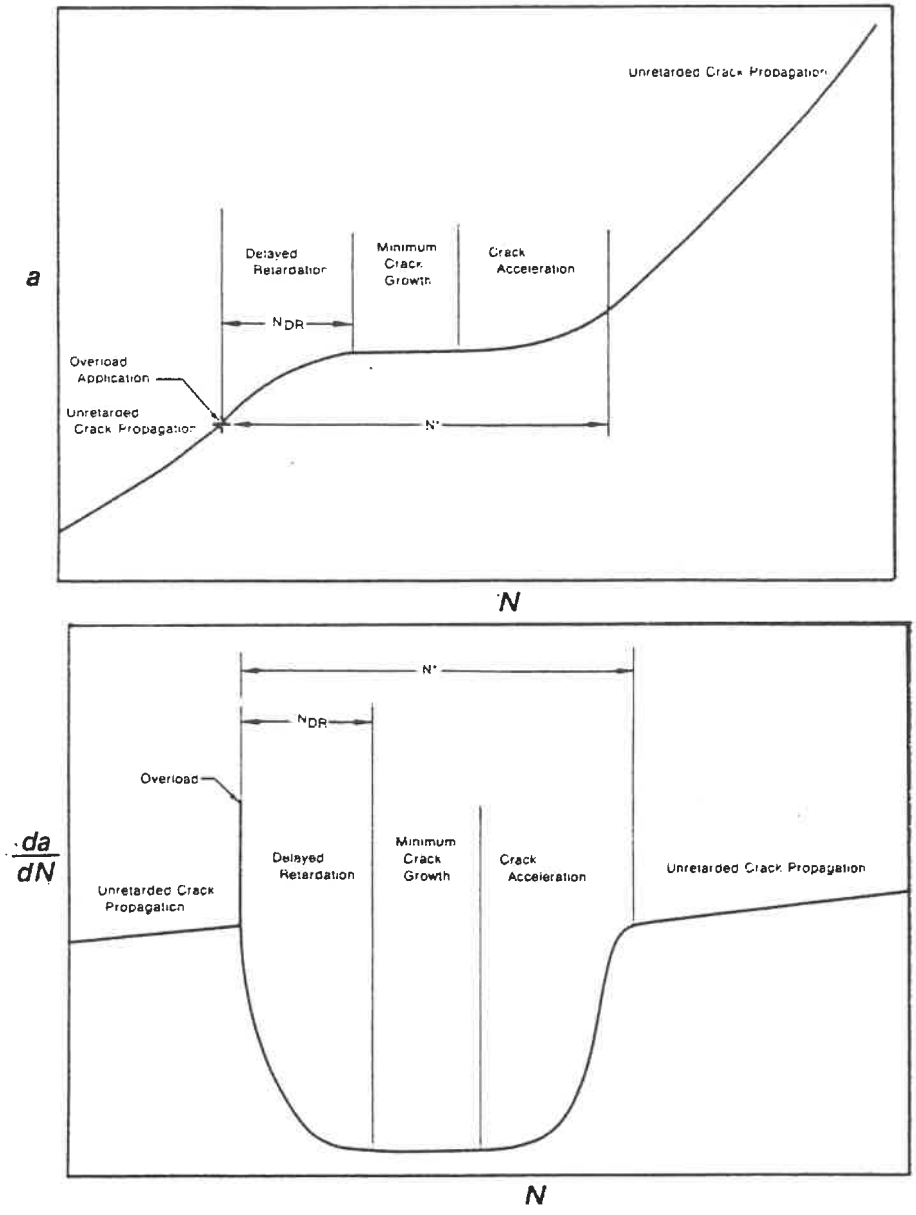

FIG. 2-21: FATIGUE CRACK RETARDATION RESULTING FROM THE APPLICATION OF A SINGLE OVERLOAD[57]

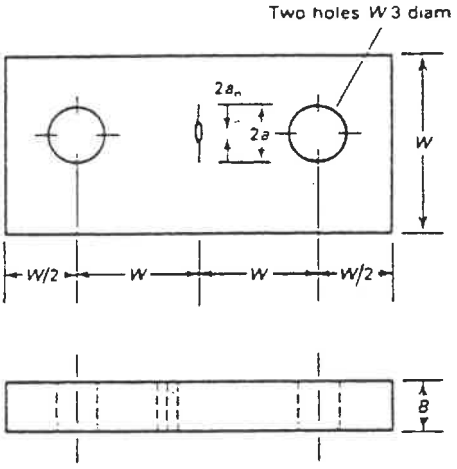

FIG. 2-22: (a) CENTER-CRACK TENSION SPECIMEN [42]

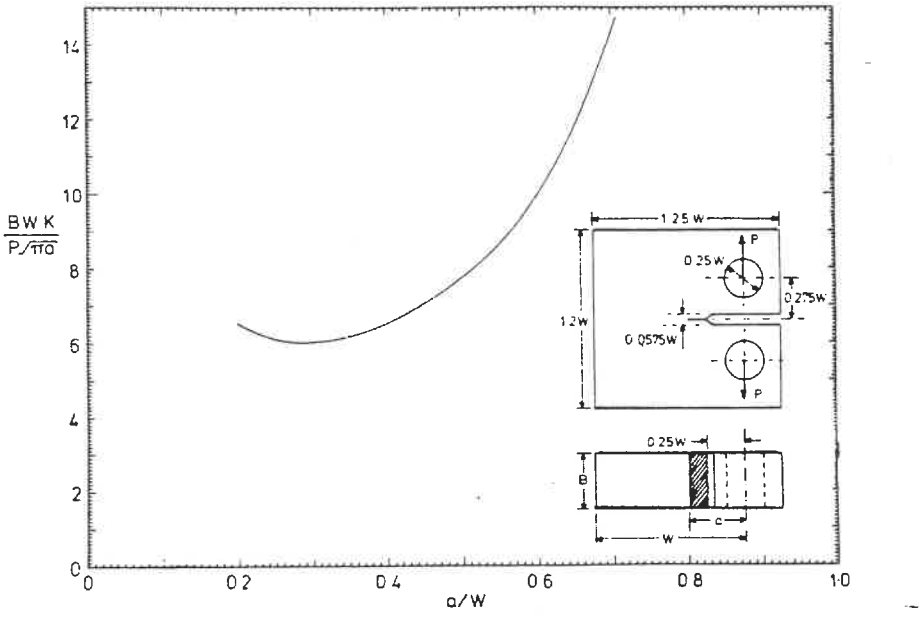

FIG. 2-22: (b) COMPACT-TYPE SPECIMEN [60]

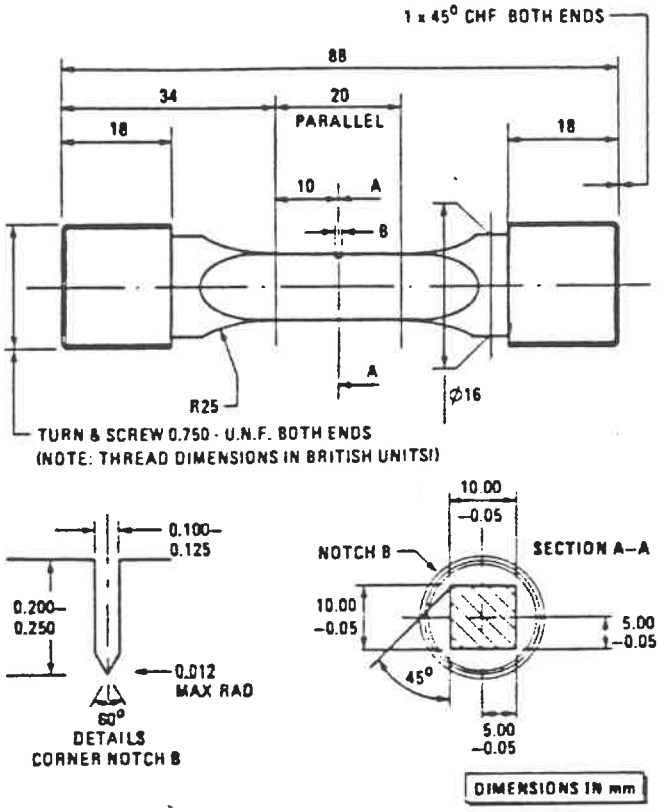

FIG. 2-22: (c)-1: CORNER CRACK SPECIMEN [2]

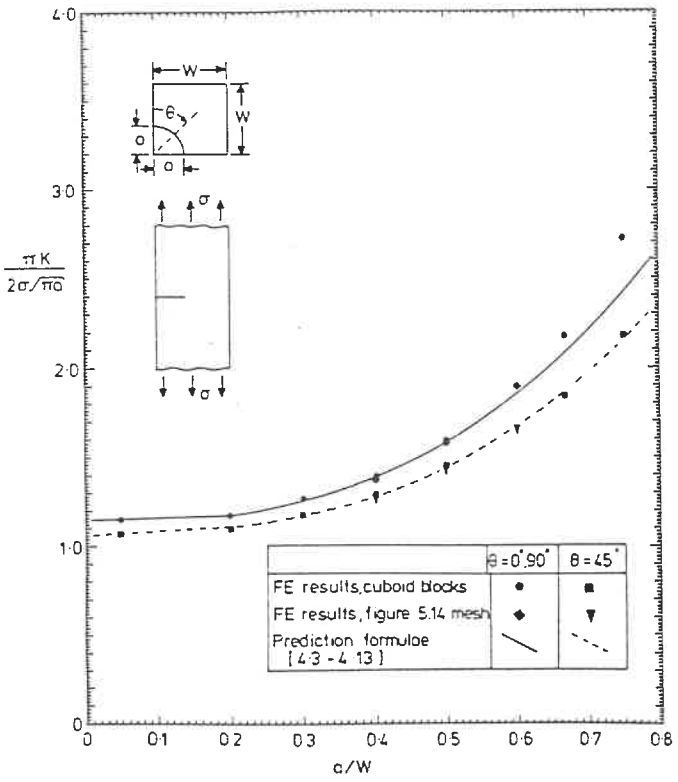

(c)-2: CORNER CRACK SPECIMEN COMPLIANCE FUNCTION [60]

FIG. 2-22: STANDARD SPECIMENS FOR FATIGUE CRACK PROPAGATION TESTING

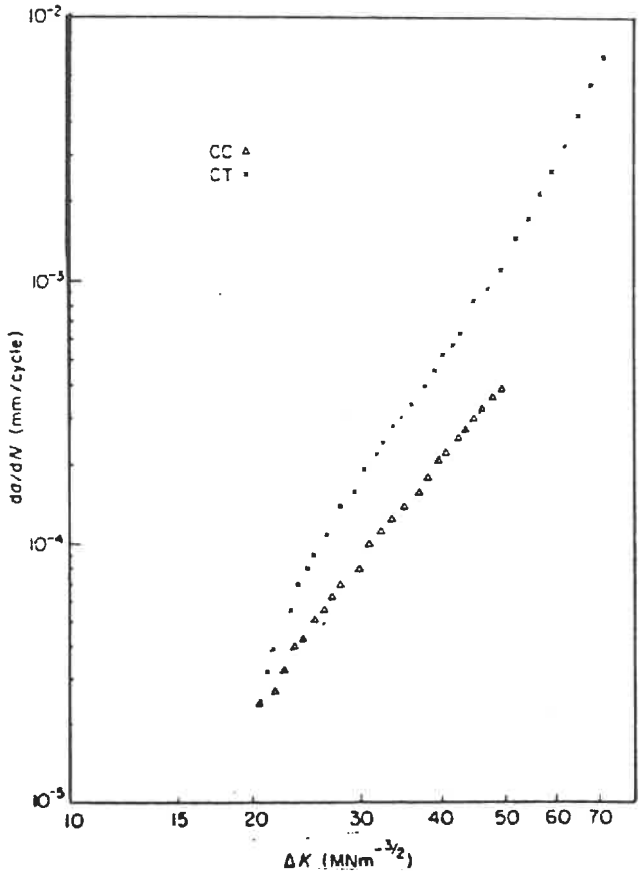

FIG. 2-23: CORNER CRACK AND COMPACT TENSION FATIGUE CRACK GROWTH RATES AT 200°C IN ASTROLOY [61]

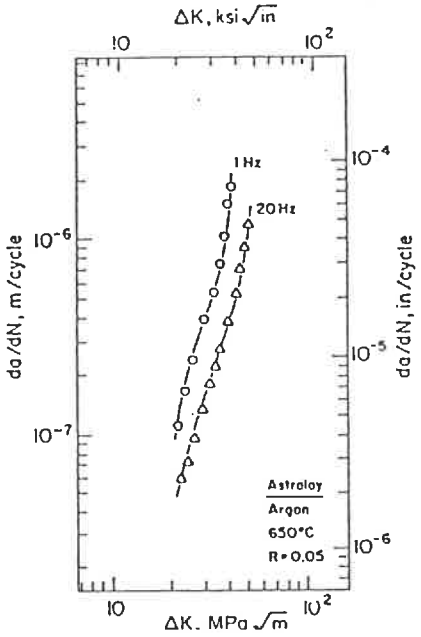

FIG. 2-24: EFFECT OF FREQUENCY ON FCG IN ASTROLOY [40]

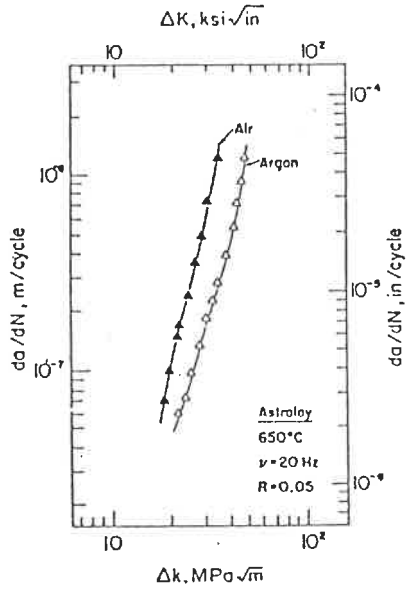

FIG. 2-25: EFFECT OF ENVIRONMENT ON FCG IN ASTROLOY [40]

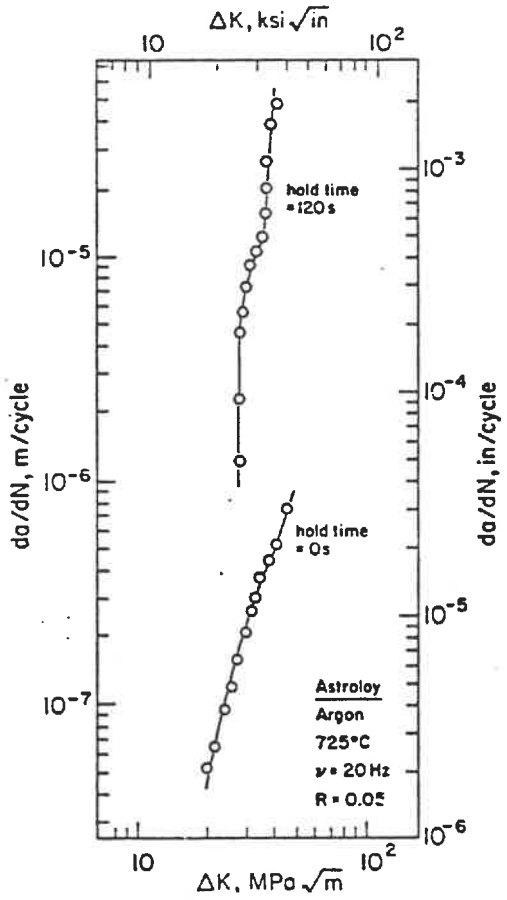

FIG. 2-26: EFFECT OF HOLD TIME ON FCG IN ASTROLOY [40]

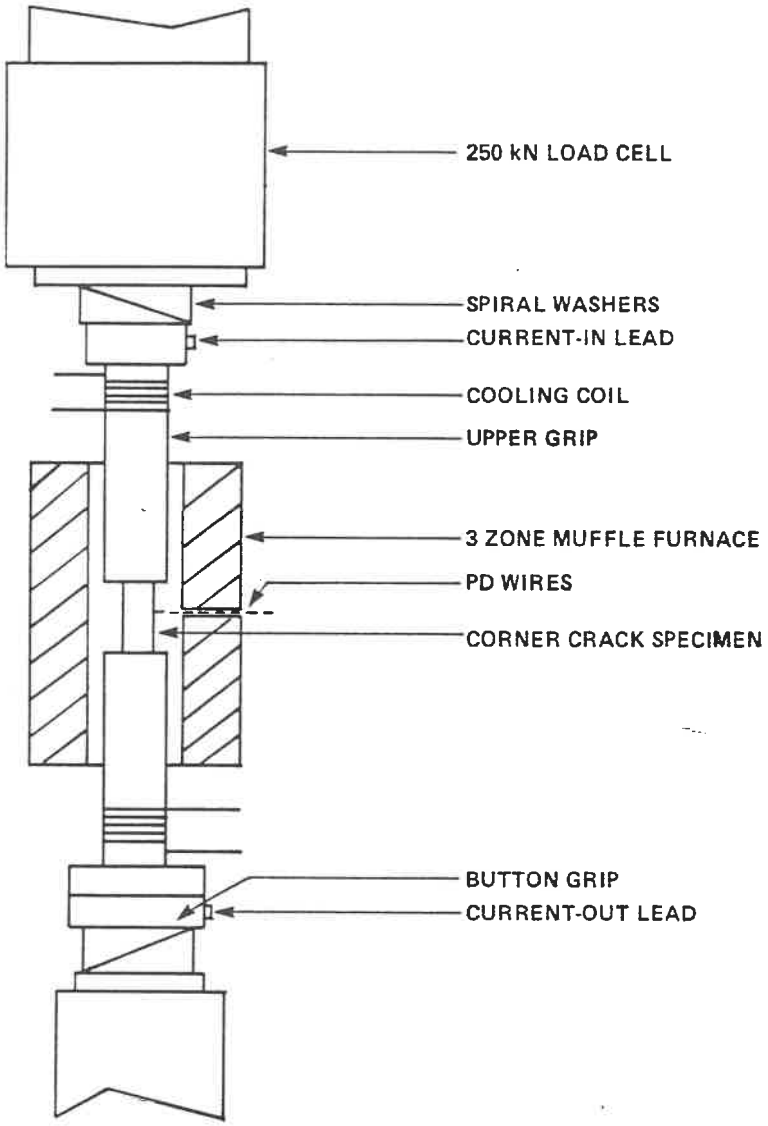

FIG. 4-1: SCHEMATIC OF HIGH TEMPERATURE FATIGUE TEST

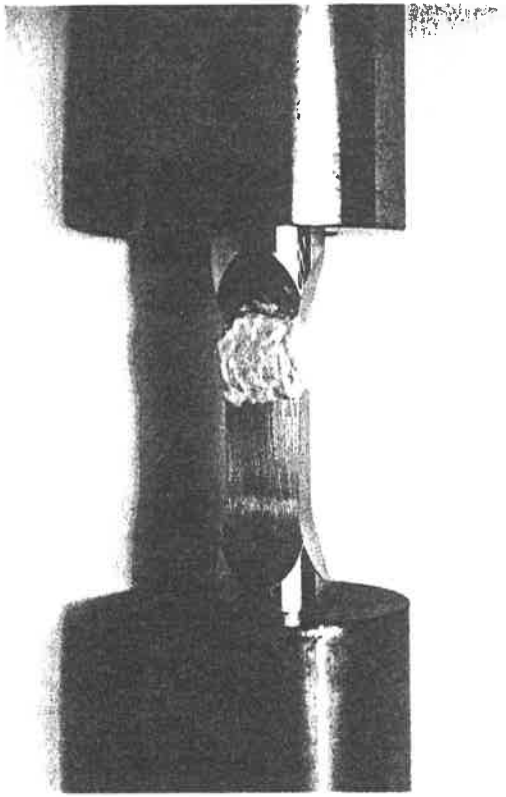

FIG. 4-2: HIGH-TEMPERATURE LOW-CYCLE FATIGUE TEST EQUIPMENT WITH SPECIMEN IN POSITION

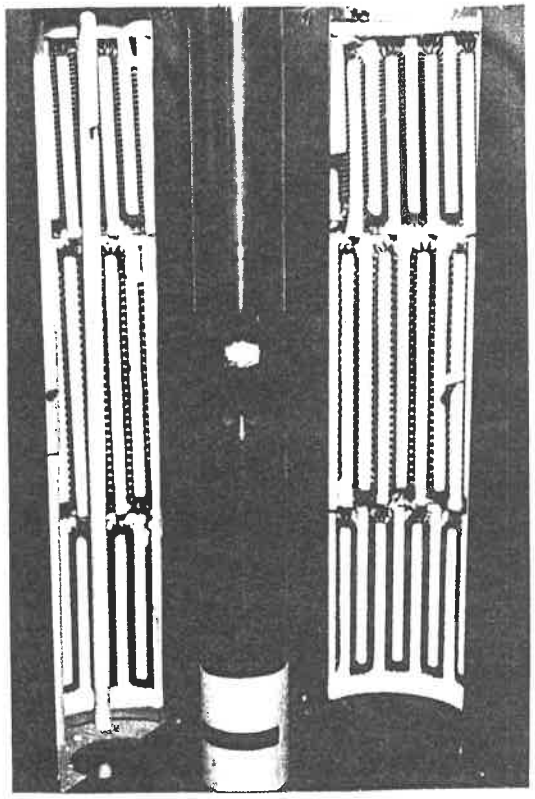

FIG. 4-3: HIGH-TEMPERATURE LOW-CYCLE FATIGUE TEST EQUIPMENT WITH FURNACE IN PLACE

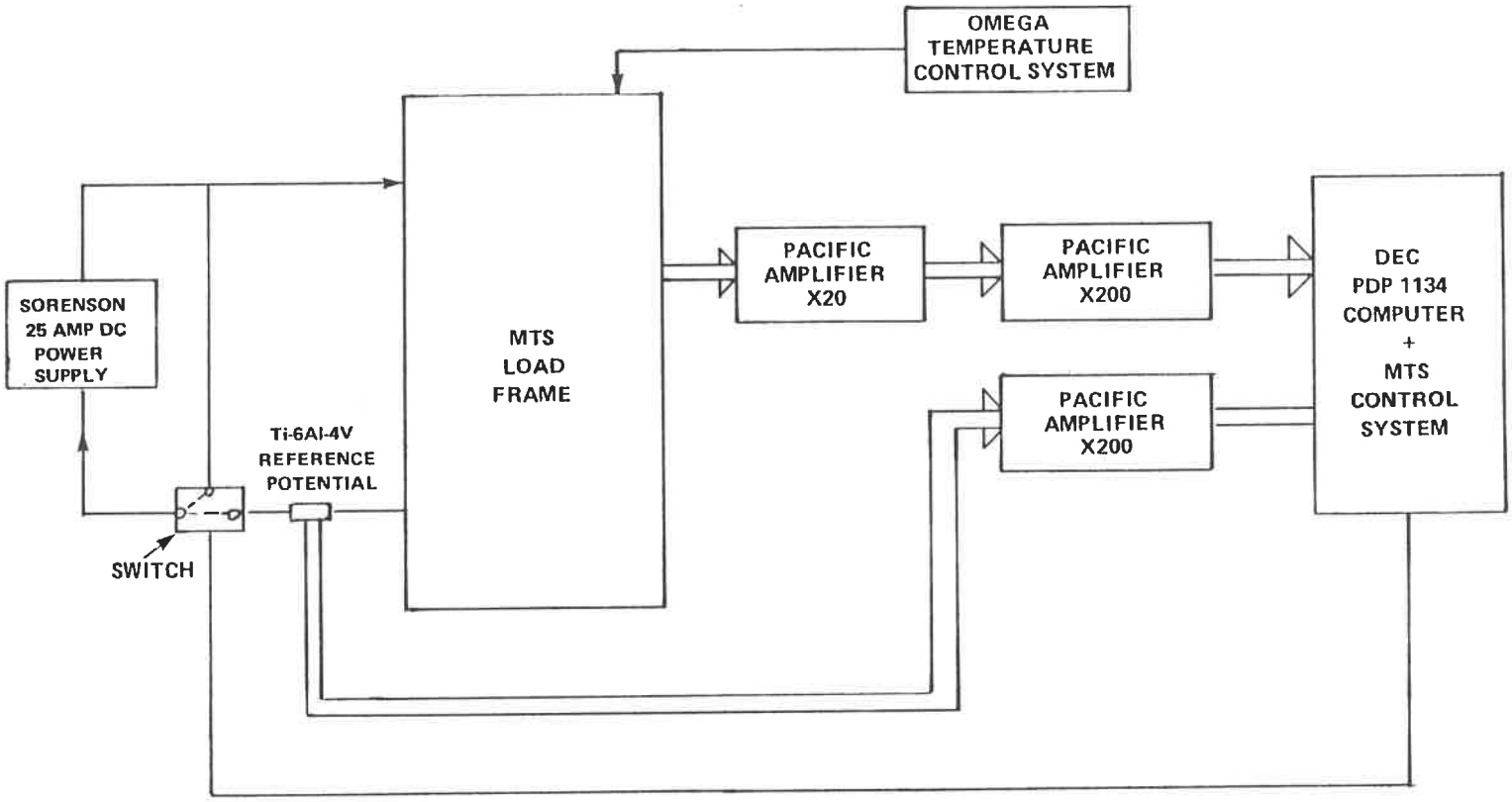

FIG. 4-4: SCHEMATIC OF dc-PD SYSTEM FOR CRACK LENGTH MEASUREMENT

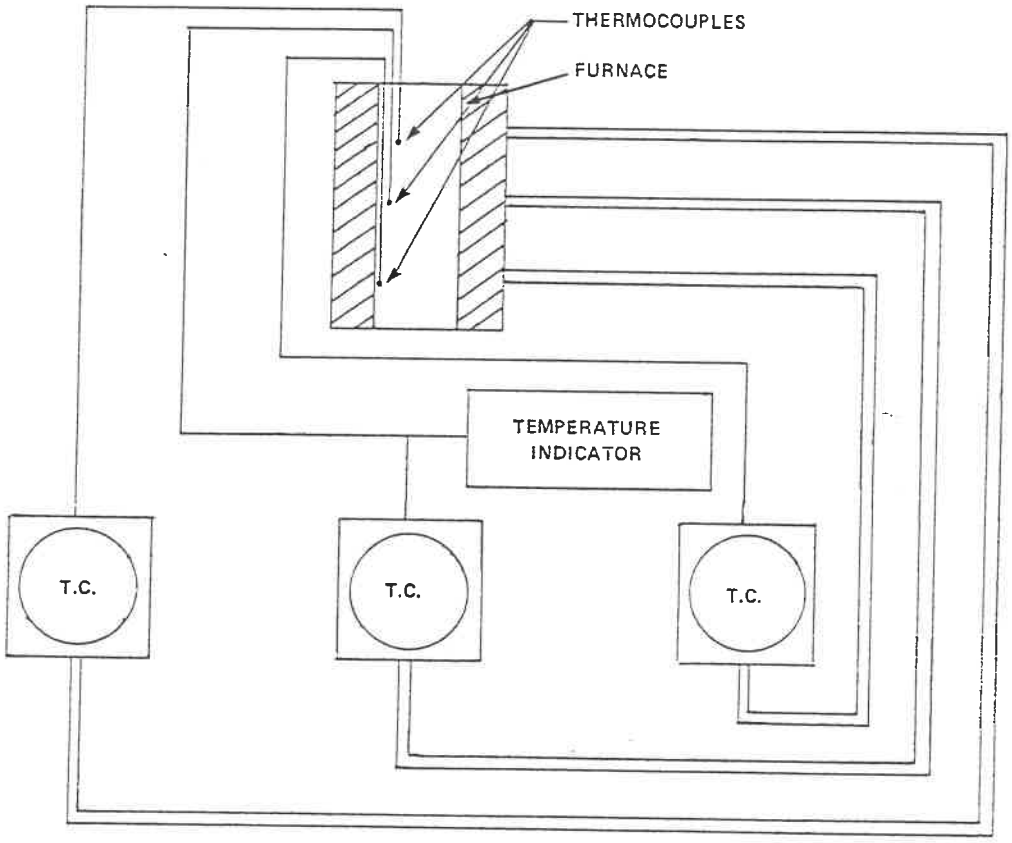

T.C. = TEMPERATURE CONTROLLER

FIG. 4-5: SCHEMATIC OF TEMPERATURE CONTROL AND MEASUREMENT SYSTEM FOR THREE ZONE MUFFLE FURNACE

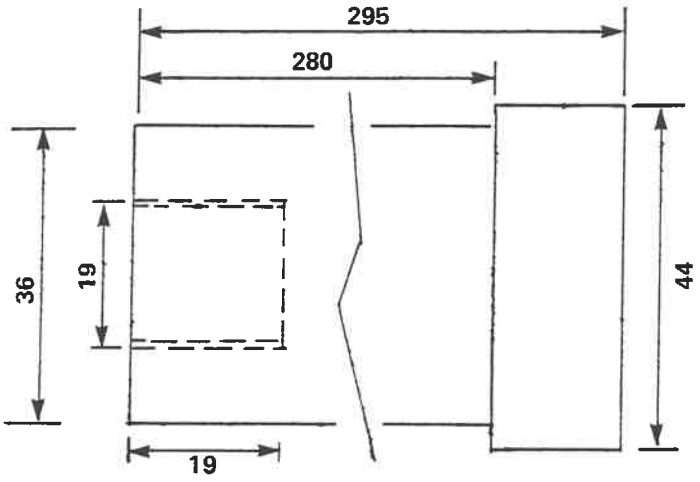

LOWER GRIP

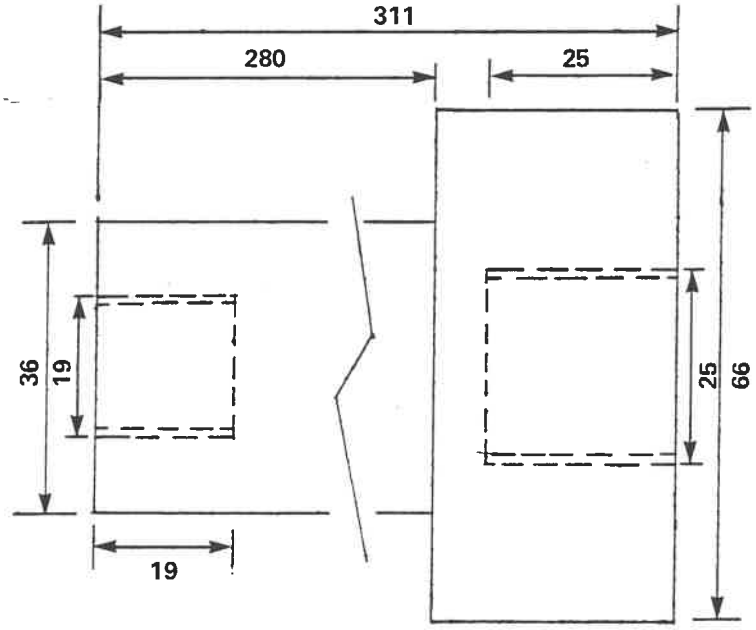

UPPER GRIP

ALL DIMENSIONS IN mm

FIG. 4-6: GRIP DIMENSIONS

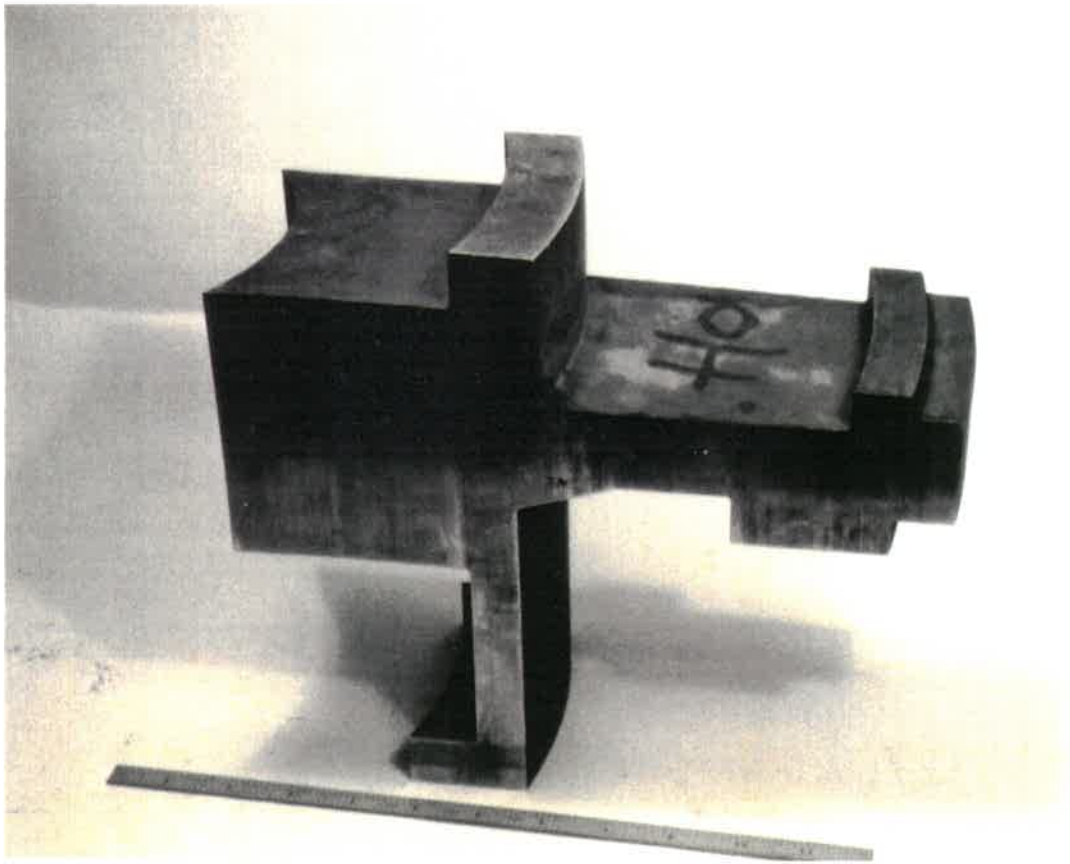

FIG. 4-7: RECEIVED RB-211 FAN DISC MATERIAL

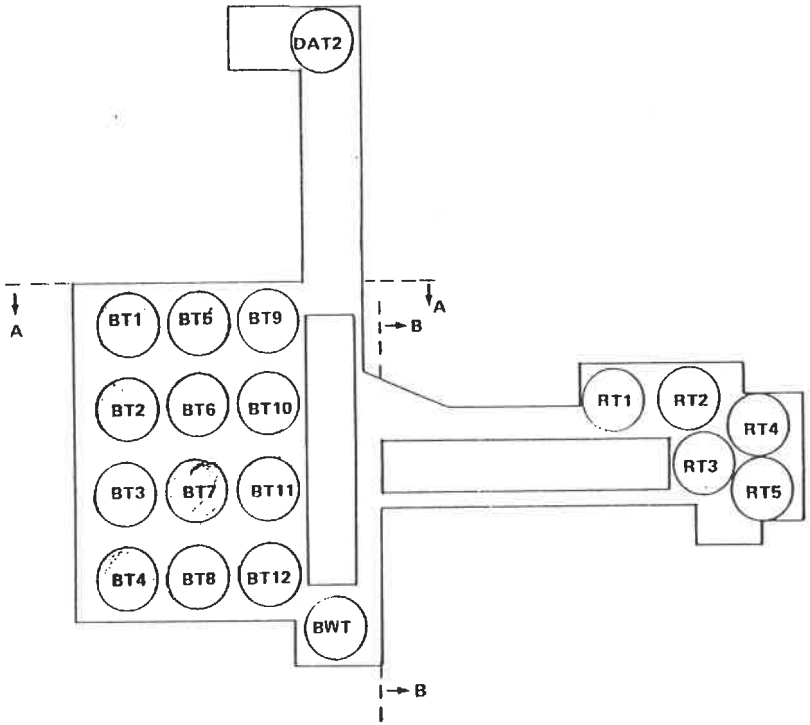

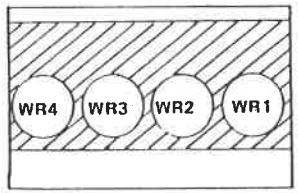

SCALE: 1 mm = 2 mm

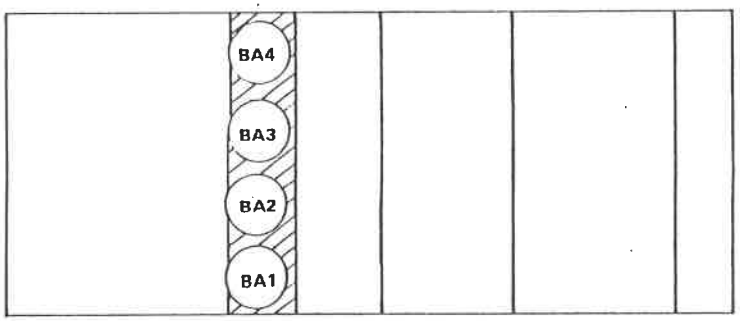

FIG. 4-8:

CUT-UP DRAWING INDICATING LOCATION AND ORIENTATION OF EACH SPECIMEN

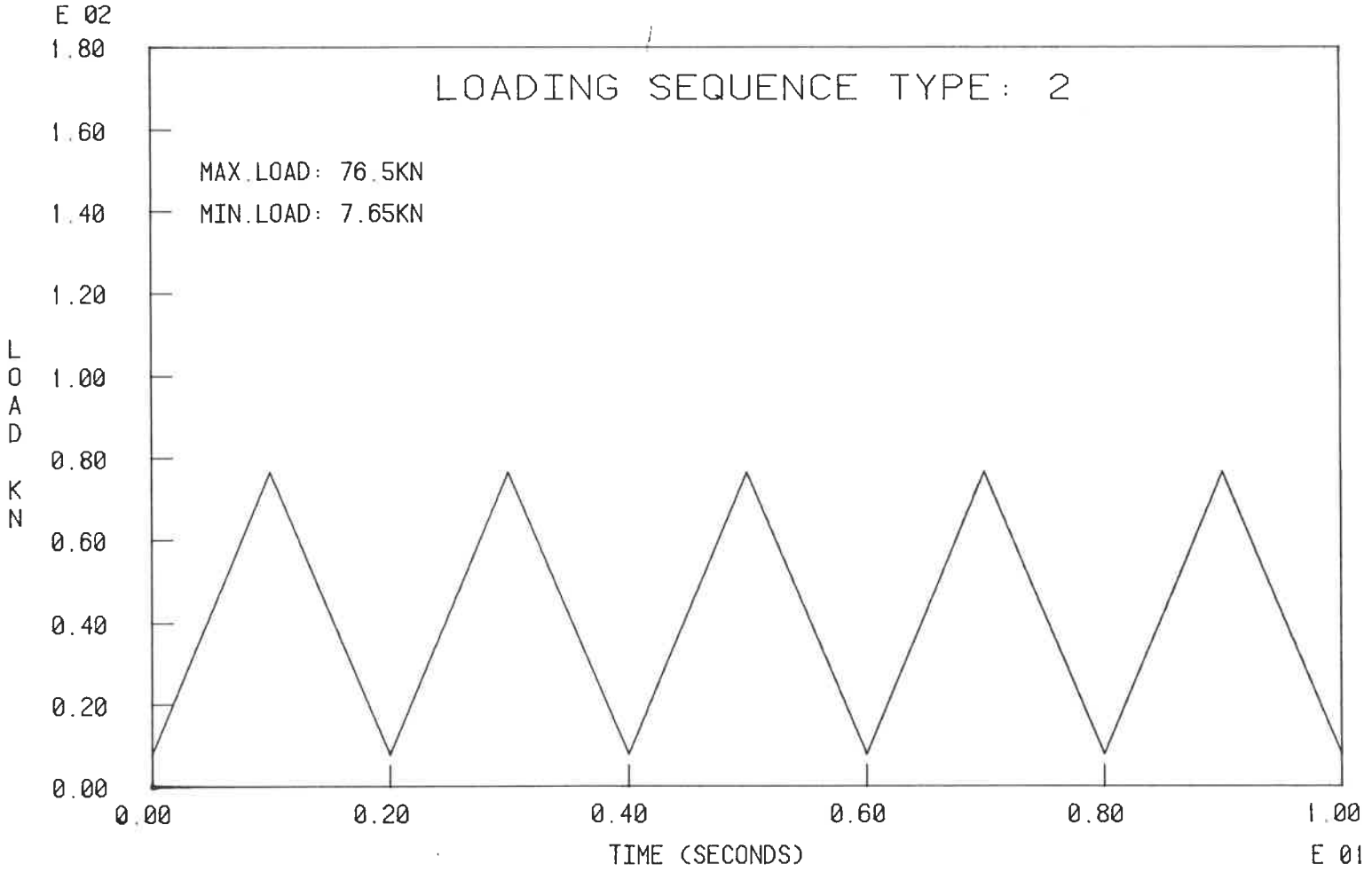

FIG. 4-9: LOADING SEQUENCE TYPE 2

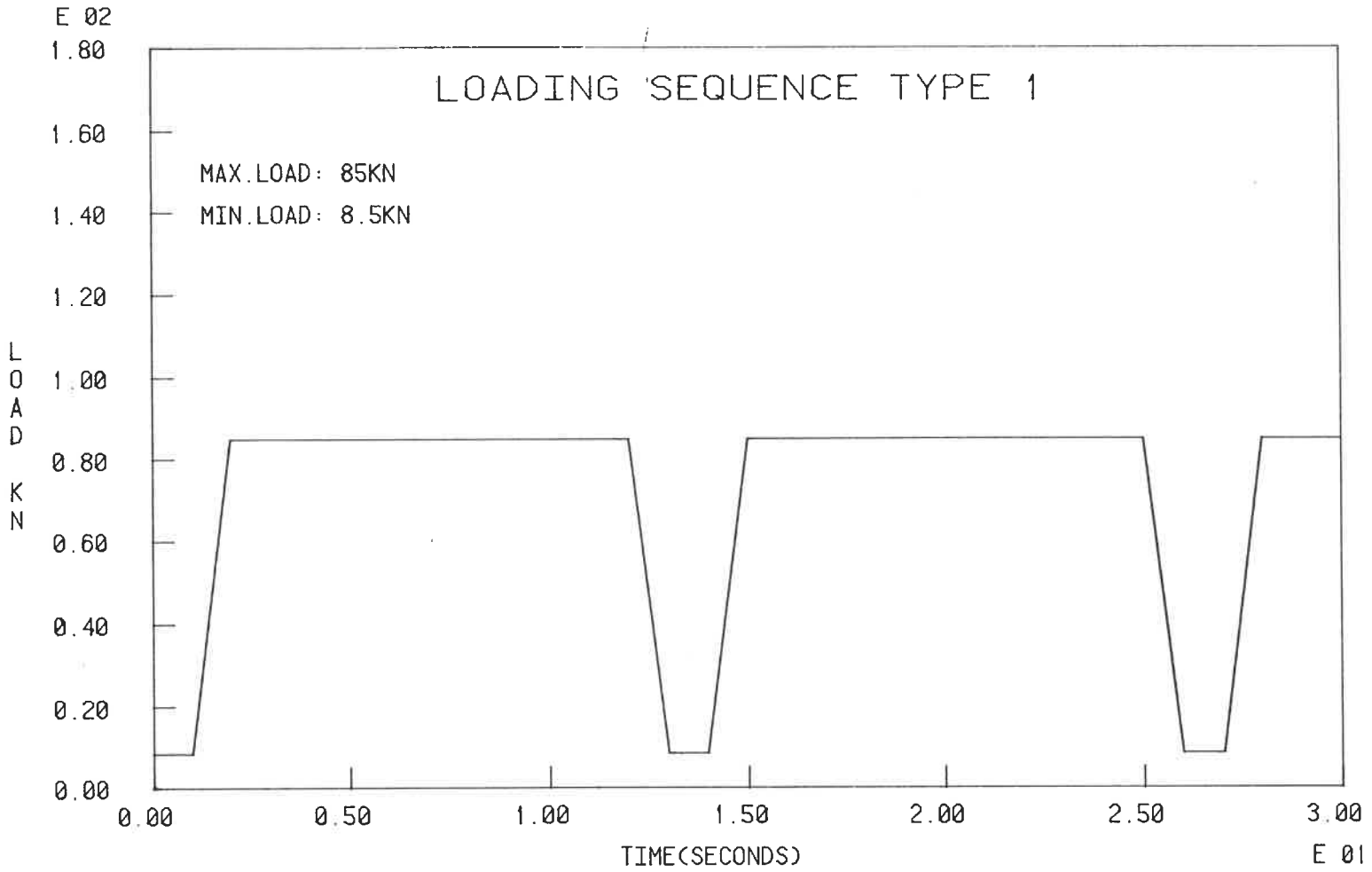

FIG. 4-10: LOADING SEQUENCE TYPE 1

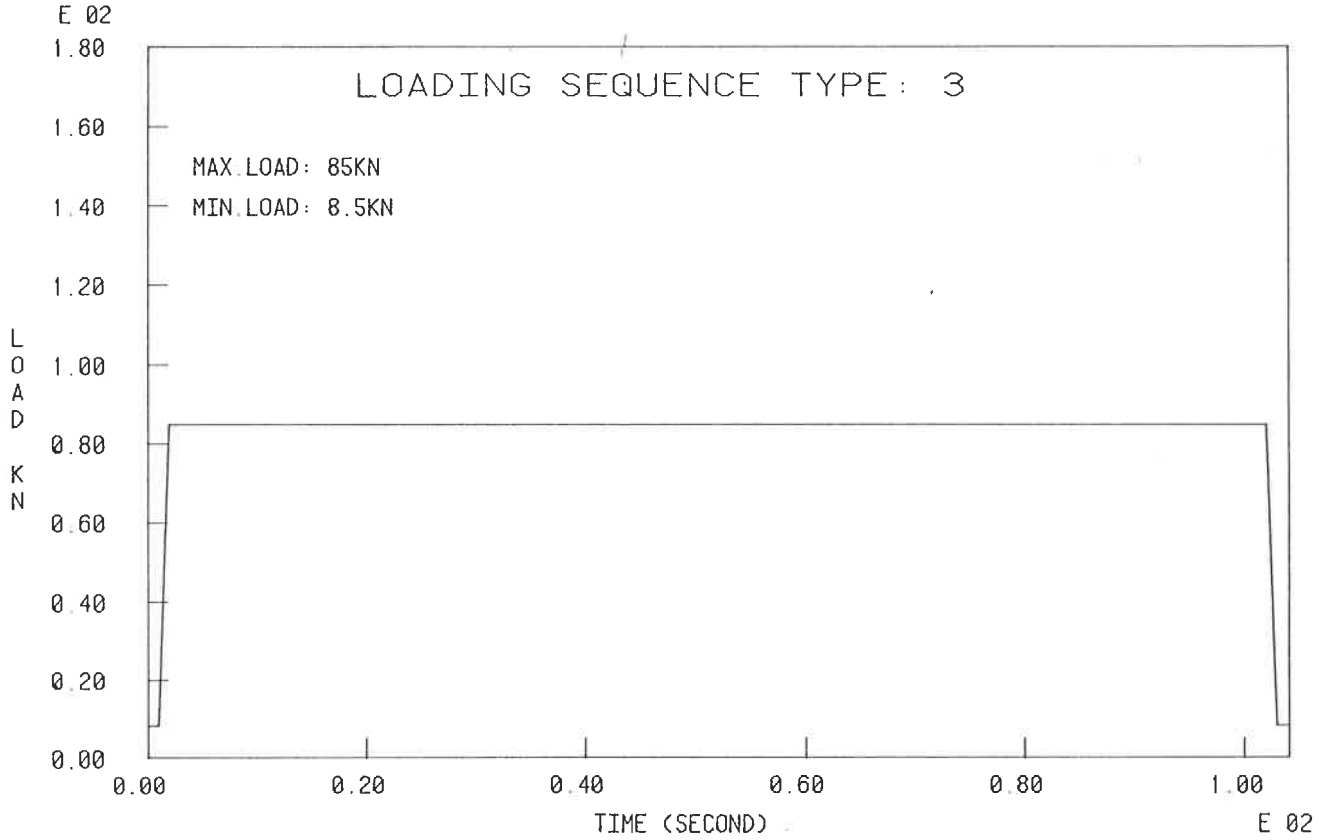

FIG. 4-11: LOADING SEQUENCE TYPE 3

174.

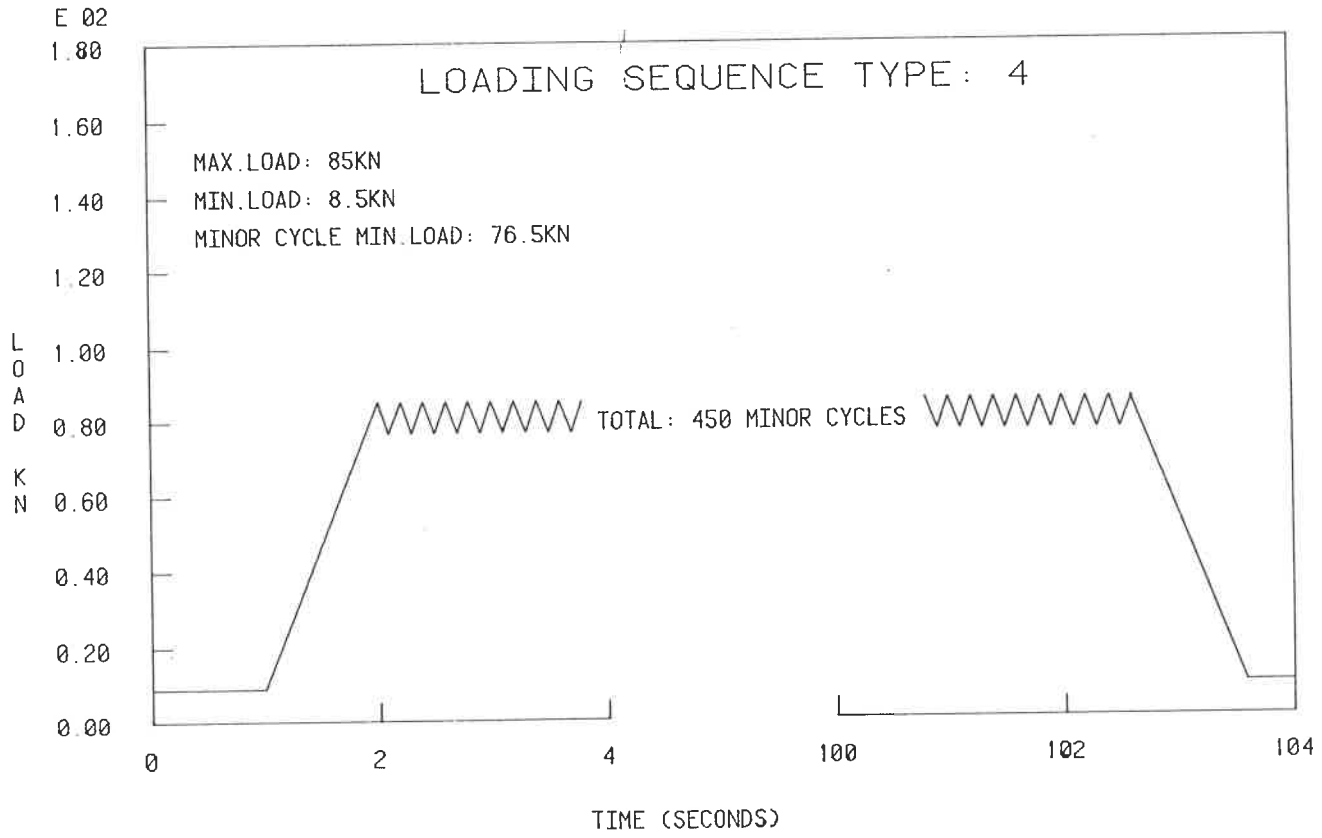

FIG. 4-12: LOADING SEQUENCE TYPE 4

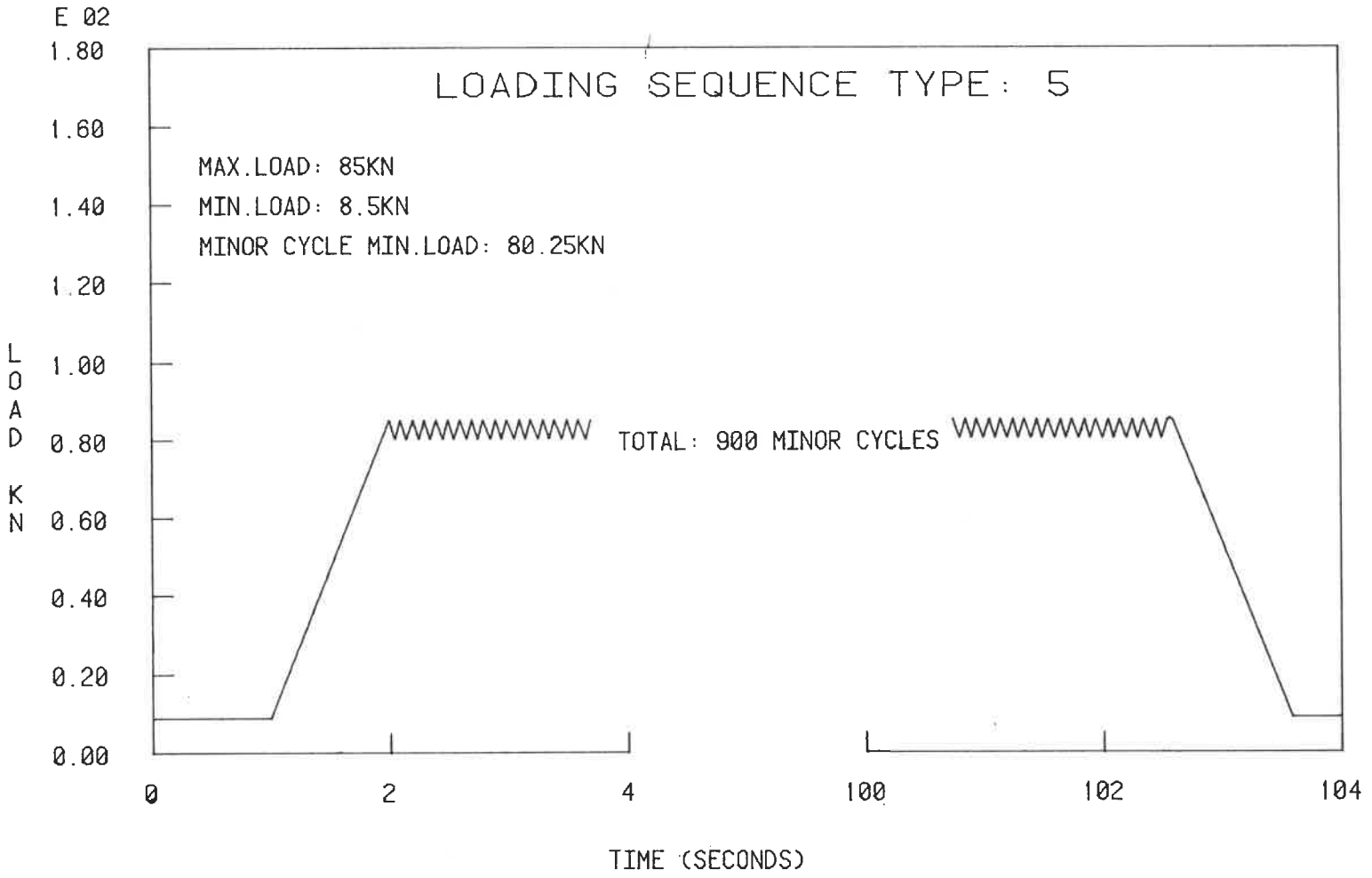

FIG. 4-13: LOADING SEQUENCE TYPE 5

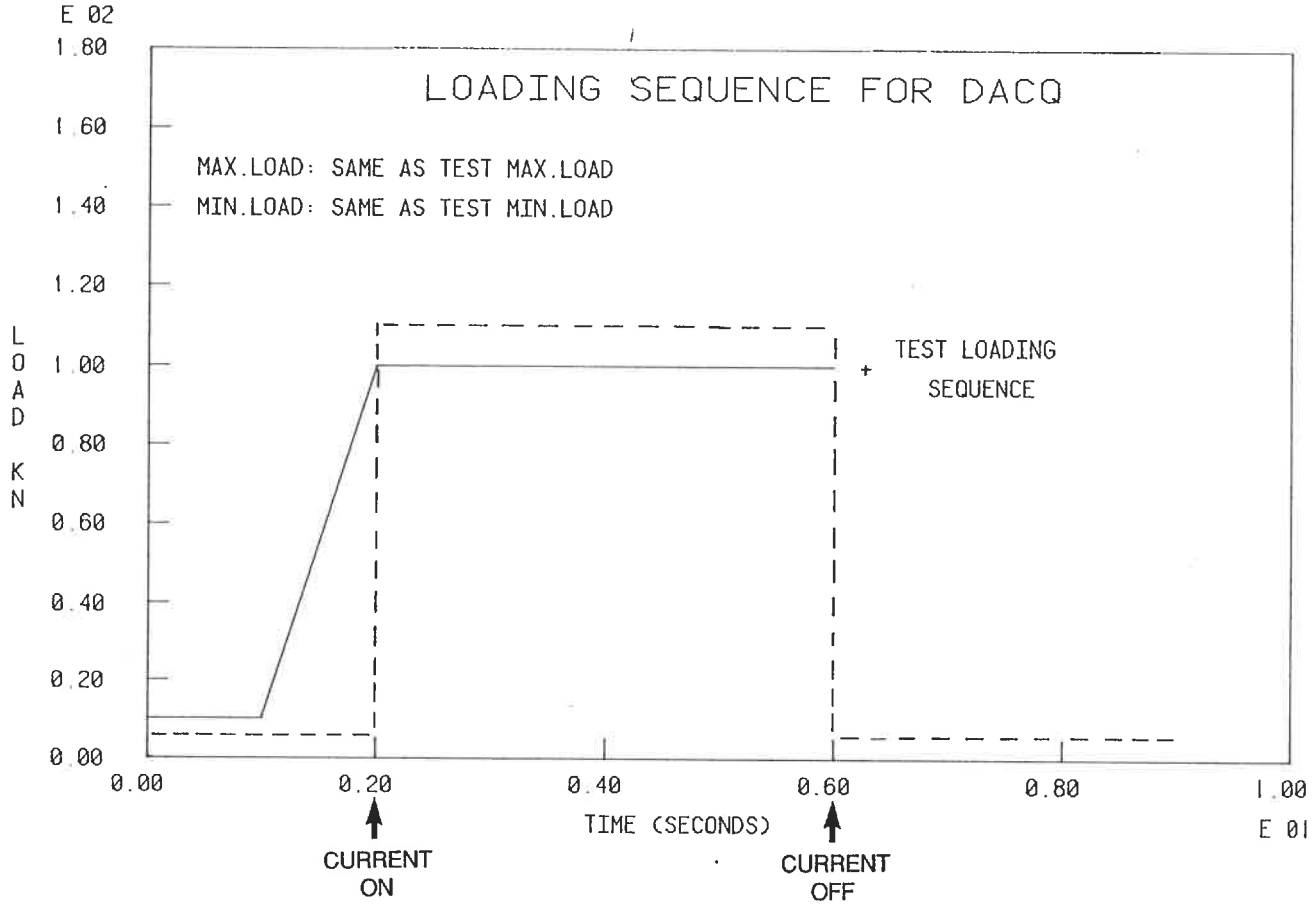

FIG. 4-14: LOADING SEQUENCE FOR DATA ACQUISITION

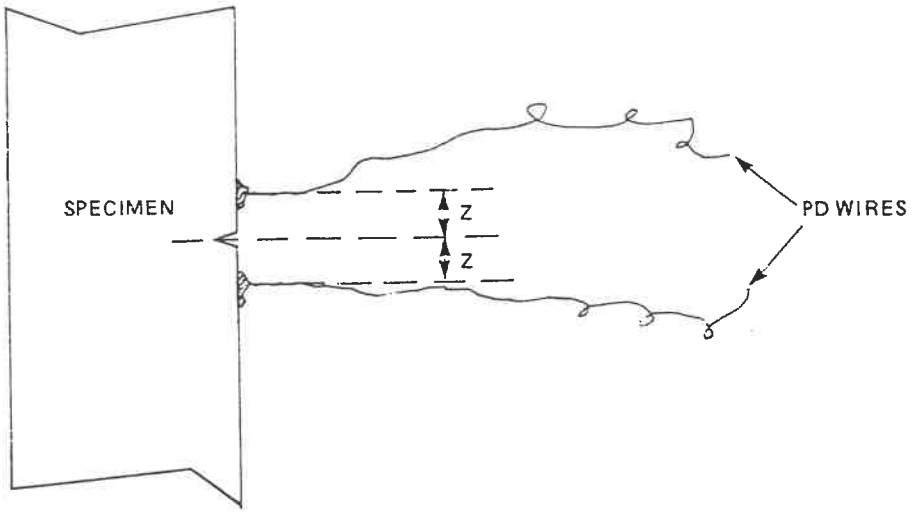

FIG. 4-15: PD WIRE POSITION ON TEST SPECIMEN

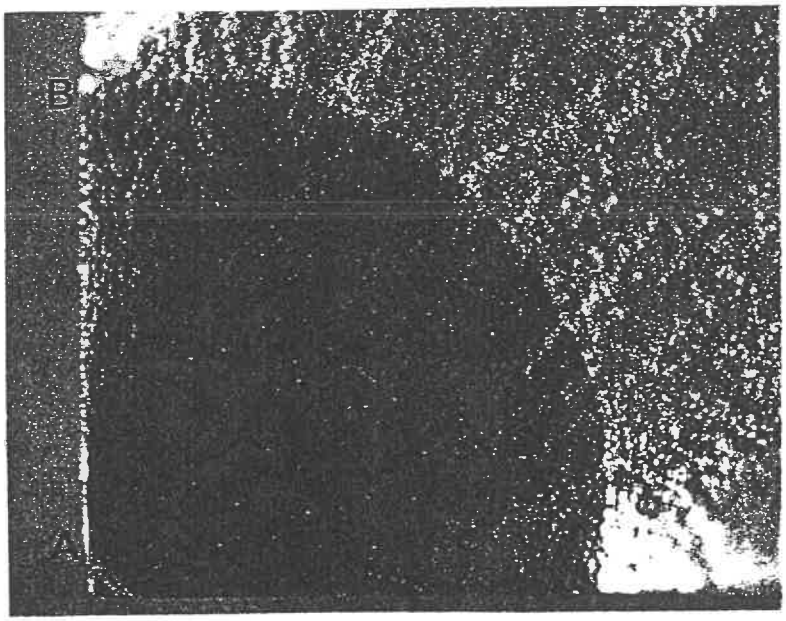

FIG. 4-16: FRACTURE FACE OF CC SPECIMEN BT4 SHOWING LOCATION OF INITIAL NOTCH LENGTH (A) AND FINAL CRACK LENGTH (B) USED FOR PD CALIBRATION CURVE

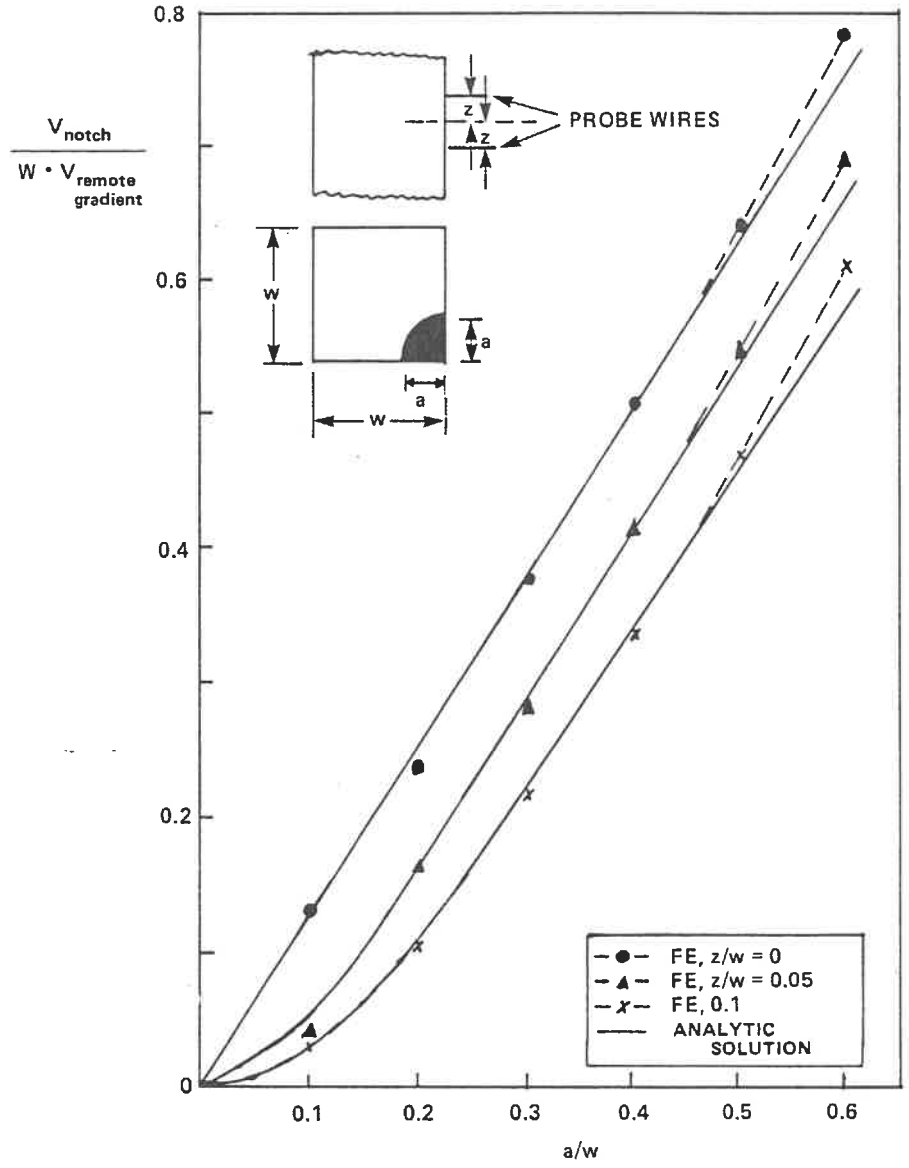

FIG. 4-17: FINITE ELEMENT AND ANALYTICAL PREDICTIONS FOR CORNER CRACK SPECIMEN

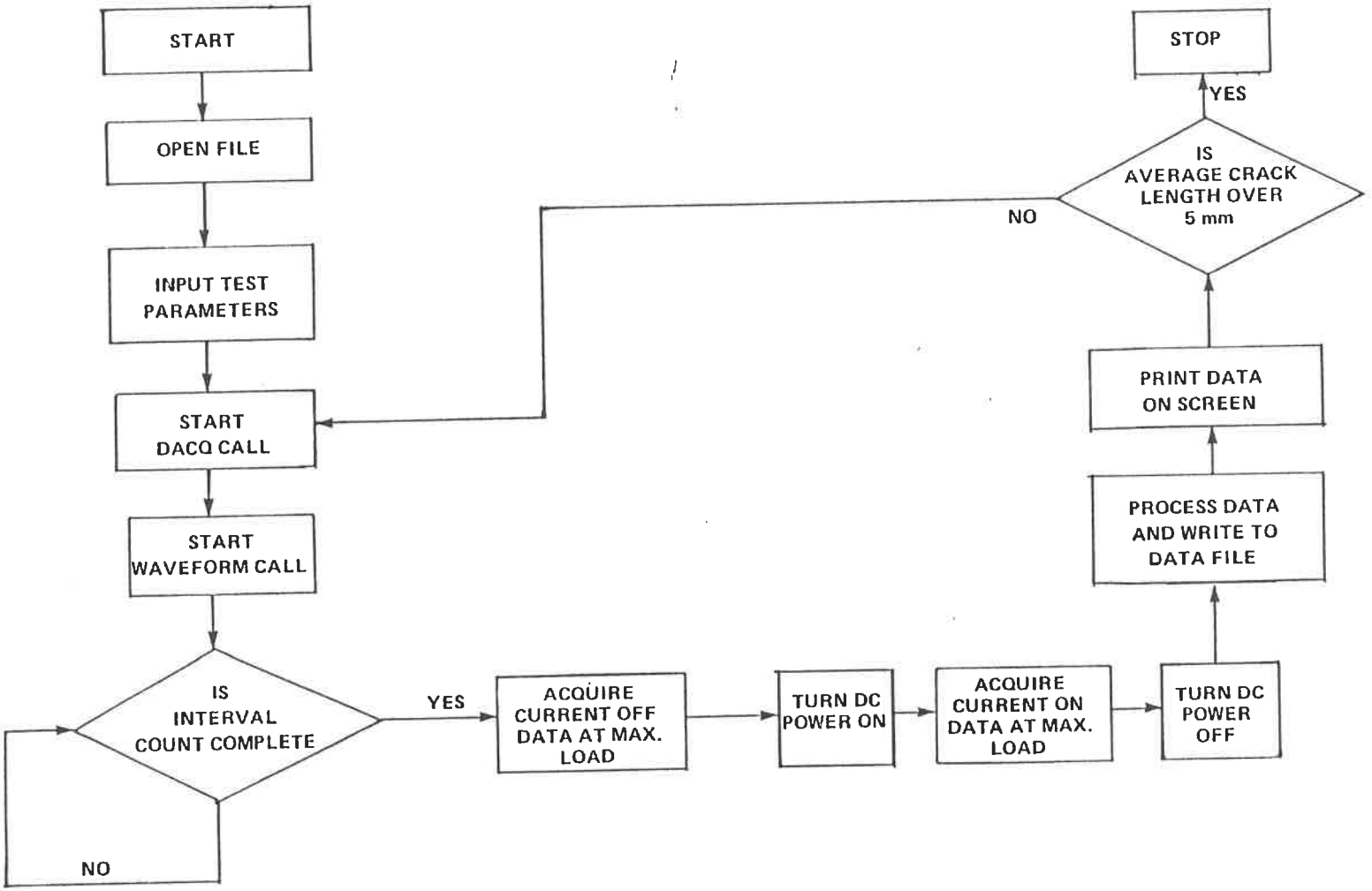

FIG. 4-18: FLOW CHART FOR TEST PROGRAM

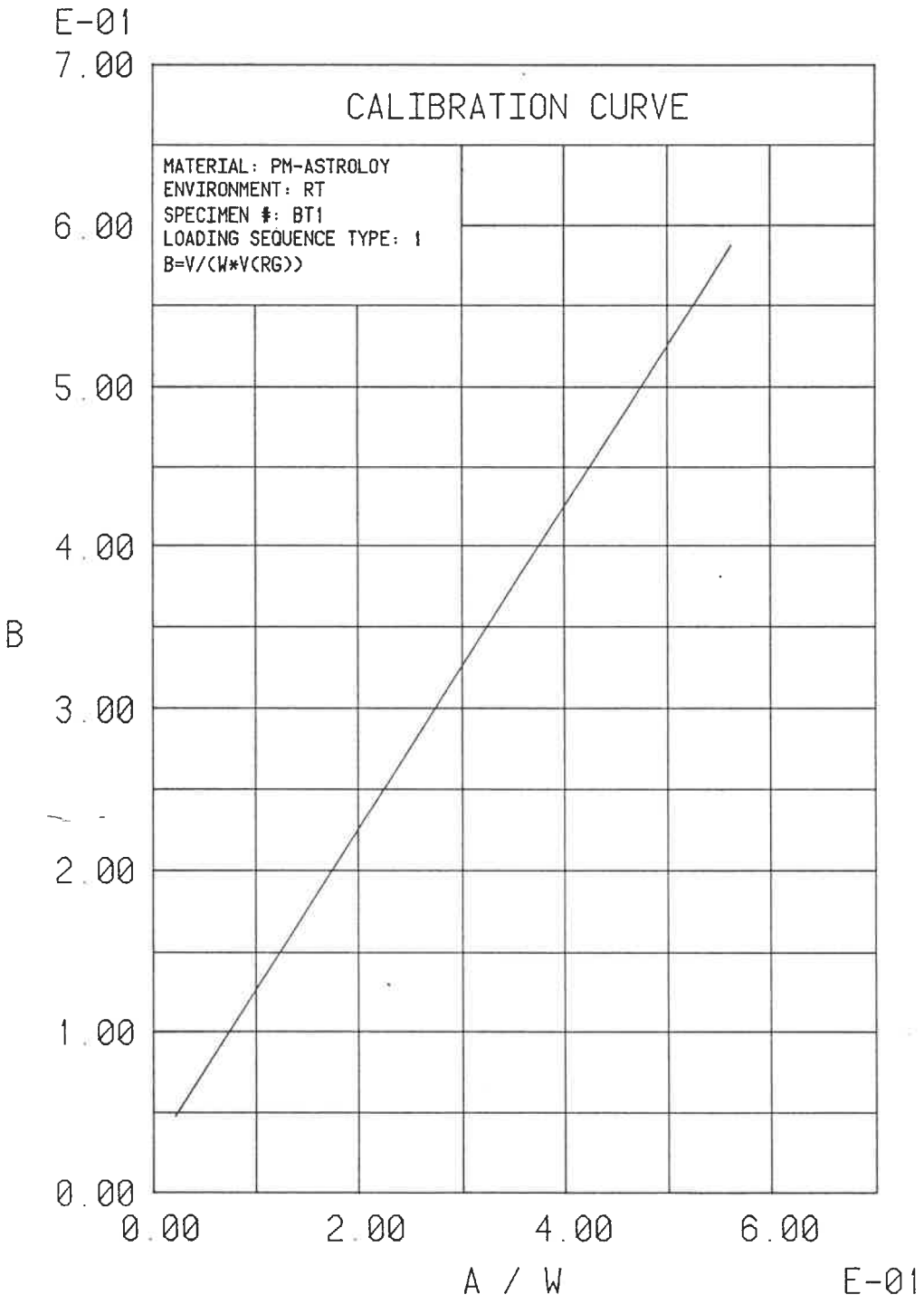

FIG. 5-1: CALIBRATION CURVE FOR SPECIMEN BT1

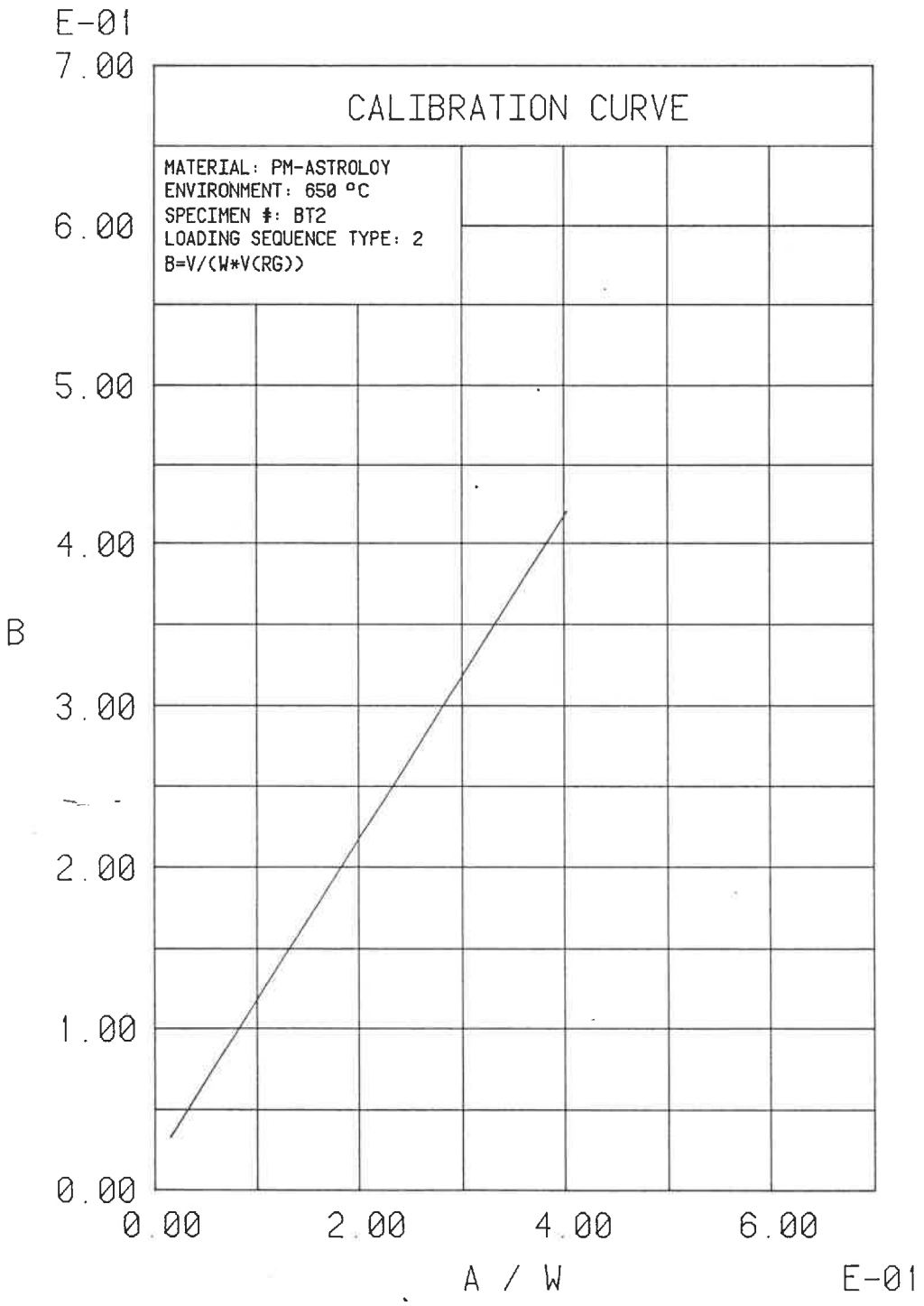

FIG. 5-2: CALIBRATION CURVE FOR SPECIMEN BT2

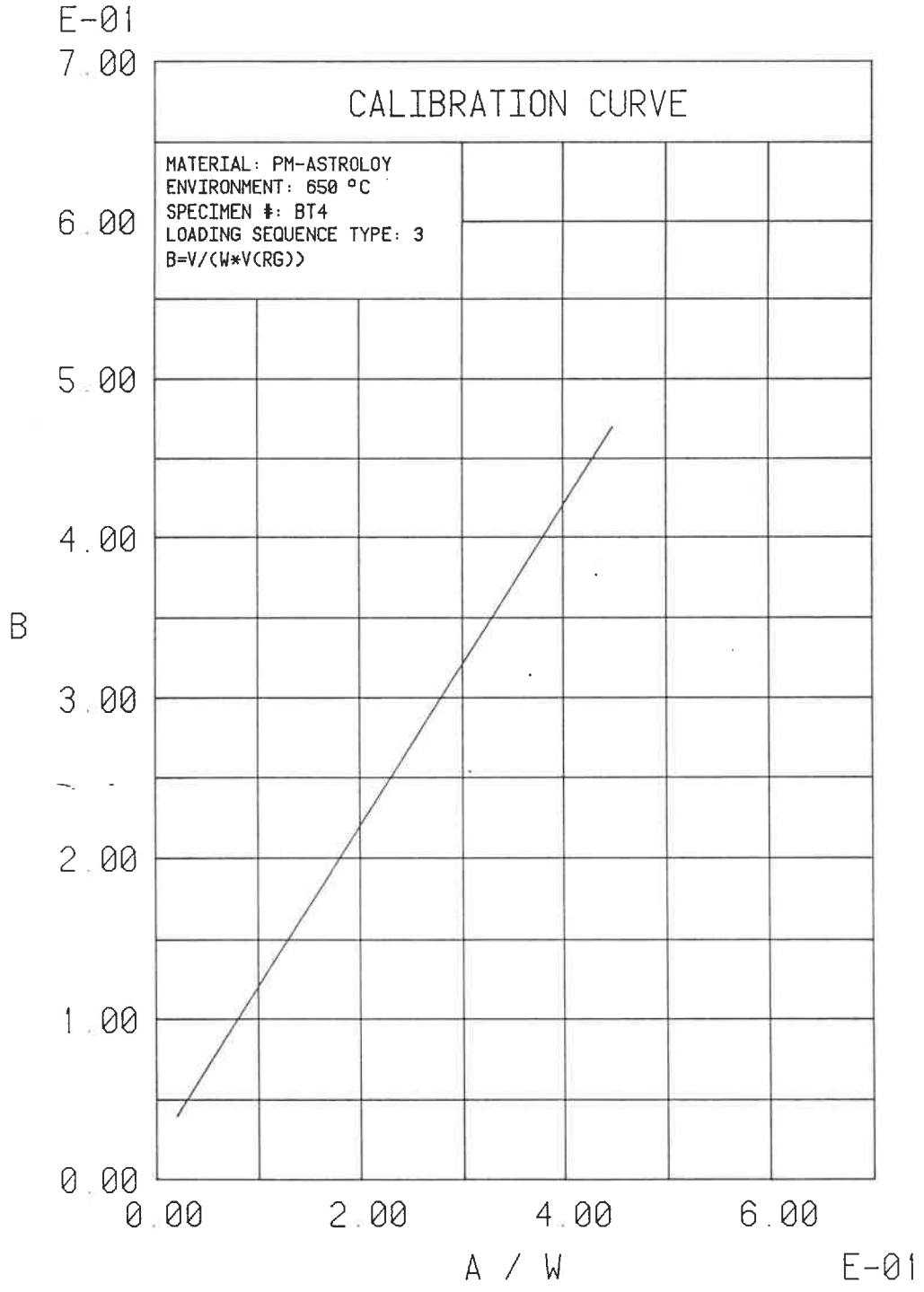

FIG. 5-3: CALIBRATION CURVE FOR SPECIMEN BT4

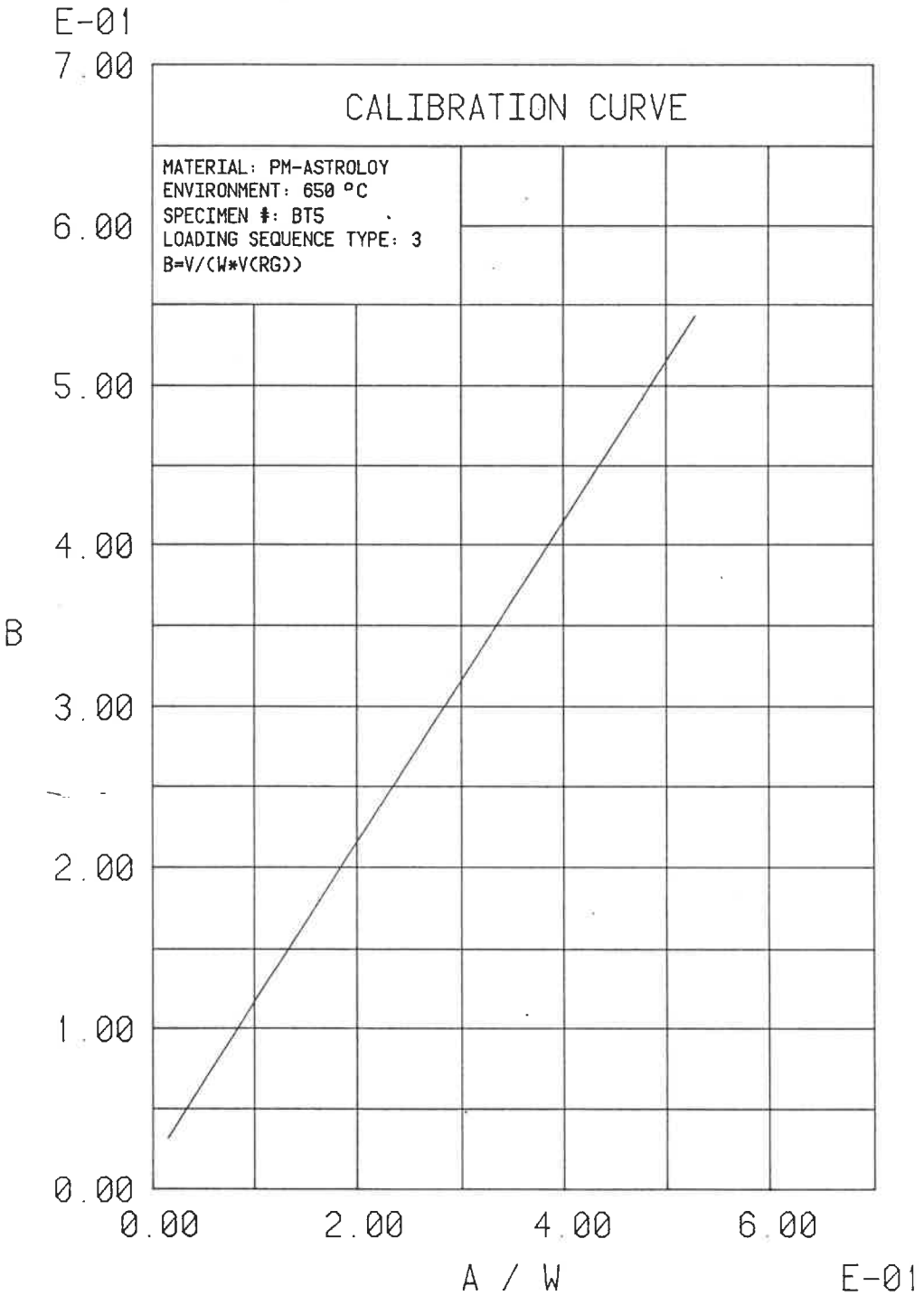

FIG. 5-4: CALIBRATION CURVE FOR SPECIMEN BT5

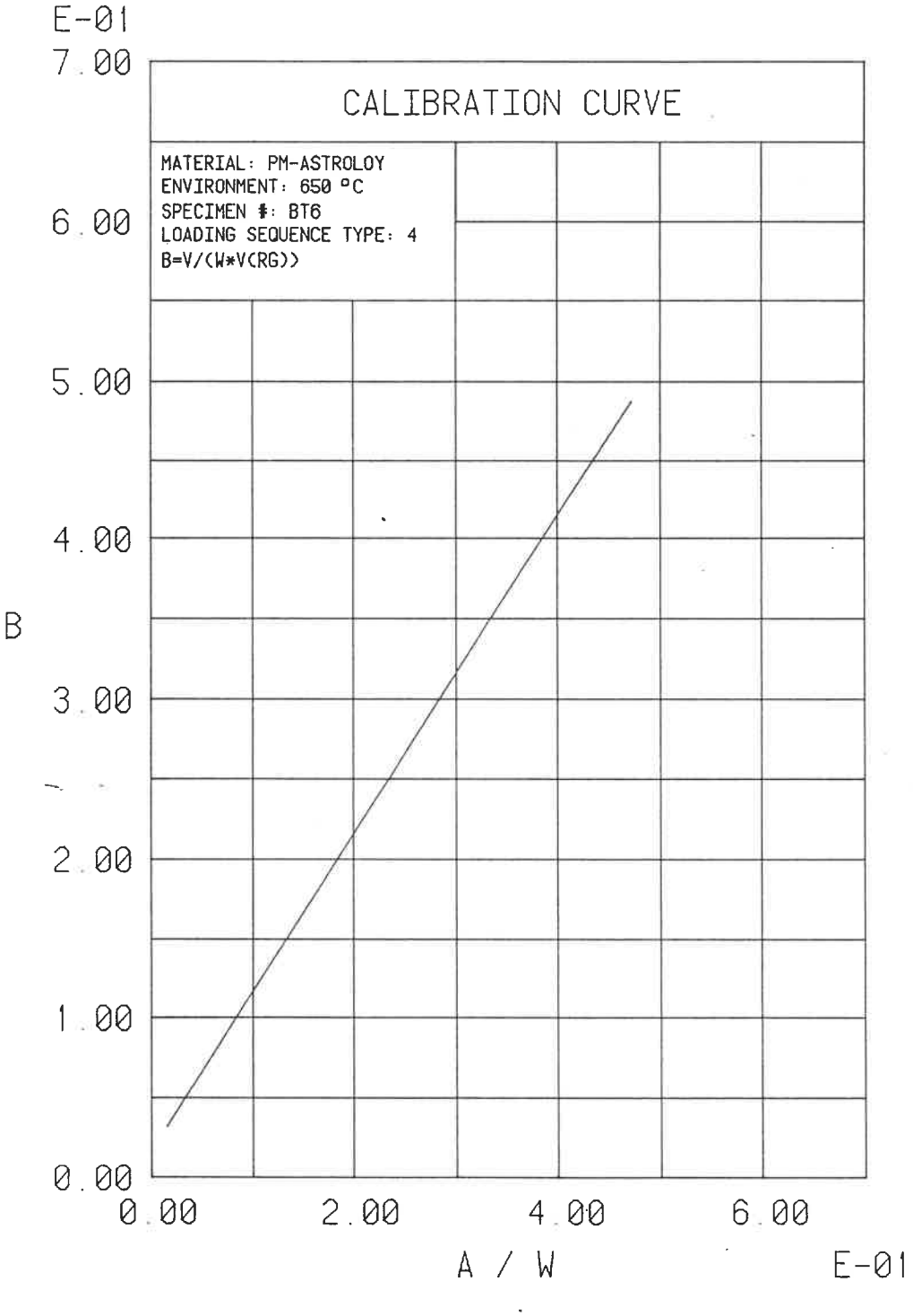

FIG. 5-5: CALIBRATION CURVE FOR SPECIMEN BT6

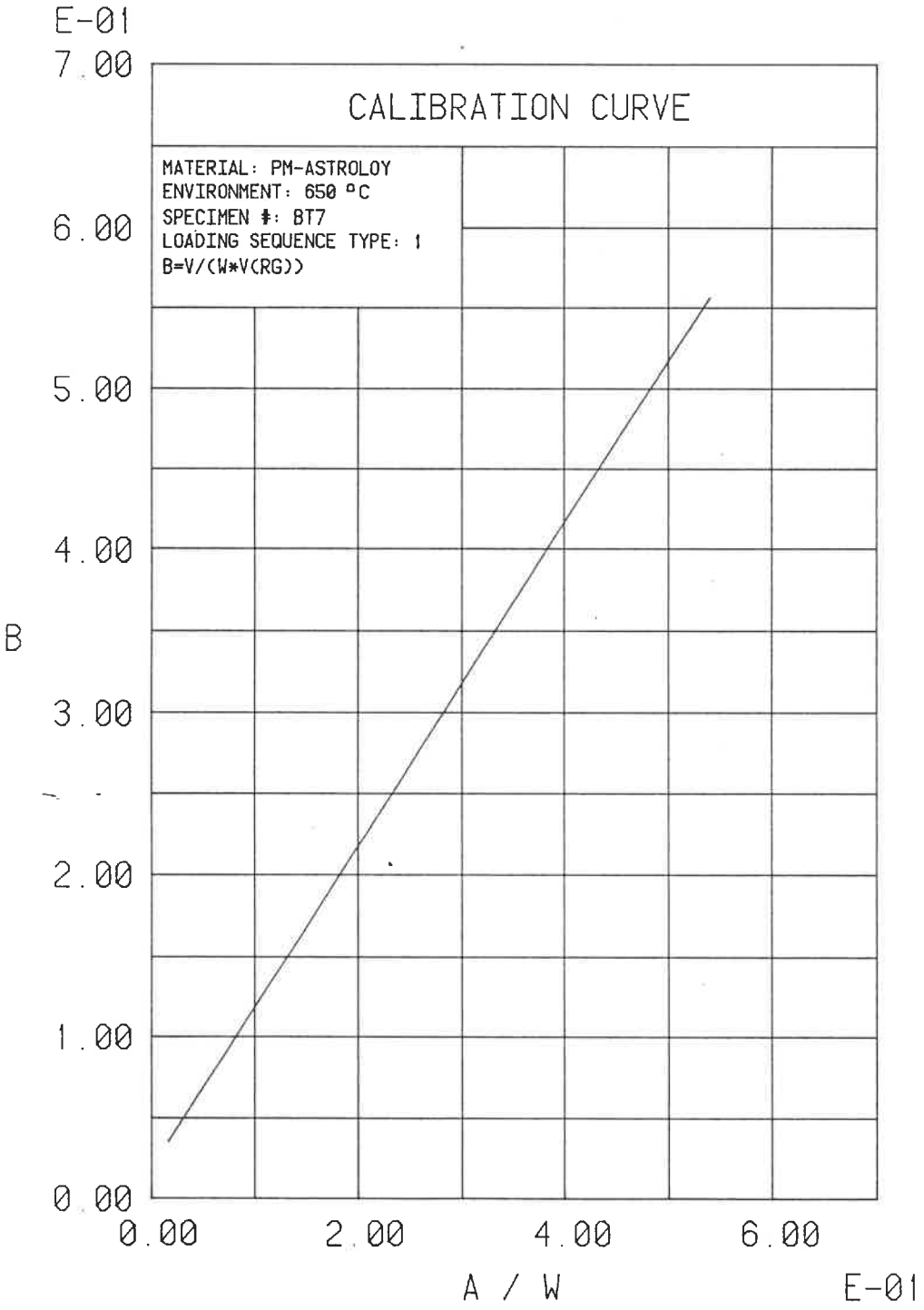

FIG. 5-6: CALIBRATION CURVE FOR SPECIMEN BT7

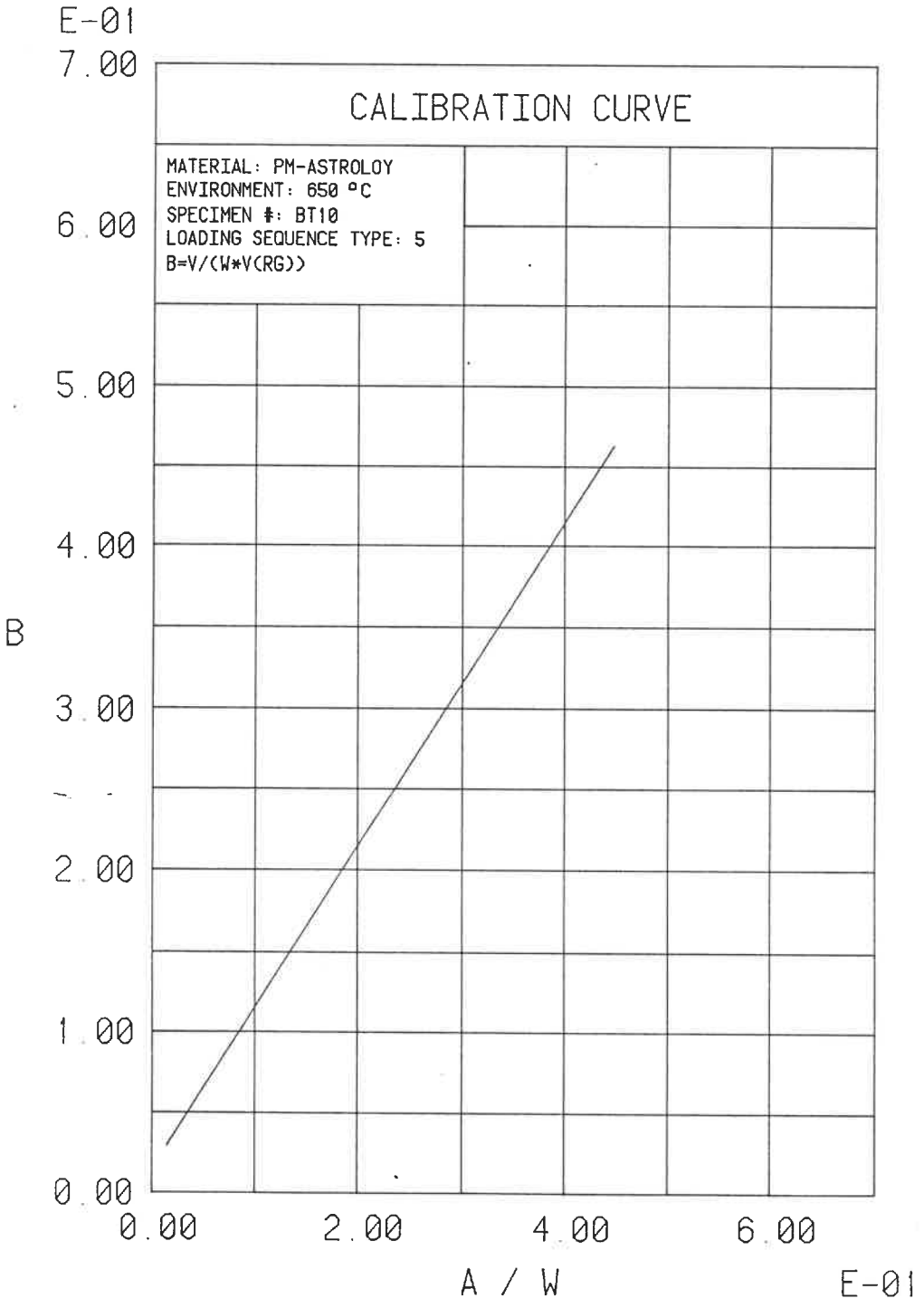

FIG. 5-7: CALIBRATION CURVE FOR SPECIMEN BT10

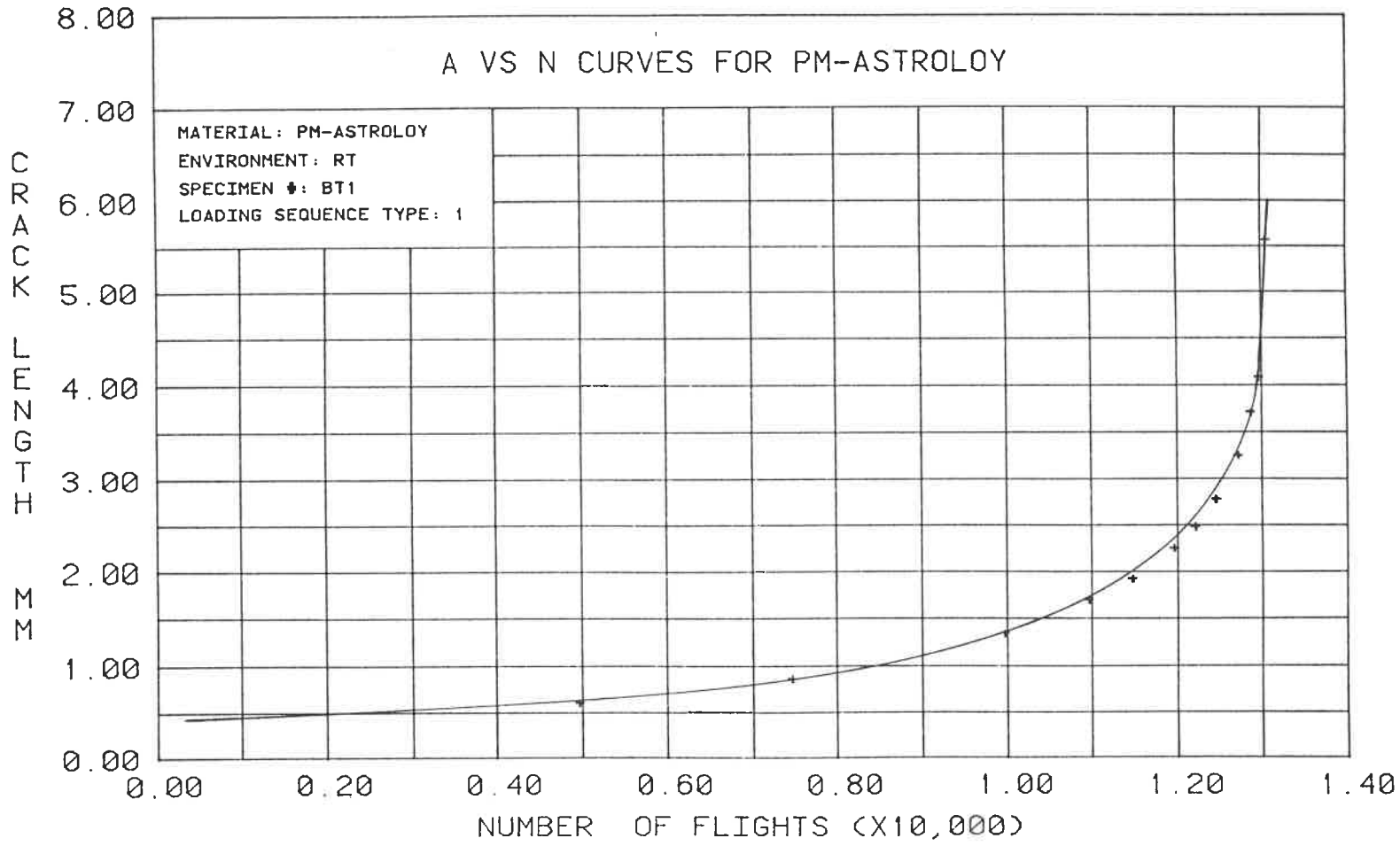

FIG. 5-8: CRACK LENGTH VS # OF FLIGHTS FOR SPECIMEN BT1

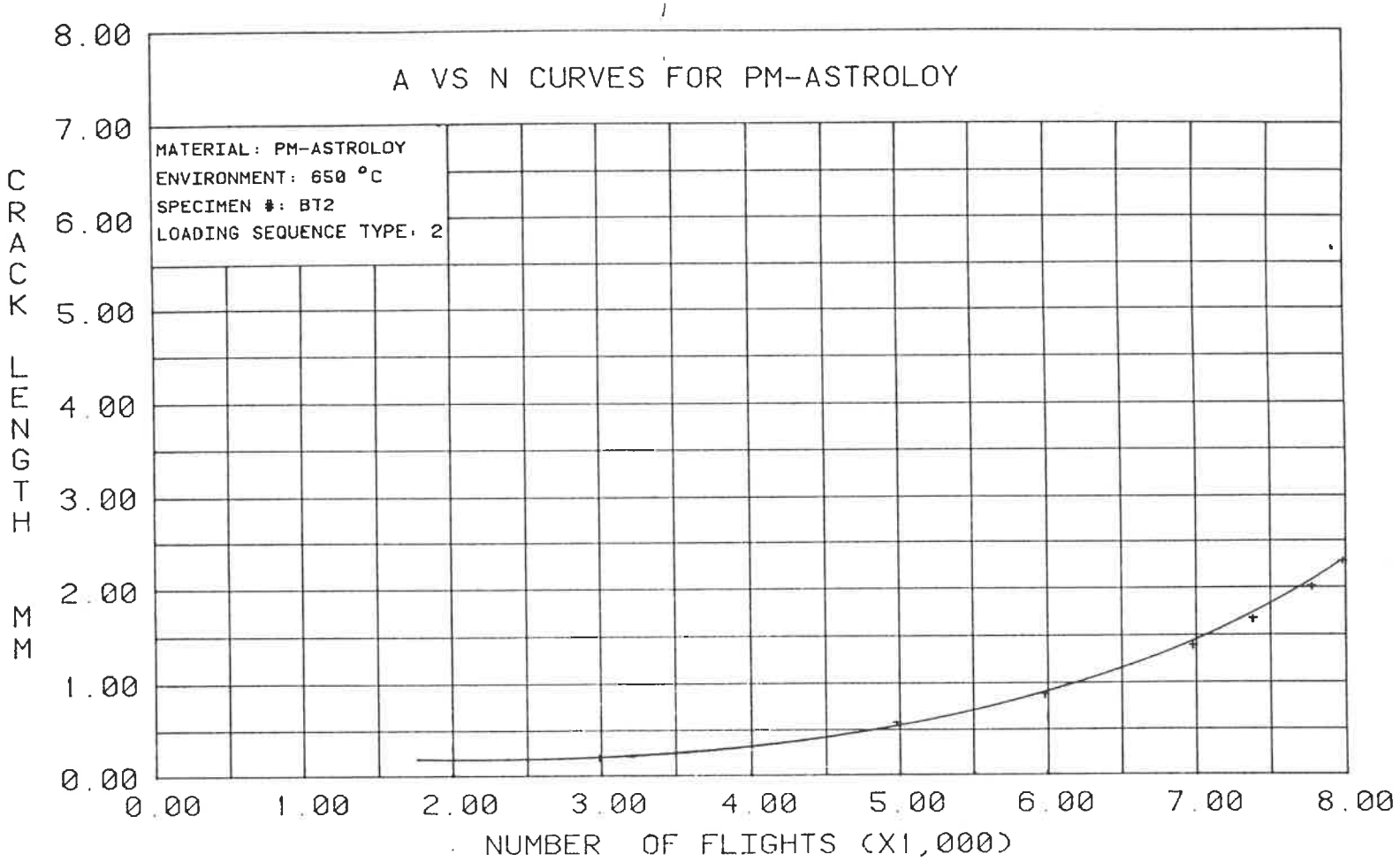

FIG. 5-9: CRACK LENGTH VS # OF FLIGHTS FOR SPECIMEN BT2

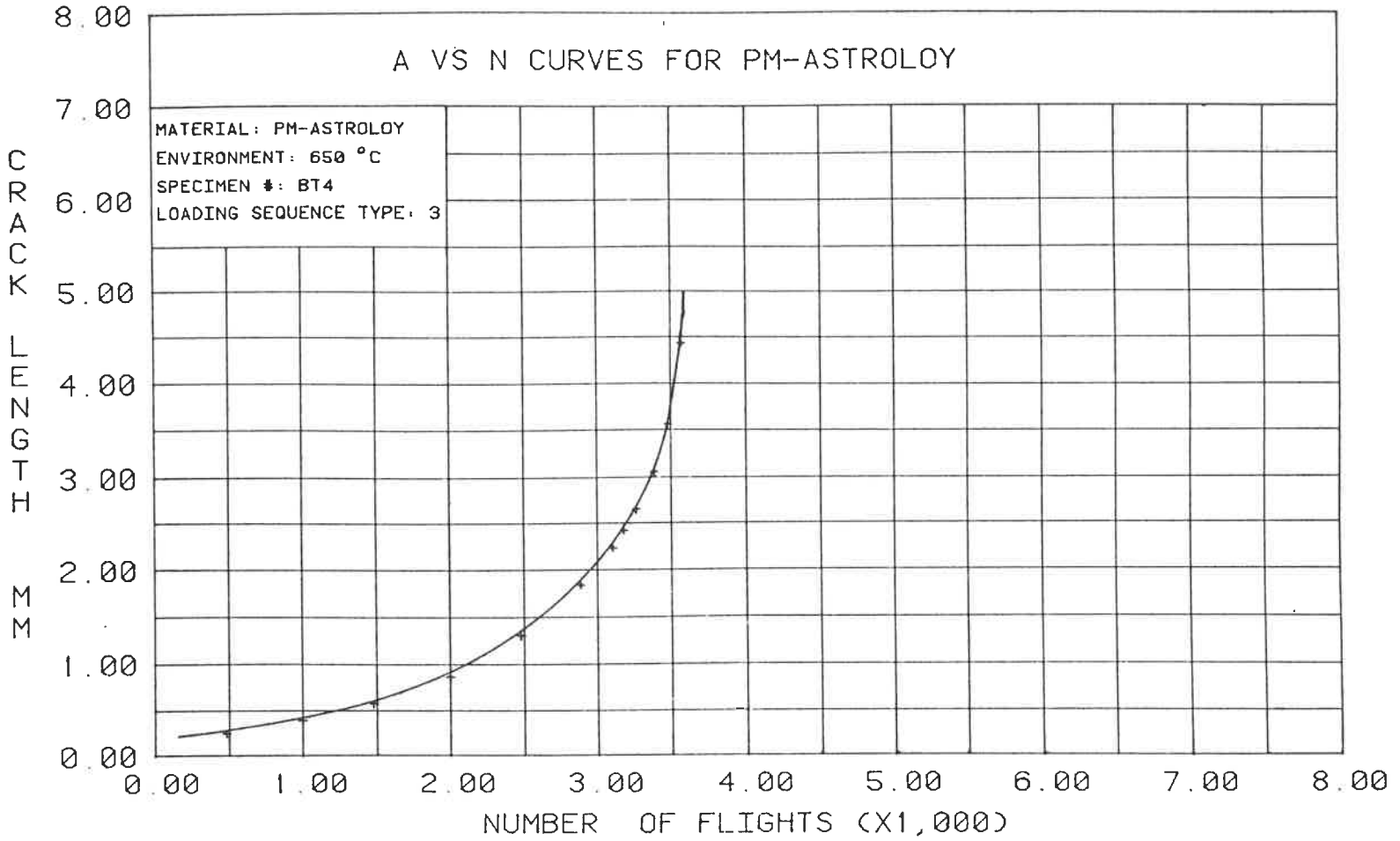

FIG. 5-10: CRACK LENGTH VS # OF FLIGHTS FOR SPECIMEN BT4

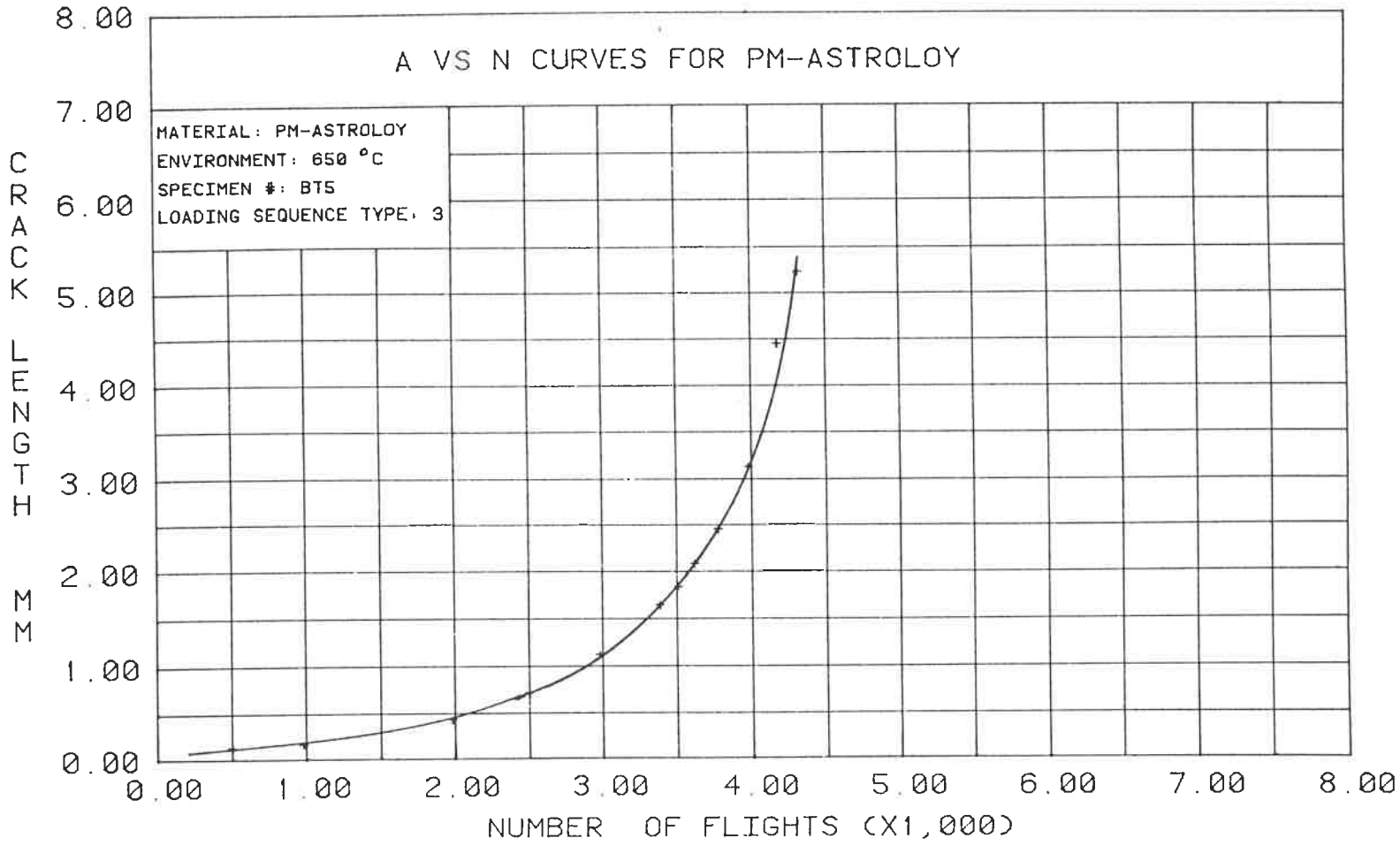

FIG. 5-11: CRACK LENGTH VS # OF FLIGHTS FOR SPECIMEN BT5

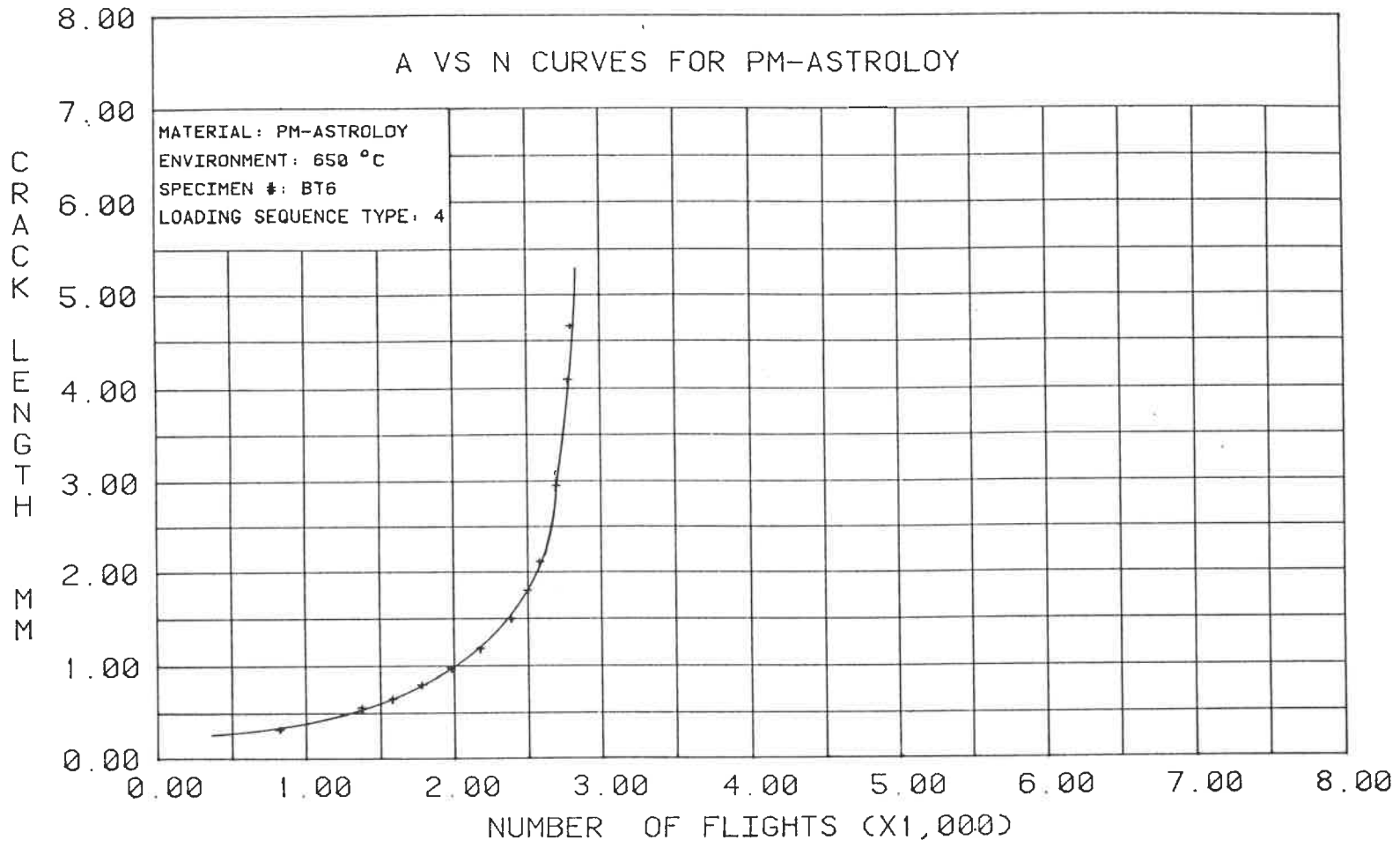

FIG. 5-12: CRACK LENGTH VS # OF FLIGHTS FOR SPECIMEN BT6

192.

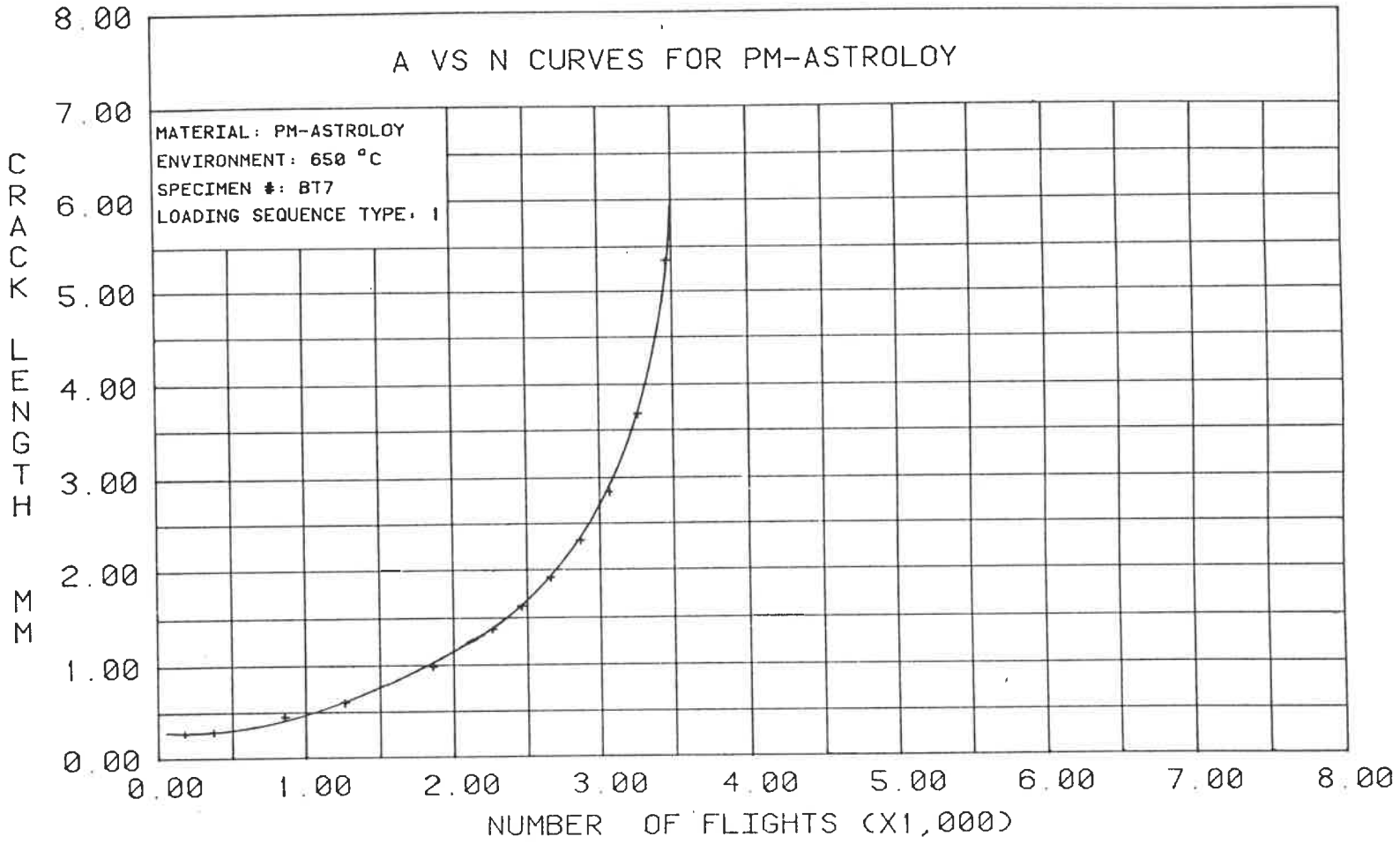

FIG. 5-13: CRACK LENGTH VS # OF FLIGHTS FOR SPECIMEN BT7

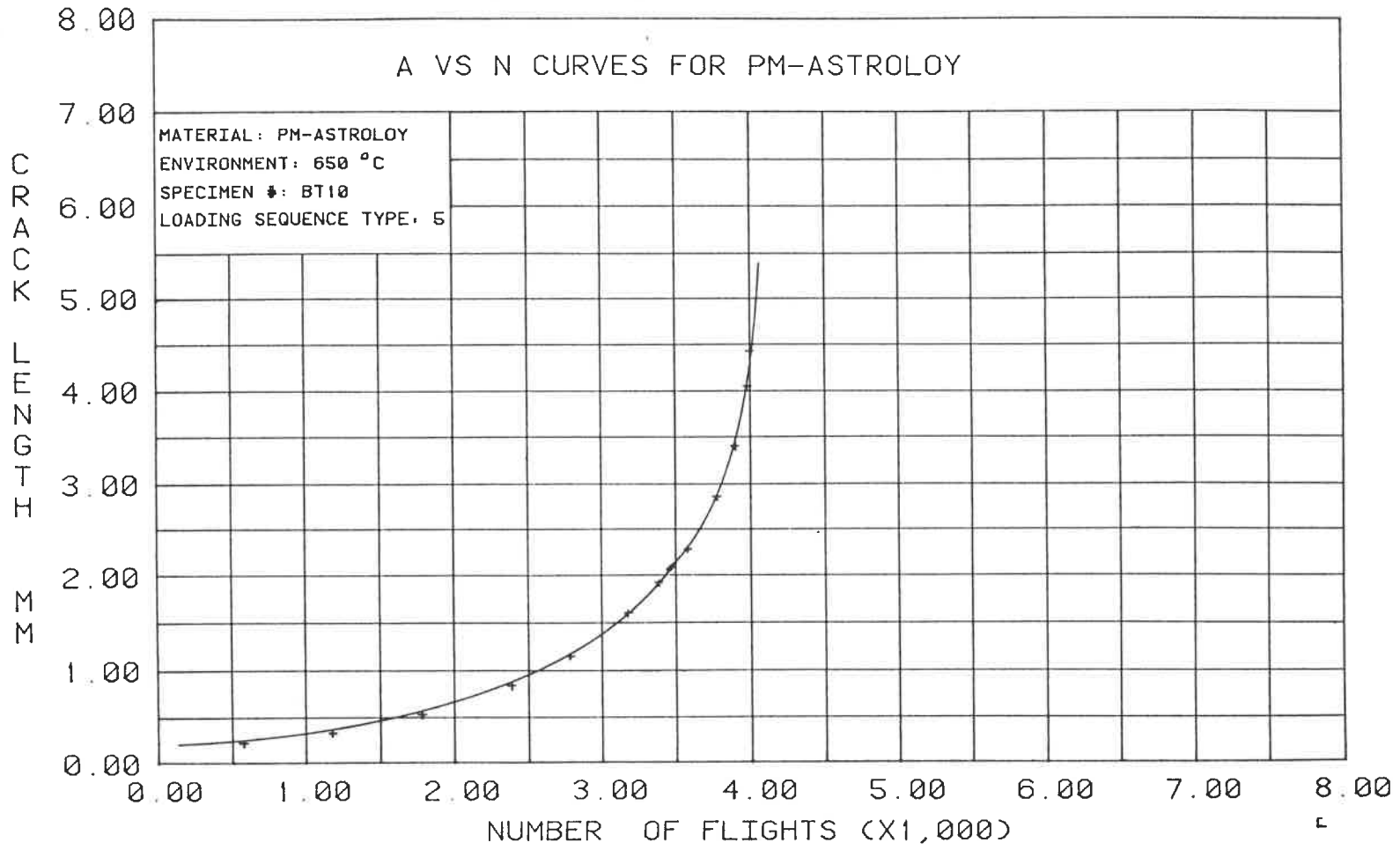

FIG. 5-14: CRACK LENGTH VS # OF FLIGHTS FOR SPECIMEN BT10

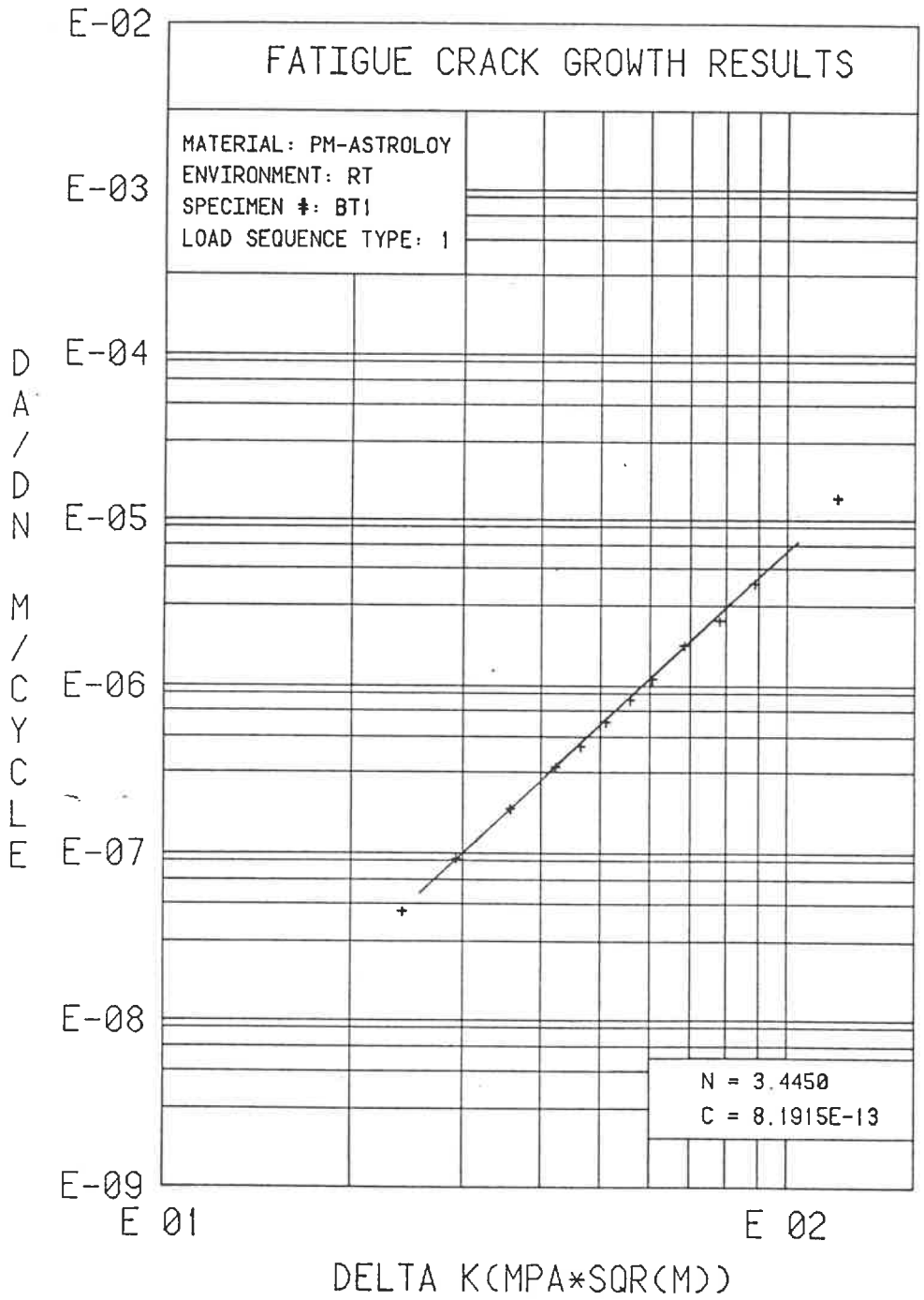

FIG. 5-15: FCPR VS ΔK FOR SPECIMEN BT1

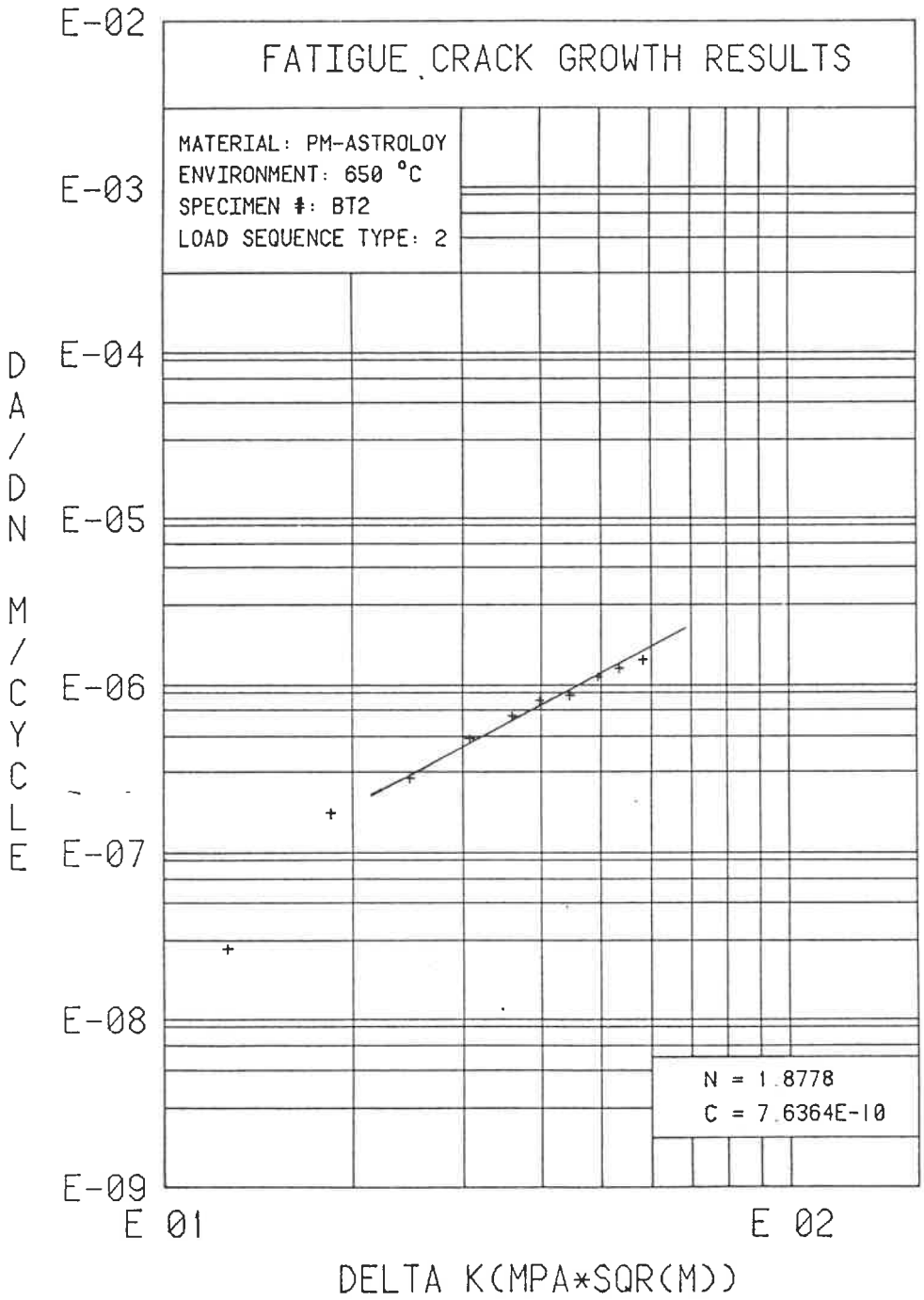

FIG. 5-16: FCPR VS ΔK FOR SPECIMEN BT2

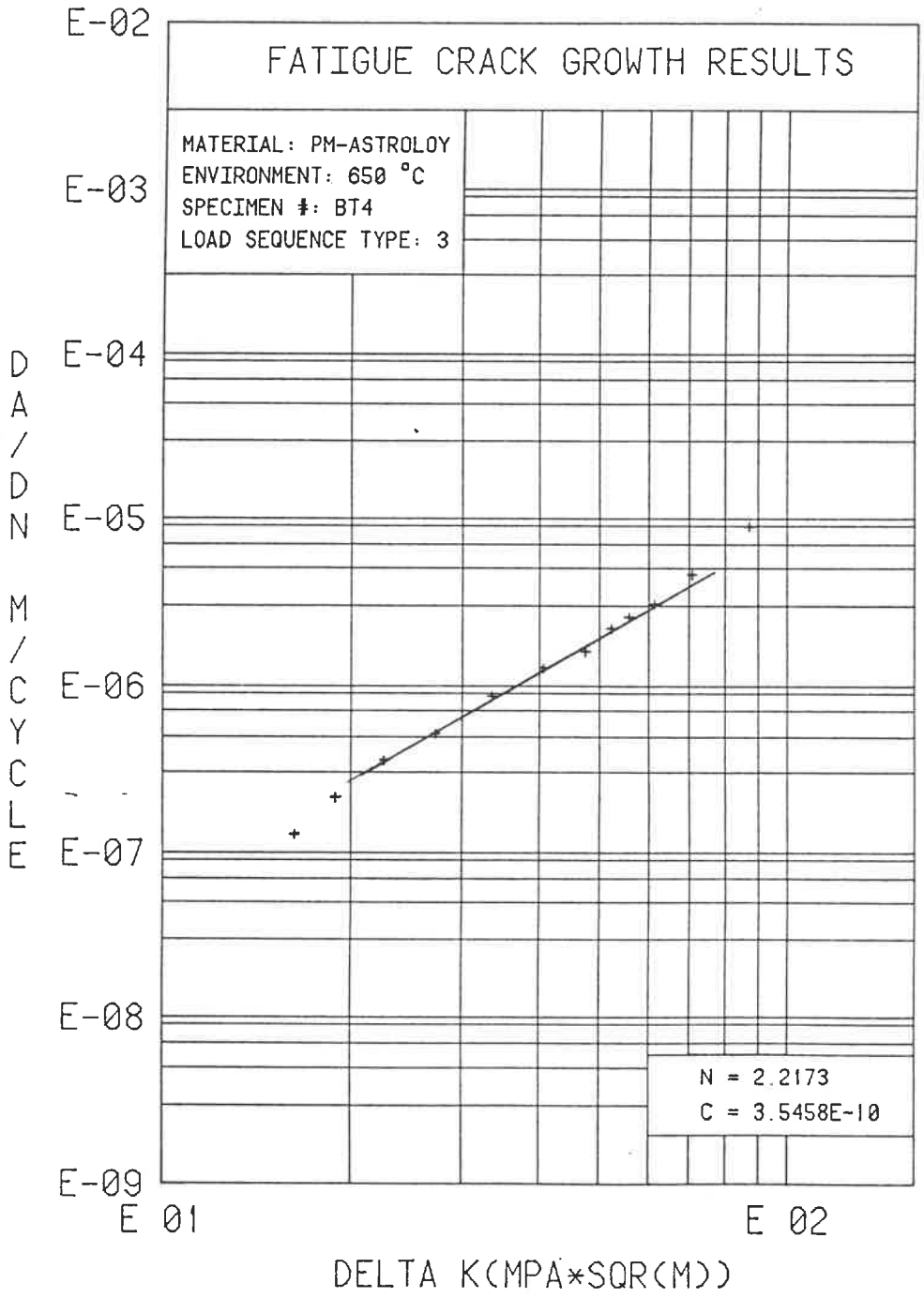

FIG. 5-17: FCPR VS ΔK FOR SPECIMEN BT4

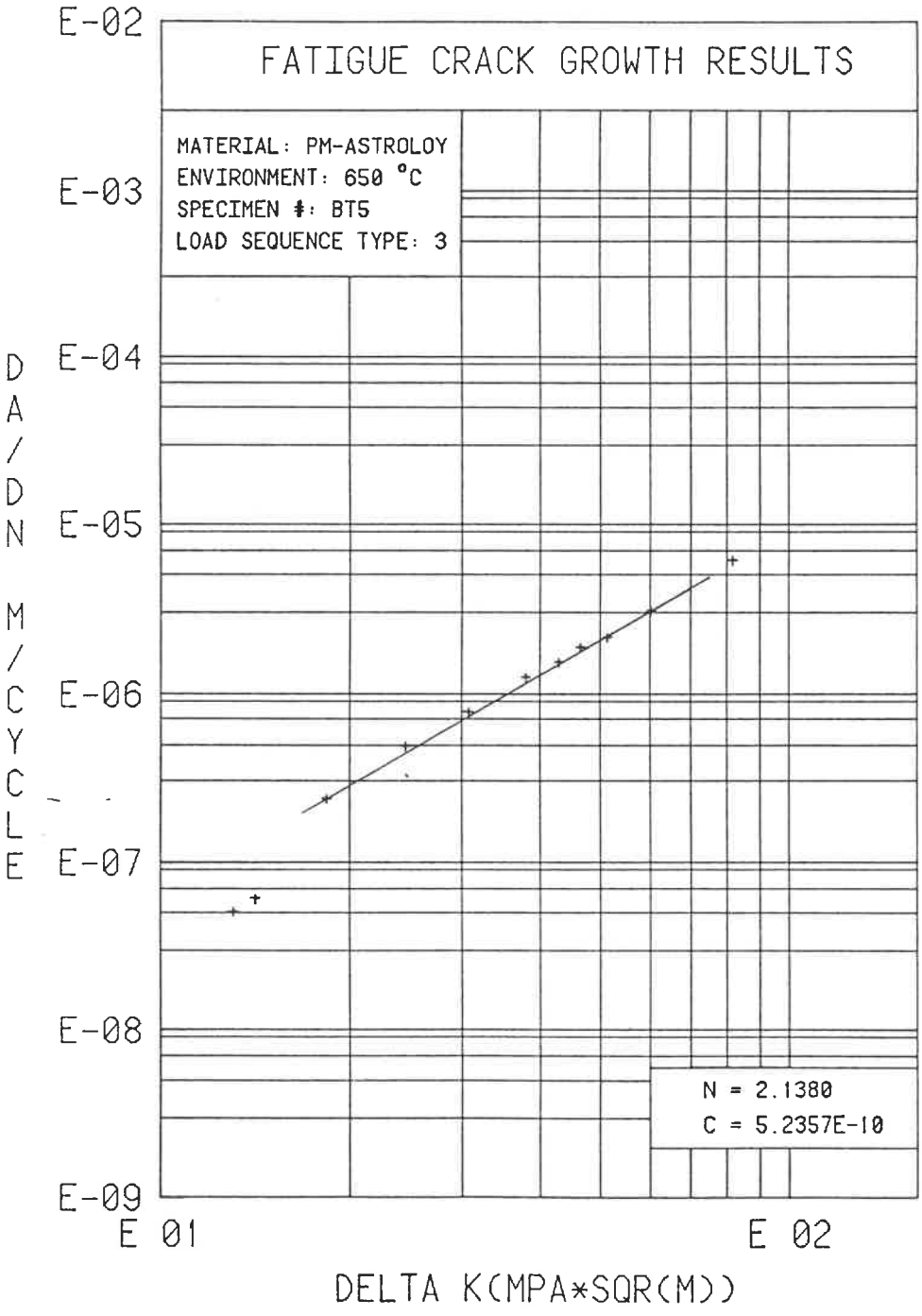

FIG. 5-18: FCPR VS ΔK FOR SPECIMEN BT5

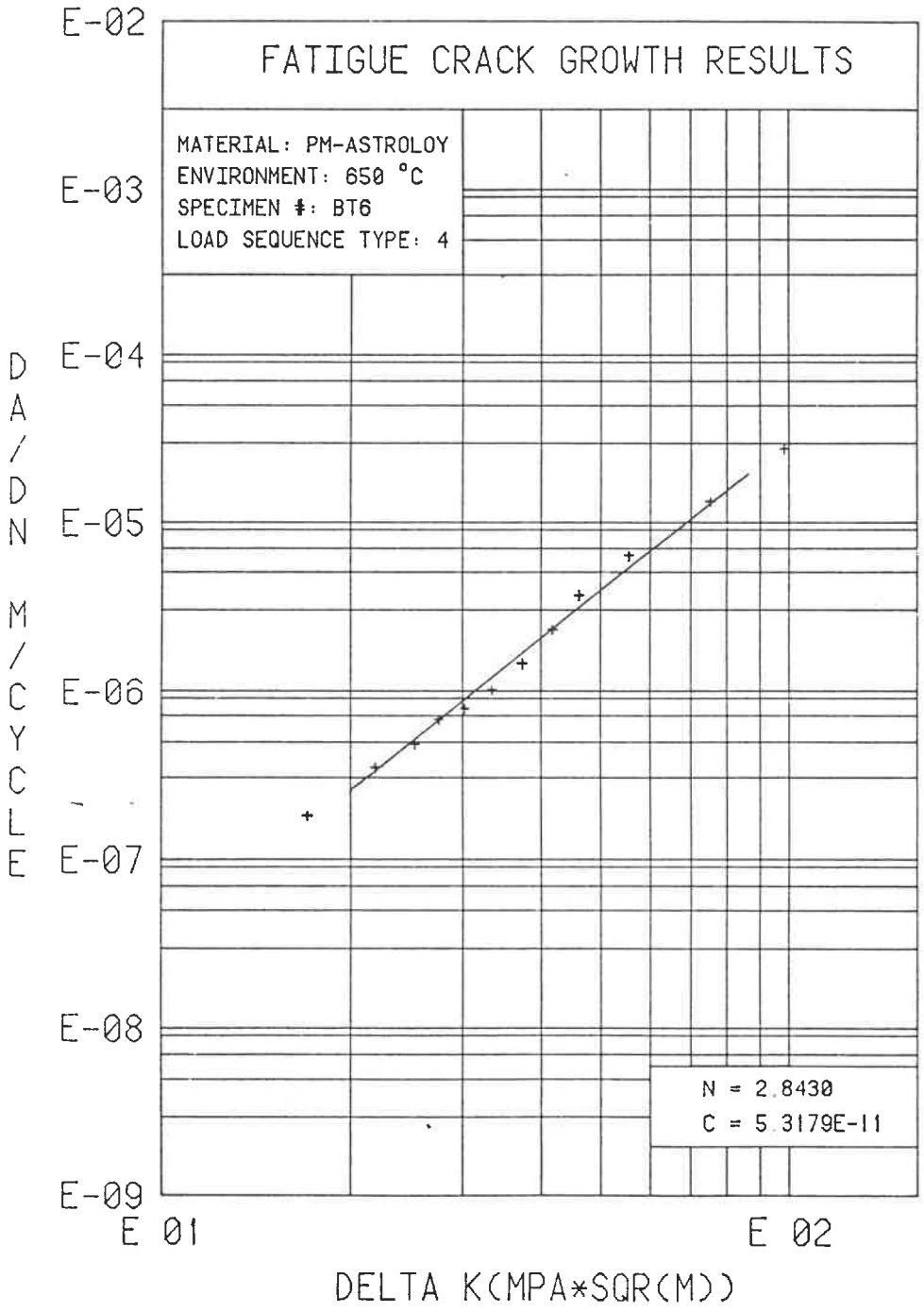

FIG. 5-19: FCPR VS ΔK FOR SPECIMEN BT6

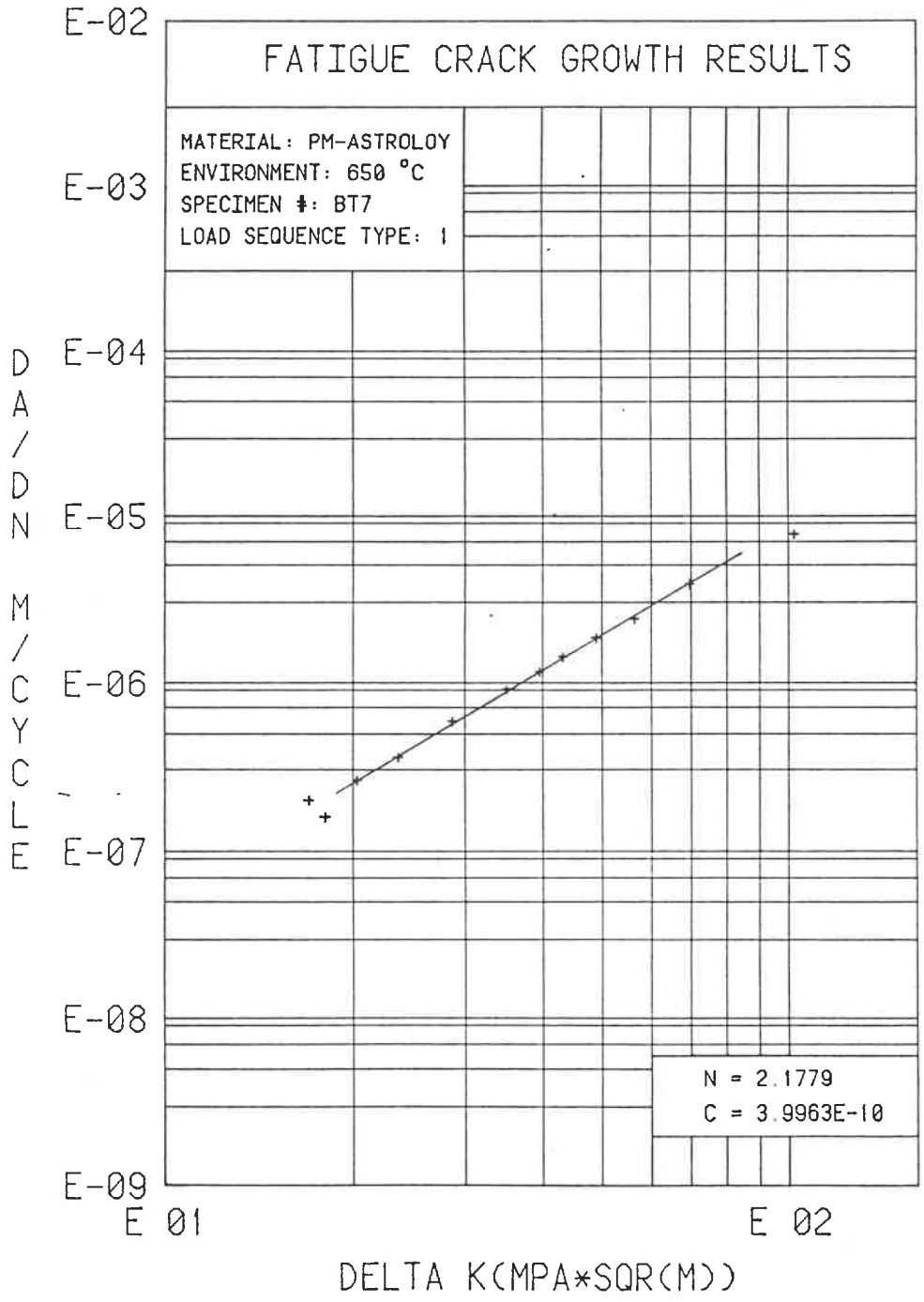

FIG. 5-20: FCPR VS ΔK FOR SPECIMEN BT7

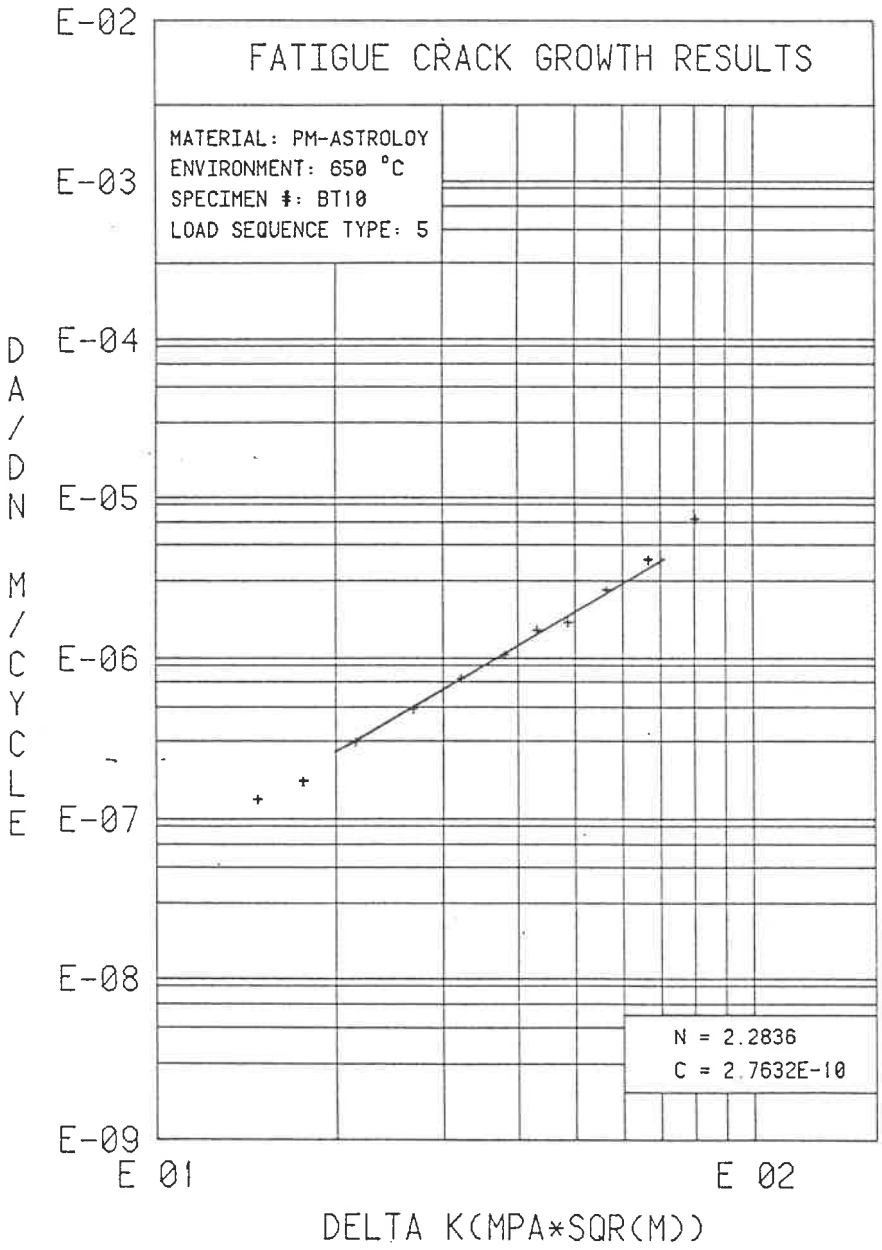

FIG. 5-21: FCPR VS ΔK FOR SPECIMEN BT10

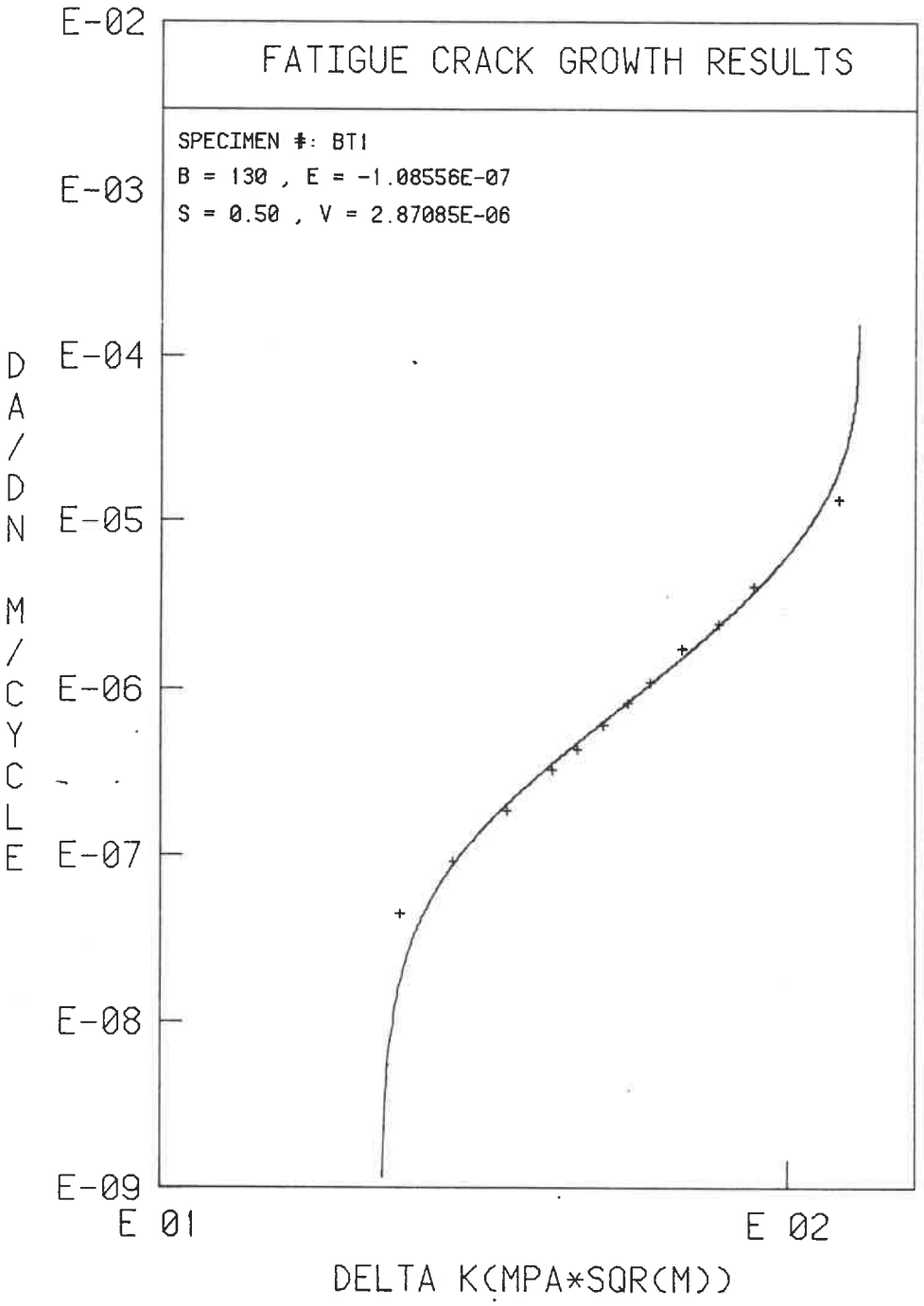

FIG. 5-22: FOUR PARAMETER WEIBULL CURVE FIT FOR SPECIMEN BT1

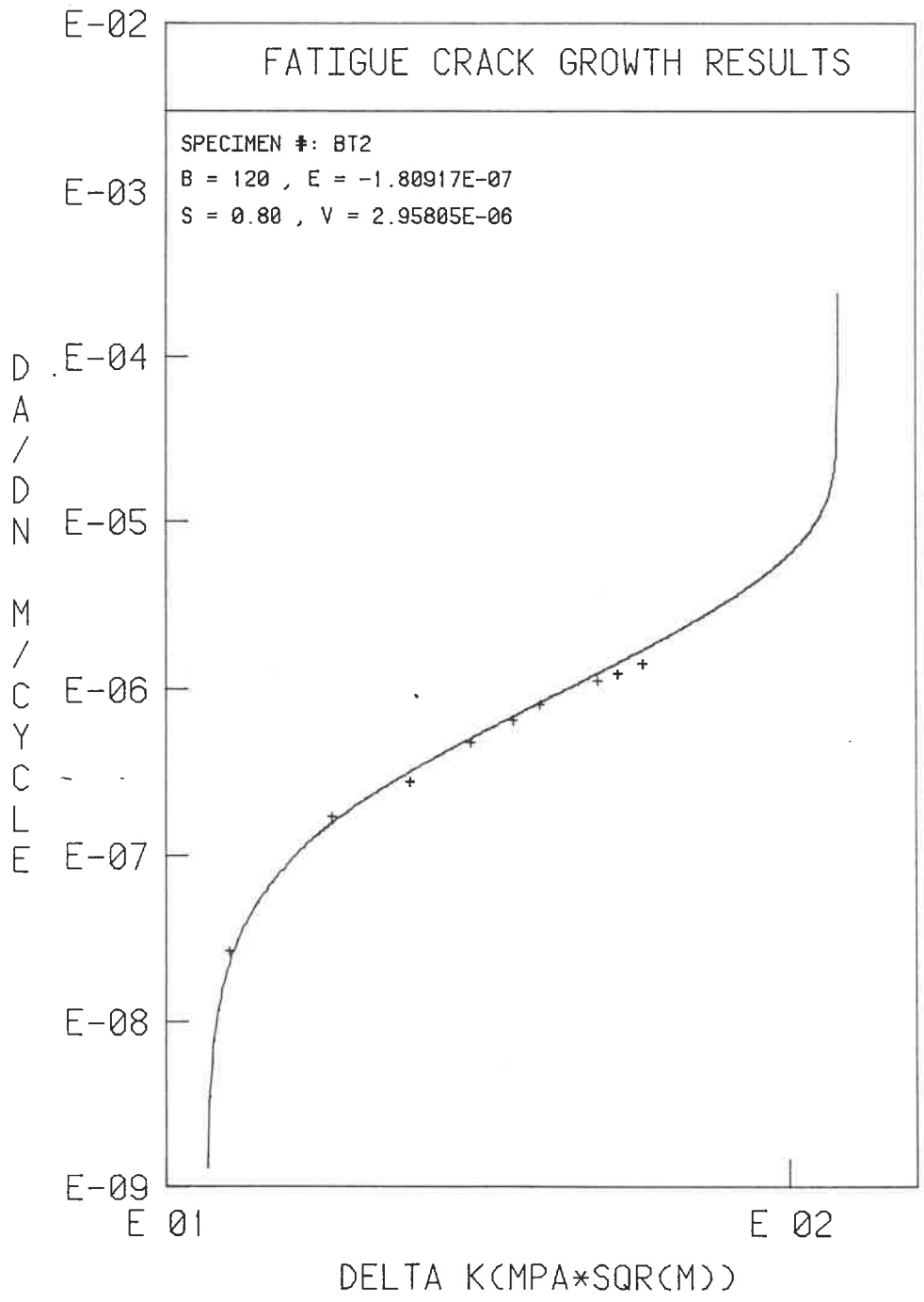

FIG. 5-23: FOUR PARAMETER WEIBULL CURVE FIT FOR SPECIMEN BT2

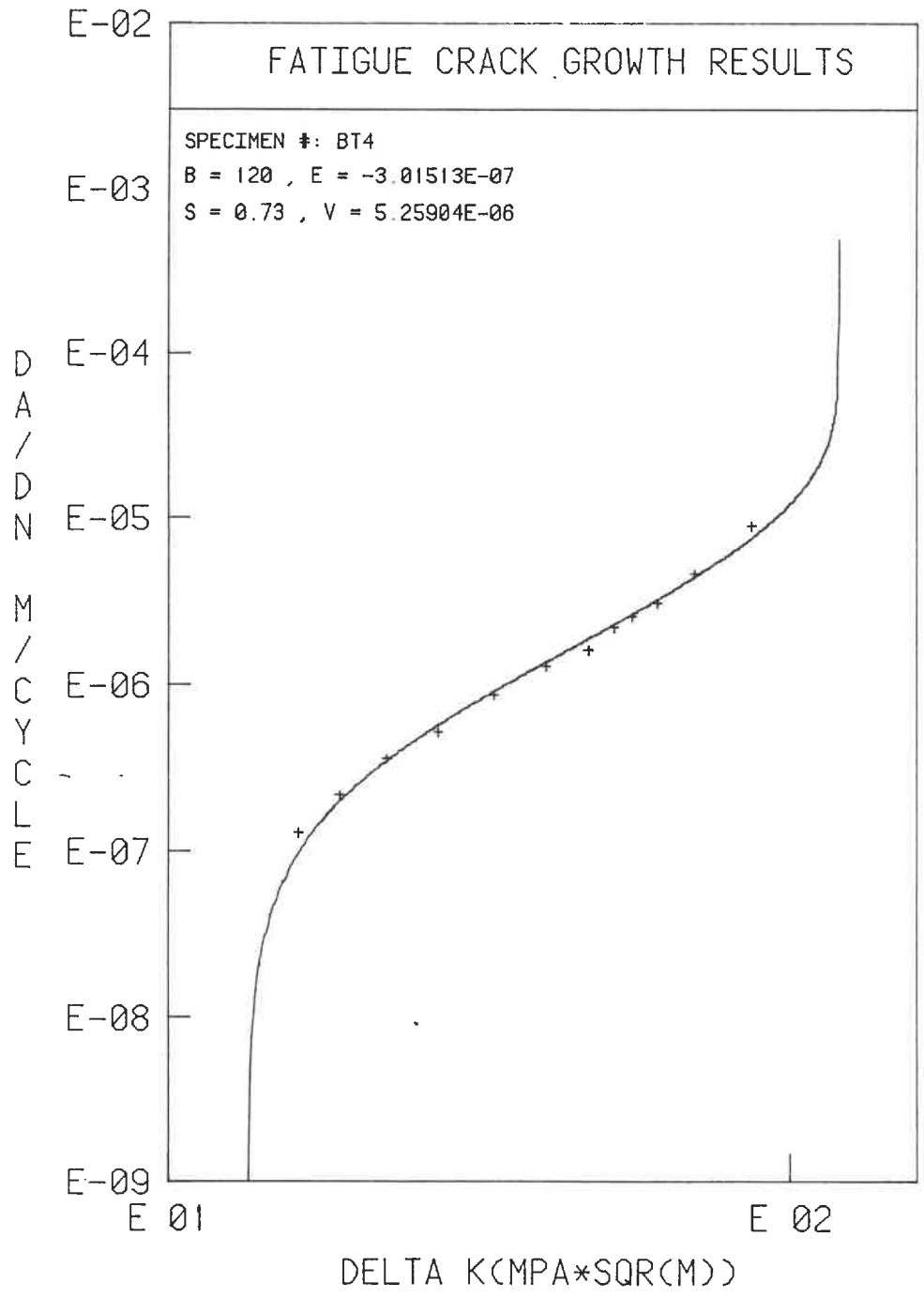

FIG. 5-24: FOUR PARAMETER WEIBULL CURVE FIT FOR SPECIMEN BT4

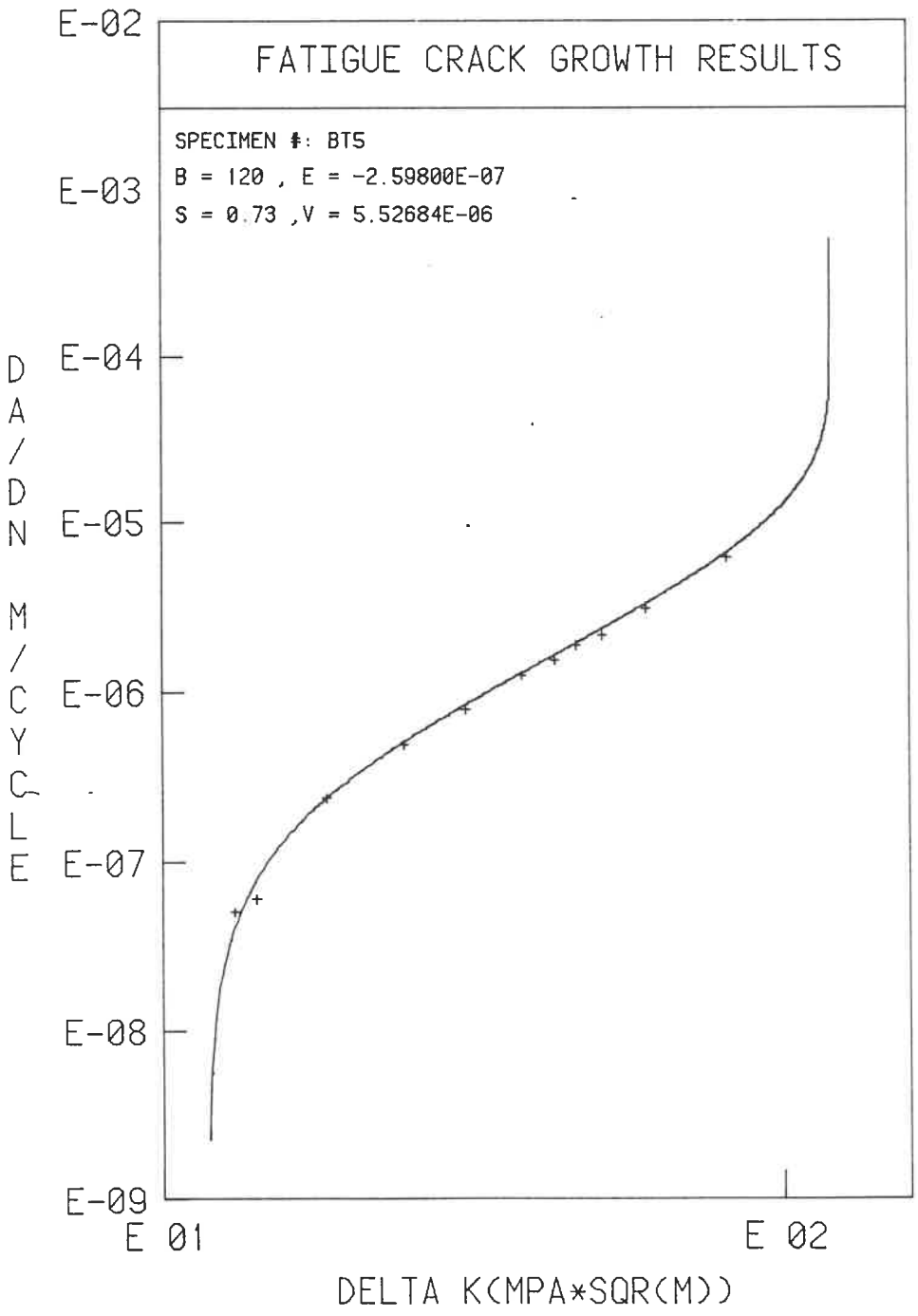

FIG. 5-25: FOUR PARAMETER WEIBULL CURVE FIT FOR SPECIMEN BT5

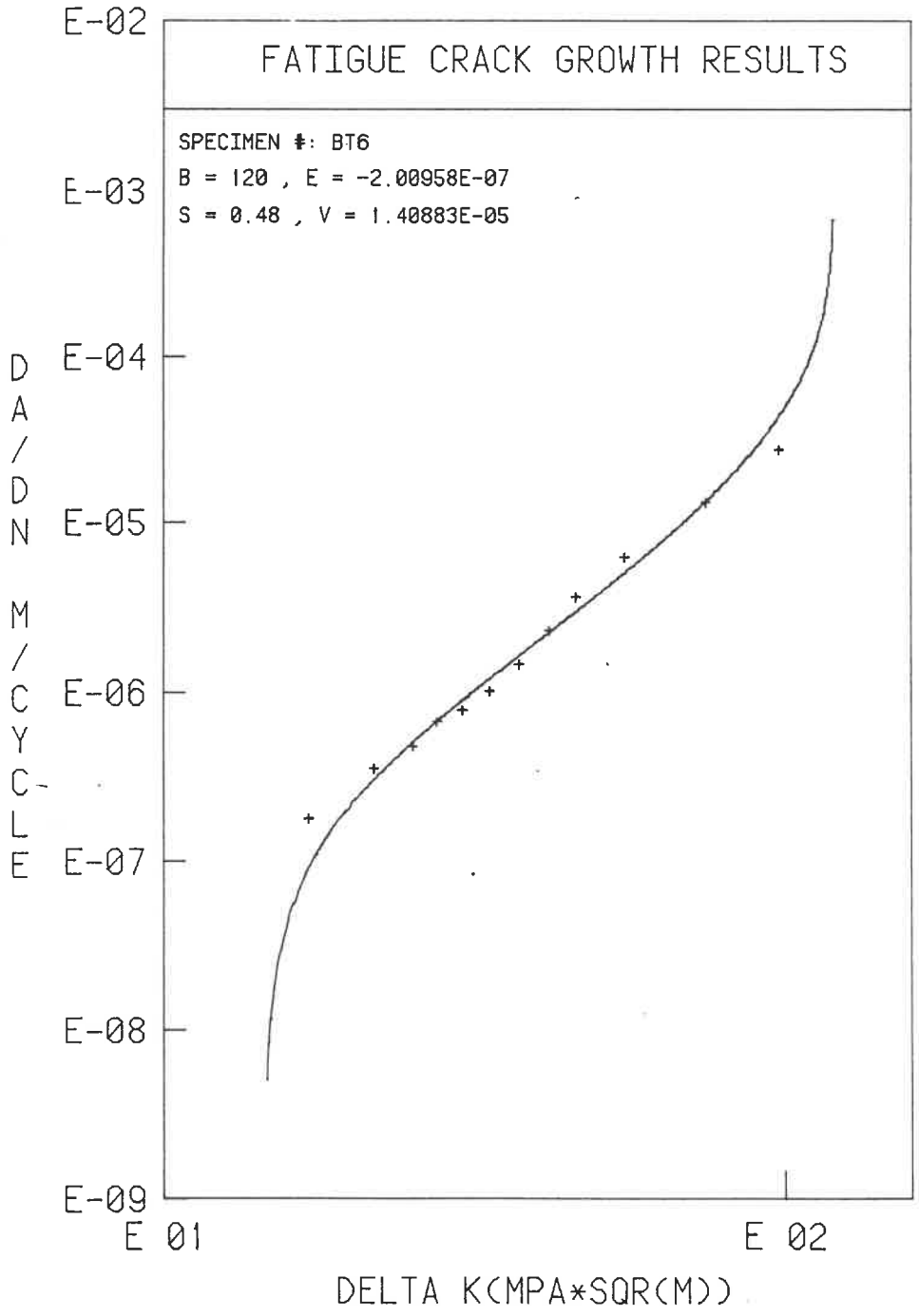

FIG. 5-26: FOUR PARAMETER WEIBULL CURVE FIT FOR SPECIMEN BT6

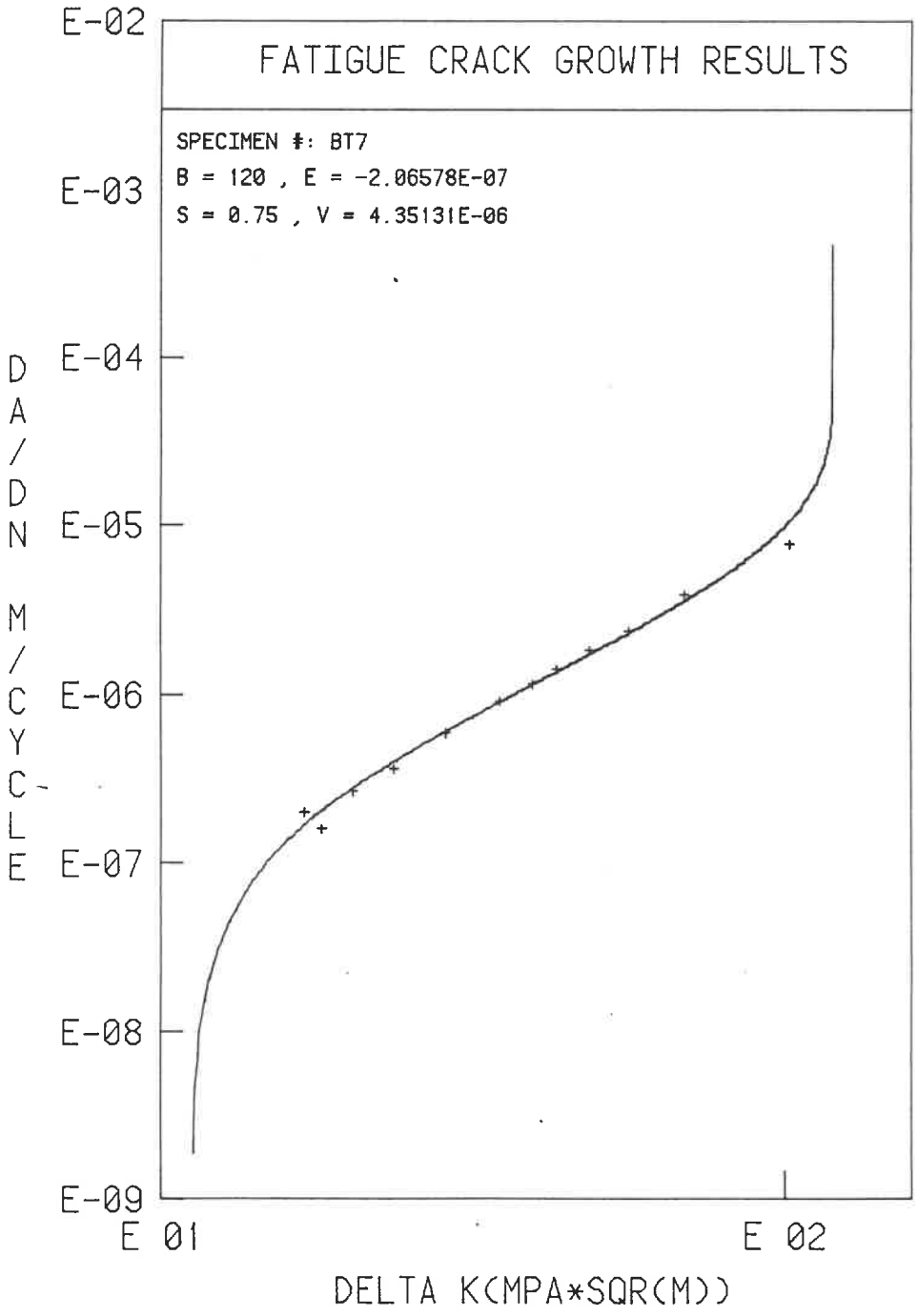

FIG. 5-27: FOUR PARAMETER WEIBULL CURVE FIT FOR SPECIMEN BT7

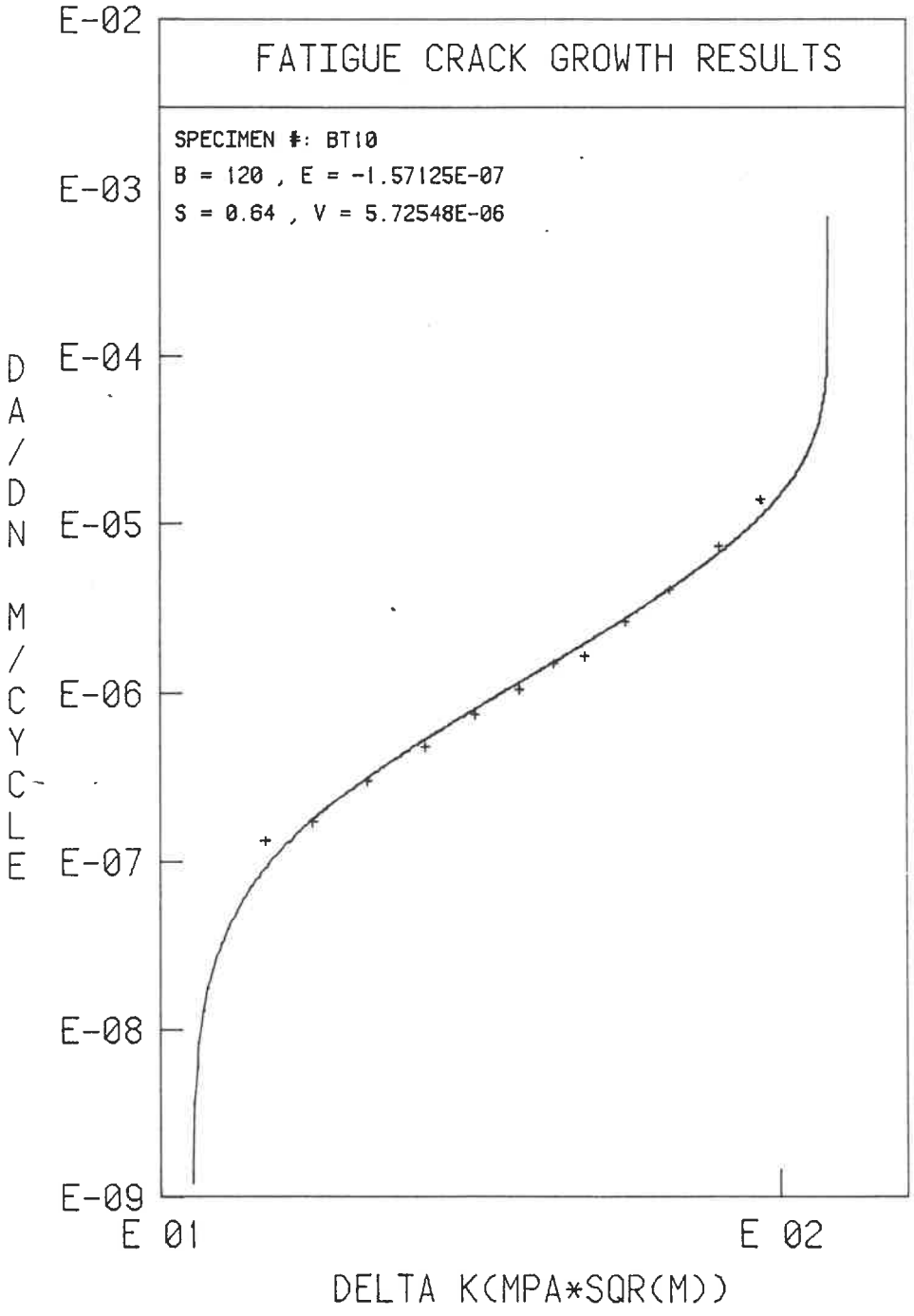

FIG. 5-28: FOUR PARAMETER WEIBULL CURVE FIT FOR SPECIMEN BT10

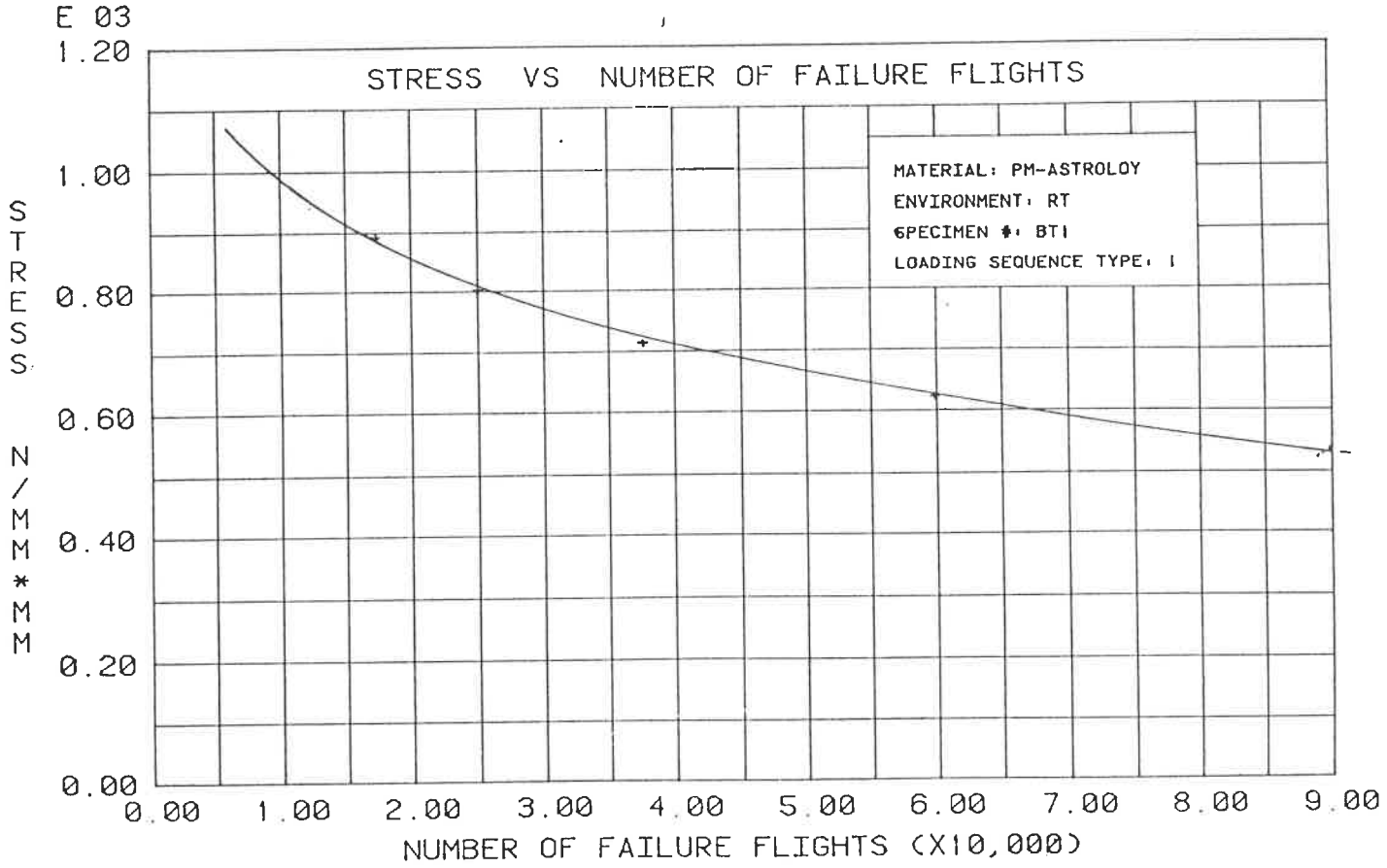

FIG. 5-29: APPLIED STRESS VS NUMBER OF FLIGHTS TO FAILURE FOR SPECIMEN BT1

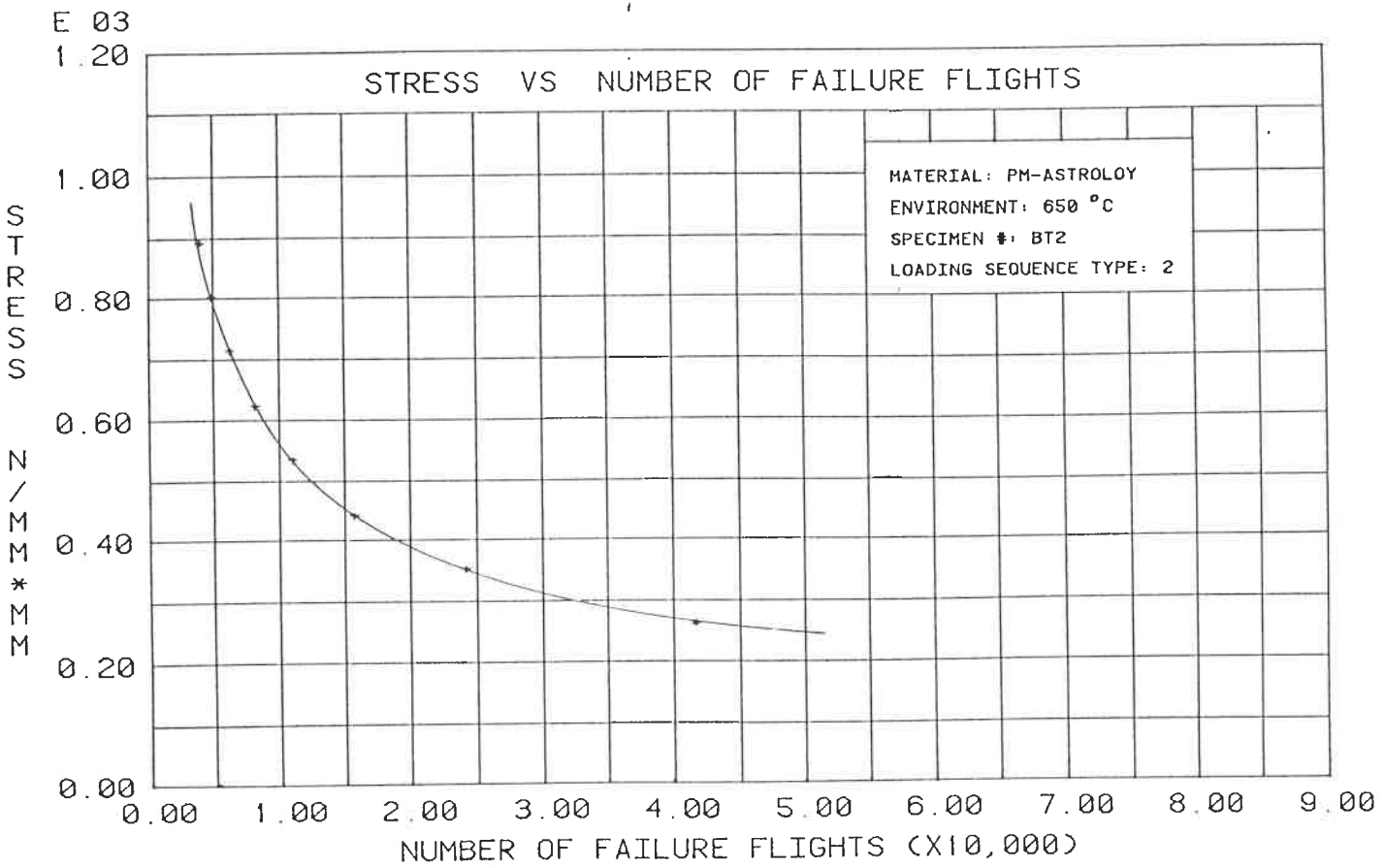

FIG. 5-30: APPLIED STRESS VS NUMBER OF FLIGHTS TO FAILURE FOR SPECIMEN BT2

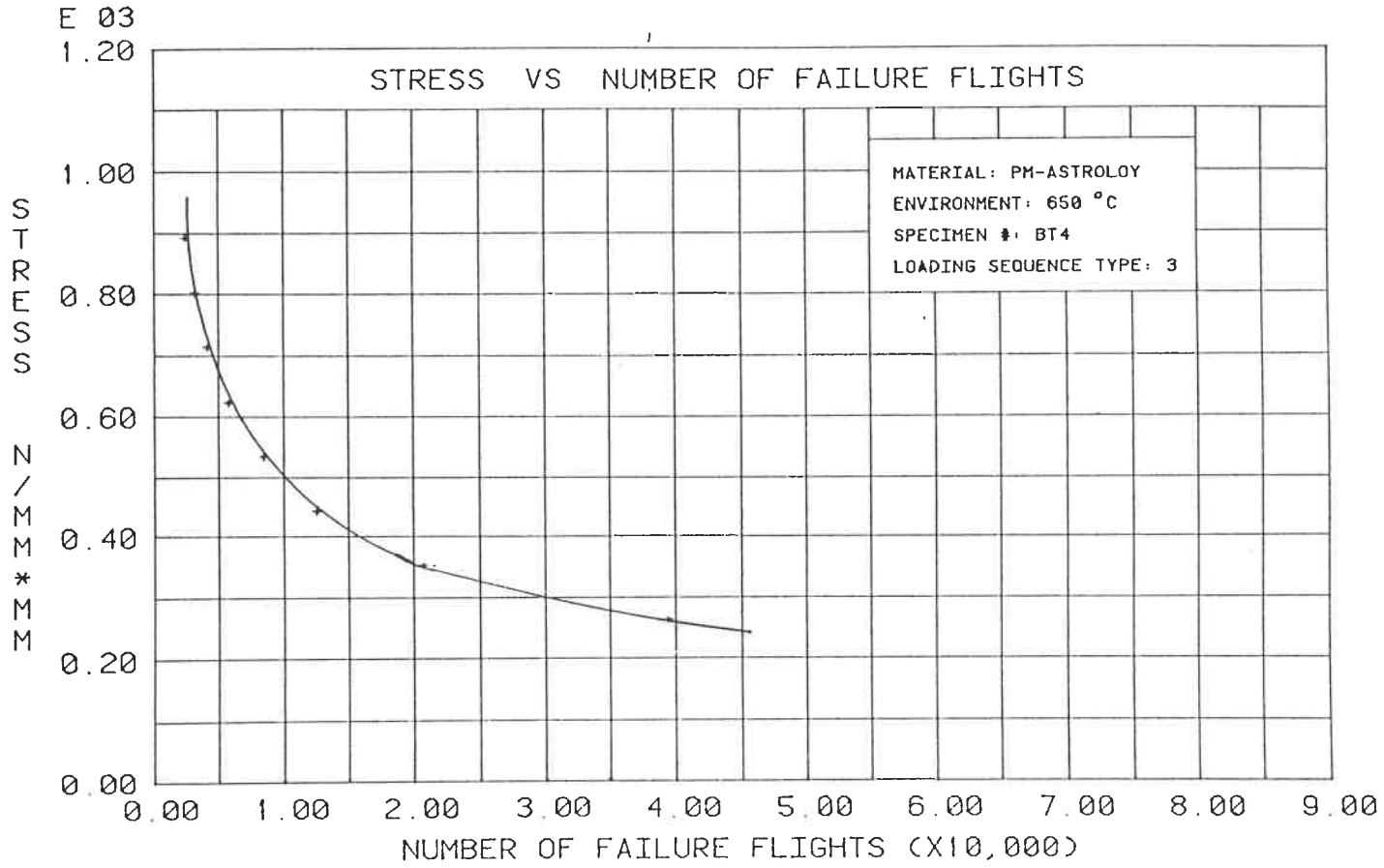

FIG. 5-31: APPLIED STRESS VS NUMBER OF FLIGHTS TO FAILURE FOR SPECIMEN BT4

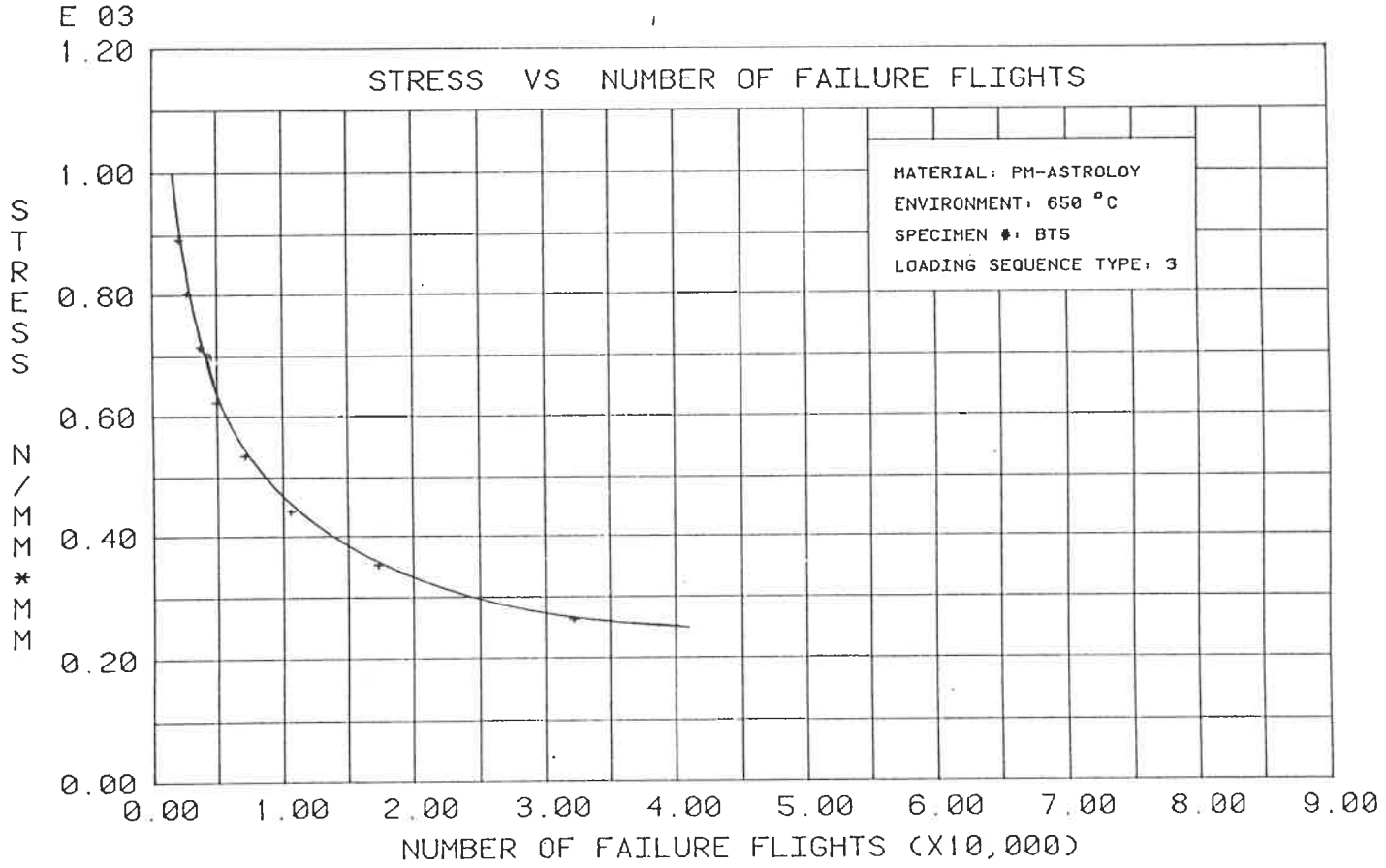

FIG. 5-32: APPLIED STRESS VS NUMBER OF FLIGHTS TO FAILURE FOR SPECIMEN BT5

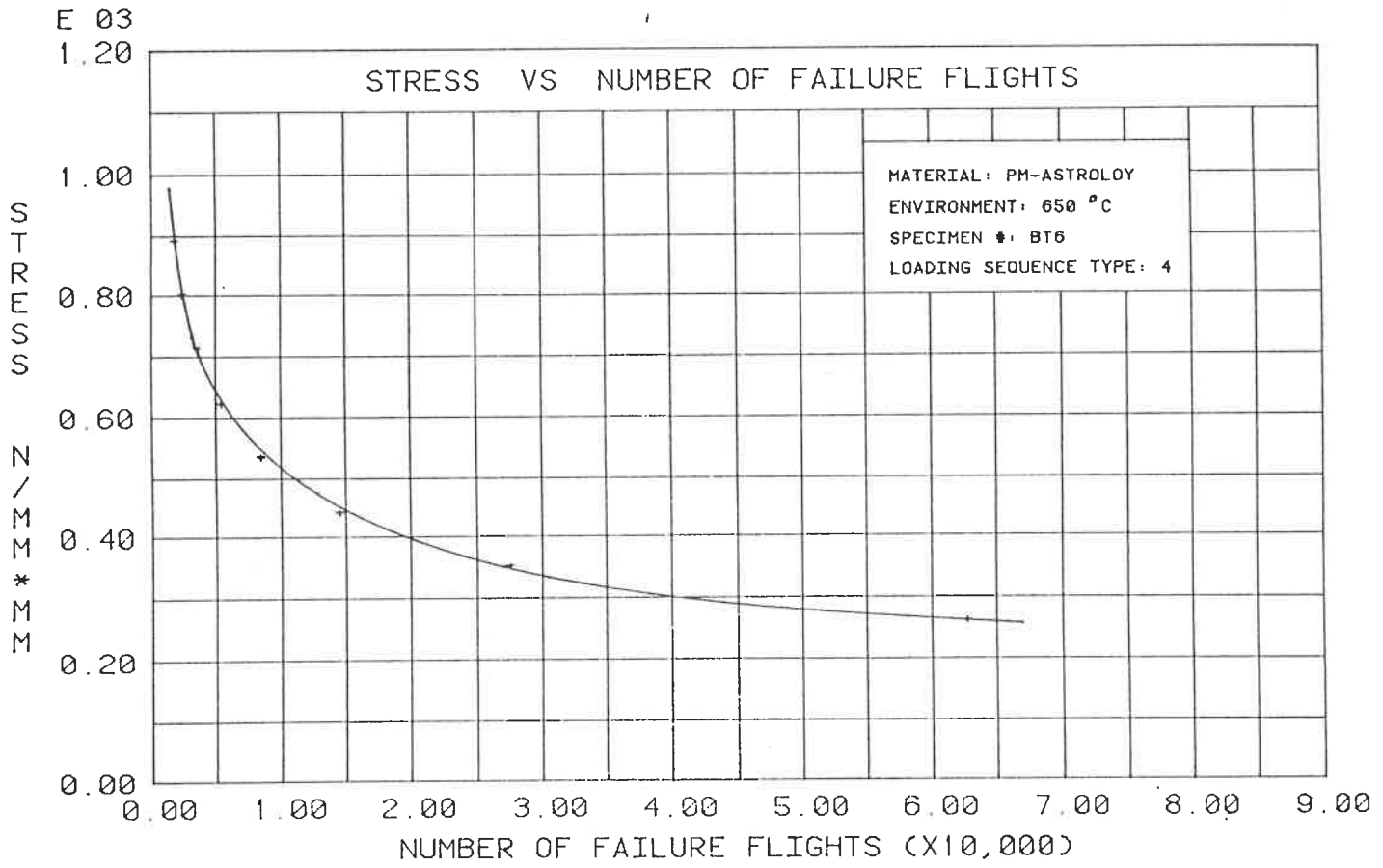

FIG. 5-33: APPLIED STRESS VS NUMBER OF FLIGHTS TO FAILURE FOR SPECIMEN BT6

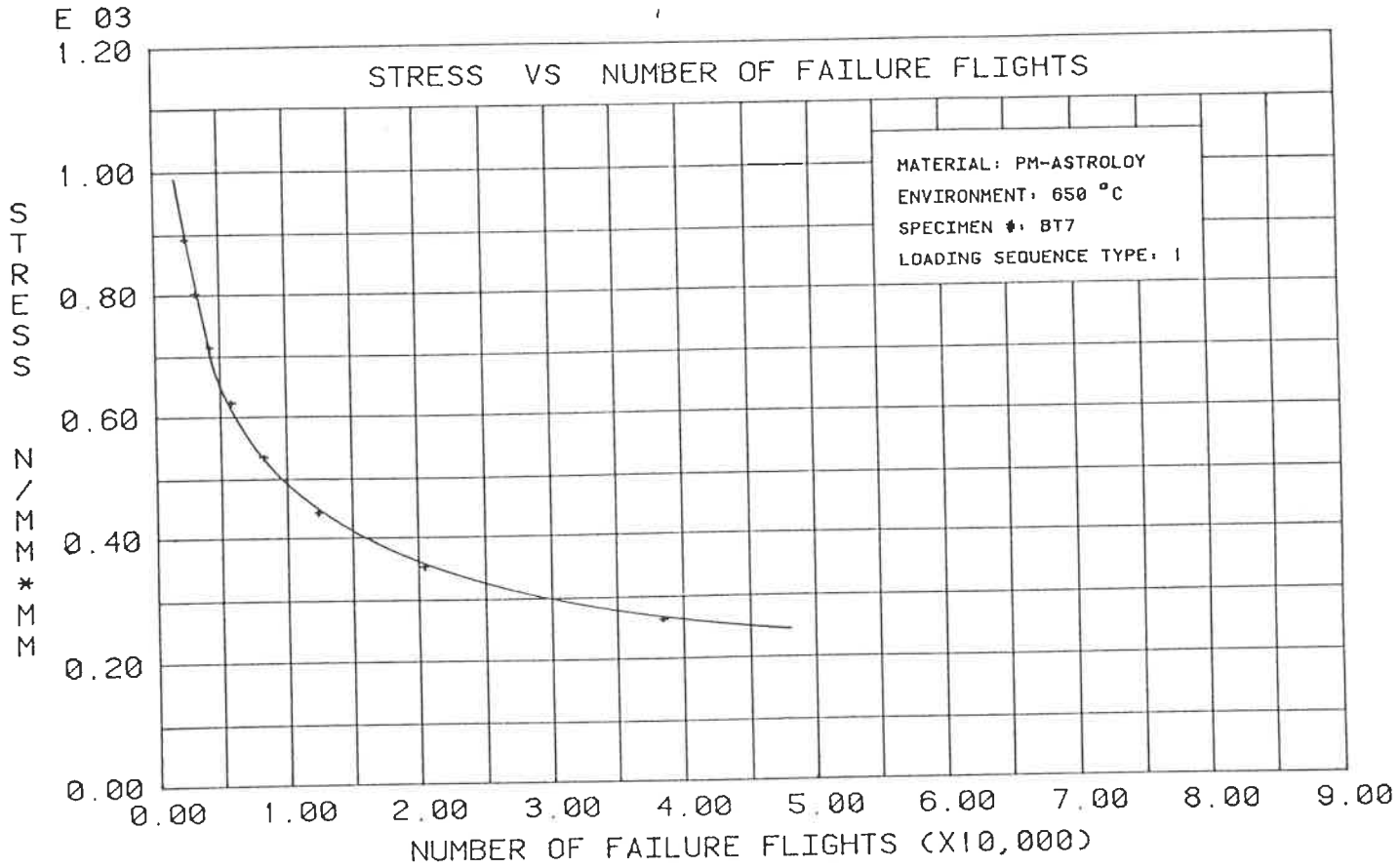

FIG. 5-34: APPLIED STRESS VS NUMBER OF FLIGHTS TO FAILURE FOR SPECIMEN BT7

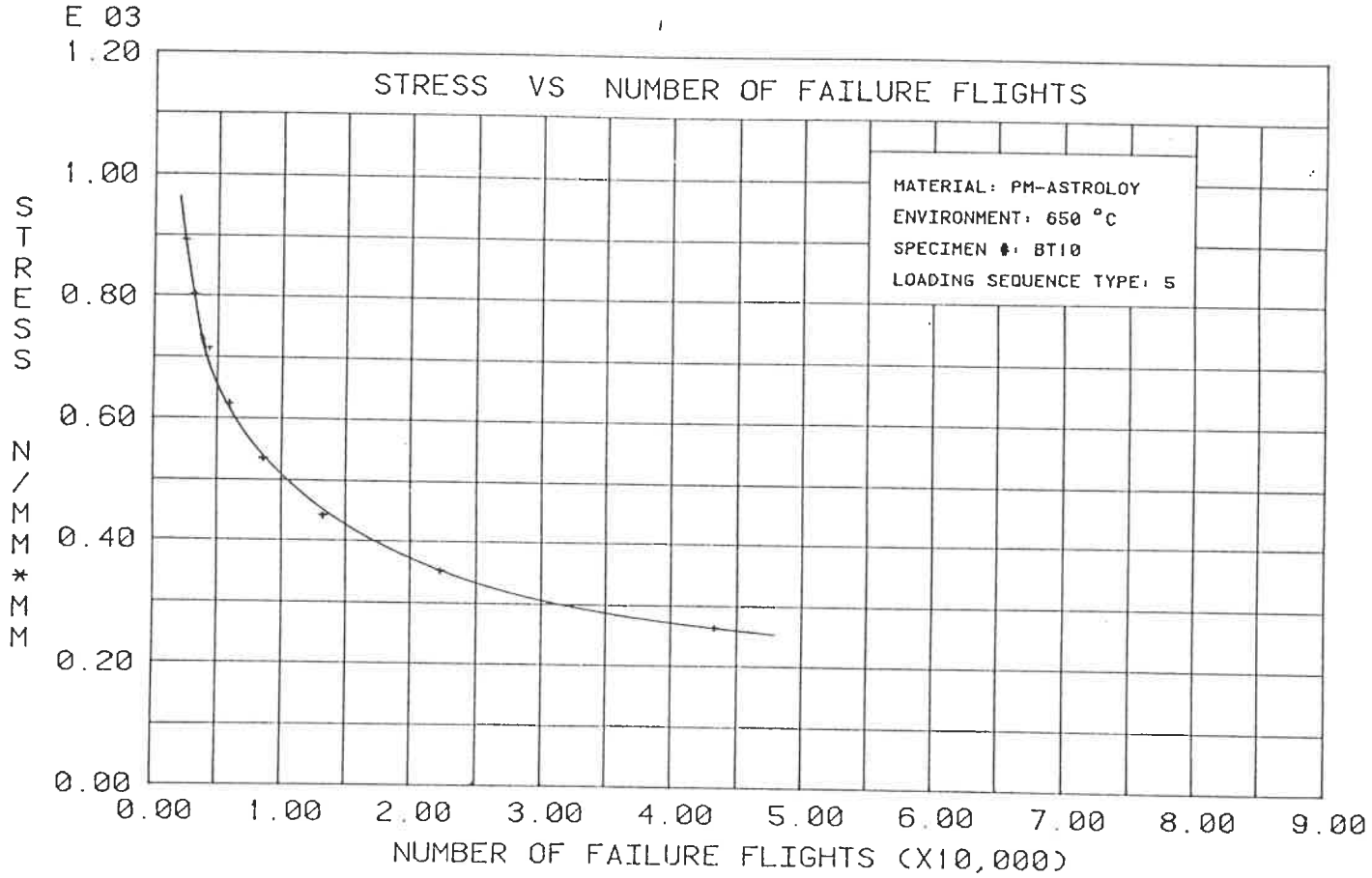

FIG. 5-35: APPLIED STRESS VS NUMBER OF FLIGHTS TO FAILURE FOR SPECIMEN BT10

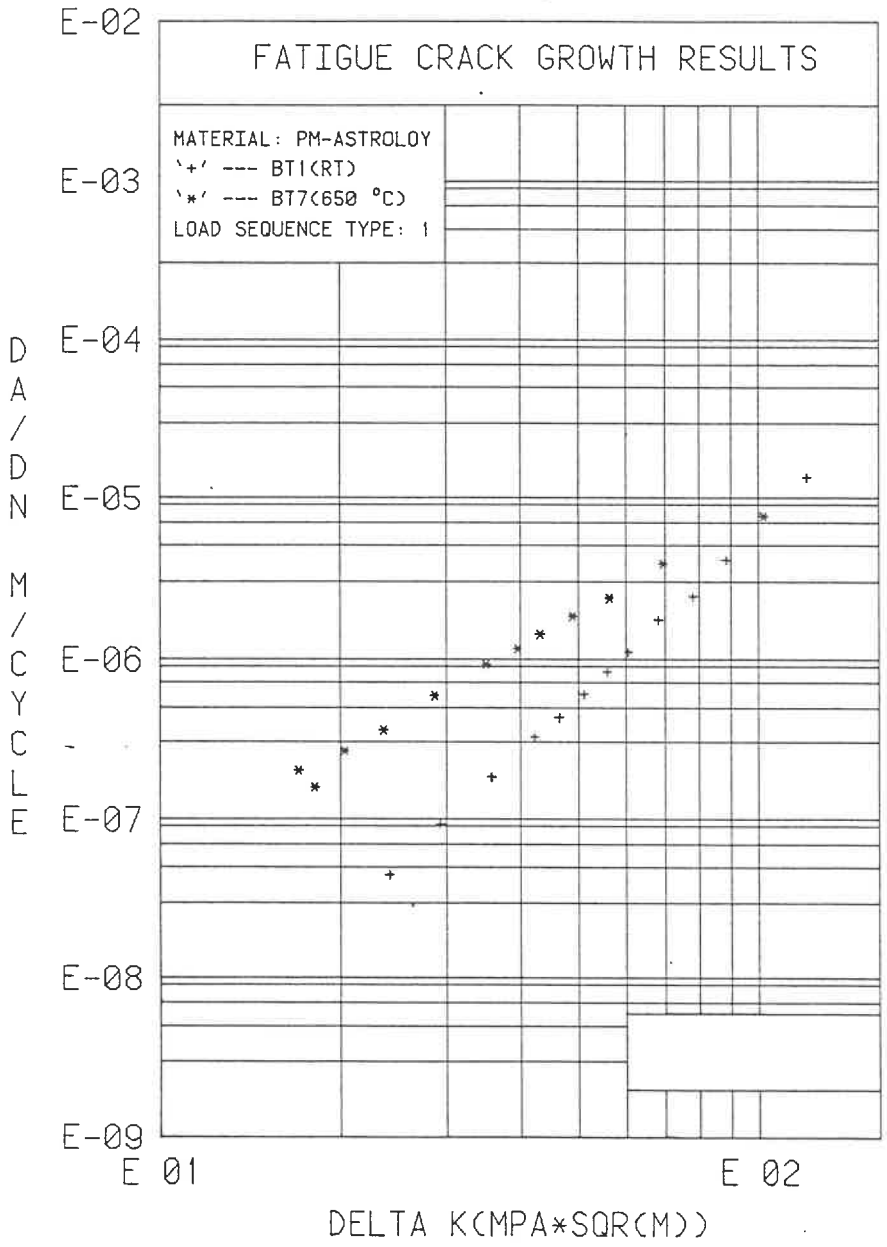

FIG. 5-36: TEMPERATURE EFFECTS ON FCPR

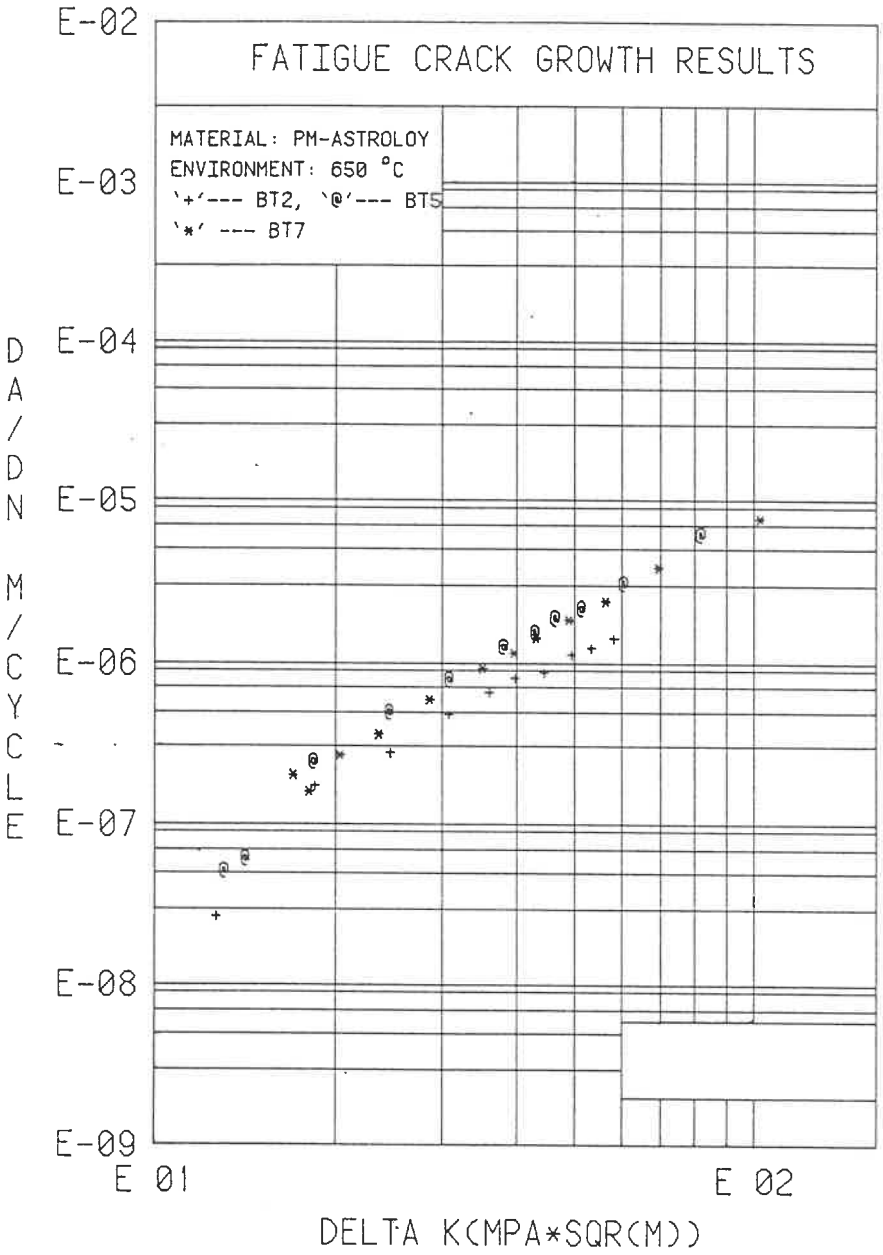

FIG. 5-37: HOLD TIME EFFECTS ON FCPR

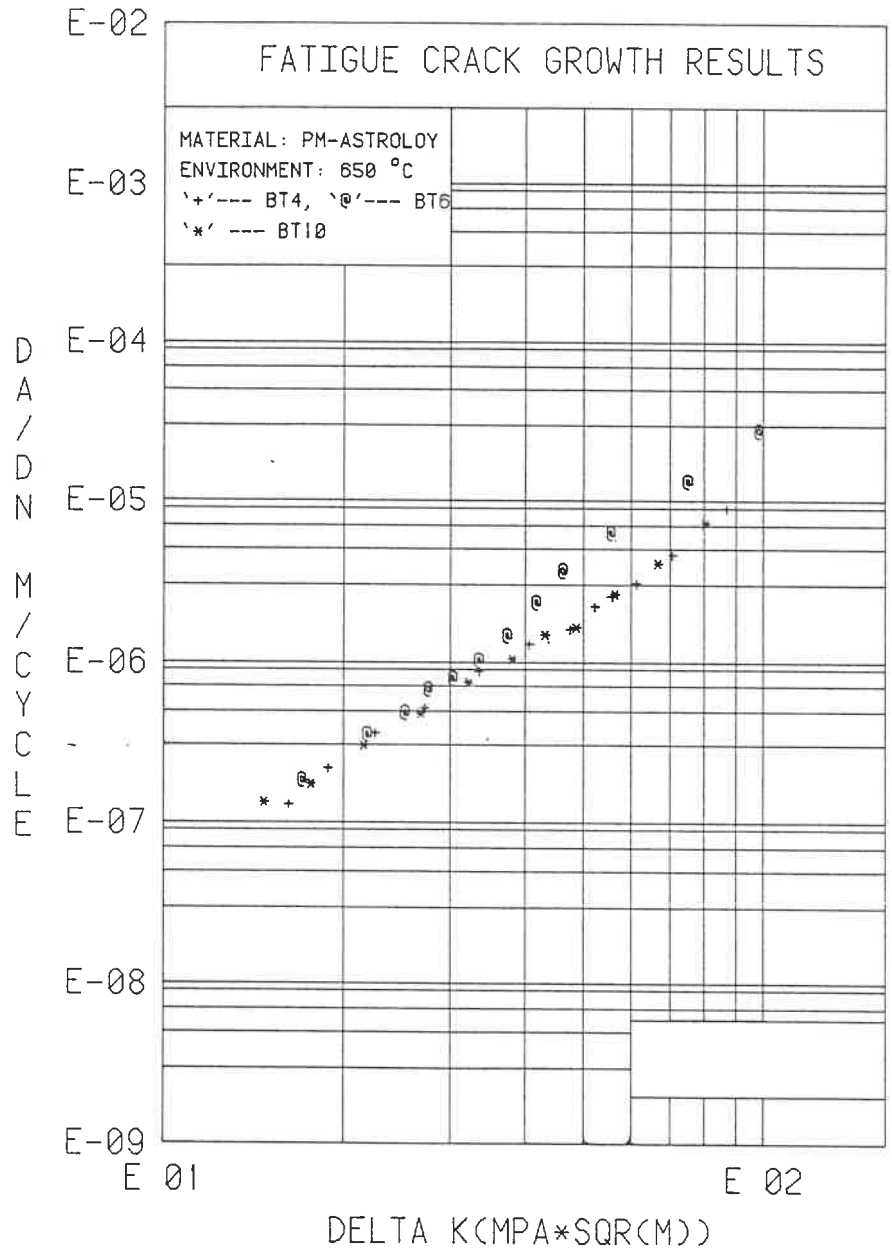

FIG. 5-38: MINOR CYCLE LOAD RATIO EFFECTS ON FCPR

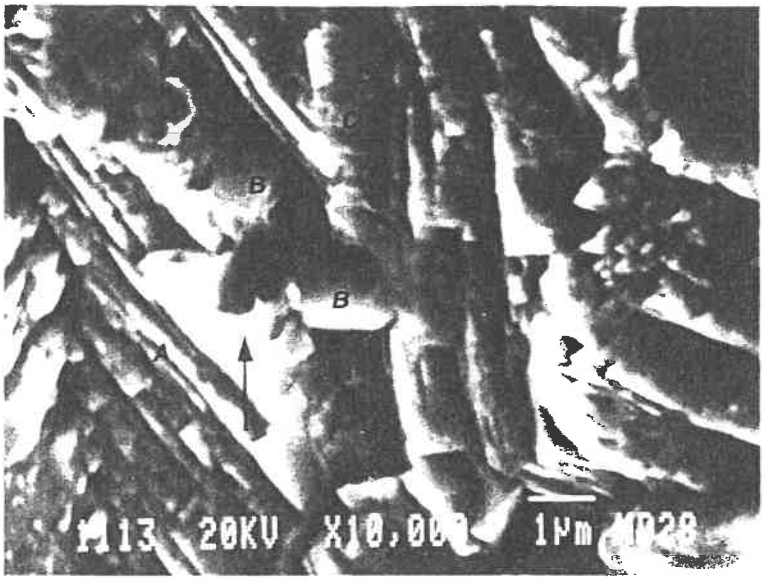

FIG. 5-39a: ROOM TEMPERATURE TEST, SPECIMEN BT1. $\Delta K = 12$ MPa$\sqrt{m}$, a = 0.2 mm. ARROWS INDICATE DIRECTION OF CRACK PROPAGATION. LINEAR AND PARALLEL RIDGES (A), FACETS (B), PLANAR MICROFACETS (C).

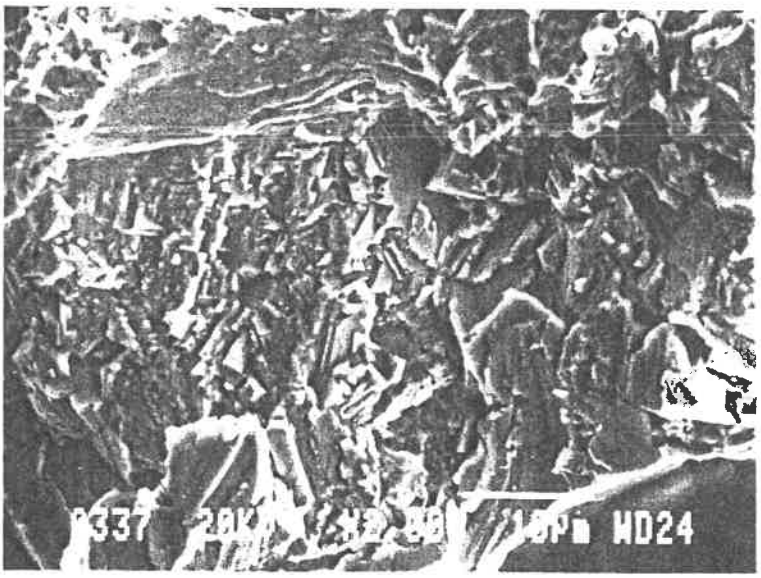

FIG. 5-39b: SAME AS FIGURE 5-39a. WITH LOWER MAGNIFICATION TRANSGRANULAR CRACKING IN LARGE AND SMALL GRAINS.

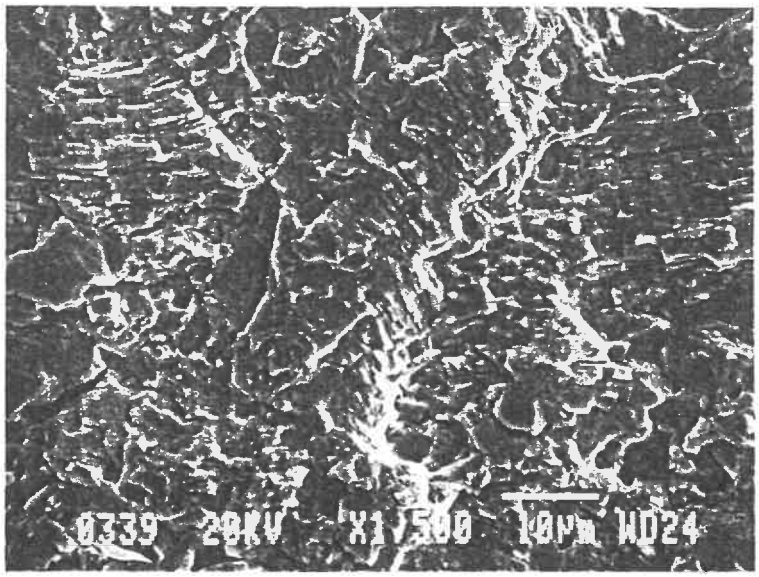

FIG. 5-39c: $\Delta K = 35.5\ MPa\sqrt{m}$, a = 1.2 mm. CRYSTALLOGRAPHIC STRIATIONS CHANGE ORIENTATION FROM GRAIN TO GRAIN

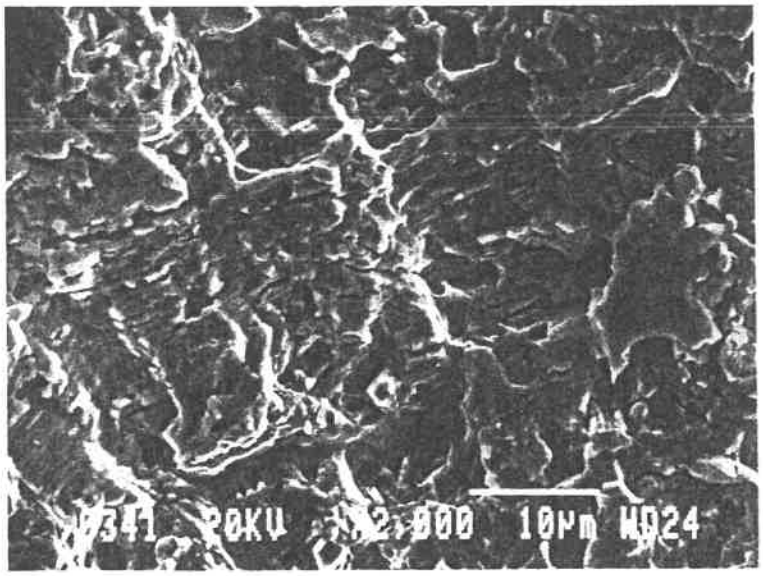

FIG. 5-39d: $\Delta K = 46.5\ MPa\sqrt{m}$, a = 1.8 mm. NON-CRYSTALLOGRAPHIC STRIATIONS WITH TRANSGRANULAR FEATURES

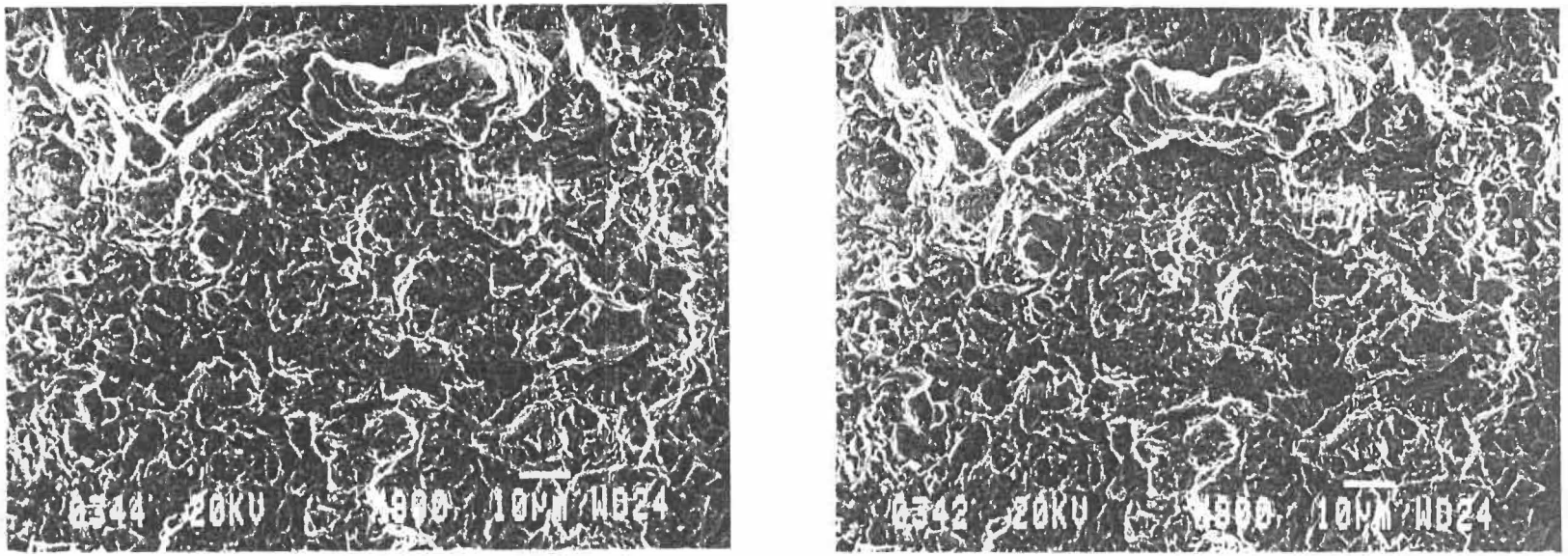

FIG. 5-39e: STEREOGRAPHIC PAIR WITH 6° DIFFERENCE IN VIEWING ANGLE. ΔK = 89 MPa$\sqrt{m}$, a = 3.9 mm. BLUNTING LINES (A)

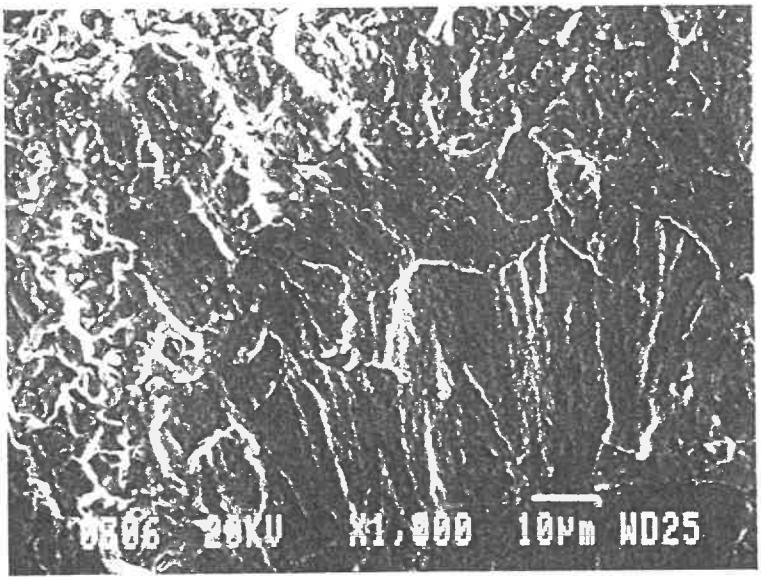

FIG. 5-40a: HIGH TEMPERATURE TEST. SPECIMEN BT4. ΔK = 13 MPa$\sqrt{m}$, a = 0.2 mm. SERRATED RIVER LINES IN LARGE AND SMALL GRAINS

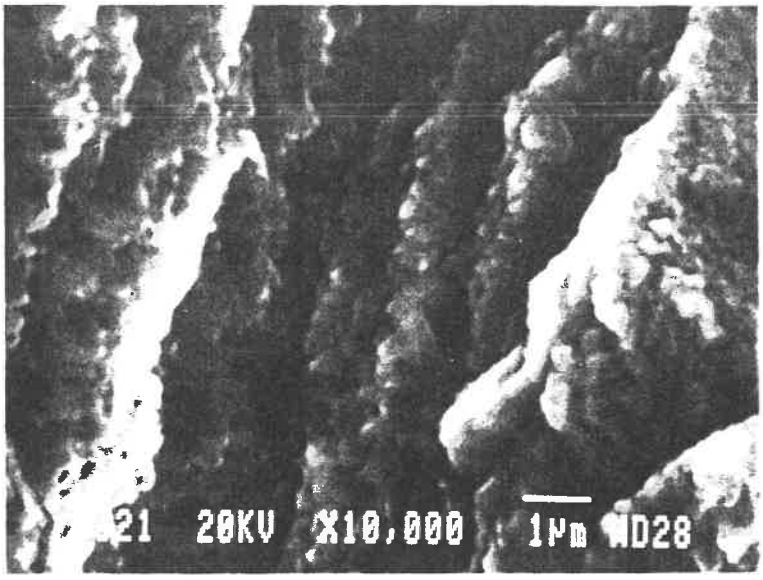

FIG. 5-40b: SAME AS FIGURE 5-40a. HIGH MAGNIFICATION IN LARGE GRAIN. MICROFACETS WITH CRYSTALLOGRAPHIC STRIATION-LIKE FEATURES AND RIVER LINES.

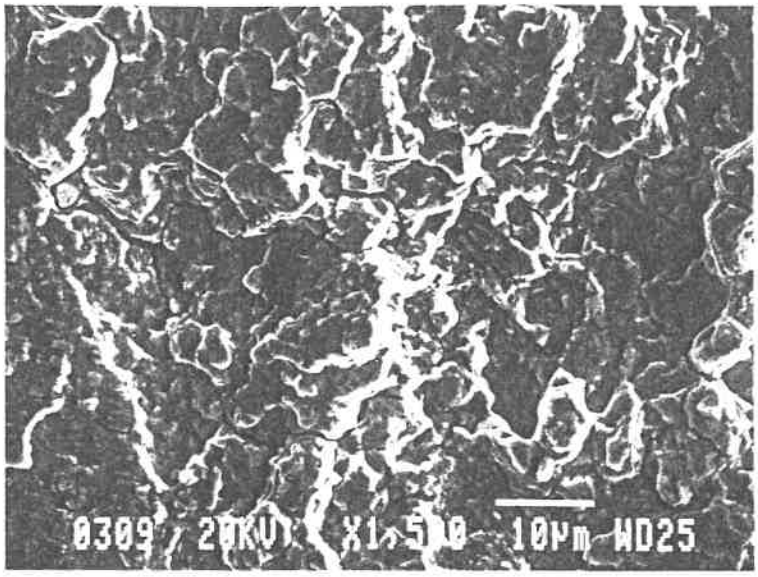

FIG. 5-40c: SAME AS FIGURE 5-40a. INTERGRANULAR CRACKING AND SECONDARY CRACKS OCCUR AT THE GRAIN BOUNDARY REGIONS.

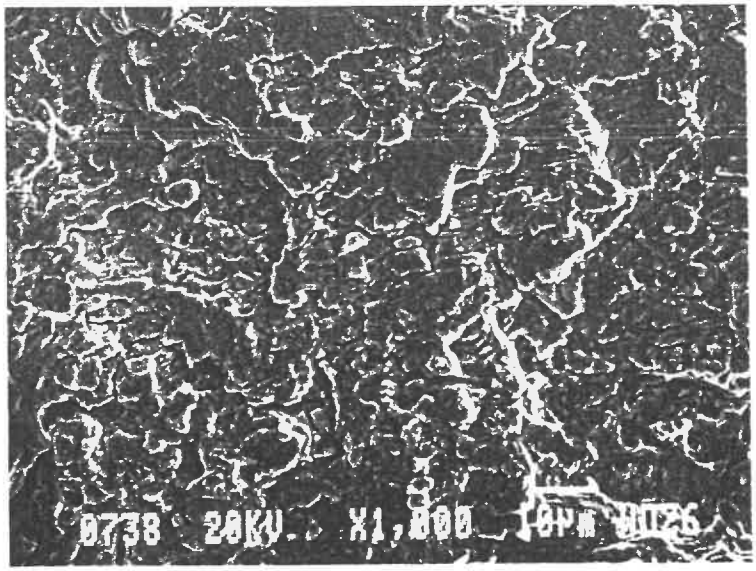

FIG. 5-40d: $\Delta K = 50\ MPa\sqrt{m}$, a = 2.2 mm. FATIGUE STRIATIONS IN LARGE GRAIN.

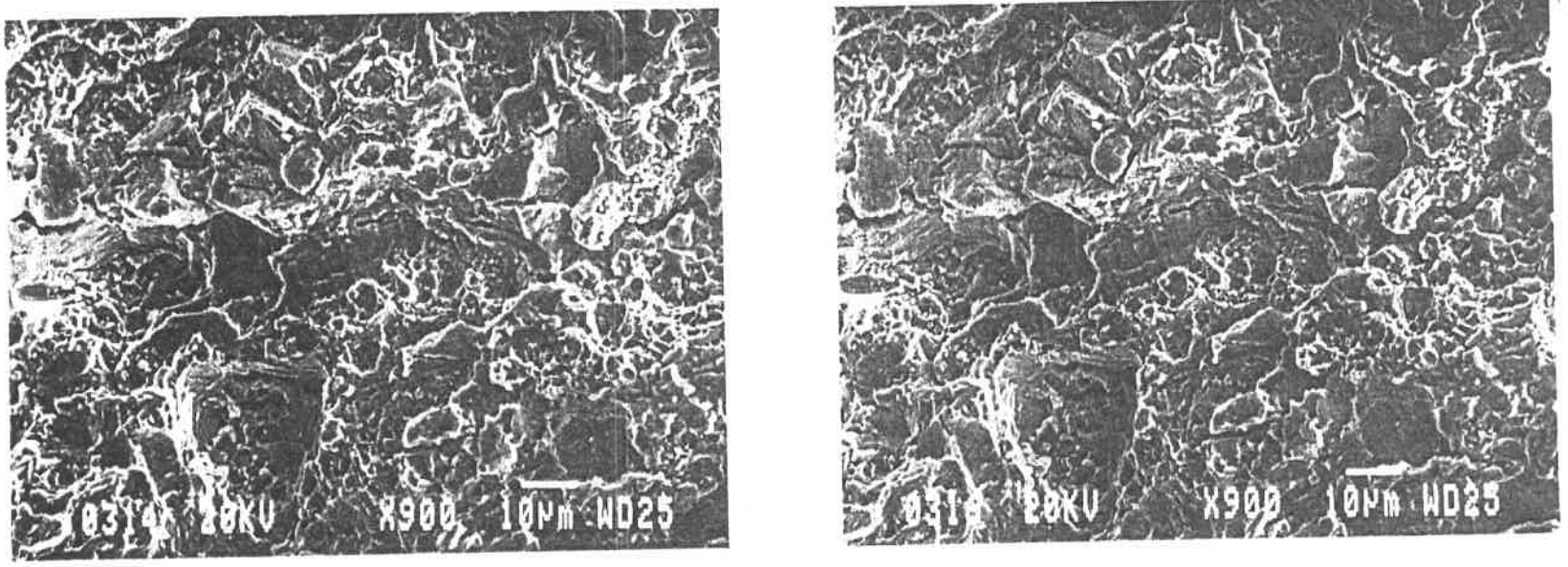

FIG. 5-40e: STEREOGRAPHIC PAIR. $\Delta K = 99.5\ MPa\sqrt{m}$, a = 4.5 mm, BLUNTING LINES WHICH START AND STOP AT THE BANDS OF DIMPLES.

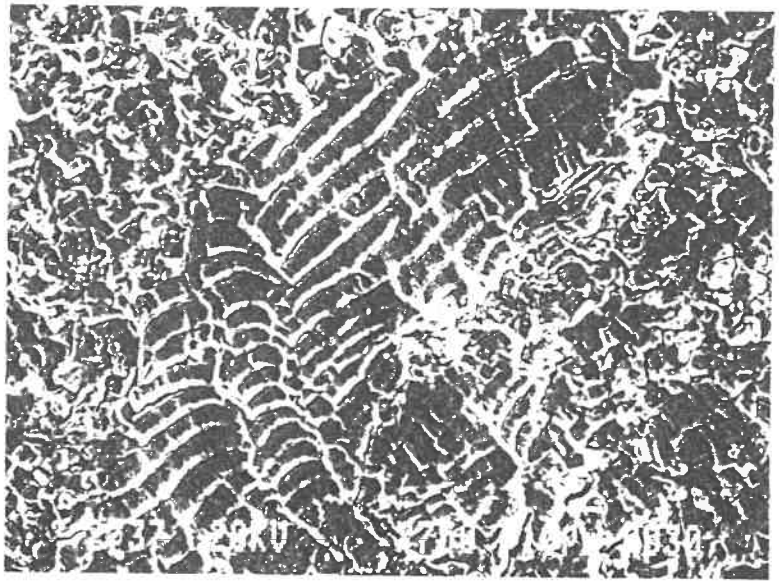

FIG. 5-41a: HIGH TEMPERATURE WITH 0.1 MINOR CYCLE. SPECIMEN BT6. $\Delta K = 56\ MPa\sqrt{m}$, a = 2.6 mm, MAJOR CYCLE FATIGUE STRIATIONS IN THE LARGE GRAINS WHICH ARE NOT AS CLEAR IN THE SMALL GRAINS

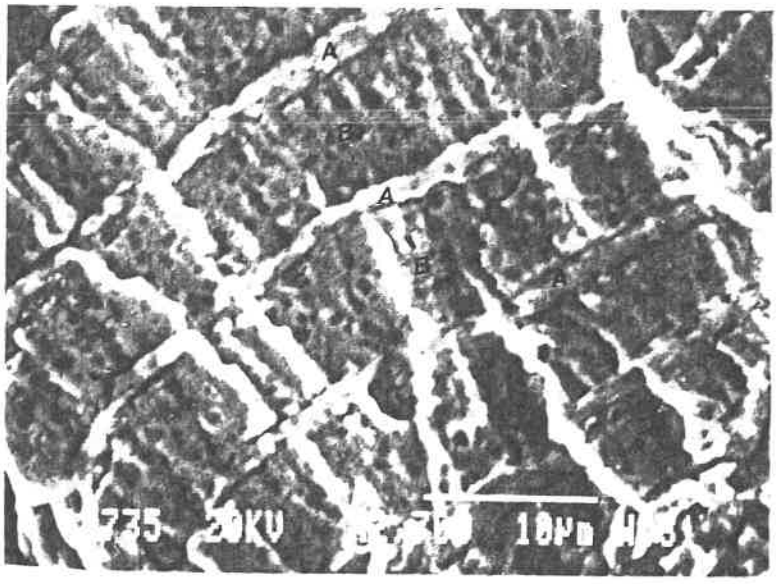

FIG. 5-41b: HIGH MAGNIFICATION IN LARGE GRAIN. MAJOR AND MINOR CYCLE PORTIONS (A AND B). HIGHER MAJOR CYCLE STRIATIONS

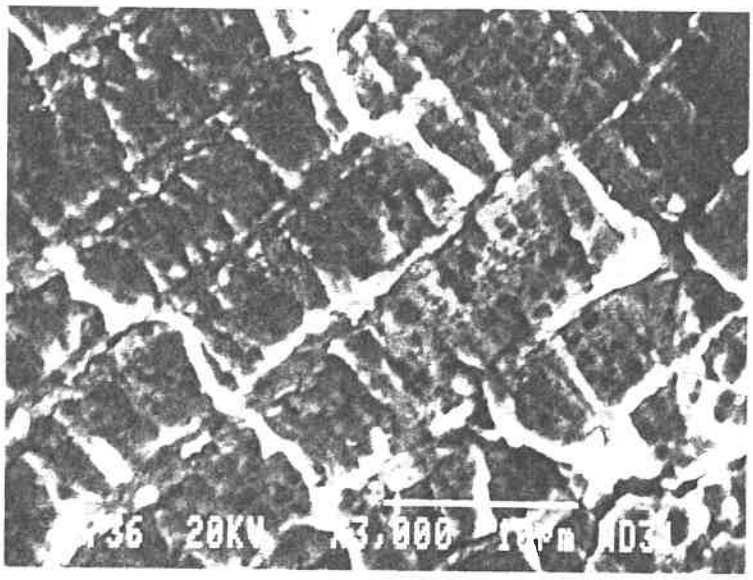

FIG. 5-41c: LOWER MAJOR CYCLE STRIATIONS

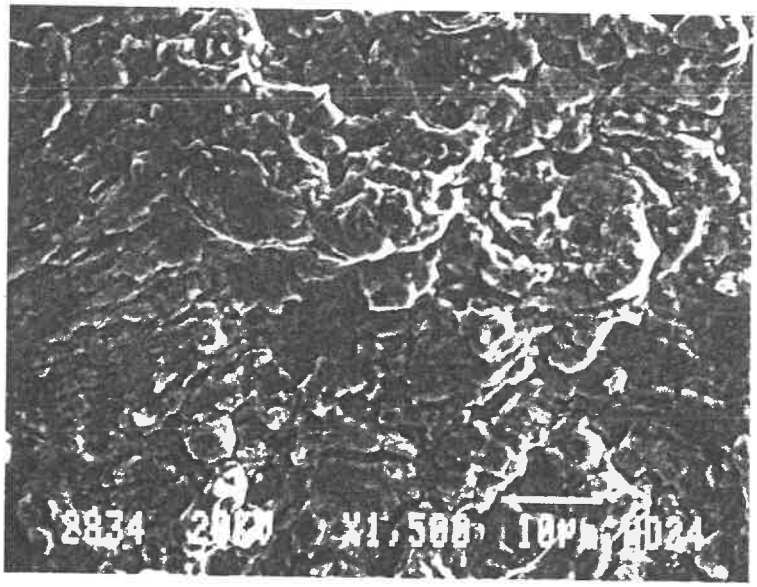

FIG. 5-42: FATIGUE STRIATIONS FOR 0.05 MINOR CYCLE. SPECIMEN BT10. NO MINOR CYCLE PROPAGATION VISIBLE.

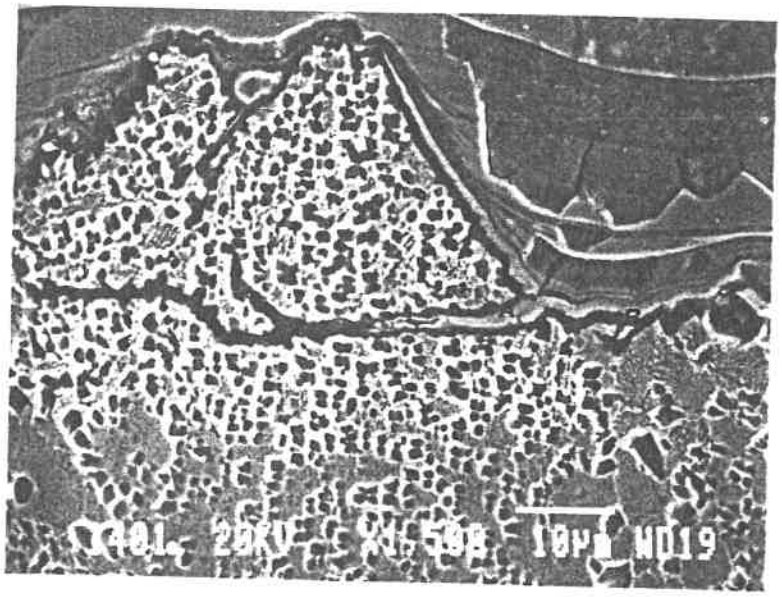

FIG. 5-43a: CRACK SURFACE PROFILE DURING ROOM TEMPERATURE FATIGUE TEST. TRANSGRANULAR SECONDARY CRACKS IN LARGE GRAINS (A) AND INTERGRANULAR SECONDARY CRACKS IN SMALL GRAINS (B).

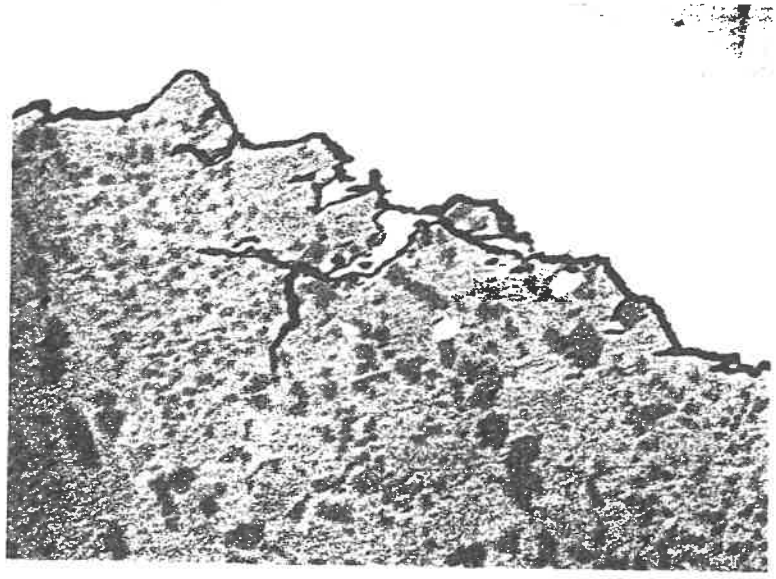

FIG. 5-43b: HIGH TEMPERATURE TEST

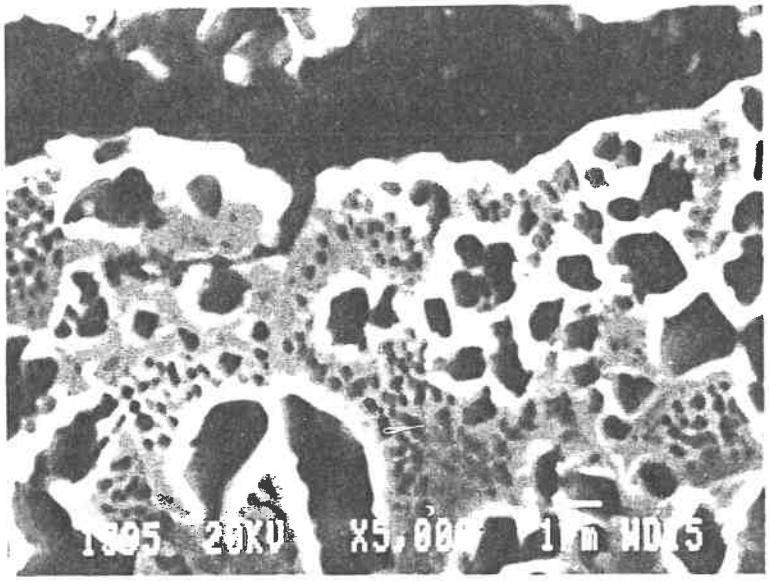

FIG. 5-43c: HIGH MAGNIFICATION IN SMALL GRAINS. SECONDARY CRACK FOLLOWING A GRAIN BOUNDARY (B)

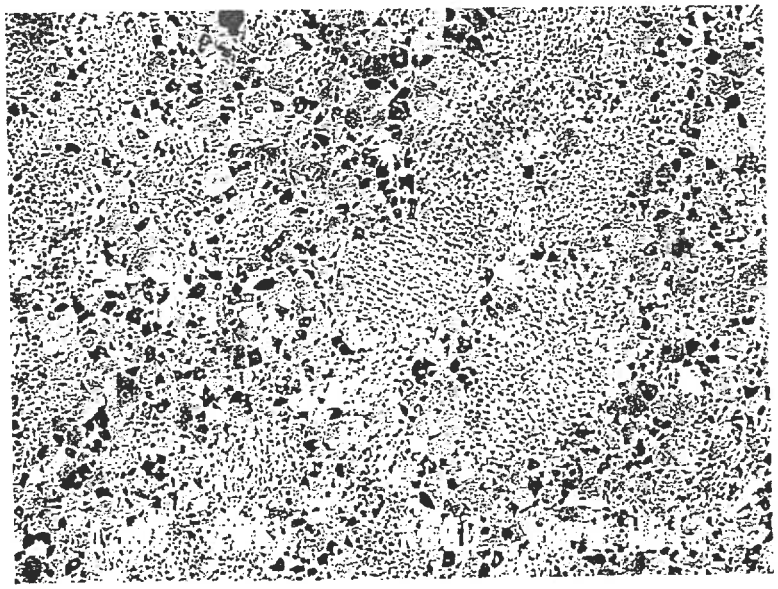

FIG. 5-44: MICROSTRUCTURE FOR THE TEST MATERIAL. DUPLEX (OR NECKLACE) STRUCTURE WITH LARGE GRAINS SURROUNDED BY SMALL GRAINS

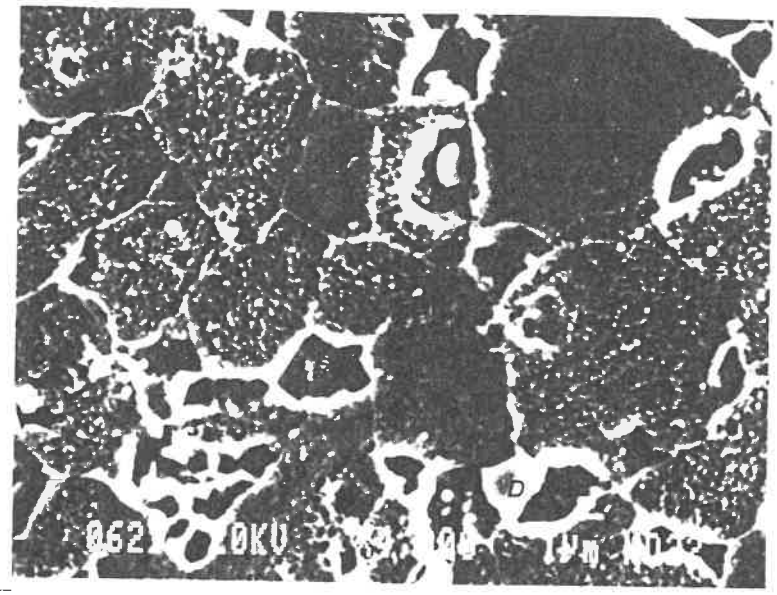

FIG. 5-45a: MICROSTRUCTURE OF AS RECEIVED MATERIAL WITH SOME WAVY GRAIN BOUNDARIES (A) AND COARSE γ' PRECIPITATES (B) AT GRAIN BOUNDARIES ANDTRIPLE POINTS. FINE γ' PRECIPITATES WITHIN GRAINS (C) AND CARBIDES AT GRAIN BOUNDARIES AND WITHIN GRAINS (D AND E).

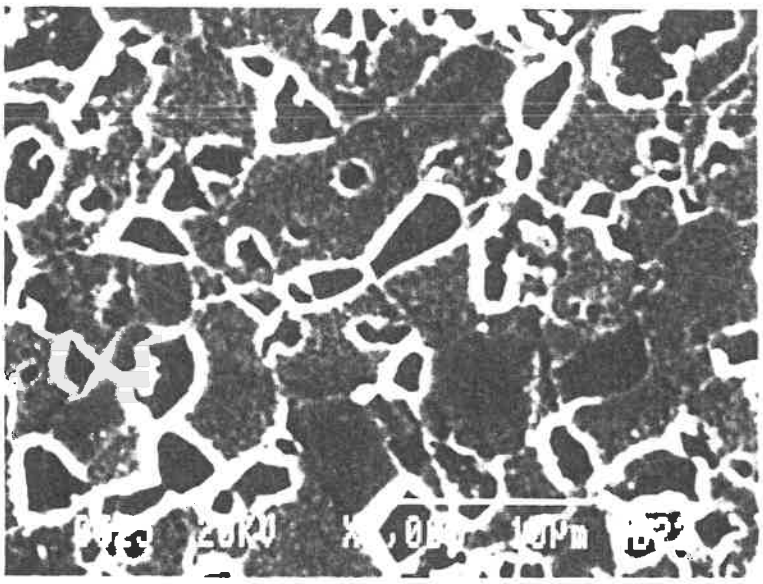

FIG. 5-45b: AFTER ROOM TEMPERATURE TEST

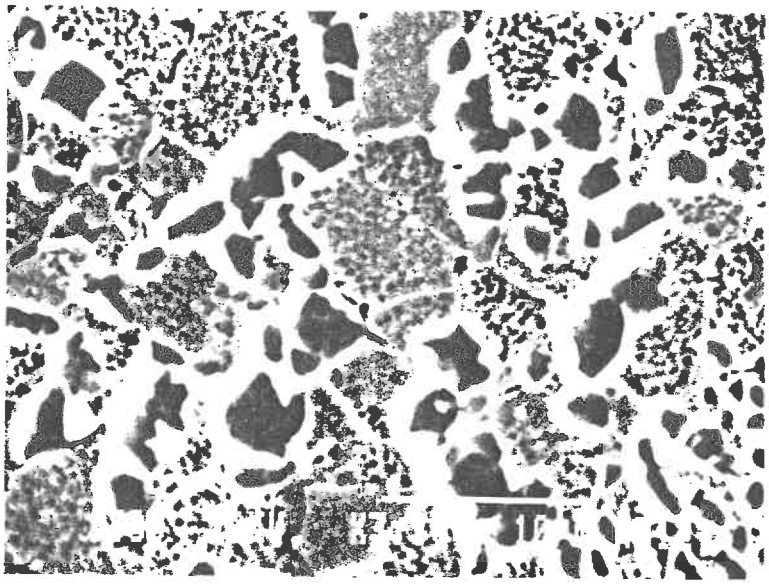

FIG. 5-45c: AFTER HIGH TEMPERATURE TEST

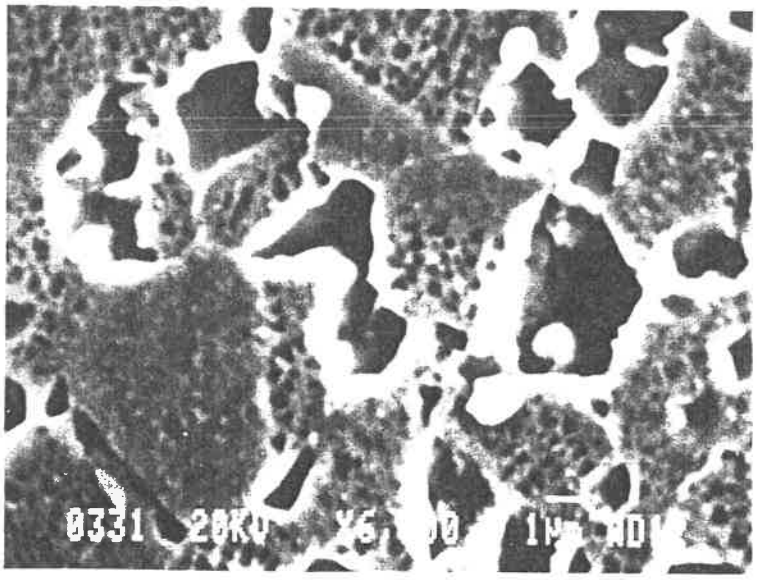

FIG. 5-45d: TWIN GRAIN BOUNDARIES AT HIGH MAGNIFICATION

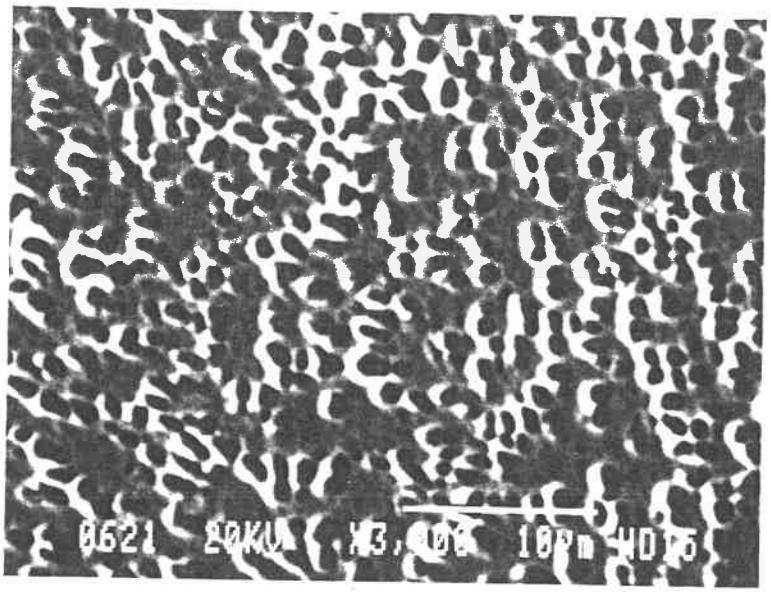

FIG. 5-45e: INTERMEDIATE SIZE OF γ' PRECIPITATES IN LARGE GRAIN

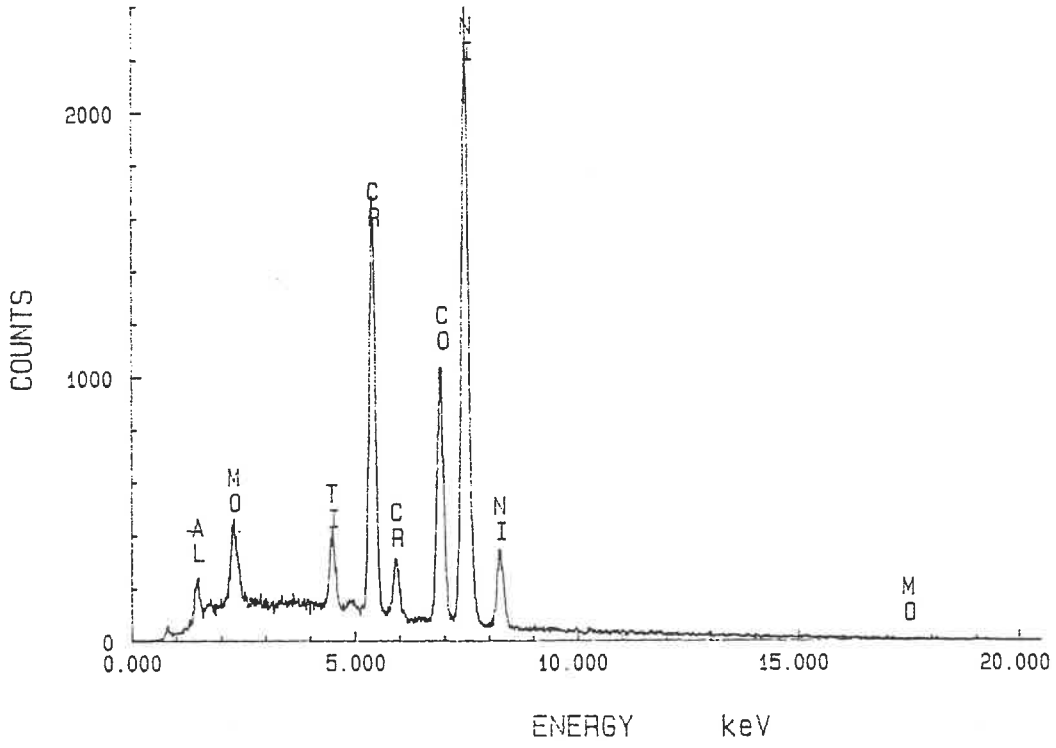

FIG. 5-46: SPECTRA FROM EDS ANALYSIS FOR MATRIX (γ)

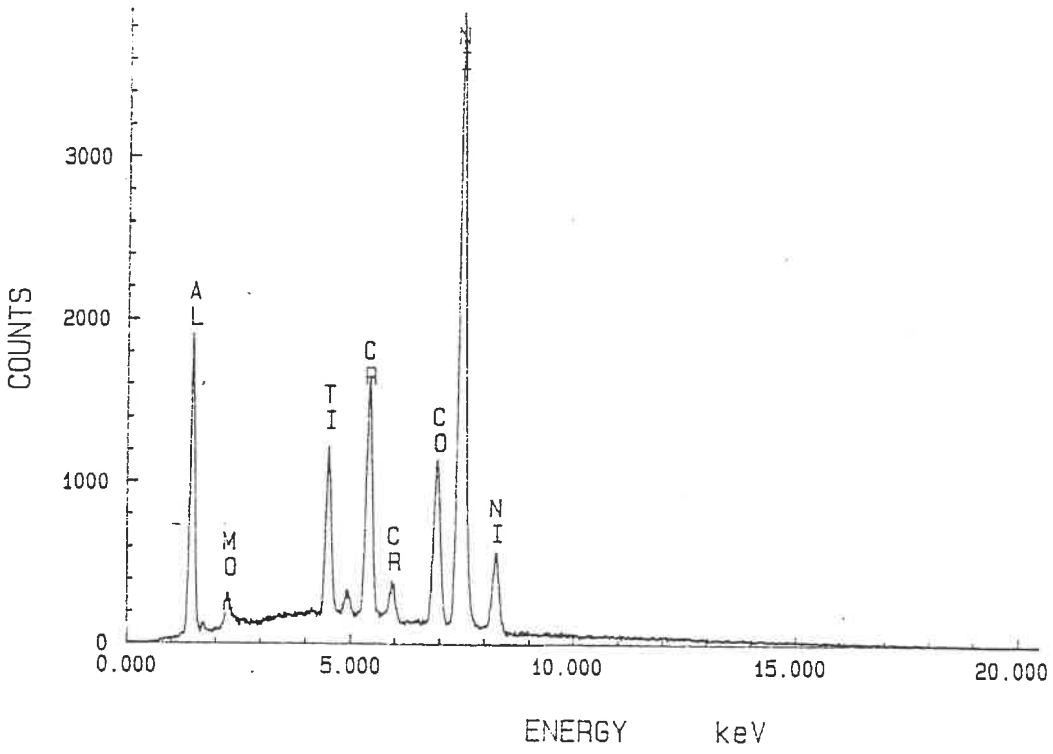

FIG. 5-47: SPECTRA FROM EDS ANALYSIS FOR γ' PRECIPITATES

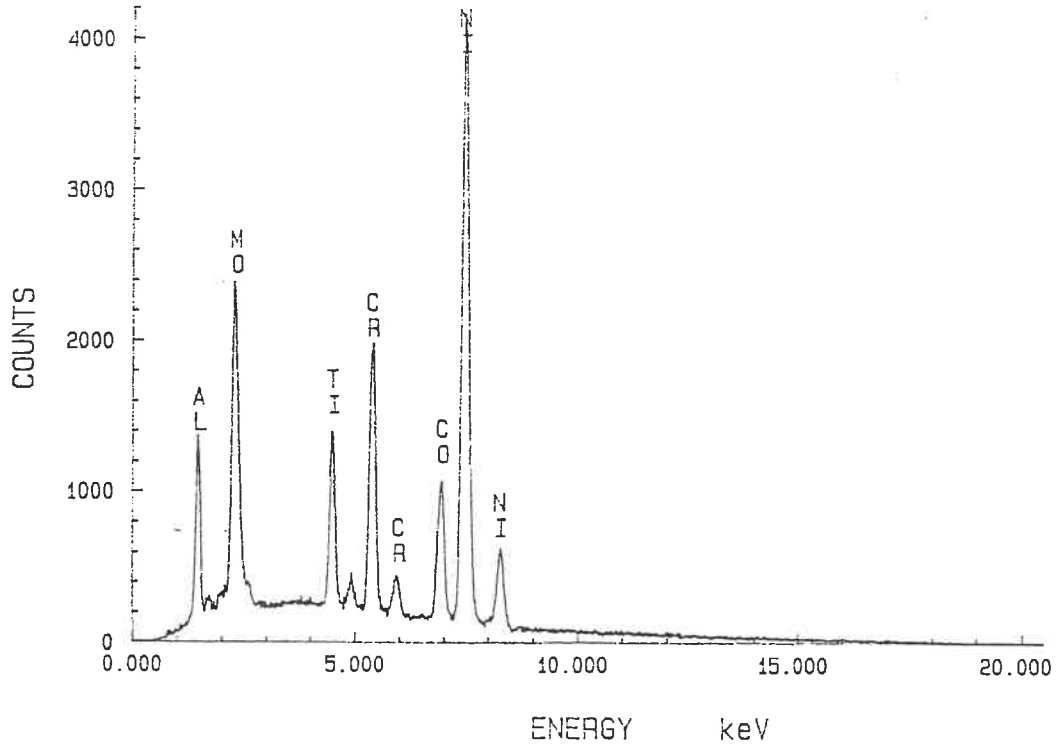

FIG. 5-48: SPECTRA FROM EDS ANALYSIS FOR CARBIDES

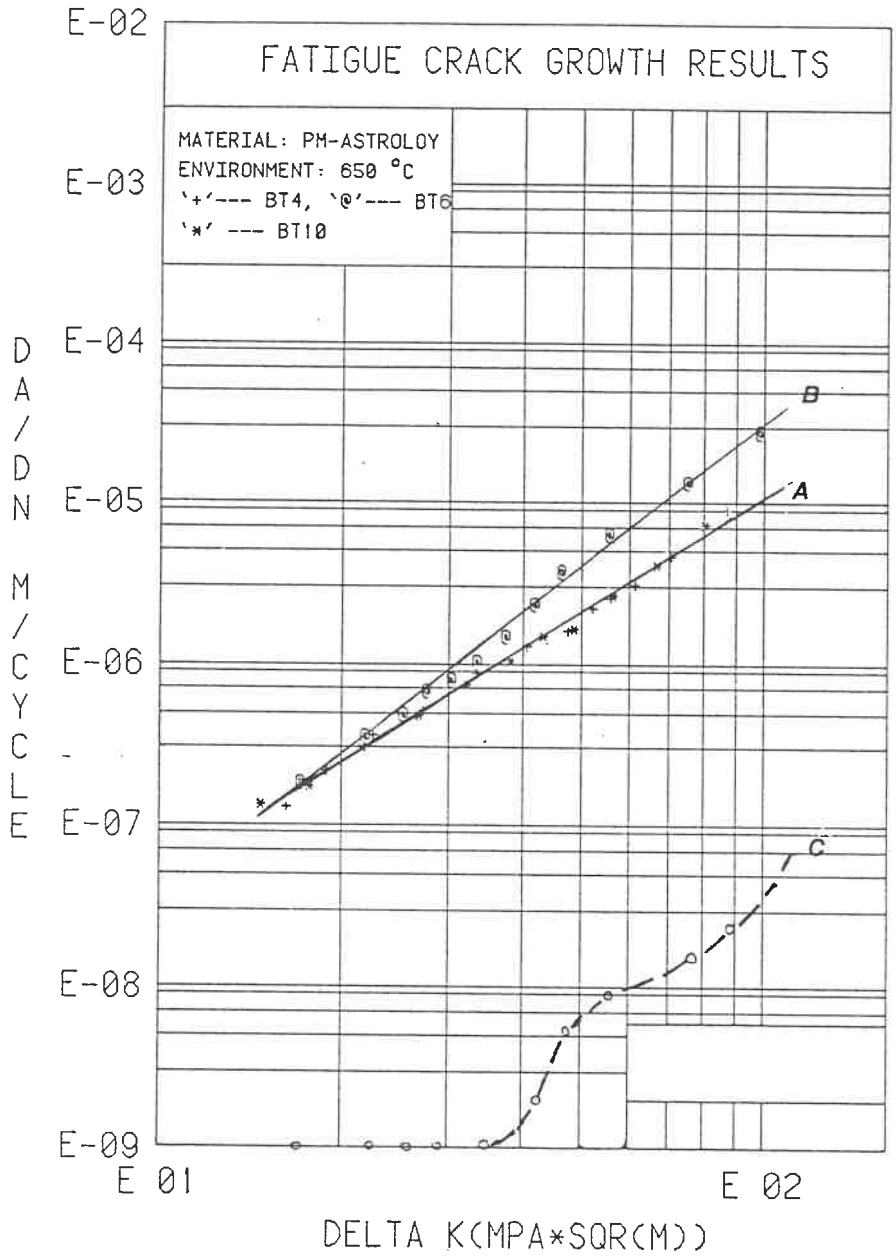

FIG. 6-1: LINEAR SUMMATION OF FCPR DAMAGE: A. ASSOCIATED WITH APPLIED MAJOR CYCLE; B. ASSOCIATED WITH MAJOR-MINOR CYCLE; C. ASSOCIATED WITH MINOR CYCLE;

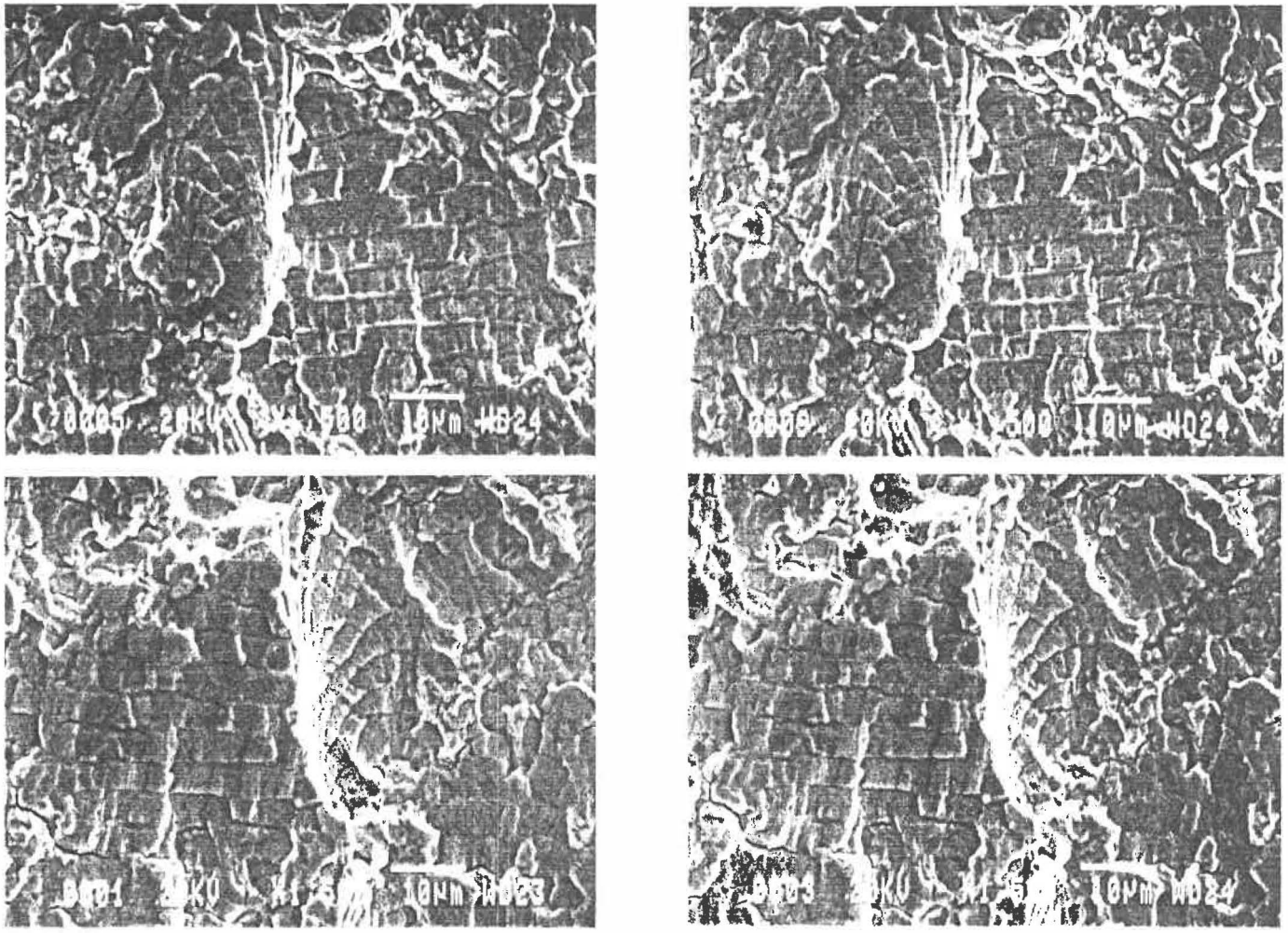

FIG. 6-2: MATCHING FRACTURE SURFACE FOR THE 0.1 MINOR CYCLE RANGE RATIO TEST (ΔK = 53.4 MPa$\sqrt{m}$, a = 2.4 mm).

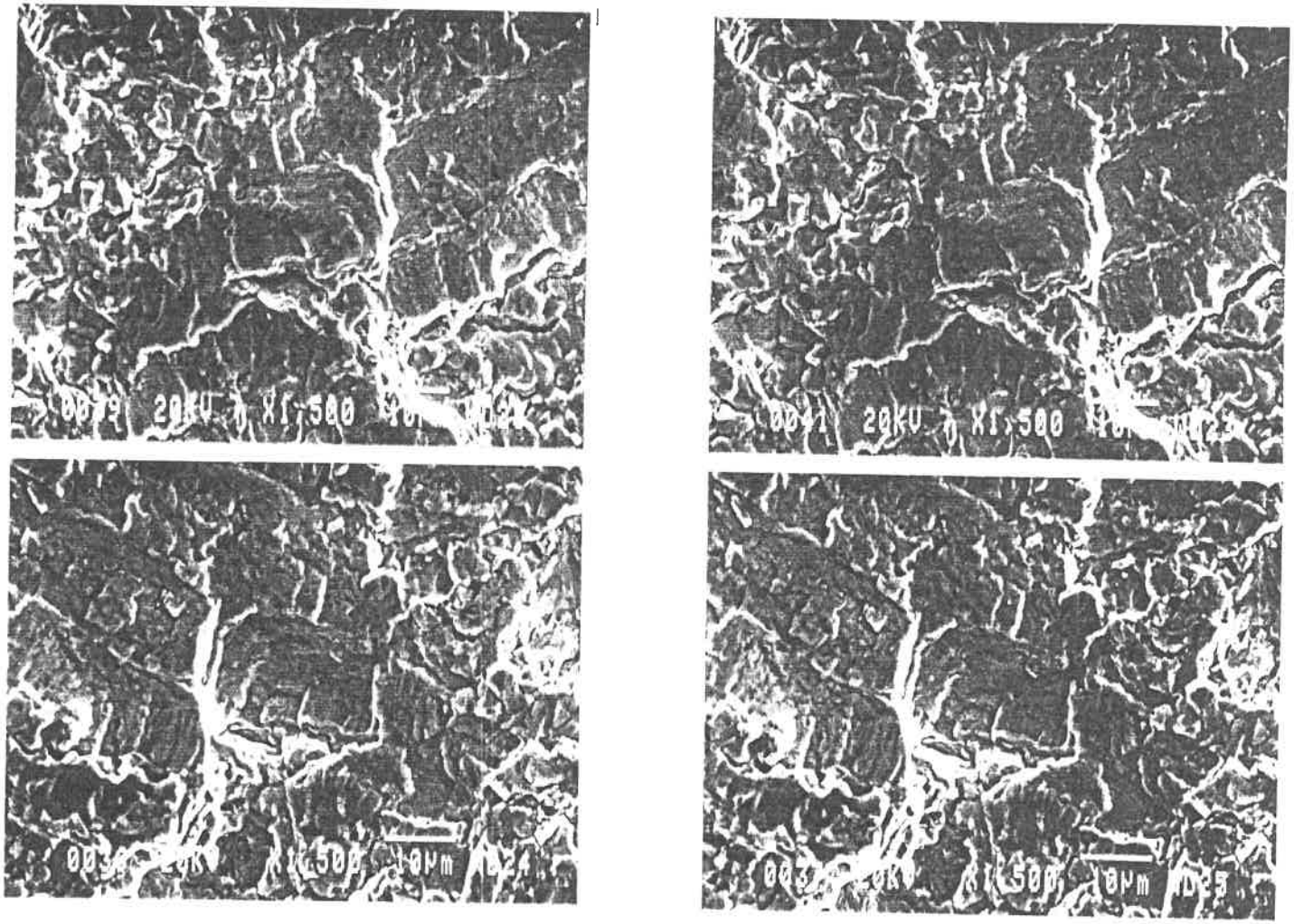

FIG. 6-3: MATCHING FRACTURE SURFACE FOR THE 0.05 MINOR CYCLE LOAD RANGE RATIO TEST (ΔK = 83 MPa$\sqrt{m}$, a = 3.9 mm).